

Understanding Drivers of Stratospheric Ozone Change and Fingerprinting its Recovery

by

Peidong Wang

B.S., University of Wisconsin-Madison (2019)

Submitted to the Department of Earth, Atmospheric, and Planetary Sciences
in partial fulfillment of the requirements for the degree of

DOCTOR OF PHILOSOPHY IN CLIMATE SCIENCE

at the

MASSACHUSETTS INSTITUTE OF TECHNOLOGY

May 2025

© 2025 Peidong Wang. This work is licensed under a [CC BY-NC-ND 4.0](#) license.

The author hereby grants to MIT a nonexclusive, worldwide, irrevocable, royalty-free license to exercise any and all rights under copyright, including to reproduce, preserve, distribute and publicly display copies of the thesis, or release the thesis under an open-access license.

Authored by: Peidong Wang

Department of Earth, Atmospheric, and Planetary Sciences

May 2, 2025

Certified by: Susan Solomon

Lee and Geraldine Martin Professor of Environmental Studies and Chemistry
Thesis Supervisor

Accepted by: David McGee

William R. Kenan, Jr. Professor

Head of the Department of Earth, Atmospheric, and Planetary Sciences

Understanding Drivers of Stratospheric Ozone Change and Fingerprinting its Recovery

by

Peidong Wang

Submitted to the Department of Earth, Atmospheric, and Planetary Sciences
on May 2, 2025 in partial fulfillment of the requirements for the degree of

DOCTOR OF PHILOSOPHY IN CLIMATE SCIENCE

ABSTRACT

Stratospheric ozone serves as Earth's natural protective layer, shielding the surface from harmful ultraviolet radiation. The discovery of the Antarctic ozone "hole" in the late 1980s raised significant societal and scientific concern, prompting the rapid regulation of ozone-depleting substances (ODSs) under international treaties. While the signs of ozone recovery have begun, new challenges continue to arise. This thesis investigates three critical factors driving stratospheric ozone changes and the influencing the detection of ozone recovery: (1) ODS emissions, (2) chemical chlorine processes, and (3) internal climate variability.

As ODS emissions being regulated under the Montreal Protocol and studies now focus on illicit new productions on the order of tens of gigagrams per year, the ocean's role as both a natural source and sink of ODSs becomes increasingly important. However, these processes have often been overlooked or highly simplified in past ozone assessments. Using a hierarchy of models, from simple box models to global ocean general circulation models, I quantified the ocean's uptake and release of various ODSs. Chapter 2 examines the ocean's uptake of chlorofluorocarbons (CFCs), particularly emphasizing its influence on recent illicit CFC emissions estimation. Chapter 3 extends this analysis to include ocean uptake and potential microbial degradation processes, evaluating their effects on emission estimates for various hydrochlorofluorocarbons (HCFCs) and hydrofluorocarbons (HFCs), which are chemical constituents that have been used to replace CFCs.

Once these man-made ODSs reach the stratosphere, they are photolyzed to chlorine reservoir species (e.g., HCl and ClONO₂), which, through heterogeneous reactions, can

transform into reactive chlorine that depletes ozone. While heterogeneous chlorine activation on volcanic ash is well understood, the unprecedented 2020 Australian wildfires raised new questions about chemical processes on smoke particles. This knowledge gap exists because only a few wildfires have injected significant amounts of smoke particles into the stratosphere during the satellite era. Leveraging over 30 years of satellite data, I separated chemical and dynamic processes affecting chlorine reservoir species to quantify chemical chlorine activation across different aerosol types. In Chapter 4, I developed a new approach to quantitatively estimate the onset temperature for chemical chlorine activation after the 2020 Australian wildfire using satellite observations. Chapter 5 applies this method to compare the impact of chemical chlorine activation from two independent wildfire events with that from a series of volcanic eruptions of varying magnitudes.

Despite emerging challenges such as illicit emissions and recent wildfires and volcanic eruptions, advancements in observational records, our understanding of ozone chemistry, and computational power have significantly enhanced our ability to quantitatively detect and attribute stratospheric ozone changes. In Chapter 6, I applied a pattern-based “fingerprinting” technique to quantitatively separate the contributions of ODS forcing from other external forcings and internal variabilities in satellite observations. This analysis shows that Antarctic ozone increases cannot be explained by climate internal variability alone, providing strong confidence that ozone recovery is underway, primarily driven by human efforts to reduce ODS emissions.

Thesis supervisor: Susan Solomon

Title: Lee and Geraldine Martin Professor of Environmental Studies and Chemistry

Acknowledgments

As I sit in my hotel room in Boulder, attending the CESM Working Group Meeting and beginning to write my acknowledgments, I find myself reflecting on the past few years. I feel incredibly fortunate to have met so many wonderful people whose support has shaped my journey and brought me to this point.

I was born in the winter, and it has always been my favorite season. I am drawn to the purity and tranquility of a world blanketed in snow. More than anything, I have long dreamed of setting foot in Antarctica, witnessing with my own eyes the last untouched wilderness on Earth. I still remember January 31, 2019—the coldest day in Madison during my undergraduate years, when the polar vortex shut down the campus for the first time. But it did not shut down my curiosity for nature. Before sunrise, I stood on the completely frozen Lake Mendota with faculty and students from our department, launching a weather balloon to study this extreme cold. A photo of me holding the weather balloon was also featured in *Moments in Time 2019* on the university’s website. That very same afternoon, I received my PhD offer from MIT to work with Dr. Susan Solomon, who had led a scientific expedition to Antarctica 40 years ago and explained the cause of the Antarctic ozone “hole”. Looking back, everything seems to have aligned as if guided by fate, much like my first encounter with Susan.

I first met Susan in Boulder during my junior year as an undergraduate. We struck up a conversation while waiting in line during the coffee break at a CESM workshop in NCAR’s Foothills Lab. Later after her seminar, many hands went up for questions and Susan chose mine, saying, “Let’s give the young people a chance.” That moment left a deep impression on me, as did her unwavering support for students, as always. In 2021, I published my very first paper with Susan. To celebrate, she ordered 30 physical copies from the publisher for me as a keepsake—something her own advisor had once done for her. Susan said, “Passing it on to the next generation is always a joyful process.” Her vast knowledge and unconditional support have given me the freedom to explore endlessly in all the directions that interest me—from the stratosphere down to the ocean, and from the tropics extending to the poles. Susan has been a role model for me, and my PhD journey with her has only strengthened my

determination to one day become a scientist like her—one who pursues research with deep curiosity, integrity, and a commitment to making a difference.

Of course, my PhD journey has not always been smooth sailing. The COVID-19 pandemic swept through Boston in early spring 2020, just as I was beginning my second semester at MIT. What followed was nearly two years of isolation—a period that reshaped not only daily life but also the way we learn, work, and conduct research. Quarantined in my dorm room, I completed my generals training for the PhD qualifying exam, a key milestone on the path to earning a doctorate. I am deeply grateful to my thesis committee—Dr. Andrew Babbin, Dr. John Marshall, Dr. Paul O’Gorman, and Dr. Dave Thompson—who were assembled during the pandemic, a time when even the simplest act of casually running into each other to discuss research felt like a luxury. Despite these challenges, they were always incredibly responsive whenever I needed to schedule virtual committee meetings. My first generals project, supervised by Susan in collaboration with Andrew, John, and Dave, became chapter 2 of my thesis, and the modeling framework we developed laid the foundation for chapter 3 as well. For my second generals project, I worked with Paul and Dr. Janni Yuval on machine learning, an area that has since surged in popularity across many disciplines. Especially, the advent of large language models in 2022 marked a turning point in how people engage with technology, fundamentally reshaping the way work is approached across fields. I feel fortunate to have taken a machine learning class at MIT and to have been advised by Paul and Janni during this special period, as machine learning was beginning to transform both research and daily life, allowing me to keep pace with this rapidly evolving world.

Despite all the changes over the years, one thing that has remained was the dedication and passion of scientists for their work. I feel incredibly fortunate to have witnessed this through collaborations with Dr. Jeff Scott, Dr. Doug Kinnison, Dr. Ben Santer, and Dr. Qiang Fu, whose lifelong commitments to climate science are truly inspiring. They are among the best scientists in developing climate models and pushing the boundaries of how we can analyze and interpret model outputs. The first climate model I worked with was the MITgcm, and I can’t imagine how long it would have taken me to couple the atmosphere with the MITgcm ocean without Jeff’s enormous help. I also greatly enjoyed working with Doug, Ben, and Qiang on the ozone recovery project, where their expertise and passion for science made every discussion inspiring. It’s just as exciting to see that same dedication in the next generation of scientists, like Dr. Jun Zhang. I still remember the 2023 AGU, when we were walking through the streets of San Francisco late at night, caught up in an exciting research discussion. Jun couldn’t resist pulling out her laptop right there on the sidewalk to check the figures. The dedication and passion for science shown by generations of researchers have always inspired me to stay true to my curiosity about nature.

My favorite TV show is *The Big Bang Theory*. It reminds me how lucky it is to have the support of friends while pursuing research. I feel incredibly fortunate to have had many friends accompany me on this journey—some for a brief moment, others for over a decade. But no matter the duration, every friendship is vibrant and worth cherishing. I want to first thank the Solomon group: Dr. Kane Stone, Dr. Megan Lickley, Dr. Michael Weimer, Dr. Brian Zambri, Dr. Shim Yook, Dr. Yaowei Li, and my past and current officemates Dr. Catherine Wilka, Dr. Kasturi Shah, Jian Guan, Selena Zhang, and Candice Chen. I’m especially grateful to Selena, Candice, and Jian, who have captured many precious moments that not only fulfilled our picture wall but also my memory, including birthdays, housewarming parties, noodle nights, and more. I also want to thank Dr. Hongwei Sun, who taught me how to run back trajectory models; Dr. Glenn Liu, with whom I explored machine learning in our class project; and Dr. Minde An, from whom I learned so much about inversions and ODS emissions. Last but not the least, I would like to thank my friends who I’ve known since my undergraduate years. Dr. Gesang Yangji, as vibrant and optimistic as the flower in her name, has always been a source of encouragement for me with her optimism and passion for life. And Dr. Ziyuan Zhang, who has stimulated me to start doing research as an undergraduate.

My undergraduate years at the University of Wisconsin-Madison were a major turning point for me; it was during this time that the world of knowledge unfolded before me, revealing not just what I wanted to learn, but who I wanted to become. I am especially grateful for the liberal arts education, which allowed me to explore various fields and discover my true interests. It also enabled me to freely pursue mathematics as a double major, a decision that has since proven invaluable in my atmospheric science research. I was introduced to the field of atmospheric chemistry by Dr. Tracey Holloway, with whom I worked for three years during my undergraduate studies. Tracey played a pivotal role in guiding and supporting me—she witnessed my growth, celebrated my achievements, and encouraged me at every step. When my parents couldn’t attend my graduation in Madison, Tracey not only went to the ceremony on my behalf but also took me out with her family for a lovely dinner and a Marvel movie night to celebrate. Even years after graduating, I still love sharing every milestone and exciting moment with her, and I look forward to sharing many more chapters of my life with her.

Finally, I would like to express my deepest gratitude to my dad Dr. Suomin Wang, my mom Qiuju Lian, and my paternal and maternal grandparents. The support of three generations has been instrumental in shaping my journey, and I would not be where I am today without their unwavering belief in the power of “education”. In my grandparents’ era, resources were scarce, yet they sacrificed their own comfort to ensure that my father could pursue his education. Coming from a rural village, my father became the first in his

family to not only attend university but also earn a PhD. On my mother's side, my maternal grandparents uprooted their lives, leaving their home in a rural village in Henan Province to move to Lanzhou, all so that their children could receive a better education in the city. I am especially grateful to my parents for supporting my every decision without hesitation. When I chose to study abroad for my undergraduate degree, even though it meant being oceans apart and seeing each other only rarely, they never discouraged me. They also never expected me to follow in my father's footsteps and study botany. Instead, they gave me the freedom to pursue what truly interested me. Growing up, I sometimes resisted the emphasis my family placed on education, but over time, I have come to deeply appreciate it. Education not only has the power to change one's future but also offers new dimensions to understand and appreciate this world. I am profoundly grateful to my parents for not only giving me the opportunity to experience this world, but also for offering me different perspectives that have allowed me to discover its beauty in my own way.

I see myself as a traveler, passing through this world for only a brief moment—meeting people from all walks of life, witnessing nature's wonders, deciphering the rules of this universe, and immersing myself in the wisdom and culture left behind by history. I must acknowledge how incredibly fortunate and privileged I am to experience the best this world has to offer. If, in this fleeting journey, I can help even a few others see its beauty—and pass it on to the next generation of travelers intact—then this journey will have been truly worthwhile.

Contents

<i>List of Figures</i>	13
<i>List of Tables</i>	31
1 Introduction	33
2 On the Effects of the Ocean on Atmospheric CFC-11 Lifetimes and Emissions	39
Abstract	39
2.1 Introduction	40
2.2 Data and methods	43
2.2.1 Emission data	43
2.2.2 Box model equations	44
2.2.3 MITgcm model	44
2.2.4 MITgcm forcing fields	45
2.2.5 MITgcm RCP8.5 setup	46
2.2.6 Top-down inferred emission based on the MITgcm output	46
2.3 Results	48
2.3.1 Near-term CFC-11	48
2.3.2 Box model sensitivity tests	49
2.3.3 Effect of the ocean on atmospheric CFC-11 concentration	51
2.3.4 Effect of the ocean on CFC-11 lifetime and emission estimates	55

2.3.5	Effect of climate change on CFC-11 ocean uptake	57
2.4	Discussion	59
	Appendix	62
3	On the Influence of Hydroxyl Radical Changes and Ocean Sinks on Estimated HCFC and HFC Emissions and Banks	73
	Abstract	73
3.1	Introduction	74
3.2	Data and methods	76
3.2.1	Ocean representation	77
3.2.2	Atmosphere representation	78
3.2.3	Inferring the atmospheric residence times and the emissions	80
3.3	Results	81
3.3.1	Relative magnitudes of different loss pathways	81
3.3.2	Inferred atmospheric residence times	81
3.3.3	Inferred global emissions and bank estimations	83
3.4	Conclusions and discussions	86
	Appendix	89
4	Stratospheric Chlorine Processing after the 2020 Australian Wildfires Derived from Satellite Data	105
	Abstract	105
4.1	Introduction	106
4.2	Data and methods	108
4.2.1	Satellite datasets	108
4.2.2	Back trajectory calculation	109
4.2.3	HCl+ClONO ₂ reaction efficiency	109
4.3	Results	110

4.3.1	Separating dynamical and chemical processes	110
4.3.2	Cl processing in the mid-latitudes	115
4.3.3	Cl processing in the polar vortex region	117
4.3.4	Altitude-dependent Cl activation in the polar vortex region	118
4.4	Discussions	121
	Appendix	124
5	Contrasting Chlorine Chemistry on Volcanic and Wildfire Aerosols in the Southern Mid-Latitude Lower Stratosphere	133
	Abstract	133
5.1	Introduction	134
5.2	Data and methods	136
5.2.1	ACE and HALOE satellite data	136
5.2.2	Tracer-tracer correlation method	138
5.3	Results	140
5.4	Conclusions	145
	Appendix	148
6	Fingerprinting the Recovery of Antarctic Ozone	153
	Abstract	153
6.1	Introduction	154
6.2	Data and methods	155
6.2.1	Satellite data	155
6.2.2	Model and scenario descriptions	156
6.2.3	Signal and noise definition and uncertainty estimation	157
6.2.4	Vortex coverage and vortex averaged ozone calculation	158
6.3	Results	159
6.3.1	Observed and model-simulated ozone trends	159

6.3.2	Noise of ozone variability and ODS forcing	162
6.3.3	Signal-to-noise analysis of ozone changes	164
6.3.4	Antarctic springtime total ozone recovery	168
6.4	Summary and outlook	169
	Appendix	172
7	Concluding Remarks and Perspectives	181
A	Non-Local Parameterization of Atmospheric Subgrid Processes With Neural Networks	187
	Abstract	187
	<i>References</i>	189

List of Figures

2.1	Schematic diagrams showing a) the box model; and b) the MITgcm setup. The box model has three layers that represent the atmosphere, ocean mixed layer and deep ocean. Each layer has two boxes that indicate the NH and the SH. The MITgcm setup replaces the four ocean boxes with the MITgcm ocean but keeps the atmospheric boxes unchanged. One-way arrows indicate CFC-11 atmospheric loss; two-way arrows indicate CFC-11 transport into/out of the box.	43
2.2	a) Model validation of CFC-11 atmospheric abundances compared to CFC-11 atmospheric surface data (14); b) the MITgcm ocean column integrated CFC-11 under Hist run; and c) observations of ocean column integrated CFC-11 (Willey et al., 2004). Panels b and c both show the CFC-11 inventories in the year 1994, and are in the same units of mol km ⁻² .	47

2.6 a) Box model CFC-11 inventories for the atmosphere (left axis and solid lines) and the ocean (right axis and dashed lines). Black lines indicate CFC-11 inventories with unmodified parameters as in Appendix Table 2.2, and colored lines display $\pm 15\%$ changes of these associated parameters (only the results from most sensitive parameters are shown in the figure). b) MITgcm CFC-11 inventories under additional ocean forcing runs. In both panels, the ocean inventory is shown inversed in sign to facilitate comparison.	63
2.7 Similar to Figure 2.3, but for CFC-12.	64
2.8 a–d) Decadal averages of CFC-11 air-sea flux (area integrated) for different time periods in the MITgcm Hist run (positive indicate fluxes going into the ocean); e–h) Zonal mean CFC-11 concentration in the ocean for the same averaging periods shown on the left.	65
2.9 Similar to Figure 2.4, but for CFC-12.	66
2.10 Same as Figure 2.3, except that atmosphere-only CFC-11 lifetime calculated from SPARC chemistry-climate models are overlaid for comparison. Thin gray lines are calculated time-dependent atmosphere-only lifetimes from the SPARC models from 1960 to 2010, while the heavy black line is the SPARC multi-model mean.	67
2.11 a) Zonal mean residual AMOC under Hist run averaged in 1930–2000; b) Zonal mean residual AMOC under RCP8.5 run averaged in 2200–2300; c) Time series of AMOC strength (maximum between 20–50 °N) under full RCP8.5, SST + Qnet only and SSS + E-P only. Under full RCP8.5, AMOC in the MITgcm has decreased by 60 % from 1930–2000 to 2200–2300. This percent decrease is comparable to MPI-ESM-LR, which shows a 56 % decrease during the same period, except that the AMOC climatology in MPI-ESM-LR started at a higher value than the MITgcm at the beginning of 1930.	68

2.12 Anomaly maps of all the forcing fields from the MPI-ESM-LR RCP8.5 scenario. The maps indicate averages of the last 100 years (2200–2300) minus the base period (1850–1930).	69
2.13 CFC-11 inventory difference between each RCP8.5 forcing run and Hist forcing run for a) atmosphere inventories; and b) ocean inventories.	70
3.1 Global atmospheric residence times for all the species used in this study. Gray dotted lines are the steady state lifetimes calculated from the AGAGE 12-box model based on atmospheric removal rates from the World Meteorological Organization (WMO), 2022 report. Black dashed lines are inferred from a model simulation with fixed OH over time and without ocean uptake. Blue solid lines are inferred from models with fixed OH over time but including ocean dissolution without degradation, while blue dashed lines assume a 5 yr ocean degradation timescale, blue shadings denote the case for ocean degradation timescale up to 1 yr. Red solid lines indicate a 10 % increase in OH from 1980 to 2005 and are constant beyond 2005, and the red shadings indicate ± 15 % OH changes from 2005 to 2050. The purple dash-dotted lines combine the increasing OH (both 10 % increase in 1980–2005 and 15 % increase in 2005–2050) with a 1 yr ocean degradation timescale to define a lower limit range.	82
3.2 Inferred global emissions for all the species modeled in this study, based on the different residence times for the cases considered in Figure 3.1.	84
3.3 Summed emissions of all the HCFCs and HFCs in this study weighted by their global warming potentials. The absolute emissions are shown in panel a), and the differences between the emissions inferred from transient residence times and steady state lifetimes (assuming no ocean and fixed OH) are shown in panel b).	85

3.4 Henry's law solubility for HCFCs and HFCs considered in this study. X-axis shows the temperature and the y-axis shows the salinity. Color bar limits in different panels vary.	93
3.5 Panel a shows the Schmidt number as a function of temperature for all the molecules considered in this study. Panel b compares the Schmidt calculated in Text S1 compared to values reported by Wanninkhof, 1992 for CFC-11 and CFC-12. Overall our calculation shows good agreement with Wanninkhof, 1992.	94
3.6 The model (without ocean uptake) simulated atmospheric mole fractions (colored lines) in the Northern Hemisphere (30–90 °N) and Southern Hemisphere (30–90 °S) compared to the observations from AGAGE measurements (black markers).	95
3.7 Different OH scenarios used in this study. The y-axis shows the prescribed percent change in OH from each year compared to the pre-1980 value. Fix OH scenario has no OH trend over time. Variable OH scenarios all have a consistent 10 % increase from 1980 to 2005, but then either keep OH constant or impose a ± 15 % trend from 2005 to 2050. The range of OH change after 2005 is represented as red shading in Figures 3.1–3.3, and Appendix Figures 3.11–3.13.	96
3.8 Loss rates for different species (each row) due to reaction with OH (left panels), ocean sink (without degradation; middle panels), and other factors (mainly stratospheric photochemistry; right panels). Different latitude bands are marked with different colors indicated in the legend in panel a).	97
3.9 Ocean (without degradation) column integrated amounts of the three HCFCs used in this study. Panels a, c, e show the decadal average from 2010 to 2020, and panels b, d, f show the decadal average from 2040 to 2050. Note that the color bar limits are different for different species.	98
3.10 Similar to Appendix Figure 3.9, but for the three HFCs.	99

3.11	Similar to Figure 3.2, but shows the differences in the inferred emissions using different transient residence times to the inferred emissions using steady state lifetimes (assuming no ocean and fixed OH).	100
3.12	Similar to Figure 3.2, but with emissions weighted by the global warming potential (for a 100-year time horizon) for each species.	101
3.13	Differences in the bank estimation calculated from emissions based on transient residence times and steady state lifetimes.	102
4.1	The monthly mean ACE data for (A) CO, (B) HF, (C) HCl, and (D) ClONO ₂ at 18.5 km averaged over 40–55 °S. Red dots are from 2020, purple dots are from 2021, blue dots are from 2012 (used as a reference year in this study), and gray dots are from 2004–2019 (excluding 2012). 40–55 °S is split into 3 equally spaced latitude bins and months with at least 5 samples (at least 1 sample per latitude bin) are considered in the averaging processes.	110
4.2	Tracer-tracer correlation between ACE-measured HF (x-axis) and (A) HCl, (B) ClONO ₂ , and (C) HCl+ClONO ₂ (y-axes), color-coded by temperature. Each dot represents a single measurement at 18.5 km over 40–55 °S. Dots in 2020 and 2021 are highlighted with triangles and crosses, respectively (with gray edges). Each subplot shows a different month from March to July, labeled at the bottom right corner. The number of data plotted in each month is shown in the legend. The thick black lines represent the “no-chemistry” baseline, from the linear fit over March 2004–2019 data points. The shaded regions indicate a conservative full range of baseline variability bounded by the maximum and minimum baselines constructed by data in individual years from 2004 to 2019. A demonstration of how ΔCl (e.g. in Figure 4.4) is calculated is shown here as the vertical blue dashed line in the April panel for HCl, representing the change in Cl due to chemical processes.	112

4.3	Monthly anomalies for (A) HCl, (B) ClONO ₂ , and (C) HCl+ClONO ₂ in May 2020 compared to the May climatology in 2004–2019. The maps show a latitudinal range between 50 °S and 90 °S since ACE measurements in May are mainly between 58–68 °S. To prevent from biasing the anomalies by latitudinal variations, the climatological mean is constructed at every 5-degree latitude bin. Therefore, the May anomalies presented here are calculated from four latitude bins from the climatology (50–55, 55–60, 60–65 and 65–70 °S).	115
4.4	Cl activation as a function of temperature at mid-latitudes (40–55 °S) for March–July at 18.5 km. Each panel shows the amount of Cl activation on the y-axes (deviation from the “no-chemistry” baseline in Figure 4.2) as a function of temperature (x-axis) for (A, D) HCl, (B, E) ClONO ₂ , and (C, F) HCl+ClONO ₂ . Panels A–C use the ACE-measured temperature at the satellite overpass, and panels D–F use the minimum temperature (T_{\min}) calculated along the 5-day back trajectories for each data point for 2020, 2021, and 2012. Thick lines are the average of Cl activation at every 2 K temperature ranges (temperature bins with less than 2 samples are not considered for the average). The shading areas indicate the full range of Cl departures from individual baselines using data from single years. Horizontal and vertical gray dashed lines indicate zero Cl activation and 195 K, respectively. The probability distribution functions (PDF) of Cl activation at $T_{\min} \geq 195$ K are shown in panels D–F for 2020, 2021, and 2012.	119
4.5	Cl activation as a function of temperature in the polar vortex region (65–90 °S), as in Figure 4.4 for mid-latitudes. Panels A–C use the ACE-measured temperature at the satellite overpass, and panels D–F use the minimum temperature (T_{\min}) calculated along the 5-day back trajectories for each data point for 2020, 2021, and 2012.	120

4.6 The altitude-dependent Cl activation in the polar vortex region ($65\text{--}90^\circ\text{S}$) for (A) 2012, (B) 2020, and (C) 2021. X-axis shows the minimum temperature calculated along the 5-day back trajectories, and the y-axis shows the Cl activation from the sum of HCl and ClONO ₂ . Only the Cl activation calculated from baselines using all available data from 2004 to 2019 is shown here. Each line represents a different altitude range from 14.5 km to 18.5 km. The panels are zoomed in for 190–205 K to focus on the onset temperature for Cl activation on PSCs.	121
4.7 Monthly anomalies of (A) HCl and (B) ClONO ₂ in 2020 compared to the 2004–2019 climatology, as a function of the month (x-axis) and altitude (y-axis) over $40\text{--}60^\circ\text{S}$	124
4.8 Tracer-tracer correlation in the polar vortex region ($65\text{--}90^\circ\text{S}$), as in Figure 4.2 for mid-latitudes. There is no data in June at this latitude range.	125
4.9 Tracer-tracer correlation between N ₂ O (x-axis) and HCl (y-axis) in the mid-latitude ($40\text{--}55^\circ\text{S}$), similar to Figure 4.2, but comparing ACE and MLS measurements in each row. Top row (panel A) shows results from ACE individual measurements at 18.5 km. Middle row (panel B) shows results from MLS zonally averaged data at 68.2 hPa. Bottom row (panel C) shows results from MLS individual measurements at 68.2 hPa.	126
4.10 Tracer-tracer correlation between N ₂ O (x-axis) and HCl (y-axis) in the polar vortex region ($65\text{--}90^\circ\text{S}$), as in Appendix Figure 4.9 for mid-latitudes.	127
4.11 Similar to Figure 4.3, but for 2021. Note that the colorbar here shows a smaller range because the magnitude of the Cl anomalies are smaller in 2021.	128

4.12 Sanity check on ACE and ERA5 temperature at 18.5 km. X-axis shows the ACE-observed temperature (ACE T), and the y-axis shows the ERA5 temperature at the closest rounded location and time with ACE satellite overpass (ERA5 T_0) for individual data points in 2020 (red), 2021 (purple), and 2012 (blue) over the full latitude range we use in this study ($40\text{--}90^\circ\text{S}$). The black dotted line indicates the 1-1 ratio. The total coefficient of determination R^2 value for ACE T and ERA5 T_0 (concatenating all three years) is 0.97, with a mean bias of 1.1 K.	129
4.13 Sensitivity test for the back trajectory calculation at different starting locations at 18.5 km. X-axis shows the minimum temperature from the 5-day back trajectory starting at the closest latitude/longitude from ACE observation. Y-axis shows a similar 5-day minimum temperature from back trajectory calculations but for data points released at ± 1 degree latitude and longitude from the satellite overpass location. The dashed black line indicates the 1-1 ratio. With such perturbations in the starting location, T_{\min} can have a mean bias at -0.8 K.	130
4.14 Cl activation as a function of temperature at the core of the polar vortex region ($70\text{--}90^\circ\text{S}$). Most of the data points in Figure 4.5 are over $65\text{--}70^\circ\text{S}$, which might not represent the behaviors within the core of polar vortex. This figure shows data points over $70\text{--}90^\circ\text{S}$, where data is only available in March and April (when temperatures are well above 200 K).	131

- 4.15 (A) shows the ACE measured July H₂O in the polar vortex region (65–90 °S) at different altitudes from 14.5 km to 18.5 km. The spread of H₂O is around 3.5 ppm to 4.5 ppm. (B) shows the γ value (reaction efficiency of HCl+ClONO₂) calculated from a similar parameterization used in WACCM at a fixed temperature of 195 K at different altitudes. γ values are normalized as ratios compared to the reaction efficiency at 18.5 km. An adopted spread in H₂O volume mixing ratio of ± 0.5 ppm from 4 ppm is shown in panel B, illustrating that water vapor mixing ratio has a small effect on the reaction efficiency, while pressure plays a dominating role for the background condition. At lower altitudes (high pressure), the efficiency of the HCl+ClONO₂ reaction is significantly enhanced compared to higher altitudes (low pressure). 132
- 5.1 Time series for monthly mean A) temperature, B) CH₄, C) HCl, and D) aerosol extinction in 1992–2005 (from HALOE) and 2004–2023 (from ACE) between 30–45°S at 68 hPa. The gray shading in aerosol extinction during the HALOE period represents uncertainty when converting aerosol extinction from 3.45 μ m to 1020 nm (discussed in Section 5.2.1 in detail). The black dashed line in panel D shows 1020 nm aerosol extinction at 18.5 km from GloSSAC averaged from a similar latitude range. 137
- 5.2 Tracer-tracer scatter plots between detrended CH₄ (x-axis) and detrended HCl (y-axis) color coded by aerosol extinction in HALOE and ACE at 30–45 °S at 68 hPa. Only the Pinatubo years (1992–1994) and ANY years (2020–2021) are identified by specific markers as they show the most significant changes during each satellite mission (Appendix Figure 5.8 shows these events in separate panels to avoid overlapping points). Shadings indicate a full range of interannual variability (discussed in detail in Section 5.2.2) for HALOE (in blue) and for ACE (in orange). Note that there is no data coverage at the chosen latitude in May from ACE. 139

5.3	ΔHCl (negative values suggest a net loss in HCl due to chemistry) in 30–45 °S at 68 hPa as a function of aerosol extinction at individual satellite overpass. Results are grouped in panels showing different temperature ranges (based on 5-day minimum temperatures from the back trajectory calculation for each point, a similar figure but using satellite observed temperature is shown in Appendix Figure 5.6). Two background years, and consecutive years after major volcanic eruptions and the wildfires are highlighted with different markers and colors. The blue and orange shadings surround zero line indicate the full range of interannual variability during the HALOE and ACE periods.	142
5.4	ΔHCl in 30–45 °S at 68 hPa from 1992 to 2023 binned by aerosol extinction (at every $5 \times 10^{-5} \text{ km}^{-1}$, each bin is averaged by at least 3 data points). The black line shows the averaged net chemical impact on HCl in background and volcanic eruption years. The red lines show the two consecutive years after the ANY fire (solid line for 2020, dashed line for 2021). The yellow line shows the 2009 ABS fire. Color shadings indicate ± 1 standard deviation from the mean for data averaged in each aerosol extinction bin.	144
5.5	ΔHCl in March–July calculated from ACE in 30–45 °S at 68 hPa during 2004–2023, using detrended HF as the inactive tracer (x-axis) and detrended CH ₄ as the inactive tracer (y-axis). The volcano and wildfire years (2009, 2015, 2016, 2020, 2021, 2022, 2023) are shown as red dots, and the rest of the years are shown as gray dots. The black dashed line indicates the 1:1 ratio. CH ₄ - and HF-derived ΔHCl are consistent with each other, although CH ₄ -derived ΔHCl has a mean bias of -0.01 ppb compared to HF-derived ΔHCl	148
5.6	Similar to Figure 5.3, but the points are grouped in panels based on satellite observed temperature instead of the 5-day minimum temperature from the back trajectory model.	149

5.7 Similar to Figure 5.2, but only for ACE data (excluding Calbuco, ANY, and Hunga), and each point is color coded by CO instead of aerosol extinction. CO serves as an indicator for biomass burning. Since CO has a strong latitudinal gradient (higher CO at lower latitudes), the CO values shown here are anomalies compared to climatological mean binned in every 3 degrees of latitude. The 2009 ABS fire is highlighted with triangle markers.	150
5.8 Similar to Figure 5.2, but Pinatubo, ANY, and background years are shown in separate rows to avoid overlapping different events.	151
6.1 Month-height patterns of ozone trends in observations and simulations. The middle row shows the least-squares linear trends in ozone over 2005–2018 as a function of month and pressure in the MLS observations (c), the WACCM 10-member ensemble mean (d), and the CCMI 19-model ensemble mean (e). Results are for spatial averages over 66–82 °S. We also show the time series of ozone anomalies (relative to the 2005–2018 mean) at four illustrative locations (indicated by different markers on the contour figures) in February at 1.8 hPa (a), June at 10 hPa (b), September at 82.5 hPa (f), and October at 12.1 hPa (g). Thick blue and red lines are the model ensemble means, while the thin lines are the ozone time series in individual model realizations. The black solid line is from MLS. Time series after 2018 are shown as dashed lines because of likely impacts of exceptional perturbations from the 2019 SSW, 2020 Australian wildfire, and 2022 Hunga eruption.	161

6.2 Ozone variability modulated by external forcing. Panels a, b show the month-height patterns of the standard deviation of ozone trends (averaged over 66–82°S) in the WACCM historical and refC2 scenarios, after first removing the ensemble mean. The standard deviation is a measure of the trend uncertainty arising from internal variability among the 10 WACCM ensemble members. Both scenarios have the same trend length of 14 years: the historical scenario analysis period is from 1955 to 1968 and the refC2 analysis period is from 2005–2018. Panel c shows (for the white dashed box in the top panels), the residual internal variability in WACCM and MLS ozone after first removing the mean forced response of monthly-mean ozone. Results are expressed as percent changes relative to the MLS annual-mean climatology. The thick lines are the Gaussian fits to the distributions. Panel d displays the same data shown in panel c, but in terms of the absolute monthly ozone mixing ratios. The number of data points in each distribution is indicated in the legend. A similar figure for CCM1 models is shown in Appendix Figure 6.7; while the noise pattern is qualitatively similar to that of WACCM, the CCM1 multi-model ensemble also reflects different model responses to forcing which can inflate noise compared to a single-model ensemble.

6.6 Ozone trends due to different forcings. Ensemble-mean ozone trends (2005–2018) averaged over 10 WACCM members for each scenario. Results indicate the forced responses in ozone due to: a combined time-evolving GHG and ODS forcing (refC2), b evolving GHG forcing only (fODS); and c evolving ODS forcing only (fGHG). A detailed description of each scenario is given in the Methods section. The observed ozone trend from MLS in 2005–2018 is also shown in panel d for visual comparison with forced ozone trends due to different forcings.	173
6.7 Ozone variability modulated by external forcing. Similar to Figure 6.2 but for the CCMI models. Note that the spread in ozone trends in CCMI arises not only from internal variability, but also from cross-model differences and errors (discussed in detail in the Methods section). This convolving of internal variability with model differences and errors contributes to the larger noise in panel a compared to the noise derived from the WACCM single-model refC2 ensemble in Figure 6.2b.	174
6.8 The local signal-to-noise characteristics of ozone changes. Similar to Figure 6.3 but with results for the CCMI models.	175
6.9 The local signal-to-noise pattern of ozone changes. Similar to Figure 6.3 but for signal and noise estimates based on ozone trends over 2005–2023 (rather than over 2005–2018). There is a significant decrease in MLS ozone in October and November in the middle stratosphere, and in January through May in the lowermost stratosphere. This raises the question of whether these two features may be linked. The bottom panel shows the timeseries of ozone mixing ratios from MLS in October at 12.1 hPa (blue) and in February at 82.5 hPa (orange). The decrease in February at 82.5 hPa is mainly due to continued low ozone after 2021 (panel c), which lags the behavior in October by about a season, suggesting that they may be linked.	176

6.10 Time of emergence of springtime total column ozone recovery. Similar to the top and bottom panels in Figure 6.3, except the trends are the TCO from WACCM and OMI.	177
6.11 Map of MLS ozone anomalies and polar vortex in October at 12.1 hPa. The color shadings indicate the ozone anomaly relative to the zonal mean in 2005–2018. Because the location of the polar vortex can vary considerably over time, dotted markers indicate that the polar vortex has occupied a given grid box for more than 25 % of the time in that month. Black dashed lines encompass the area between latitudes 66–82 °S.	178
6.12 MLS springtime ozone trends (2005–2018) using fixed latitude averages versus vortex averages. Monthly mean ozone trends in September, October, and November from 2005 to 2018 are shown as blue lines (where ozone is averaged across fixed latitudes between 66–82 °S) and red lines (where ozone is averaged inside the polar vortex) at different pressure levels. A detailed description of the vortex calculation is provided in the Methods section. Dots and crosses indicate trends significant at the 5 % and 10 % levels, respectively. Note that the statistical confidence in this figure is based solely on p-values from linear regression. It does not rely on internal variability noise generated by WACCM or the CCMI models, as shown in other figures.	179

List of Tables

2.1	Calculated loss of CFC-11 in the atmosphere assuming a constant 55-year lifetime, loss of CFC-11 to the ocean as air-sea flux (positive values indicate a flux of CFC-11 from the atmosphere to the ocean), and relative loss in the ocean compared to that in the atmosphere from the MITgcm simulations. Values for several decades around the period of maximum loss in the atmosphere (1990s), the period of maximum flux of CFC-11 from the ocean to the atmosphere (2120s) and the outgassing late in the 23rd century are shown in the table. Error bars indicate ± 1 standard deviation associated with the decadal average.	54
2.2	A list of parameters and variables used in the box model.	71
3.1	Henry's law solubility for HCFCs and HFCs used in MITgcm. T is the ocean temperature in degrees Kelvin, and S is the ocean salinity in the units of per mille. $A1$ to $A4$ and $B1$ to $B3$ are coefficients fitted from the Ostwald solubility from P. Li et al., 2019	103
3.2	Schmidt number for HCFCs and HFCs used in the MITgcm. t is ocean temperature in degrees Celsius. A detailed description of the calculation of coefficients $Sca1$ to $Sca3$ is presented in the Appendix Text: Schmidt number estimation.	104

Chapter 1

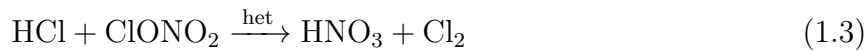
Introduction

Stratosphere, roughly located between 10 to 50 km above the Earth’s surface, contains a substantial amount of ozone (O_3), which plays a crucial role in absorbing harmful ultraviolet radiation from the Sun. This natural ozone layer is vital for protecting life on Earth. Molina and Rowland, 1974 first raised concerns that man-made chlorofluorocarbons (CFCs), primarily used as refrigerants and in spray foams, release chlorine atoms that can catalytically destroy O_3 in the stratosphere through the following reactions:



With atmospheric lifetimes ranging from a few decades to hundreds of years, CFCs can lead up to 20 % total column ozone loss in steady state if CFC emissions continued to increase indefinitely (Rowland & Molina, 1975). But in the short term, this catalytic cycle due to CFCs was expected to deplete total column O_3 by the order of 1 % (Rowland & Molina, 1975). Surprisingly, Farman, Gardiner, and Shanklin, 1985 found an up to 50 % depletion in column ozone during spring over Antarctic, which underscored the urgency of understanding and addressing the Antarctic ozone “hole” problem immediately. S. Solomon, Garcia, Rowland,

and Wuebbles, 1986 found that polar stratospheric clouds (PSC), typically formed under extremely low temperatures in the Antarctic winter in the lower stratosphere, provide surface area that is key for heterogeneous reactions such as:



to activate chlorine from their reservoir species, Cl₂ then photolyzes to Cl in the sunlit atmosphere during polar spring and destroys O₃ via catalytic reactions 1.1 and 1.2. A comprehensive list of key heterogeneous reactions is summarized in S. Solomon, 1999.

These and other scientific findings provided strong support for the implementation of the Montreal Protocol on Substances that Deplete the Ozone Layer. By 1996, the global production of CFCs had been completely phased out. CFCs were subsequently replaced by hydrochlorofluorocarbons (HCFCs), which, due to the presence of an additional hydrogen atom, can be removed more rapidly in the troposphere through reactions with hydroxyl radicals (OH). And HCFC production is also set for a complete global phase-out by 2030. Thanks to these global efforts to reduce emissions of ozone-depleting substances (ODS), the decreasing trend in global upper stratospheric ozone levels has paused in the early 2000s (Newchurch et al., 2003), and the Antarctic ozone levels during spring has also shown significant increases (S. Solomon et al., 2016). Not only has the Montreal Protocol been instrumental in addressing ozone layer depletion, but its Kigali Amendment, which targets the phase-out of greenhouse gas hydrofluorocarbons (HFCs), is also expected to contribute significantly to combating global warming (Velders et al., 2022). These achievements have established the Montreal Protocol as “the single most successful international environmental agreement to date,” according to Kofi Annan, the former Secretary General of the United Nations (United Nations Environment Programme, 2012).

In the era of ozone recovery, despite the continued decline in anthropogenic ODS emissions, unexpected illicit emissions, extreme wildfires and volcanic eruptions, and coupled chemistry-

climate feedbacks still pose significant challenges to understanding stratospheric ozone recovery. Investigating these drivers of stratospheric ozone changes is critical to strengthening the scientific foundation that underpins the Montreal Protocol. This thesis is organized as follows:

Chapter 2 develops a hierarchy of coupled atmosphere-ocean models, from a simple box model to an ocean general circulation model, to quantify the oceanic uptake and outgassing of CFCs and their impact on emission estimates. Recent studies have reported a slowdown in the decline of atmospheric CFC-11 mole fractions since 2012 (Montzka et al., 2018; Rigby et al., 2019). Inversion study based on measured atmospheric mole fractions of CFC-11 suggest an increase in emissions of ~ 10 Gg/yr from eastern China (Rigby et al., 2019). If such illicit emissions were to persist, ozone recovery could be delayed by about a decade (Dhomse et al., 2019; Fleming, Newman, Liang, & Daniel, 2020). Encouragingly, these illicit emissions have ceased after 2018 (Montzka et al., 2021; Park et al., 2021). On the other hand, CFC-11 is soluble in seawater and has been widely used as a passive tracer for studying ocean circulation (e.g., Ito, Marshall, and Follows, 2004; Romanou, Marshall, Kelley, and Scott, 2017). However, the oceanic uptake of CFC-11 has historically been neglected in emission estimates during periods of high anthropogenic emissions (Golombek & Prinn, 1986). As the focus of the ODS community shifts to unexpected emissions on the order of 10 Gg/yr, it is increasingly important to quantify how the ocean affects emission estimates of CFCs.

Chapter 3 extends the coupled atmosphere-ocean model to evaluate the ocean's role in emission estimates for a list of HCFCs and HFCs. HCFC emissions are set for a global phase-out by 2030. However, their use as feedstocks for manufacturing other compounds remains exempted from the Montreal Protocol. Over the past two decades, feedstock emissions have increased by fivefold (Daniel & Reimann, 2022), with leakage rates also larger than expected (Western et al., 2022). It is therefore important to quantify the uncertainties in emission estimates for these species due to natural processes, which could inform future policy decisions such as regulations on feedstock emissions (Andersen et al., 2021). Previous studies have primarily focused on estimating the oceanic partial lifetime by accounting for

destruction-only processes such as hydrolysis in seawater (Yvon-Lewis & Butler, 2002). These studies indicate that oceanic partial lifetimes for HCFCs and HFCs range from hundreds to thousands of years, which has led to the ocean being largely overlooked from emission estimations (Laube & Tegtmeier, 2022; Liang & Rigby, 2022). In this chapter, I treat the ocean as a temporary reservoir for HCFCs and HFCs, evaluating how its physical uptake and outgassing influence observed atmospheric mole fractions and emission estimates over the short term. In addition, this chapter also estimates the uncertainties in HCFC and HFC emissions arising from model-data discrepancies in atmospheric OH trends (Stevenson et al., 2020), which is a major atmospheric loss pathway for these species.

Chapter 4 examines the temperature dependence of chemical chlorine activation on wildfire aerosols. The 2019–2020 Australian New Year (ANY) wildfire was the largest wildfire since the satellite era. It injected about 1 Tg of aerosols into the stratosphere (Peterson et al., 2021), equivalent to a small volcanic eruption. This event was followed by unprecedented changes in chlorine reservoir species, such as HCl and ClONO₂ in the mid-latitudes (Bernath, Boone, & Crouse, 2022; Santee et al., 2022). However, mid-latitude temperatures are generally too warm for heterogeneous chlorine activation via reaction 1.3 to occur efficiently on stratospheric background or volcanic aerosols, which mainly consist a mixture of inorganic sulfate and water (Hanson & Ravishankara, 1993; Kawa et al., 1997; Q. Shi, Jayne, Kolb, Worsnop, & Davidovits, 2001). It is plausible that organic aerosols from wildfire plumes (Boone, Bernath, & Fromm, 2020; Murphy et al., 2021) enhance HCl uptake at warmer temperatures (Y. Q. Li et al., 2002). Chapter 4 investigates this temperature dependence of chemical chlorine activation using satellite data. A more inert tracer observed from the same satellite overpass is introduced in the analysis along with HCl and ClONO₂, deviations from the expected tracer-tracer correlation primarily reflect chemistry-driven changes in these chlorine reservoir species (Chipperfield, Lutman, Kettleborough, Pyle, & Roche, 1997; Tilmes, Müller, Grooß, & Russell III, 2004). Additionally, a back-trajectory model is used to calculate the minimum temperature experienced by air parcels for each satellite overpass. Together,

these results reveal the temperature dependence of chemical chlorine processes following the 2020 ANY fire and the lingering effects in 2021.

Chapter 5 contrasts mid-latitude chemical chlorine processes following two independent wildfire events with a series of volcanic eruptions of varying sizes, using satellite data from the past three decades. Volcanic eruptions are well known to indirectly cause mid-latitude ozone depletion through heterogeneous N_2O_5 hydrolysis ($\text{N}_2\text{O}_5 + \text{H}_2\text{O} \xrightarrow{\text{het}} 2 \text{HNO}_3$), which reduces NO_x by depleting N_2O_5 , a nighttime reservoir for NO_x, and therefore suppresses the conversion of reactive ClO back into its reservoir species, ClONO₂ (S. Solomon et al., 1996). This mechanism contributed to significant ozone depletion following the catastrophic 1991 Pinatubo eruption (Kinnison, Grant, Connell, Rotman, & Wuebbles, 1994). Water vapor partial pressure also plays a key role in influencing heterogeneous reaction rates and can impact mid-latitude ozone depletion (S. Solomon, 1999). The 2022 Hunga-Tonga volcanic eruption, which injected an unprecedented amount of water vapor into the stratosphere (Carn, Krotkov, Fisher, & Li, 2022; Millán et al., 2022), together with atmospheric dynamic responses, significantly impacted chlorine species and ozone concentrations in the mid-latitudes (Manney et al., 2023; X. Wang et al., 2023; Wohltmann, Santee, Manney, & Millán, 2024; Zhang, Kinnison, et al., 2024; Zhang, Wang, et al., 2024). This chapter employs the tracer-tracer correlation to quantify chemical chlorine activation following these two volcanic eruptions, as well as the 2015 Calbuco eruption. S. Solomon et al., 2023 suggests that HCl uptake is more efficient on organic aerosols from the 2020 ANY wildfire. Building on this, Chapter 5 explores the aerosol extinction required for volcanic eruptions to achieve a similar magnitude of HCl impact as observed after the 2020 ANY fire. This chapter also investigates the effects of the 2009 Australian Black Saturday wildfire, which, despite being a much smaller event, still managed to reach the lower stratosphere (Glatthor et al., 2013; Peterson et al., 2021).

Chapter 6 presents a quantitative detection and attribution (D&A) analysis of Antarctic ozone changes. While studies have shown significant ozone increases in certain months over Antarctica (Chipperfield & Santee, 2022; S. Solomon et al., 2016), recent research has

raised concerns that the recovery of Antarctic springtime ozone is slower and may even be decreasing in October (Kessenich, Seppälä, & Rodger, 2023; Krzyścin & Czerwińska, 2024). Climate internal variability, such as the El Niño–Southern Oscillation (ENSO) and the Quasi-Biennial Oscillation (QBO), as well as other natural forcings such as the solar cycle and volcanic eruptions, can strongly influence stratospheric ozone. It is critical to understand whether Antarctic ozone is recovering as a response to declining ODS emissions, and whether the observed October ozone decrease falls within the spread of internal variability or if it indicates missing external forcings or other processes. Earlier stratospheric ozone D&A studies have typically used multiple linear regression to fit these sources of variabilities based on a few decades of available observations (summarized in Chipperfield and Santee, 2022). In contrast, Chapter 6 applies a pattern-based “fingerprinting” technique widely used in climate science (e.g., Hasselmann, 1993; Santer et al., 2023) to identify characteristic month-height ozone change patterns associated with different forcings, using initial-condition large ensembles coupled with interactive chemistry (Garcia, Smith, Kinnison, Cámarra, & Murphy, 2017; Marsh et al., 2013; Morgenstern et al., 2017). The observed satellite ozone trends are compared to these sought-after fingerprint patterns against model-simulated internal variability “noise”, which consists of hundreds of years of simulations that capture the nonlinear coupled feedbacks between ozone and internal climate variability. Additionally, this chapter also examines how the choice of coordinate systems may introduce potential biases in the interpretation of the observed ozone trends in October.

Chapter 7 synthesizes the key findings of this thesis and outlines potential directions for future research.

Chapter 2

On the Effects of the Ocean on Atmospheric CFC-11 Lifetimes and Emissions

Abstract

The ocean is a reservoir for CFC-11, a major ozone-depleting chemical. Anthropogenic production of CFC-11 dramatically decreased in the 1990s under the Montreal Protocol, which stipulated a global phase-out of production by 2010. However, studies raise questions about current overall emission levels, and indicate unexpected increases of CFC-11 emissions of about 10 Gg yr⁻¹ after 2013 (based upon measured atmospheric concentrations and an assumed atmospheric lifetime). These findings heighten the need to understand processes that could affect the CFC-11 lifetime, including ocean fluxes. We evaluate for the first time

This chapter is adapted from Wang, P., Scott, J. R., Solomon, S., Marshall, J., Babbin, A. R., Lickley, M., Thompson, D. W. J., DeVries, T., Liang, Q., & Prinn, R. G. (2021). On the effects of the ocean on atmospheric CFC-11 lifetimes and emissions. *Proceedings of the National Academy of Sciences*, 118(12), e2021528118. <https://doi.org/10.1073/pnas.2021528118>

how ocean uptake and release through 2300 affects CFC-11 lifetimes, emission estimates, and the long-term return of CFC-11 from the ocean reservoir. We show that ocean uptake yields a shorter total lifetime and larger inferred emission of atmospheric CFC-11 from 1930 to 2075 compared to estimates using only atmospheric processes. Ocean flux changes over time result in small but not completely negligible effects on the calculated unexpected emissions change (decreasing it by 0.4 ± 0.3 Gg yr $^{-1}$). Moreover, it is expected that the ocean will eventually become a source of CFC-11, increasing its total lifetime thereafter. Ocean outgassing should produce detectable increases in global atmospheric CFC-11 abundances by the mid-2100s, with emission of around 0.5 Gg yr $^{-1}$; this should not be confused with illicit production at that time. An illustrative model projection suggests that climate change is expected to make the ocean a weaker reservoir for CFC-11, advancing the detectable change in global atmospheric mixing ratio by about 5 years.

2.1 Introduction

Man-made chlorofluorocarbons (CFCs) are the primary cause of the Antarctic ozone hole (S. Solomon, 1999). The atmospheric lifetimes of these chemicals range from about 50–500 years. The Montreal Protocol agreed to a complete phase out of CFC production and consumption worldwide by 2010. Evidence for healing of the Antarctic ozone layer has indeed emerged (S. Solomon et al., 2016; World Meteorological Organization (WMO), 2003), indicating the overall success of the Montreal Protocol. Atmospheric loss processes of CFC-11, the most abundant ozone-destroying chlorofluorocarbon, are due to photolysis and reaction with excited oxygen (O^1D) once the gas reaches the stratosphere. The atmospheric lifetime of CFC-11 is assumed to be inversely related to the atmospheric abundance of the molecule, with due consideration of the lag times between tropospheric and stratospheric burdens (Chipperfield et al., 2014). Given its lifetime of about 50–60 years and continued emissions from storage banks such as chillers and building insulation foams (Lickley et al., 2020), the

CFC-11 inventory in the atmosphere is decreasing slowly. However, the rate of decrease in atmospheric concentrations has been slowing down since about 2012, suggesting higher overall emission and an unexpected additional post-2013 emission increase of CFC-11 of about 7–13 Gg yr⁻¹ (10–20 % of the total global emission during that time; Montzka et al., 2018; Rigby et al., 2019). The latter is clearly inconsistent with the zero global new production that has been agreed by the Montreal Protocol.

CFC-11 is soluble in water, and therefore the ocean has absorbed some CFC-11 from the atmosphere. CFC-11 ocean uptake is greatest in high latitudes where cold sea surface temperatures (SST) enhance CFC-11 solubility (Warner & Weiss, 1985), and mixing and transport from the surface into the deep ocean is enhanced. By 1994, the ocean had stored up to 1 % of the total anthropogenic emissions of CFC-11 (Willey et al., 2004), and by 2014 the ocean held roughly 110 Gg of CFC-11 (DeVries & Holzer, 2019), or about 5–10 % of the CFC-11 inventory in the various anthropogenic storage banks (Lickley et al., 2020). While some CFC-11 is removed in sulfidic anoxic waters (Bullister & Lee, 1995), this effect is small for the current climate, and CFC-11 has long been employed as a useful passive tracer to study ocean circulation (e.g., Ito et al., 2004; Romanou et al., 2017). Early studies using a global model incorporating CFC-11 air-sea fluxes suggested that the ocean's effects on atmospheric CFC-11 lifetimes and concentrations were negligible in the 1980s, when anthropogenic emissions were high (Golombek & Prinn, 1986). However, now that anthropogenic emissions have dramatically decreased and attention is focused on unexpected emissions of 10 Gg yr⁻¹ or even less, changes in ocean uptake of CFC-11 could be affecting the atmospheric CFC-11 inventory enough to influence emission estimates, and could introduce a time-dependent effect on its total lifetime. Further, as anthropogenic emissions continue to decrease in the future, the ocean must eventually become supersaturated with respect to atmospheric CFC-11, and turn into a source instead of a sink. No study has yet estimated when that should be expected to occur, and what its magnitude will be.

Here, we address the following questions: (i) How is the ocean affecting the atmospheric

CFC-11 inventory, the lifetime of CFC-11 in the atmosphere and its time dependence, and how does this in turn influence emission estimates based on observed concentrations?; (ii) When will the ocean become a source of CFC-11 to the atmosphere, and how much will ocean outgassing affect the apparent emission and atmospheric mixing ratio in the future? (iii) How will climate change affect ocean CFC-11 uptake in the future?

For a conceptual understanding, we use a hierarchy of models starting with a simple 6-box model that simulates the CFC-11 inventory in the atmosphere, ocean mixed layer, and deep ocean layers (each layer has 2 boxes representing the two hemispheres, see the schematic in Figure 2.1a). CFC-11 in each box is assumed to be well mixed in this illustrative model. The atmospheric CFC-11 lifetime is kept constant at 55 years and estimated emissions are taken from published work (Engel & Rigby, 2019). We assume constant inter-hemispheric exchange timescales for each layer, and constant cross-layer timescales for mixed layer to deep ocean exchange (see Appendix Table 2.2). Atmospheric CFC-11's vertical distribution does affect its lifetime and surface concentration. Here, we subsume stratosphere-troposphere exchange into our adopted atmospheric lifetime estimates assuming a well-mixed atmosphere, and focus on the ocean's effect on atmospheric CFC-11. We then replace the four ocean boxes with a more sophisticated albeit low-resolution representation of the ocean ($2.8^\circ \times 2.8^\circ$ horizontal resolution and 15 vertical layers down to 5000 m), the MIT general circulation model (MITgcm; Marshall, Adcroft, Hill, Perelman, and Heisey, 1997; Marshall, Hill, Perelman, and Adcroft, 1997), which includes a physics-based CFC-11 air-sea flux and transport into the interior ocean, and treats CFC-11 as a conservative tracer in the ocean (depicted in Figure 2.1b). The MITgcm (for brevity, we refer to the combined coupled box model atmosphere-ocean model simply as the MITgcm) is run in two modes. First, we use the model forced with climatological average wind stress and buoyancy fluxes (Hist run) to assess the influence of parameters including SST, wind stress, etc. on air-sea CFC-11 fluxes. Second, we force the MITgcm using global monthly RCP8.5 output from the MPI-ESM-LR (Max-Planck-Institute Earth System Model low resolution version) fully coupled global climate model (RCP8.5 run; Giorgetta et al.,

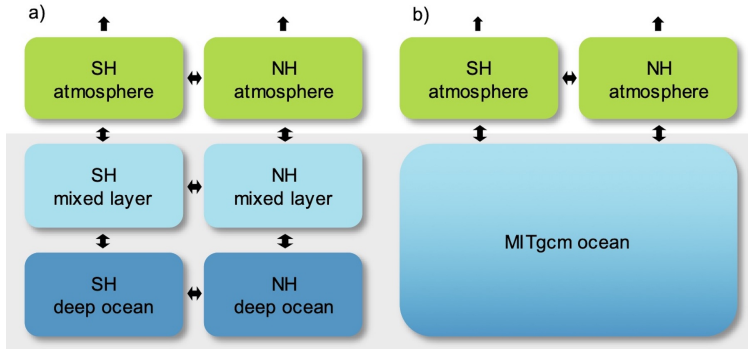


Figure 2.1: Schematic diagrams showing a) the box model; and b) the MITgcm setup. The box model has three layers that represent the atmosphere, ocean mixed layer and deep ocean. Each layer has two boxes that indicate the NH and the SH. The MITgcm setup replaces the four ocean boxes with the MITgcm ocean but keeps the atmospheric boxes unchanged. One-way arrows indicate CFC-11 atmospheric loss; two-way arrows indicate CFC-11 transport into/out of the box.

2013; Jungclaus et al., 2013). This model has been shown to provide a realistic response of the Southern Ocean (55–70 °S), the region that stores the most CFC-11, to the southern annular mode (Kostov et al., 2017). In the RCP8.5 run, interannual variability within the MPI-ESM-LR output provides changes in the forcing of the ocean applied after 1930, but variability in the atmospheric circulation is not explicitly incorporated into the box model atmosphere. We compare these runs to a “no ocean” run in which the CFC-11 air-sea flux is turned off. Both the box model and MITgcm runs extend from 1930 (essentially the start of emission of this anthropogenic gas) to 2300.

2.2 Data and methods

2.2.1 Emission data

Global CFC-11 emissions up to 2016 (Engel & Rigby, 2019) are split into NH and SH (Rigby et al., 2013). We adopted a simple constant declining rate of CFC-11 emission from 1995 to 2016 to predict emissions beyond 2016. Emissions in both hemispheres reached zero at around 2100 and were kept zero to the end 2300. A similar treatment is applied for CFC-12

emissions.

2.2.2 Box model equations

$$\frac{dm_{nh}^a}{dt} = E_{nh} + F_{nh} - (T_{n2s}^a + L_{nh}^a) \times m_{nh}^a + T_{s2n}^a \times m_{sh}^a \quad (2.1)$$

$$\frac{dm_{sh}^a}{dt} = E_{sh} + F_{sh} - (T_{s2n}^a + L_{sh}^a) \times m_{sh}^a + T_{n2s}^a \times m_{nh}^a \quad (2.2)$$

$$\frac{dm_{nh}^t}{dt} = -F_{nh} - T_{n2s}^t \times m_{nh}^t + T_{s2n}^t \times m_{sh}^t + T_{nh}^{d2t} \times m_{nh}^d \quad (2.3)$$

$$\frac{dm_{sh}^t}{dt} = -F_{sh} - T_{s2n}^t \times m_{sh}^t + T_{n2s}^t \times m_{nh}^t + T_{sh}^{d2t} \times m_{sh}^d \quad (2.4)$$

$$\frac{dm_{nh}^d}{dt} = -(T_{nh}^{d2t} + T_{n2s}^d) \times m_{nh}^d + T_{nh}^{t2d} \times m_{nh}^t + T_{s2n}^d \times m_{sh}^d \quad (2.5)$$

$$\frac{dm_{sh}^d}{dt} = -(T_{sh}^{d2t} + T_{s2n}^d) \times m_{sh}^d + T_{sh}^{t2d} \times m_{sh}^t + T_{n2s}^d \times m_{nh}^d \quad (2.6)$$

$$F_{nh} = -k \times ([CFC]_{nh}^a - [CFC]_{nh}^t) \quad (2.7)$$

$$F_{sh} = -k \times ([CFC]_{sh}^a - [CFC]_{sh}^t) \quad (2.8)$$

where m indicates mass of CFC-11, L is the CFC-11 atmospheric loss rate, T is the exchange timescale between each box, E is the CFC-11 emission, F is the flux of CFC-11 between the atmosphere and ocean, k is the piston velocity at 10 cm hr⁻¹ (England, Garçon, & Minster, 1994), $[CFC]$ indicates the concentration in the atmosphere and mixed layer boxes. Superscripts indicate layers and subscripts indicate the hemisphere. Appendix Table 2.2 shows a description of each term as well as the numerical values associated with each parameter.

2.2.3 MITgcm model

Emission, atmospheric loss rate, and the atmosphere inter-hemispheric exchange timescale for CFC-11 in the MITgcm runs are the same as used in the box model setup. The CFC-11

air-sea flux equation is the same as shown in equations 2.7–2.8 (Wanninkhof, 1992), except that each term is calculated locally and dynamically given changes in the ocean forcing. Transport of CFC-11 within the ocean is done by the MITgcm. The MITgcm ocean model used here has $2.8^\circ \times 2.8^\circ$ horizontal resolution and 15 vertical layers down to 5000 m. This is a fairly coarse resolution, but appears sufficient to provide a first order estimate of CFC-11 uptake in the past based on Figure 2.2, and hence is used to estimate the long-term future. A mesoscale eddy parameterization (Gent & Mcwilliams, 1990) is used with an eddy diffusivity set to $1000 \text{ m}^2 \text{ s}^{-1}$. Convective adjustment is applied to statically unstable water columns, and background vertical diffusivity is set to $5 \times 10^{-5} \text{ m}^2 \text{ s}^{-1}$. Improved resolution and adjustments in ocean model parameters have been shown to impact details of CFCs storage within the ocean (Beismann & Redler, 2003; Romanou et al., 2017), but we would not expect such changes to alter our qualitative results. Appendix Figure 2.11 shows the resulting residual mean meridional overturning circulation in the Atlantic Ocean, which appears reasonable.

2.2.4 MITgcm forcing fields

The MITgcm is forced by monthly net evaporation-precipitation-river runoff (E-P-R) and Q_{net} climatologies (Jiang, Stone, & Malanotte-Rizzoli, 1999). In addition, SST and sea surface salinity (SSS) in the upper 50 m ocean layer are restored to a monthly climatology based on survey data taken from 1950 to 1990 (Levitus, Burgett, & Boyer, 1994a, 1994b), with restoring timescales of 60 and 90 days respectively. Wind stress and wind speed climatologies over this period are from the European Centre for Medium-Range Weather Forecasts (ECMWF; Trenberth, Olson, and Large, 1989; Trenberth, Large, and Olson, 1990). Wind speed is decoupled from the wind stress in this setup and is only used to calculate the piston velocity for CFC-11 air-sea flux (i.e., it has no impact on ocean dynamics, in contrast with applied wind stress). The monthly sea ice concentration climatology (Chapman & NCAR Staff, 2022; Zwally et al., 1983), like the surface wind speed, is only used in the calculation of CFC uptake; note our MITgcm setup does not include a prognostic sea ice model. The ocean was subject

to 5900 years of spinup with the above climatology to produce an equilibrium state, followed by runs with CFC-11 from 1930 to 2300.

2.2.5 MITgcm RCP8.5 setup

In this simulation the ocean dynamical model is spun up to equilibrium in the same way as the Hist run. Modified forcing fields using RCP8.5 output from MPI-ESM-LR (Giorgetta et al., 2013; Jungclaus et al., 2013) during the transient simulation from 1930–2300 were constructed as follows. First we coarse-grained the output from MPI-ESM-LR using a nearest neighbor algorithm to MITgcm’s $2.8^\circ \times 2.8^\circ$ resolution, and constructed a base period from 1850 to 1930 (using MPI-ESM-LR’s historical simulation). Monthly anomalies from 1930 to 2300 compared to the base period were then added to the MITgcm Hist forcing discussed above (anomalies were imposed beginning in the early 20th century to avoid any abrupt changes in forcing fields that might cause unphysical changes in ocean circulation). Appendix Figure 2.12 shows the spatial patterns of the RCP8.5 anomalies for all the forcing variables nudged in MITgcm. Unlike in the Hist simulation, in the RCP8.5 simulation the ocean circulation and air-sea gas exchange piston velocity both evolve over time. Atlantic Meridional Overturning Circulation (AMOC) strength in the MITgcm RCP8.5 run decreases by 60 % from 1930–2000 to 2200–2300 (Appendix Figure 2.11), comparable to a 56 % decrease obtained in the MPI-ESM-LR.

2.2.6 Top-down inferred emission based on the MITgcm output

We inferred the emission and the atmospheric lifetime from the MITgcm output of the CFC-11 (and CFC-12) inventory by:

$$E_{inf} = \frac{dm}{dt} + \frac{m}{\tau} \quad (2.9)$$

$$\tau_{atm} = \frac{m}{L_{nh}^a + L_{sh}^a} \quad (2.10)$$

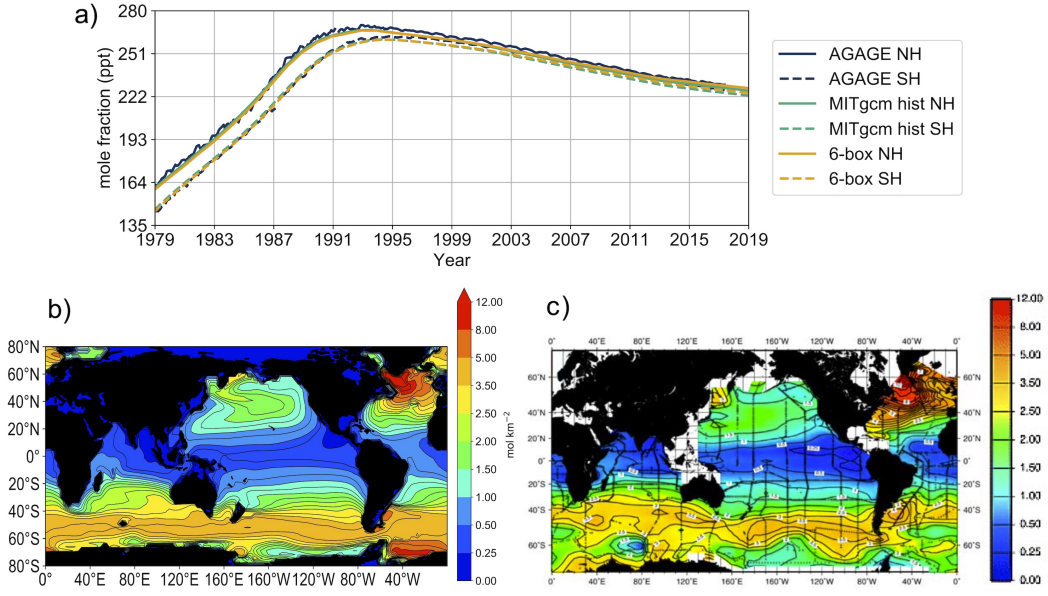


Figure 2.2: a) Model validation of CFC-11 atmospheric abundances compared to CFC-11 atmospheric surface data (14); b) the MITgcm ocean column integrated CFC-11 under Hist run; and c) observations of ocean column integrated CFC-11 (Willey et al., 2004). Panels b and c both show the CFC-11 inventories in the year 1994, and are in the same units of mol km⁻².

$$\tau_{atm+ocn} = \frac{m}{L_{nh}^a + L_{sh}^a + F_{nh} + F_{sh}} \quad (2.11)$$

where E_{inf} is the inferred emission, m is the mass of CFC-11 (and CFC-12) as calculated from the MITgcm, $\frac{dm}{dt}$ is the tendency of the CFC-11 (and CFC-12) inventories. τ_{atm} is the inferred CFC-11 (and CFC-12) lifetime only considering the atmospheric loss, and $\tau_{(atm+ocn)}$ is the total lifetime considering both the atmospheric loss and the bi-directional flux from the ocean. τ in equation 2.9 is replaced with inferred lifetimes from equations 2.10–2.11 as well as assumed constant 52- and 58-year lifetime for the inferred emission estimates in Figure 2.4b for CFC-11 (assumed constant 90- and 100-year lifetime in Appendix Figure 2.9b for CFC-12).

2.3 Results

2.3.1 Near-term CFC-11

To evaluate the performance of the box model and MITgcm, we compared the computed CFC-11 atmospheric concentrations with observations (Figure 2.2a). While the box model is essentially tuned (both atmosphere and ocean parameters), the MITgcm setup is a fairly standard, off-the-shelf coarse resolution global ocean model without any specific tuning for this application. Both the box model and MITgcm agree well with observations, capturing the increase in CFC-11 before 1990 due to the large anthropogenic emissions, as well as the concentration decrease after 1990 given the decline in the emissions and losses due to chemical reactions in the atmosphere and exchange with CFC-11 depleted ocean waters. The gradient in CFC-11 between the northern hemisphere (NH) and southern hemisphere (SH) is also well captured. Because most of the emissions (around 90 %) occur in the NH and the CFC-11 lifetime is long, the NH minus SH difference can be up to 17 ppt when anthropogenic emissions are large (comparable to 20 ppt reported in Bullister and Warner, 2017). As the emissions decrease, the inter-hemispheric exchange brings the NH and SH CFC-11 abundances closer to each other. Both the box model and MITgcm slightly underestimate the observed CFC-11 mixing ratio after 1990, as emissions decline (2.0 ppt lower in box model; 2.7 ppt lower in MITgcm averaged from 1990 to 2017). Reasons for the underestimation of the atmospheric CFC-11 concentration could be either 1) the ocean uptake is overestimated; 2) the CFC-11 atmosphere-only lifetime at that time is larger than our adopted constant value; and/or 3) CFC-11 emissions are higher than those prescribed in this simulation.

Figures 2.2b–c provide a qualitative comparison of the MITgcm global ocean column-integrated CFC-11 with observations for 1994 (Willey et al., 2004). The MITgcm captures the spatial distribution of observed CFC-11 in the ocean rather well given a well-mixed atmospheric CFC-11 distribution, indicating that local dynamics is the driving factor for

ocean uptake. Intercomparisons between the MITgcm and other models of similar resolution as well as observations (Dutay et al., 2002) also indicate that the MITgcm does a favorable job in simulating CFC-11 distribution. In the MITgcm, CFC-11 is overestimated in the Weddell Sea, although the Weddell Sea only stores less than 4.5 % of the global ocean CFC-11 inventory (Appendix Figure 2.5) and has only a minor impact on the global estimate (also note Dutay et al., 2002 showed large model spread in the Southern Ocean inventory due to ventilation differences among models). Most CFC-11 in the NH ocean is stored in the North Atlantic, with subduction into the thermocline and the AMOC playing key roles (Romanou et al., 2017). The SH is the major reservoir for CFC-11, which is transported in Antarctic Intermediate Water and Subantarctic Mode Water (Fine, Maillet, Sullivan, & Willey, 2001) and accumulates in the interior ocean between 40 °S to 60 °S. In 1994, the best estimate of the global ocean CFC-11 inventory from the World Ocean Circulation Experiment (WOCE) is 75.6 Gg (with cumulative error of 16.5 Gg; Willey et al., 2004), while the MITgcm suggests about 82 Gg of CFC-11 in the same year, which is slightly larger but well within the uncertainty range of the observational value.

2.3.2 Box model sensitivity tests

For a conceptual understanding of the primary factors affecting CFC-11 inventories in the atmosphere and ocean, we perturbed key parameters (Appendix Table 2.2) in the box model by $\pm 15\%$ (Appendix Figure 2.6a). Before 1990, all the sensitivity tests produce similar CFC-11 inventories for both the atmosphere and ocean, underscoring that high anthropogenic emission dominated the behavior during that time. After 1990 as global emissions decrease, the importance of other drivers in affecting CFC-11 inventories increases. For example, a 15 % change in the prescribed atmospheric CFC-11 lifetime affects the atmospheric inventory by up to about 570 Gg in 2050s, or about 15 % of the total atmospheric CFC-11 inventory at that time. A 15 % change in mixed layer depth (MLD; a proxy in the box model for the rate of ventilation of intermediate waters) affects the atmospheric inventory by up to 13 Gg in 1990s.

The biggest impact of MLD on CFC-11 inventory is expected to occur in the 20th century because larger CFC-11 emissions and undersaturated ocean waters result in the highest ocean uptake then. Changing the piston velocity only has a small effect on the CFC-11 atmospheric inventory, up to 0.1 Gg. Changes in inter-hemispheric exchange constants adopted for the atmospheric and ocean reservoirs only affect the NH to SH gradient, but do not affect the total inventory in each reservoir, and $\pm 15\%$ changes in this parameter only generate differences within computational error. However, in the real world if the exchange timescales between different CFC-11 reservoirs (for example between the atmosphere and ocean, or the atmospheric loss in the stratosphere versus the troposphere) are significantly different in each hemisphere, the effects of inter-hemispheric exchange could become more significant.

The MLD in the box model affects the CFC-11 concentration in the shallow ocean boxes. A deeper MLD implies that the ocean has a larger capacity to store CFC-11. This is crucial to determining whether the ocean is supersaturated or undersaturated with CFC-11 at the air-sea interface. Our box model assumes a constant MLD in time. In the real world and in more complex ocean models, ocean circulation changes can be expected to be dominant factors driving surface ocean CFC-11 concentration, and changes in the meridional overturning circulation with climate change are likely to be important. This highlights the importance of using an ocean model with realistic ocean dynamics to understand CFC-11 evolution in the atmosphere and ocean, as done here with the MITgcm (albeit with low spatial resolution in this configuration of the MITgcm). Appendix Figure 2.6b shows CFC-11 inventories using the MITgcm. Ocean inventories in the box model and MITgcm agree well before 1990 because emission is the driving factor for CFC-11 air-sea fluxes, but they deviate significantly in the future, when ocean dynamics begins to drive changes in surface ocean CFC-11 concentration and the air-sea flux. Our box model only has two ocean layers, which equilibrate CFC-11 between the atmosphere and ocean more rapidly than the MITgcm. Further, some CFC-11 can be transported very deep in the ocean. With 15 ocean layers in the MITgcm, the ocean is able to sequester more CFC-11 in the interior and it takes more time to release that CFC-11

back to the atmosphere, such that the ocean CFC-11 inventory peaks in the year 2075 in the MITgcm, roughly 80 years after the peak in atmospheric CFC-11 concentrations.

Box model results should be considered illustrative rather than quantitative regarding the future CFC-11 inventory. Nonetheless, although some parameters in the box model may have co-dependencies in the real world, our sensitivity analysis qualitatively highlights the importance of two key factors that affect the CFC-11 inventory as anthropogenic emissions drop: the atmospheric lifetime and ocean dynamics. We next focus on the MITgcm results to further explore these issues.

2.3.3 Effect of the ocean on atmospheric CFC-11 concentration

We first present results using the climatological ocean forcing adopted in the Hist scenario. Figure 2.3a shows the difference in CFC-11 atmospheric inventories and abundances between the MITgcm run and no ocean runs. A similar plot but for dichlorodifluoromethane, or CFC-12, is shown in Appendix Figure 2.7. CFC-11 and CFC-12 are treated in the same manner in the MITgcm but CFC-12 is less soluble; therefore results for CFC-12 generally follow the same pattern as CFC-11 but the magnitude is smaller. Under this forcing, the cumulative effect of the ocean reaches its maximum in 2009, at which point the atmospheric CFC-11 inventory is 76.6 Gg less with the presence of the ocean (equivalent to 3.5 ppt less mole fraction) compared to the no ocean run. As anthropogenic emissions further decrease, the CFC-11 gradient between the atmosphere and the ocean decreases, decreasing the flux going into the ocean. Atmospheric CFC-11 differences between the ocean and no ocean runs reach zero around 2135. After that, the atmosphere accumulates more CFC-11 due to release from the ocean, and this outgassing accumulates in the atmosphere. Based on the current typical detection precision of CFC-11 measurements (Prinn et al., 2018) for the AGAGE (Advanced Global Atmospheric Gases Experiment) network, the net increase of global CFC-11 released from the ocean is expected to become detectable by 2145 or earlier based on this model. At that point, the atmosphere is expected to contain about 0.5 ppt more average

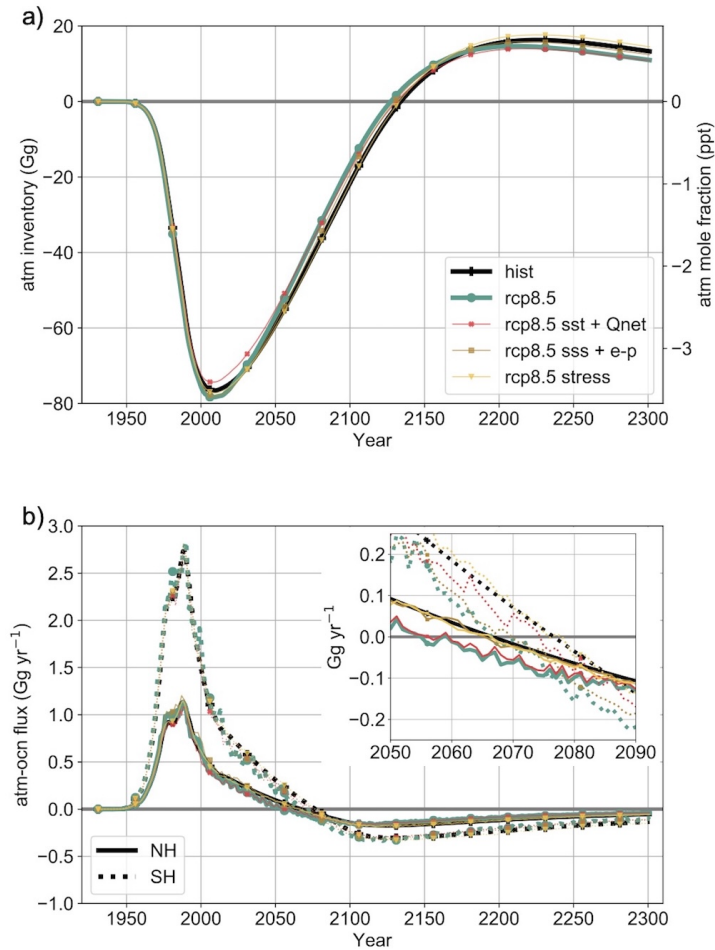


Figure 2.3: a) Atmospheric CFC-11 inventory (left axis) and abundance (right axis) for different ocean forcing tests (different colors and markers) in the MITgcm minus the atmosphere under no ocean run; results are shown both for the Hist and RCP8.5 runs (the differences between sea ice only and the wind speed only forcing results are nondifferentiable from the Hist run in this figure); b) MITgcm hemispherically-integrated CFC-11 air-sea flux under different ocean forcings. Positive values indicate fluxes going from the atmosphere to the ocean. Solid lines are the NH integrated flux and dashed lines are the SH integrated flux. Bottom panel is zoomed in between 2050 and 2090, when the flux changes sign.

CFC-11 compared to a no ocean run (and the global average abundance of CFC-11 is about 50 ppt at that time). Future instrument improvements may allow earlier detection. By 2225, the atmosphere contains about 16 Gg more CFC-11 than in the no ocean run (about 0.8 ppt). The ocean keeps releasing CFC-11 back to the atmosphere until the end of our study period. By the end of the run in 2300, the effect of the ocean on atmospheric CFC-11 remains significant.

The calculated CFC-11 hemispherically integrated air-sea flux is shown in Figure 2.3b. Most of the uptake in the NH happens in northward-flowing western boundary currents of the North Atlantic and North Pacific (Appendix Figure 2.8a–d), due to local cooling and the upwelling of deep undersaturated water favorable for CFC-11 uptake in the subpolar gyres. Even though 90 % of the emissions are in the NH, inter-hemispheric exchange in the atmosphere mixes the CFC-11 concentration quickly. The Southern Ocean is a hotspot of CFC-11 uptake due to cold SSTs, upwelling of CFC-poor deep waters, and strong surface winds conducive to CFC-11 uptake. Upwelling brings undersaturated circumpolar deep water to the surface south of the Antarctic polar front in the Southern Ocean, inducing CFC-11 uptake. These surface waters are transported northward and are ultimately subducted into the interior ocean with intermediate and mode water formation in the sub-Antarctic, accumulating CFC-11 in the interior ocean and preventing it from readily escaping back to the atmosphere in the near future (Appendix Figure 2.8e–h). Due to these processes, more than twice as much CFC-11 is effectively stored in the SH ocean reservoir. The uptake of CFC-11 into the global ocean via the air-sea flux is about 8.8 % of the destructive loss in the atmosphere in the 1950s (Table 2.1). The flux going into the ocean reaches a maximum in the 1980s at 3.6 Gg yr^{-1} . As anthropogenic emissions increase and more CFC-11 accumulates in the atmosphere given its long lifetime, loss in the atmosphere reaches a maximum in the 1990s (at 103.1 Gg yr^{-1}). By the 2010s, the flux going into the ocean is only about 1.2 Gg yr^{-1} , or about 1.3 % of the loss occurring in the atmosphere at that time, a significantly smaller percentage than in the 1950s. This reduction suggests a similar fractional increase of

Table 2.1: Calculated loss of CFC-11 in the atmosphere assuming a constant 55-year lifetime, loss of CFC-11 to the ocean as air-sea flux (positive values indicate a flux of CFC-11 from the atmosphere to the ocean), and relative loss in the ocean compared to that in the atmosphere from the MITgcm simulations. Values for several decades around the period of maximum loss in the atmosphere (1990s), the period of maximum flux of CFC-11 from the ocean to the atmosphere (2120s) and the outgassing late in the 23rd century are shown in the table. Error bars indicate ± 1 standard deviation associated with the decadal average.

Time	Atmosphere loss (Gg yr ⁻¹)	Ocean loss (Gg yr ⁻¹)	Ocean/atmosphere loss (%)
1951–1960	2.3 ± 1.4	0.2 ± 0.1	8.8 ± 1.1
1961–1970	14.2 ± 6.5	1.0 ± 0.4	7.1 ± 0.3
1971–1980	50.4 ± 12.7	2.8 ± 0.4	5.7 ± 0.7
1981–1990	88.3 ± 10.5	3.6 ± 0.2	4.1 ± 0.3
1991–2000	103.1 ± 1.2	2.6 ± 0.4	2.5 ± 0.4
2001–2010	96.6 ± 2.3	1.6 ± 0.2	1.6 ± 0.2
2011–2020	90.0 ± 1.4	1.2 ± 0.1	1.3 ± 0.0
...
2101–2110	35.0 ± 1.8	-0.4 ± 0.0	-1.2 ± 0.1
2111–2120	29.3 ± 1.5	-0.5 ± 0.0	-1.6 ± 0.1
2121–2130	24.5 ± 1.3	-0.5 ± 0.0	-2.0 ± 0.1
2131–2140	20.5 ± 1.0	-0.5 ± 0.0	-2.3 ± 0.1
2141–2150	17.2 ± 0.9	-0.5 ± 0.0	-2.7 ± 0.1
...
2281–2290	1.6 ± 0.1	-0.2 ± 0.0	-12.7 ± 0.4
2291–2300	1.4 ± 0.1	-0.2 ± 0.0	-14.0 ± 0.4

the overall CFC-11 lifetime due to the weakening of the ocean uptake.

The calculated global net flux is expected to reverse direction around 2075, with the NH displaying an earlier release of CFC-11 to the atmosphere in 2067, while the SH begins outgassing in 2077 in this model. The reason for the late release of the CFC-11 flux in the SH is due to more CFC-11 being transported into the deeper ocean, which then takes longer to get back to the surface (Appendix Figure 2.8). The maximum flux of CFC-11 out of the ocean occurs in the 2120s, with up to 0.5 Gg yr^{-1} of flux coming back into the atmosphere globally. By the end of 2300, the total flux from the ocean is still 0.2 Gg yr^{-1} . At this point, the loss of CFC-11 in the atmosphere is only 1.4 Gg yr^{-1} given the low atmospheric burden. The effect of the ocean source is counteracting the atmospheric loss by 14 % in the 2290s, suggesting that the CFC-11 lifetime should continue to increase far into the future.

2.3.4 Effect of the ocean on CFC-11 lifetime and emission estimates

The effects of the ocean on CFC-11 lifetimes and therefore on emissions inferred from concentration data are significant. Figure 2.4a presents lifetimes calculated by taking the model-calculated atmospheric abundances of CFC-11 and dividing by the loss rates in the atmosphere-only and in the atmosphere and ocean together (and similar results for CFC-12 are also given in Appendix Figure 2.9). As expected, when only the atmospheric loss is considered, the lifetime is a constant 55-year as prescribed, but the results including the ocean loss are quite different, at around 50-year in 1950, increasing to about 54-year by 2000 and 60-year by 2250.

To evaluate the effect of the ocean on inferred emissions estimates, we adopt the concentrations from the MITgcm as if they were measured data and infer emissions considering different lifetime assumptions (see Methods section). We then compare these inferred emissions to the emissions used to drive the model. As expected, inferred emission using the dynamic lifetime that includes both the ocean and atmosphere loss (the red curve in Figure 2.4a) fully recovers the input emissions that drive the MITgcm. Because knowing the exact atmospheric loss rate is not possible in real world, assumed constant atmospheric lifetimes are typically used to estimate emissions. We thus tested using constant 52-, 55- and 58-year lifetimes to explore the range of uncertainty in emission estimates. From the 1970s to 1990s, when the ocean uptake was large, inferred emissions using a constant atmospheric lifetime of 52 years provide a closer match to the prescribed emissions that were input to the MITgcm. From 2000 and beyond, when the ocean uptake is small, inferred emissions using a constant 55-year atmospheric lifetime provide a closer match to the prescribed emissions, showing how the large ocean uptake in earlier decades is equivalent to having a shorter atmosphere-only CFC-11 lifetime. Thus, the ocean CFC-11 uptake acts to decrease the overall atmosphere plus ocean lifetime over 1970–2000 by about 3 years.

For the key period from 2002–2012 to 2014–2016, the increase in the input emission

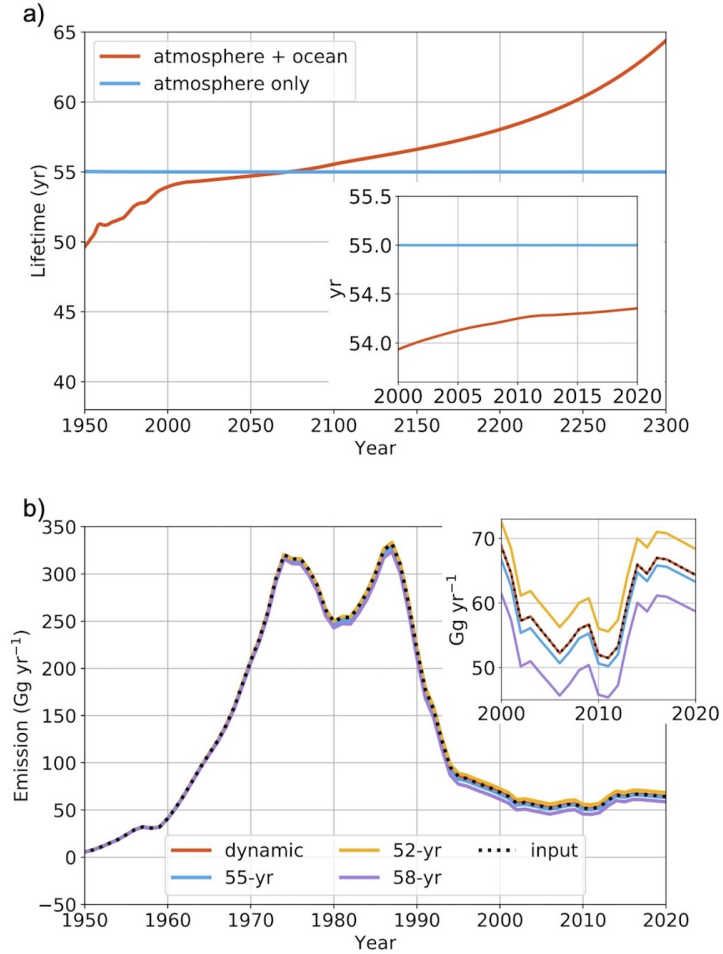


Figure 2.4: a) Lifetime of atmospheric CFC-11 in the model calculated by including only atmospheric losses (blue line) and including both atmosphere and ocean (red line); b) Comparison between emissions prescribed in the MITgcm runs to those inferred by treating the model calculated concentrations as data and ignoring the effect of the ocean on the lifetime. Black dashed line shows the emission input to the run. We use a 1-box model to do a top-down estimate of the emission (see Methods) given the CFC-11 concentrations that are output from the MITgcm using: a dynamic CFC-11 atmospheric-ocean lifetime (same as the red line in panel a); constant 55-year atmosphere-only lifetime (same as the blue line in panel a); and constant 52- and 58-year lifetimes to test the sensitivity of the inferred emissions. Inferred emission is shown from 1950 to 2020; emission after 2020 approaches zero linearly.

for the MITgcm is 11.2 Gg yr^{-1} , while the increase in the inferred emission assuming a constant 55-year lifetime is 11.6 Gg yr^{-1} . This highlights the time-dependent influence of the ocean on atmospheric loss rates of CFC-11. If the ocean’s role is ignored, and a constant atmosphere-only lifetime is assumed, then inferring emissions from concentration changes for 2014–2016 compared to 2002–2012 would overestimate the unexpected emission of CFC-11 by $0.4 \pm 0.3 \text{ Gg yr}^{-1}$ (assuming a constant lifetime of 55 ± 3 years).

In addition, the atmospheric CFC-11 lifetime has also been shown to be time-dependent rather than constant, largely as a result of the lag time between surface release and stratospheric loss (Chipperfield et al., 2014). Appendix Figure 2.10 overlays calculated atmosphere-only lifetimes from a suite of chemistry-climate models studied in the SPARC (Stratosphere-troposphere Processes And their Role in Climate) intercomparison. While atmospheric processes alone act to decrease the calculated total lifetime from 1930–2010, ocean processes have the opposite effect. The total lifetime would be best captured by models including both effects, which offset each other to some extent. Changes in atmospheric lifetimes likely explain why our model underestimates the CFC-11 mole fraction after 1990 in Figure 2.2, since we used a constant atmospheric CFC-11 lifetime throughout those model runs.

2.3.5 Effect of climate change on CFC-11 ocean uptake

The MITgcm simulation under the MPI model’s RCP8.5 scenario makes the ocean a weaker reservoir for CFC-11, leading to less uptake in the earlier period and less outgassing in the later period, and climate change affects the timing at certain critical periods. The global ocean starts to release CFC-11 in 2075 under Hist forcing, but the outgassing begins 10 years earlier under the RCP8.5 scenario (Figure 2.3b). Without climate change, the ocean’s effect on the atmospheric concentration of CFC-11 becomes detectable after 2145, compared to 2140 under RCP8.5, suggesting that climate change accelerates the shift towards outgassing CFC-11.

We tested the drivers of these changes using the MITgcm simulations with only certain

ocean forcing fields changing under RCP8.5, in order to identify which factors dominate CFC-11 ocean uptake under a changing climate. Zooming in on the period between 2050 and 2090 in Figure 2.3, the flux of CFC-11 in the NH under the full RCP8.5 forcing most closely follows that obtained under SST + Qnet (surface heat flux, calculated as latent heat + sensible heat + shortwave + longwave) only forcing. The additional warming of the surface ocean under this forcing leads to more stratified conditions, and reduces the solubility of CFC-11 in seawater, which results in earlier outgassing in the NH. In SST + Qnet only and full RCP8.5 runs, the AMOC decreased similarly (Appendix Figure 2.11c), suggesting that changes in ocean circulation are also playing a major role in weakening uptake, as found in other model studies (Romanou et al., 2017). In the SH, the SST does not increase as much as in the NH, due to the upwelling of deep cold water (Armour, Marshall, Scott, Donohoe, & Newsom, 2016; Marshall et al., 2015); as such, we find that the SH air-sea CFC-11 flux is mainly affected by changes in salinity as forced by changes in E-P and surface restoring of SSS. In particular, increases in net precipitation in the Southern Ocean (Appendix Figure 2.12f) decrease mixed layer depths, leading to weaker ventilation of the intermediate and deep ocean. Thus, more CFC-11 is stored in shallower ocean depths in response to these changes, leading to an earlier outgassing of CFC-11 to the atmosphere in the SH. Note that changes in SSS + E-P forcing do not cause an appreciable weakening of the AMOC (Appendix Figure 2.11c) in this model, unlike changes in SST + Qnet. We emphasize that other models could have different responses to these forcings, and this analysis is intended to be illustrative rather than quantitative.

When the ocean is acting as a sink for CFC-11, the atmosphere has up to 5.0 Gg more CFC-11 under full RCP8.5 forcing than under Hist forcing (Appendix Figure 2.13). In contrast, when the ocean turns into a source of CFC-11, the atmosphere has up to 2.4 Gg less CFC-11 with the full RCP8.5 scenario, which is due to weaker outgassing from the ocean. The combined effect of changes in SST, SSS, and buoyancy fluxes exceeds those in the full RCP8.5 forcing run, because the effects of wind stress on ocean circulation, and of sea ice

fraction on air-sea CFC-11 exchange partially counteract the ocean CFC-11 uptake due to thermal and saline changes in this model. Under RCP8.5, there is a poleward intensification of the SH westerly winds (Appendix Figure 2.12), which modifies the ventilation rate and transport of CFC-11 into the ocean (Waugh, 2014). In a simulation that isolates the effects of changes in wind stress on the ocean dynamics, there is enhanced ocean uptake, especially over 50–60 °S during the early ocean sink period (Appendix Figure 2.8), and the atmosphere has up to 0.8 Gg less CFC-11 compared to the Hist forcing run. When the ocean turns into a source of CFC-11, changes in wind stress forcing can lead to 1.4 Gg more CFC-11 in the atmosphere, due to enhanced equatorward Ekman transport and stronger upwelling in the Southern Ocean (Lovenduski & Gruber, 2005).

2.4 Discussion

Previous work has not explicitly analyzed the effects of the ocean on atmospheric CFC-11 and has generally assumed that the effects of ocean uptake and outgassing can be accounted for by adjusting the uncertainty in atmospheric lifetimes. The results shown here reveal that ocean uptake and outgassing have a much more pronounced effect on our understanding of the lifetime of atmospheric CFC-11 than previously anticipated. The results have small but significant implications for past CFC-11 emission estimates, and key conceptual implications for the future.

Here we summarize our findings on the three primary questions posed in the introduction: First, our model suggests that the ocean’s CFC-11 uptake ability varies significantly in time, translating to time-dependence in the total CFC-11 lifetime if the ocean’s effect is subsumed into the atmospheric lifetime estimate. This result does not significantly affect calculated ozone depletion or radiative forcing, which often employ prescribed concentrations based on observations. The significance of our work is that knowledge of lifetimes is required to estimate emissions from concentrations and, in turn, to examine emissions sources and

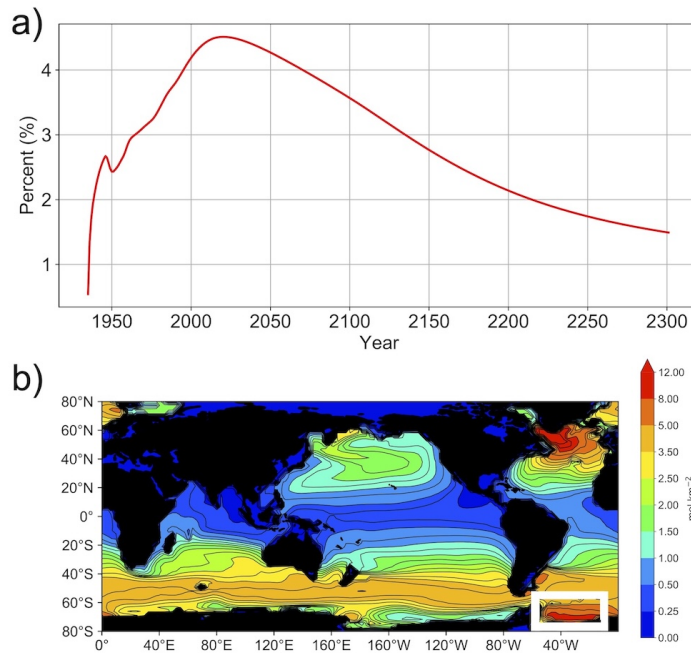
consistency with the Montreal Protocol. The calculated 7.5 % increase in lifetime from the 1950s to the 2010s due to weakening ocean uptake affects estimates of CFC-11 emissions by up to 4 Gg yr^{-1} , and it also affects their time dependence, compared to calculations neglecting this effect. We estimate that the ocean's influence reduces inferred unexpected emission of CFC-11 after 2013 (Montzka et al., 2018; Rigby et al., 2019) by about $0.4 \pm 0.3 \text{ Gg yr}^{-1}$ (assuming a constant lifetime of 55 ± 3 years) compared to calculations that neglect the ocean effect. This is because the ocean's weakening sink leads to an increased accumulation of CFC-11 in the atmosphere, which biases estimates of new emissions if the ocean's effect is unaccounted for. Second, a global net flux coming out of the ocean is projected to begin around 2075, and the release of CFC-11 from this bank implies an accumulating influence on atmospheric CFC-11 abundances that should become detectable in the global average after about 2145, with outgassing up to 0.5 Gg yr^{-1} . Detectable signals could be greatly enhanced and occur sooner if observation sites are located close to ocean upwelling regions, where stronger CFC-11 outgassing can be expected (Appendix Figure 2.8). The ocean ultimately leads to up to a 0.8 ppt increase in the global average atmospheric abundance by 2225. Such observations will signal the return of CFC-11 from the ocean, rather than new production outside the Montreal Protocol at that time.

Finally, an illustrative model projection suggests that climate change will likely make the ocean turn into a source of CFC-11 about 10 years earlier, and will make the effect on atmospheric mixing ratio detectable 5 years earlier according to the scenario presented here. Different models or scenarios could yield differences in detail regarding these findings but are unlikely to alter the general result.

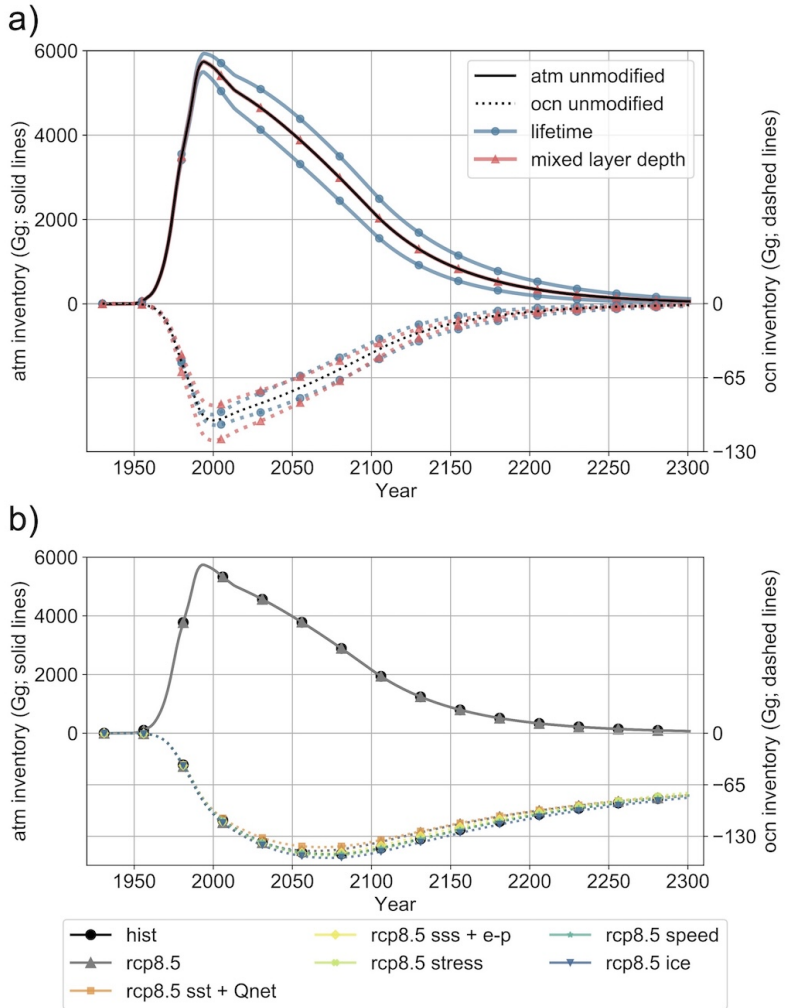
In closing, we note that our results illustrate the importance of the ocean in the new era of the Montreal Protocol in which global anthropogenic productions of ozone depleting substances (ODSs) has dramatically decreased, which means that small sources, sinks, or differences in estimates of lifetimes have now become extremely important because they affect emissions estimates. Atmospheric CFC-11 is not the only ODS taken up to some extent

by the ocean. Other gases including for example CFC-12, CCl_4 (carbon tetrachloride) and CH_3CCl_3 (methyl chloroform) are also subject to significant ocean uptake and sequestration, even though it has been demonstrated that CCl_4 and CH_3CCl_3 are not entirely conserved within the ocean (Huhn, Roether, Beining, & Rose, 2001; Prinn et al., 2001; Wallace, Beining, & Putzka, 1994; Wennberg, Peacock, Randerson, & Bleck, 2004). Indeed CFC-11 is also not entirely conserved in sufficiently anoxic water characterized by sulfide accumulation (Bullister & Lee, 1995). Whether this effect could become more significant in future climates depends on where and how deep the ocean sequesters CFC-11, and if sizable regions of anoxic conditions develop in future oceans. Together with changes in ocean temperatures and circulation patterns, these effects could be important in the future for detection of global and regional sources of ODSs. This work highlights the need for the atmospheric chemistry and oceanography communities to further examine these questions involving other ODSs. High-resolution global atmosphere-ocean models, and continued observational programs for global monitoring of ODSs in both the atmosphere and ocean, will be key tools for predicting and detecting these changes in the future.

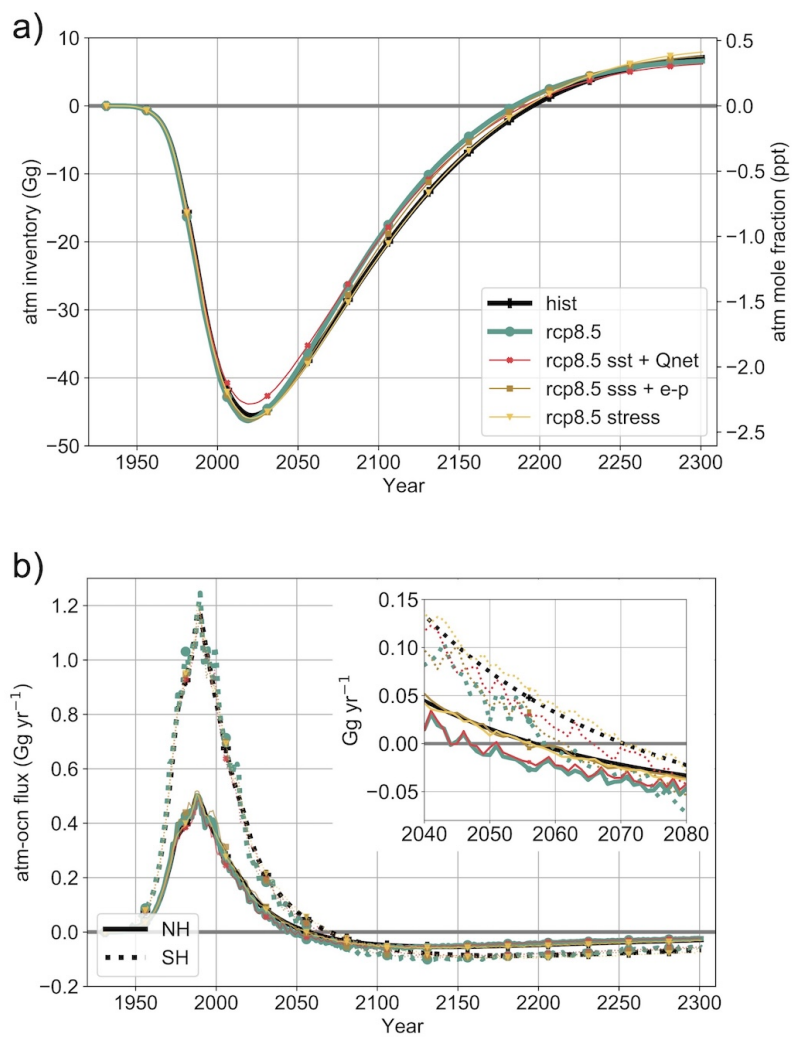
Appendix



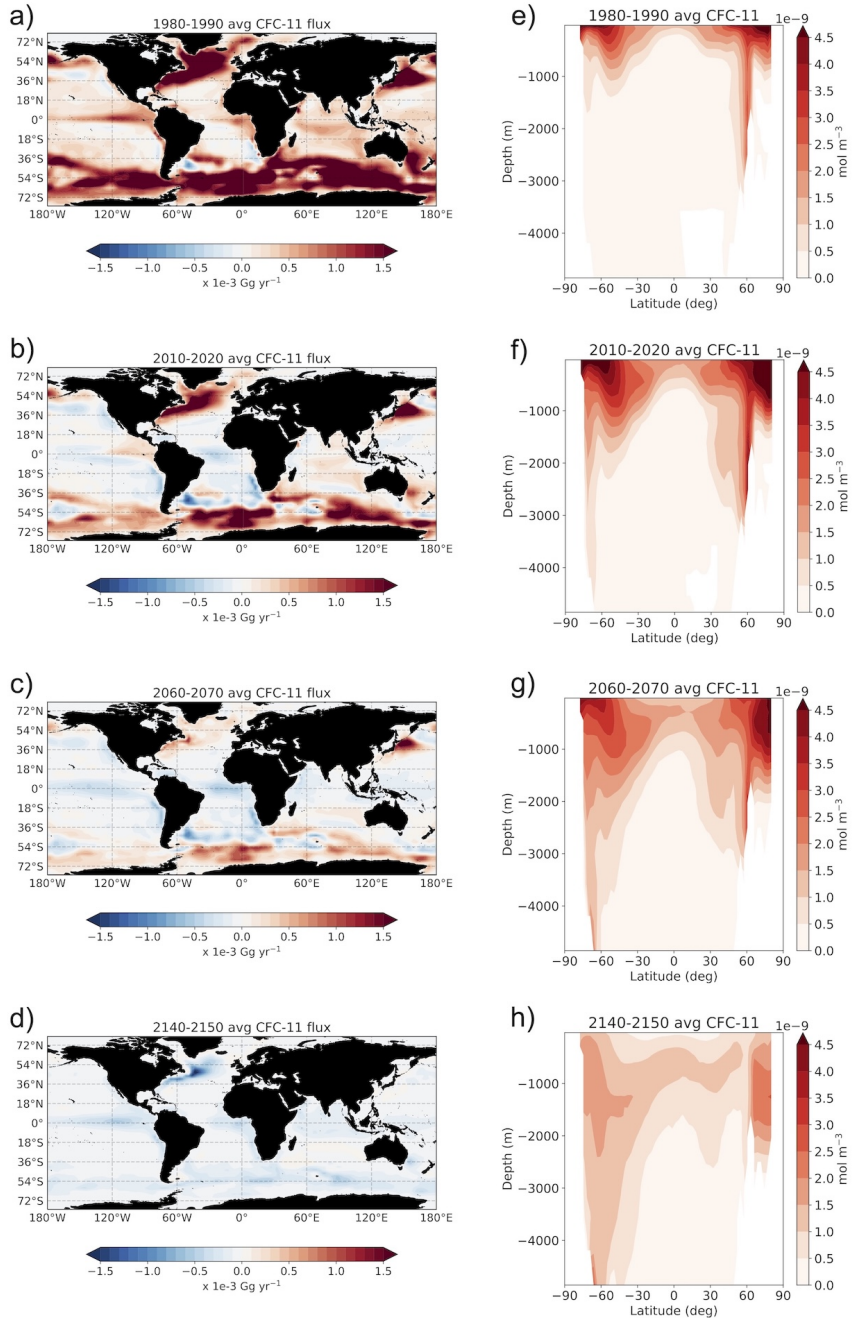
Appendix Figure 2.5: a) Time series of the percent column integrated CFC-11 in the Weddell Sea compared to the global ocean. b) Same figure to Figure 2.2b but overlaid the Weddell Sea region (in white box) used to calculate percent CFC-11 in panel a).



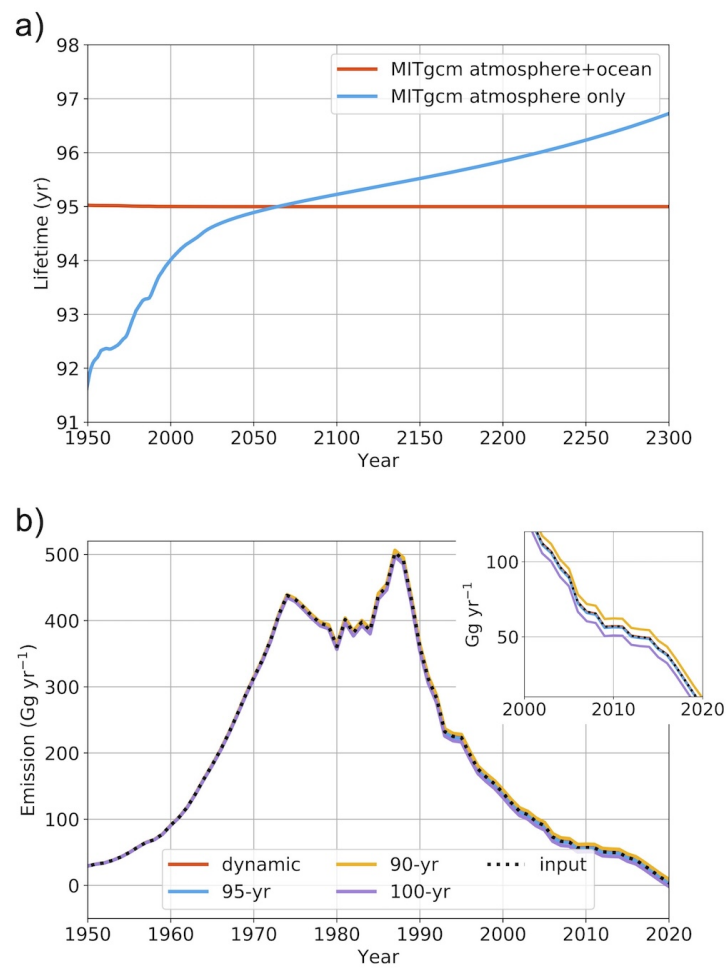
Appendix Figure 2.6: a) Box model CFC-11 inventories for the atmosphere (left axis and solid lines) and the ocean (right axis and dashed lines). Black lines indicate CFC-11 inventories with unmodified parameters as in Appendix Table 2.2, and colored lines display $\pm 15\%$ changes of these associated parameters (only the results from most sensitive parameters are shown in the figure). b) MITgcm CFC-11 inventories under additional ocean forcing runs. In both panels, the ocean inventory is shown inversed in sign to facilitate comparison.



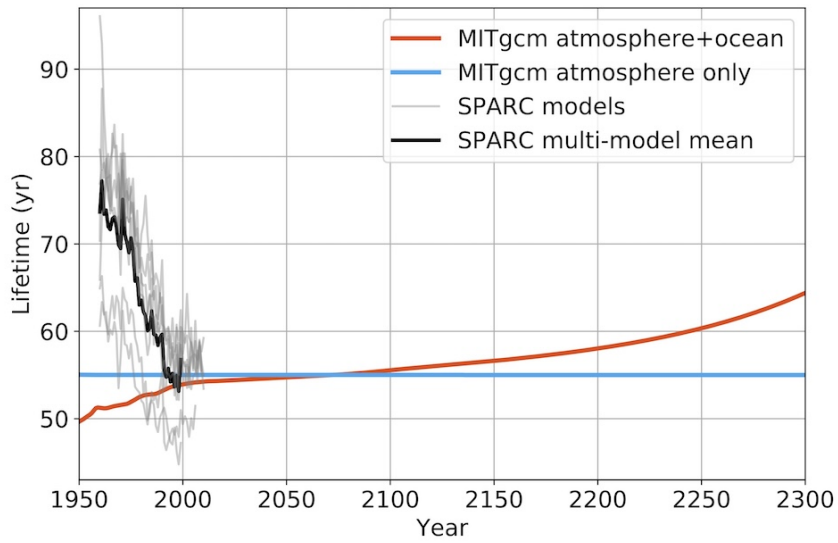
Appendix Figure 2.7: Similar to Figure 2.3, but for CFC-12.



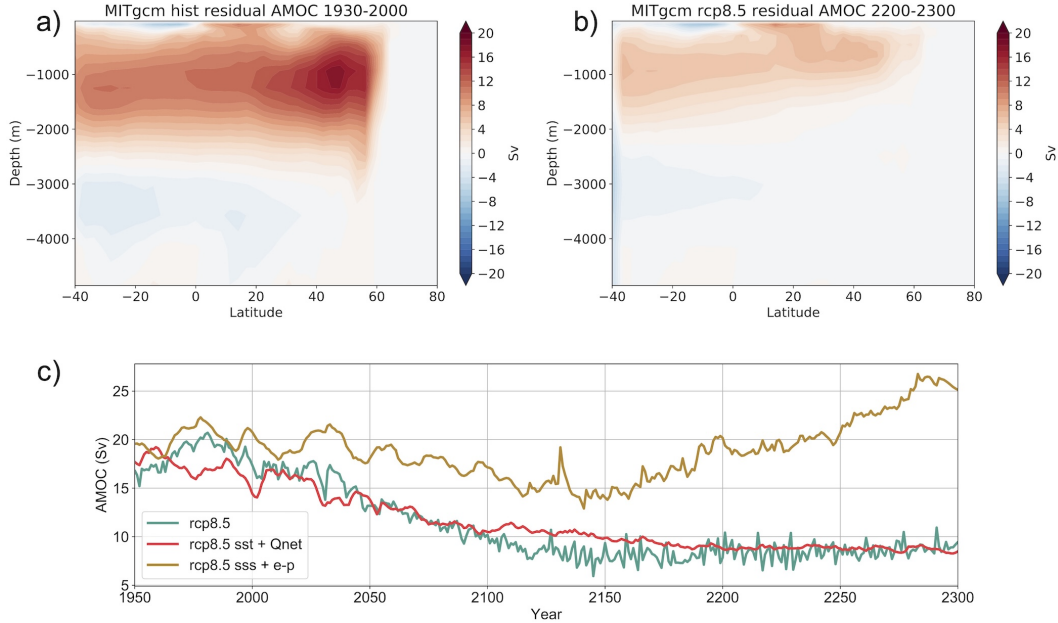
Appendix Figure 2.8: a–d) Decadal averages of CFC-11 air-sea flux (area integrated) for different time periods in the MITgcm Hist run (positive indicate fluxes going into the ocean); e–h) Zonal mean CFC-11 concentration in the ocean for the same averaging periods shown on the left.



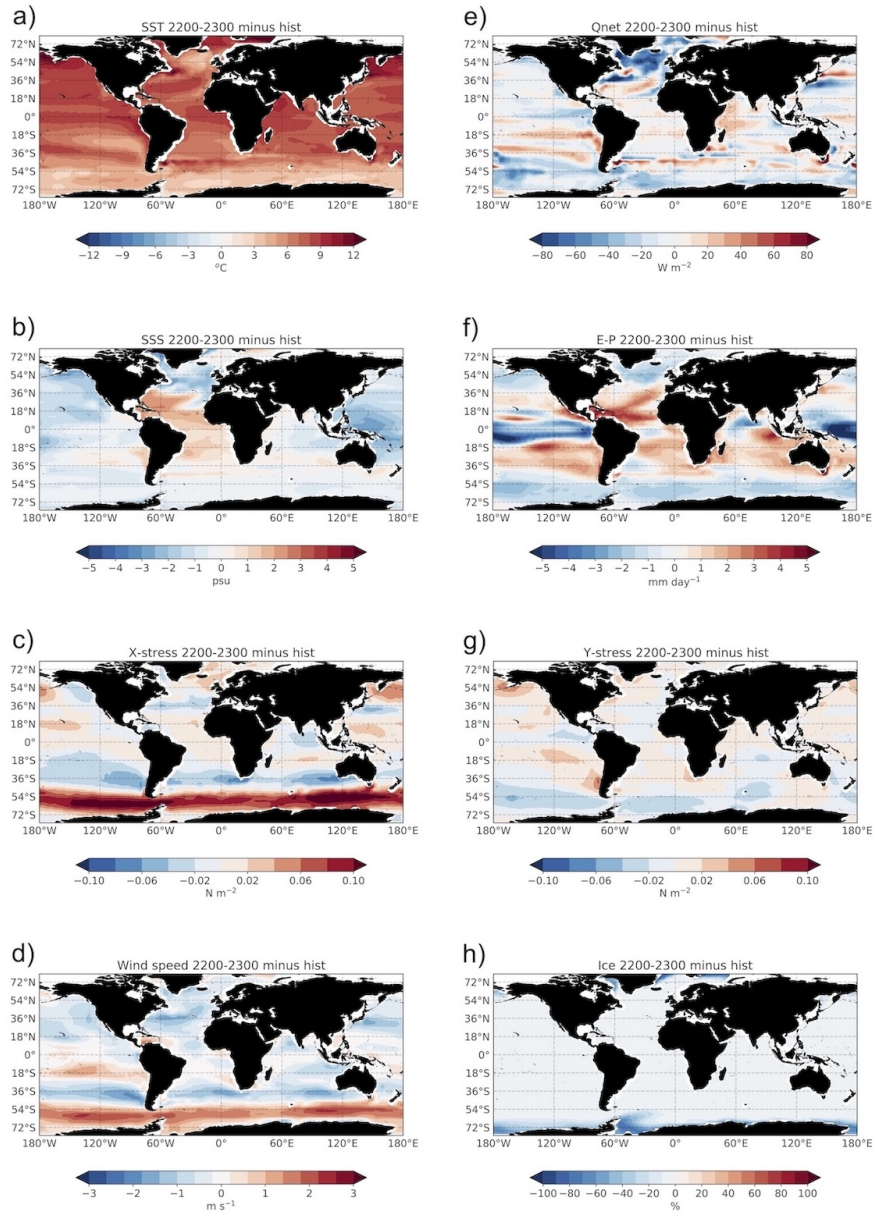
Appendix Figure 2.9: Similar to Figure 2.4, but for CFC-12.



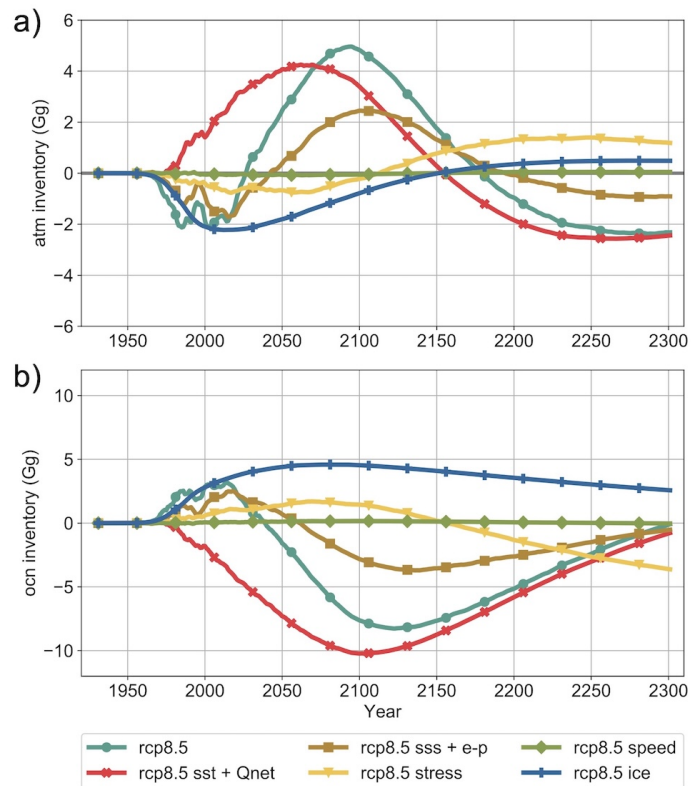
Appendix Figure 2.10: Same as Figure 2.3, except that atmosphere-only CFC-11 lifetime calculated from SPARC chemistry-climate models are overlaid for comparison. Thin gray lines are calculated time-dependent atmosphere-only lifetimes from the SPARC models from 1960 to 2010, while the heavy black line is the SPARC multi-model mean.



Appendix Figure 2.11: a) Zonal mean residual AMOC under Hist run averaged in 1930–2000; b) Zonal mean residual AMOC under RCP8.5 run averaged in 2200–2300; c) Time series of AMOC strength (maximum between 20–50 °N) under full RCP8.5, SST + Qnet only and SSS + E-P only. Under full RCP8.5, AMOC in the MITgcm has decreased by 60 % from 1930–2000 to 2200–2300. This percent decrease is comparable to MPI-ESM-LR, which shows a 56 % decrease during the same period, except that the AMOC climatology in MPI-ESM-LR started at a higher value than the MITgcm at the beginning of 1930.



Appendix Figure 2.12: Anomaly maps of all the forcing fields from the MPI-ESM-LR RCP8.5 scenario. The maps indicate averages of the last 100 years (2200–2300) minus the base period (1850–1930).



Appendix Figure 2.13: CFC-11 inventory difference between each RCP8.5 forcing run and Hist forcing run for a) atmosphere inventories; and b) ocean inventories.

Appendix Table 2.2: A list of parameters and variables used in the box model.

Name	Value Used	Description
m_{nh}^a, m_{sh}^a	Calculated in the model	CFC-11 mass in the atmospheric boxes, subscript indicates the NH and SH
m_{nh}^t, m_{sh}^t	Calculated in the model	CFC-11 mass in the mixed layer boxes, subscript indicates the NH and SH
m_{nh}^d, m_{sh}^d	Calculated in the model	CFC-11 mass in the deep ocean boxes, subscript indicates the NH and SH
F_{nh}, F_{sh}	Calculated in the model	CFC-11 air-sea flux
E_{nh}, E_{sh}	Discussed in the text	CFC-11 emission in the NH and SH
L	$1/55 \text{ yr}^{-1}$	CFC-11 atmospheric loss rate
T_{n2s}^a, m_{s2n}^a	$1/1.3 \text{ yr}^{-1}$	Atmospheric exchange rate between the NH and SH
T_{n2s}^t, m_{s2n}^t	$1/50 \text{ yr}^{-1}$	Mixed layer exchange rate between the NH and SH
T_{n2s}^d, m_{s2n}^d	$1/100 \text{ yr}^{-1}$	Deep ocean exchange rate between the NH and SH
$T_{nh}^{t2d}, m_{sh}^{t2d}$	$1/3 \text{ yr}^{-1}$	Mixed layer to deep ocean exchange rate in the NH and SH
$T_{nh}^{d2t}, m_{sh}^{d2t}$	$1/5 \text{ yr}^{-1}$	Deep ocean to mixed layer exchange rate in the NH and SH
k	10 cm hr^{-1}	Piston velocity
H^a	13 km	Atmosphere height
A^a	$5.1 \times 10^{14} \text{ m}^2$	Atmospheric total surface area
H^t	150 m	Mixed layer depth
A^t	$3.1 \times 10^{14} \text{ m}^2$	Ocean total surface area (assume 15 % sea ice)

Chapter 3

On the Influence of Hydroxyl Radical Changes and Ocean Sinks on Estimated HCFC and HFC Emissions and Banks

Abstract

Hydrochlorofluorocarbons (HCFCs) and hydrofluorocarbons (HFCs) are potent greenhouse gases regulated under the Montreal Protocol and its amendments. Emission estimates generally use constant atmospheric lifetimes accounting for loss via hydroxyl radical (OH) reactions. However, chemistry-climate models suggest OH increases after 1980, implying underestimated emissions. Further, HCFCs and HFCs are soluble in seawater and could be destroyed through in situ oceanic microbial activity. These ocean sinks are largely overlooked. Using a coupled atmosphere-ocean model, we show that increases in modeled OH imply

This chapter is adapted from Wang, P., Solomon, S., Lickley, M., Scott, J. R., Weiss, R. F., & Prinn, R. G. (2023). On the Influence of Hydroxyl Radical Changes and Ocean Sinks on Estimated HCFC and HFC Emissions and Banks. *Geophysical Research Letters*, 50(18), e2023GL105472. <https://doi.org/10.1029/2023GL105472>

underestimated HCFC and HFC emissions by 10 % near their respective peak emissions. Our model results also suggest that oceanic processes could lead to up to an additional 10 % underestimation in these halocarbon emissions in the 2020s. Ensuring global compliance to the Protocol and accurate knowledge of contributions to global warming from these gases therefore requires understanding of these processes.

3.1 Introduction

Chlorofluorocarbons (CFCs) are the main reason for the Antarctic ozone “hole” (e.g. S. Solomon, 1999). Under the Montreal Protocol on Substances that Deplete the Ozone Layer, the production of these molecules has been strictly regulated since the early 1990s. Hydrochlorofluorocarbons (HCFCs) were used to replace CFCs as they can react with the hydroxyl radical (OH) rapidly in the troposphere, reducing the chlorine reaching the stratosphere, and thus depleting ozone. However HCFC emissions were not globally regulated until the early 2010s, and the amount of chlorine delivered to the stratosphere from HCFCs rose by more than 60 % from 1993 to 2020 (Laube & Tegtmeier, 2022). While a complete global phase-out of HCFCs is expected to happen in 2030, their use as feedstocks to manufacture other compounds remains exempted from the Montreal Protocol. In the past two decades, HCFC emissions from feedstocks are believed to have increased by five-fold (Daniel & Reimann, 2022) and leakage rates are higher than expected (Western et al., 2022), prompting discussions about narrowing feedstock exemptions (Andersen et al., 2021). HCFCs were replaced by hydrofluorocarbons (HFCs). HFCs are not ozone depleters but are potent greenhouse gases that have global warming potentials ranging from thousands to tens of thousands times that of carbon dioxide on a mass basis (Liang & Rigby, 2022). The Kigali Amendment to the Montreal Protocol to regulate HFCs entered into force in 2019. The amendment is expected to lead to a global emissions peak in the 2030s. If effective mitigation of HFCs occurs worldwide, the projected global warming, compared to continuing production of HFCs,

will be reduced by up to 0.4 °C by the end of 2100 (Velders et al., 2022).

The primary loss pathway for HCFCs and HFCs is through reaction with OH. But due to a lack of direct measurements of global-scale OH concentrations and uncertainties in the inferred OH concentration based on methyl chloroform observations (Prinn et al., 2018), current emission estimations for HCFCs and HFCs generally assume OH is seasonally-varying but annually-repeating over time. Here we consider time-varying potential trends in OH. Turner, Frankenberg, Wennberg, and Jacob, 2017 found that changes in methane may be explained by an increase in OH from 1980 to 2005 and a decrease afterward. A similar decreasing trend in OH after 2005 was also found in several inversion studies (Montzka et al., 2011; Rigby et al., 2017). In contrast, while a suite of CMIP6 (Coupled Model Intercomparison Project Phase 6) models suggest a 10 % increase in OH from 1980 to 2005 similar to Turner et al., 2017, they indicate ongoing increases afterward (Stevenson et al., 2020). Recently, using methyl chloroform with 3D model inversions incorporating observed meteorology, Patra et al., 2021 also deduced a significant OH increase after 2005. We explore increasing OH trends from 1980 to 2005 and increasing or decreasing trends thereafter.

Halocarbons (mainly CFC-11 and CFC-12) have a long history of use as inert tracers to study ocean circulation (e.g. Bullister and Weiss, 1983; Ito et al., 2004; Romanou et al., 2017; Waugh, 2014). In an earlier study (P. Wang et al., 2021), we showed that ocean uptake can affect the inferred atmospheric residence times of CFC-11 and CFC-12, therefore affecting their emission estimates. Similarly, the ocean represents a potential loss pathway for HCFCs and HFCs since they are also soluble in seawater. However, the ocean could be a larger sink for these gases than previously thought, because certain microbes can feed on hydrogen-bearing compounds (Dworkin, Falkow, Rosenberg, Schleifer, & Stackebrandt, 2006), such as methyl halides (Cox, Schäfer, Nightingale, McDonald, & Murrell, 2012; Tokarczyk, Goodwin, & Saltzman, 2003; Tokarczyk, Saltzman, Moore, & Yvon-Lewis, 2003). Similarly, aerobic oxidation can also degrade certain HCFCs and HFCs (Chang & Criddle, 1995; DeFlaun, Ensley, & Steffan, 1992; Streger, Condee, Togna, & DeFlaun, 1999). But due to limited

measurements, ocean degradation of HCFCs and HFCs via biological processes has not been considered in previous estimations of ocean partial lifetimes (Liang & Rigby, 2022; Yvon-Lewis & Butler, 2002). Hydrolysis is another ocean degradation process for halogenated species such as methyl chloroform (Wennberg et al., 2004), but is considered minor for HCFCs and HFCs (Yvon-Lewis & Butler, 2002). Here we explicitly evaluate the atmospheric residence time, treating the ocean destruction and reservoir both as sinks insofar as the atmosphere (as appropriate for deriving emissions) is concerned; previous work has often used a different definition of ocean destruction only, which leads to much smaller impacts (Yvon-Lewis & Butler, 2002).

Given debate regarding feedstock emissions for HCFCs and new regulations on HFCs, it is crucial to consider uncertainties in emission estimates inferred from observed atmospheric abundance data to ensure the continued success of the Montreal Protocol and its amendments. In this study, we quantify uncertainties in emission estimations and banks due to different OH scenarios (time-varying OH trends versus fixed OH) and ocean scenarios (only involving physical dissolution or with additional microbial ocean degradation) for three HCFCs (HCFC-141b, HCFC-142b, and HCFC-22) and three HFCs (HFC-125, HFC-134a, and HFC-23) whose seawater solubilities are provided by P. Li et al., 2019.

3.2 Data and methods

We couple the ocean representation of the MITgcm (Massachusetts Institute of Technology General Circulation Model; Marshall, Adcroft, et al., 1997; Marshall, Hill, et al., 1997) with the atmosphere from the AGAGE (Advanced Global Atmospheric Gases Experiment) 12-box model (Rigby et al., 2013). This coupled model runs independently from the start of emissions for each species to 2050.

3.2.1 Ocean representation

We use a similar MITgcm ocean configuration as P. Wang et al., 2021, adopting a $2.8^\circ \times 2.8^\circ$ horizontal resolution and 15 vertical layers down to 5 km depth. Despite its coarse resolution, this configuration simulates the oceanic distributions and the overall ocean burdens of CFCs reasonably well (P. Wang et al., 2021). The ocean is forced with monthly climatologies of wind stress and buoyancy fluxes. A detailed description of each of the forcing fields is discussed in P. Wang et al., 2021. Prior to the introduction of halocarbon emissions, the ocean was spun-up for 5900 years with these climatological forcings to effectively reach a steady state. We only consider climatological forcing in this study since our earlier study showed that future climate change had a rather small impact on the global CFC ocean burden (although it does affect the timing for the ocean to switch from a net sink to a net source (P. Wang et al., 2021)).

P. Li et al., 2019 report the Ostwald solubilities as functions of temperature and salinity for several HCFCs and HFCs. Freshwater solubilities are compared with other studies using various methods, and good agreement is achieved for most of the species except HFC-125 (P. Li et al., 2019). These temperature- and salinity-dependent solubilities are then fitted to a polynomial that has the format used by the MITgcm. Appendix Table 3.1 shows the fitted coefficients for HCFCs and HFCs used in this study. Appendix Figure 3.4 plots the solubility for each species as a function of temperature and salinity. These molecules are generally more soluble in colder and less salty conditions.

The Schmidt number (Sc) is used in the MITgcm to calculate the gas transfer velocity. It characterizes the ratio between the kinematic viscosity of the solution and the diffusion coefficient of the gas in the solution (Wanninkhof, 1992). We follow a similar process to obtain seawater Sc values for HCFCs and HFCs as in Wanninkhof, 1992. Sc in the MITgcm is parameterized only as a function of temperature at a constant salinity of 35 ‰(per mille); see Appendix Text: Schmidt number estimation, Appendix Table 3.2, and Appendix Figure

[3.5](#) for details.

Several studies indicate that aerobic microbial processes in the ocean can destroy certain HCFCs and HFCs (Chang & Criddle, [1995](#); DeFlaun et al., [1992](#); Streger et al., [1999](#)). However, ocean degradation rates can vary significantly depending upon spatial and temporal variations in biology and other properties such as oxidation state. Due to limited knowledge of the ocean degradation processes, we perform several ocean scenarios to explore various assumptions: 1) no ocean uptake (noOCN), 2) with ocean dissolution but without any degradation (OCN), and 3) with an e-folding ocean degradation timescale at 1 yr (degradeOCN). We choose 1 yr as the upper limit of ocean degradation losses because HCFC-22, which experiences faster decay than other species (Chang & Criddle, [1995](#)), degrades with a timescale on the order of a year in the ocean mixed layer (detailed calculation in Appendix Text: Biological degradation estimation). We also present results for ocean degradation with a timescale of 5 yr to illustrate the differences found between no biological degradation and a 1 yr degradation timescale.

3.2.2 Atmosphere representation

We use the AGAGE 12-box model as the atmospheric portion of our coupled ocean-atmosphere framework. This model has three vertical layers (surface to 500 hPa, 500–200 hPa, and above 200 hPa) and four zonally-averaged latitudinal bands (90–30 °N, 30 °N–equator, equator–30 °S, and 30–90 °S). It employs monthly OH concentrations and transport parameters for each box. A detailed description is provided in Rigby et al., [2013](#). Note that we do not consider year-to-year changes in the atmospheric transport parameters, but such interannual dynamical changes can also influence variations in inferred lifetimes and emissions (Ko, Newman, Reimann, & Strahan, [2013](#)).

Historical input emissions for HCFCs and HFCs between the 1970s and 2021 are from the posterior mean emission (later referred to as posterior emission) obtained by inverse modeling of the AGAGE measured mole fractions of each species combined with a 12-box

model that assumes fixed OH and constant lifetimes from the WMO (World Meteorological Organization) 2022 report (Laube & Tegtmeier, 2022; Liang & Rigby, 2022; Rigby et al., 2013). However, anthropogenic emissions for HCFC-22 and HFC-23 started long before the AGAGE observations began and posterior emissions are available. For these two species, we run the coupled ocean-atmosphere model starting in the 1940s with zero initial concentrations in both the ocean and atmosphere, employing a priori emissions (Miller et al., 2010) to produce reasonable tracer distributions, and then switch to the posterior emissions after the 1970s. Here we focus on the period when we switch to the posterior emission inputs. Appendix Figure 3.6 shows the model simulated atmospheric mole fractions for all the species used in this analysis using the posterior emissions compared to the AGAGE observations (Prinn et al., 2018, updated through 2021 using data from <https://agage.mit.edu/data>), and they show good agreement.

Future emissions for HFC-125 and HFC-134a are from the upper limit of the Kigali Amendment projection from Velders et al., 2022. Future emissions for HCFC-141b, HCFC-142b, and HCFC-22 are obtained from the inverse study of the projected mole fractions from Daniel and Reimann, 2022 using a one-box model assuming a perfectly mixed atmosphere and constant lifetimes. HFC-23 is mainly a by-product of HCFC-22 production, and we assume future HFC-23 emissions follow the same rate of change as HCFC-22 (neglecting potential differences during leakage from banks such as refrigeration). To prevent discontinuity in the input emissions, we scale global projected emissions from 2022–2050 to emissions in 2021, and apply this scaling to generate a smooth transition from the historical to future emissions.

Different OH scenarios are considered in order to infer HCFC and HFC atmospheric residence times and emissions. In the “fixOH” scenario, we use repeating monthly OH concentrations every year from Rigby et al., 2013. In the “varyOH” scenario, OH does not change before 1980, but it increases by 10 % between 1980 and 2005 (in each box and month). Future projections of OH to 2050 vary greatly among different models (Murray, Fiore, Shindell, Naik, & Horowitz, 2021). We therefore apply a $\pm 15\%$ change of OH between

2005 and 2050 (spanning the range from different warming scenarios in Murray et al., 2021). Appendix Figure 3.7 summarizes different OH assumptions used in this study. Note that the absolute amount of OH concentration from inversions based on methyl chloroform can have large uncertainties (Rigby et al., 2017). These absolute uncertainties largely cancel insofar as they exist in both the “fixOH” and “varyOH” scenarios, and only the relative change in the emissions between different OH scenarios is affected.

3.2.3 Inferring the atmospheric residence times and the emissions

We refer to the e-folding decay timescale for each species as the atmospheric residence time in this study since the residence time involves not only atmospheric loss rates (i.e., reaction with OH) but also ocean processes (such as ocean uptake and outgassing) characterized by:

$$\tau(t) = \frac{B(t)}{L_{OH}(t) + L_{OCN}(t) + L_{OTHER}(t)} \quad (3.1)$$

where B is the total atmospheric burden, L_{OH} , L_{OCN} , and L_{OTHER} are the total loss rates due to OH, ocean sinks, and other photochemistry (largely stratospheric), respectively. L_{OCN} can be negative when the ocean becomes supersaturated and returns gas back to the atmosphere.

To infer global emissions, we use different residence times τ calculated from various combinations of ocean and OH scenarios, using the equation:

$$E(t) = \frac{dB(t)}{dt} + \frac{B(t)}{\tau(t)} \quad (3.2)$$

where the atmospheric burden B is the simulated “noOCN” and “fixOH” case, i.e., what we would have “observed” in the atmosphere in the absence of time-varying OH and ocean uptake.

3.3 Results

3.3.1 Relative magnitudes of different loss pathways

We first quantify a baseline magnitude (without varying OH and neglecting ocean degradation) of each loss pathway for HCFCs and HFCs (Appendix Figure 3.8). Without considering ocean degradation, the global ocean sink and stratospheric loss through photochemistry are generally about an order of magnitude smaller than loss due to OH. However, HFC-23 has a slow reaction with OH and an atmospheric lifetime greater than 200 years (while other species considered here display decadal lifetimes), and ocean loss is comparable to OH loss for this molecule. For all species, loss rates due to ocean sinks differ between the two hemispheres. Ocean uptake in the Southern Hemisphere is twice that in the Northern Hemisphere (Appendix Figures 3.9–3.10), due in part to the larger open ocean area and enhanced upwelling of undersaturated waters driven by strong surface wind stress. Therefore, loss to the ocean in the 30–90 °S latitude band accounts for 10–20 % of the loss to OH in that region for most of the species considered here. Globally summed, loss to the ocean is less than about 5 % of the total loss to OH for HCFCs and HFCs in this analysis, with the important exception of HFC-23.

3.3.2 Inferred atmospheric residence times

Figure 3.1 shows the inferred atmospheric residence times for each species. Species other than HCFC-22 and HFC-23 have close to zero emissions in the 1980s, reflected in steep changes in the residence times in the first few years. The impact of the ocean on the inferred residence times is largest in the early period, when the ocean is less saturated and has a greater ability to dissolve these gases. Overall, the ocean shortens the inferred residence times during most of the time before 2050, as the ocean is still a net sink for these species globally (although earlier ocean outgassing is occurring regionally in the tropical and coastal upwelling zones).

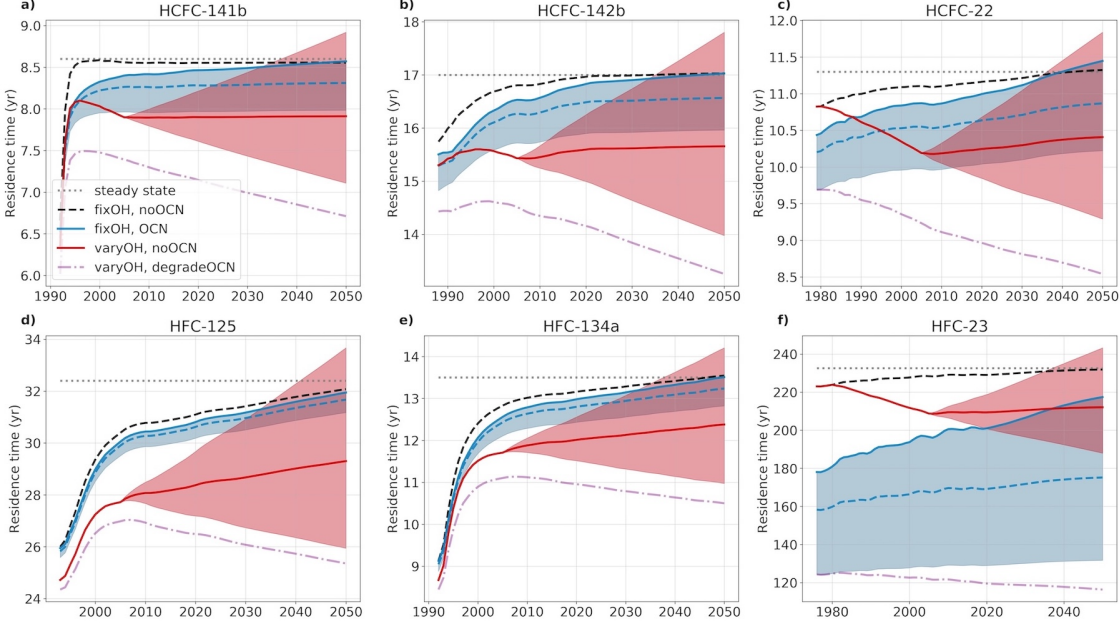


Figure 3.1: Global atmospheric residence times for all the species used in this study. Gray dotted lines are the steady state lifetimes calculated from the AGAGE 12-box model based on atmospheric removal rates from the World Meteorological Organization (WMO), 2022 report. Black dashed lines are inferred from a model simulation with fixed OH over time and without ocean uptake. Blue solid lines are inferred from models with fixed OH over time but including ocean dissolution without degradation, while blue dashed lines assume a 5 yr ocean degradation timescale, blue shadings denote the case for ocean degradation timescale up to 1 yr. Red solid lines indicate a 10 % increase in OH from 1980 to 2005 and are constant beyond 2005, and the red shadings indicate ± 15 % OH changes from 2005 to 2050. The purple dash-dotted lines combine the increasing OH (both 10 % increase in 1980–2005 and 15 % increase in 2005–2050) with a 1 yr ocean degradation timescale to define a lower limit range.

However, an exception is HCFC-22, for which the ocean starts to become a net source of emission in the 2040s globally (Appendix Figure 3.8h), and hence its residence times increase afterward. Without ocean degradation, adding the ocean shortens the inferred residence times by up to 2 % before 2020 for most of the species, and 15 % for HFC-23. As the ocean becomes more saturated over time, the difference in the inferred residence times with versus without the ocean shrinks.

However, if a dissolved HCFC or HFC is degraded in the ocean, the ocean will have a greater ability to uptake these gases and will be difficult to oversaturate relative to its declining trend in the atmosphere. By 2020, assuming halocarbons degrade in the ocean with a timescale of 5 yr, their residence times are shortened by 2–5 % compared to the noOCN case for most species (and a 25 % decrease in residence time for HFC-23). And if the ocean degradation timescale is 1 yr, we obtain a 3–10 % decrease in the inferred residence times for most of the species (and a 40 % decrease for HFC-23).

Increasing OH concentrations would also shorten residence times in the atmosphere. A 10 % increase in the OH concentration from 1980 to 2005 leads to about an 8 % decrease in the inferred residence time by 2005 for all the species in this study. After 2005, if OH increased by another 15 % by 2050 as some models indicate, this would result in a 15–20 % decrease in the inferred residence time by the end of 2050 compared to the fixed OH scenario. However, if OH decreases after 2005, the inferred residence time would return to the fixed OH scenario by the end of 2040. The purple dot-dashed lines in Figure 3.1 show the lower limits of residence times obtained by combining both a 1 yr ocean degradation timescale and an increasing OH of 25 % from 1980 to 2050.

3.3.3 Inferred global emissions and bank estimations

Figure 3.2 shows the inferred global emissions for HCFCs and HFCs using different inferred atmospheric residence times obtained from Section 3.3.2 (changes in the emissions shown in Appendix Figure 3.11). Comparing cases with ocean uptake (no ocean degradation) to those

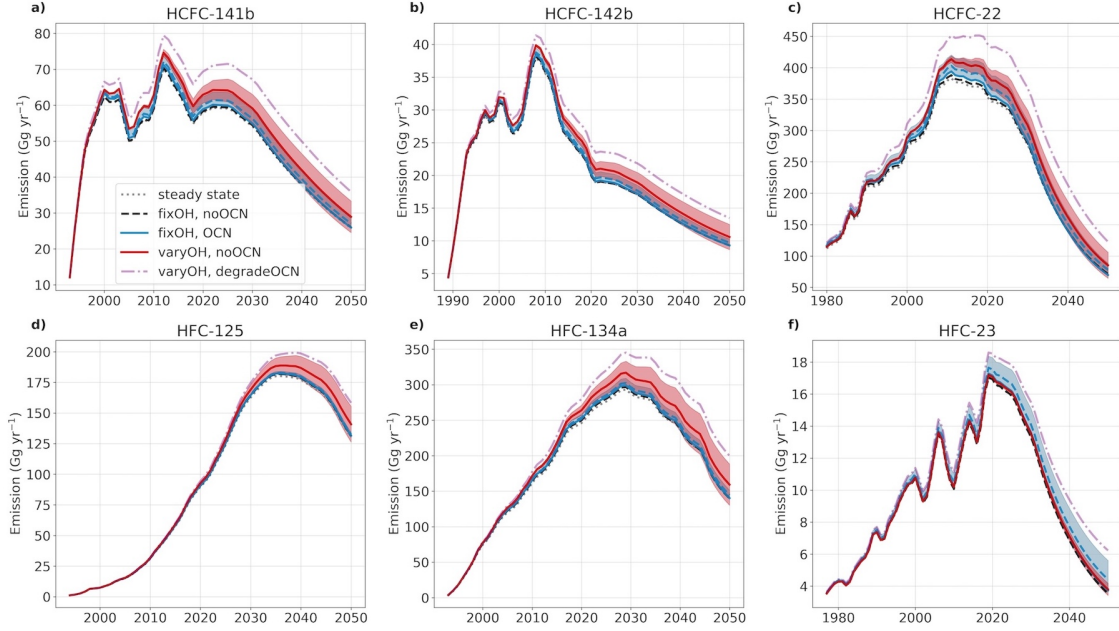


Figure 3.2: Inferred global emissions for all the species modeled in this study, based on the different residence times for the cases considered in Figure 3.1.

without ocean uptake implies that neglect of the ocean leads to a 1–2 % underestimation in the inferred emissions for all three HCFCs and HFC-23, and less than 1 % for HFC-125 and HFC-134a around 2020. If there is a 5 yr ocean degradation timescale, we obtain another 2–3 % underestimation in the inferred emissions. However, if the ocean degrades these halocarbons at a 1 yr timescale, an 8–10 % underestimation in the inferred emissions for HCFCs and HFC-23 is obtained, with less than 5 % underestimation for HFC-125 and HFC-134a. Ocean uptake can significantly decrease the HFC-23 atmospheric residence time, but it is still above 100 years, so the relative impact on its inferred emission is not as large as the impact on its residence time.

With a 10 % increase in OH concentration only from 1980 to 2005, we obtain a 5–7 % underestimation in the inferred global emissions by the end of 2005 for all three HCFCs compared to the case of the fixed OH scenario. For HFCs, there is a 1–5 % underestimation in the inferred emissions by 2005. There is a large variation in the inferred emissions after 2005 given different OH scenarios, and the corresponding variations in the emission due to different OH scenarios by the end of 2050 can be up to 40 %. Considering both a 1 yr ocean

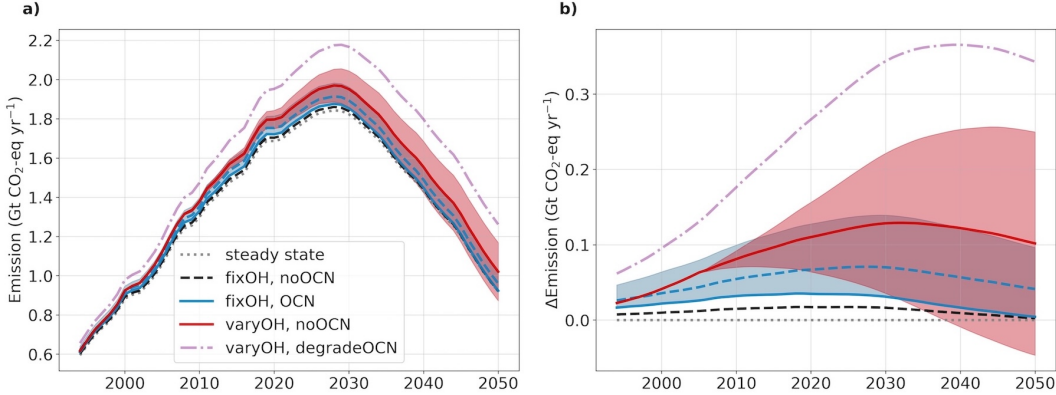


Figure 3.3: Summed emissions of all the HCFCs and HFCs in this study weighted by their global warming potentials. The absolute emissions are shown in panel a), and the differences between the emissions inferred from transient residence times and steady state lifetimes (assuming no ocean and fixed OH) are shown in panel b).

degradation timescale and increasing OH would imply an underestimate of the emissions, by around 10–20 % during the peak of emissions for HCFCs and HFCs.

By weighting the emissions of each species by its global warming potential compared to CO₂ (on a 100-year horizon; Burkholder and Hodnebrog, 2022), we calculate the CO₂-equivalent emissions summed from all six HCFCs and HFCs in this study (Figure 3.3; Appendix Figure 3.12 breaks the summed emission into different species). During the peak total emission period in the 2020s, this would underestimate the emission by 1 % if one does not include the ocean uptake (and by 6 % if the ocean degrades at 1 yr). And if OH keeps increasing from 1980 to the 2020s, using fixed OH would underestimate the emission by another 7 %. And combining ocean degradation and increase in OH could underestimate the CO₂-equivalent emission by up to 15–20 % in the 2020s.

The estimated bank is the difference between production (or bottom-up emission) and the inferred (top-down) emission (calculated from equation 3.2). If we assume that production has been accurately reported, then with higher inferred emissions resulting in banks depleting faster than currently expected. We quantify the resulting impact on banks by integrating the inferred emissions (from Figure 3.2) over time. Appendix Figure 3.13 shows the difference between HCFC and HFC banks estimates calculated from the (noOCN and fixOH) steady state

residence times based on atmospheric removal rates reported in Burkholder and Hodnebrog, 2022 and banks calculated from transient residence times. In the current decade, if we do not consider the ocean processes, we would overestimate the bank by 22–101 Gg for HCFC-141b, 8–40 Gg for HCFC-142b, 197–1090 Gg for HCFC-22, 3–9 Gg for HFC-125, 40–152 Gg for HFC-134a, and 6–34 Gg for HFC-23 (the range spans no ocean degradation to a 1 yr decay timescale). If we do not consider the increase in OH from 1980 to 2005, we would have overestimated the banks by 76–140 Gg for HCFC-141b, 35–63 Gg for HCFC-142b, 537–940 Gg for HCFC-22, 16–45 Gg for HFC-125, 148–340 Gg for HFC-134a, and 2–4 Gg for HFC-23 in the 2020s (the range spans continued OH increases or decreasing after 2005). Ocean uptake/loss and increasing OH would add to each other, resulting in an even larger overestimation in the global banks for these molecules (shown as the purple dash-dotted line in Appendix Figure 3.13). Alternatively, if we assume that bank estimates are accurate, higher emissions could be an indication of higher than reported production, where emissions in the year of production could be anywhere between 6 and 83 %, depending on the application and gas (Lickley, Daniel, Fleming, Reimann, & Solomon, 2022), with the remaining 17–94 % of production going into the banks. This would imply that banks are in fact higher than published estimates suggest, and the bias could be an order of magnitude (if initial releases are closer to 6 %) and of the opposite sign than that shown in Appendix Figure 3.13. This wide range of uncertainty underscores the need to account for the ocean and OH lifetime effects in future bank assessments.

3.4 Conclusions and discussions

In this study, we have explored the uncertainties from the ocean uptake and OH sinks for several Montreal Protocol-regulated molecules. We show that if one does not consider oceanic dissolution, and assumes no oceanic degradation, this would underestimate the emissions of HCFCs and HFCs by about 1–2 % in the current decade. This impact is rather small. Due to

limited knowledge of ocean degradation rates, these species are often treated as conservative tracers within the ocean (Liang & Rigby, 2022; Yvon-Lewis & Butler, 2002). But evidence suggests certain species can be destroyed in the ocean (Chang & Criddle, 1995; DeFlaun et al., 1992; Streger et al., 1999). If there is a significant ocean degradation pathway, the emission of HCFCs and HFCs would be underestimated by up to 10 % depending on how fast these species are destroyed in the ocean. Climate change can add more uncertainty in emission estimations by directly affecting HCFC and HFC solubilities, ocean circulation (P. Wang et al., 2021) and/or influencing the oceanic biological activity (Kirchman, Morán, & Ducklow, 2009).

The main loss pathways for HCFCs and HFCs are through their reactions with OH. Models and inversions consistently suggest a 10 % increase in OH from 1980 to 2005 (Stevenson et al., 2020; Turner et al., 2017), but current emission estimations for HCFCs and HFCs are based on fixed OH concentrations over time. If one assumes that OH is fixed, whereas it is actually increasing, emissions would be underestimated by 5–7 % by 2005. Future emissions estimation also depends strongly on an accurate estimation of OH concentration changes out to 2050.

The relative importance of including the ocean and OH trend for emission estimation is determined by how these processes compete. The ocean plays a significant role for HFC-23, whose reaction rate with OH is more than 20 times slower than the other modeled species, even though it is 2–5 times less soluble in seawater. For other species whose reaction rates with OH are faster: the ocean plays a more significant role for HCFC-141b and HCFC-22 due to their relatively high solubilities compared to HCFC-142b, HFC-125 and HFC-134a.

Although new production of HCFCs is now controlled, utilizing these species as feedstocks is exempted from the Montreal Protocol, based on the assumption that feedstock emissions should be small. By 2019, however, up to 8 % and 33 % of the global emissions of HCFC-22 and HCFC-142b appear to be from the feedstock emissions (Daniel & Reimann, 2022). The feedstock market has increased sharply in the past decade and is likely to continue increasing

if there are no further actions on the feedstock exemption (Andersen et al., 2021). Inferences of banks and emissions (including feedstock emissions) depend on knowledge of residence times, for which OH trends and possible ocean degradation are important uncertainties. HCFC and HFC total emissions represent about 1.8 Gt CO₂-equivalent per year, or about 5 % of total emissions of all global warming agents (IEA, 2022). Our study suggests a total uncertainty in their contribution to warming of up to 15–20 % in the current decade and draws attention to the need for additional information on oceanic degradation processes and on OH trends to better quantify the atmospheric emissions of these compounds. This will add a perspective that has been overlooked in the past to the discussion of ensuring the success of the Montreal Protocol and its following amendments.

Appendix

Appendix Text: Schmidt number estimation

Following Wanninkhof, 1992, the Schmidt number for gas in seawater is expressed as:

$$Sc = \frac{\mu_{sw}}{D_{sw}} \quad (3.3)$$

where μ_{sw} is the kinematic viscosity of seawater, and D_{sw} is the gas diffusion coefficient in the seawater. We first acquire μ and D under freshwater conditions, and then correct to seawater conditions (corresponding to a constant salinity of 35 ‰), following Wanninkhof, 1992:

$$D_{sw} = (1 - 0.06)D \quad (3.4)$$

$$\mu_{sw} = (1.052 + 1.3 \times 10^{-3}t + 5 \times 10^{-6}t^2 - 5 \times 10^{-7}t^3)\mu \quad (3.5)$$

where t is the temperature in °C.

Freshwater D is parameterized below (Wilke & Chang, 1955):

$$D = 7.4 \times 10^{-8} \times \frac{T(qM_w)^{0.5}}{V_a^{0.6}\eta} \quad (3.6)$$

where T is the temperature (in K), q is the water association factor ($q=2.26$), M_w is the molar mass of water ($M_w=18$), V_a is the molar volume of the molecule at normal boiling point, and η is the dynamic viscosity of water. We use the parameterization for freshwater η from Belessiotis, Kalogirou, and Delyannis, 2016 which is a function of t (in °C):

$$\eta = \exp\left(-3.79418 + \frac{604.129}{139.18 + t}\right) \quad (3.7)$$

and kinematic viscosity of water μ can be calculated from dynamic viscosity of water η by

$$\mu = \eta/\rho.$$

For freshwater density ρ , we use the parameterization from Bigg, 1967 and Millero and Poisson, 1981 as a function of temperature t (in $^{\circ}\text{C}$):

$$\begin{aligned} \rho = 999.842594 + 6.793952 \times 10^{-2}t - 9.09529 \times 10^{-3}t^2 + 1.001685 \times 10^{-4}t^3 \\ - 1.120083 \times 10^{-6}t^4 + 6.536336 \times 10^{-9}t^5 \end{aligned} \quad (3.8)$$

To acquire the molar volume at normal boiling point V_a (with units in $\text{cm}^3 \text{ mol}^{-1}$) for HCFCs and HFCs, we use the additive method discussed in Reid, Prausnitz, and Poling, 1987. The additive method sums the number of occurrences for carbon, hydrogen, chlorine, and fluorine atoms (add 1 for a double bond) multiplied by 7, 7, 24.5, and 10.5, respectively. This method performs surprisingly well and yields an average 3 % error compared to experimental measurements (Reid et al., 1987).

Finally, seawater Sc for different HCFCs and HFCs depends only on the temperature and the molar volume at the normal boiling point. We then fit the Sc for each species to a polynomial in the same format for Sc used by the MITgcm. Appendix Table 3.2 shows the polynomial-form of the Sc in the MITgcm, and the fitted coefficients for each HCFC and HFC. Appendix Figure 3.5a shows the temperature-dependent Sc relationships for all of the species used in this study. Appendix Figure 3.5b also compares our calculation of the Sc for CFC-11 and CFC-12 to the Sc reported in Wanninkhof, 1992. Overall, our calculation agrees well with Wanninkhof, 1992, especially at warmer temperatures. However, our calculation can underestimate the Sc by up to 5 % at temperatures close to 0°C . This could be mainly due to different values for water density and dynamic viscosity (which are both temperature-dependent quantities) in this study compared to Wanninkhof, 1992.

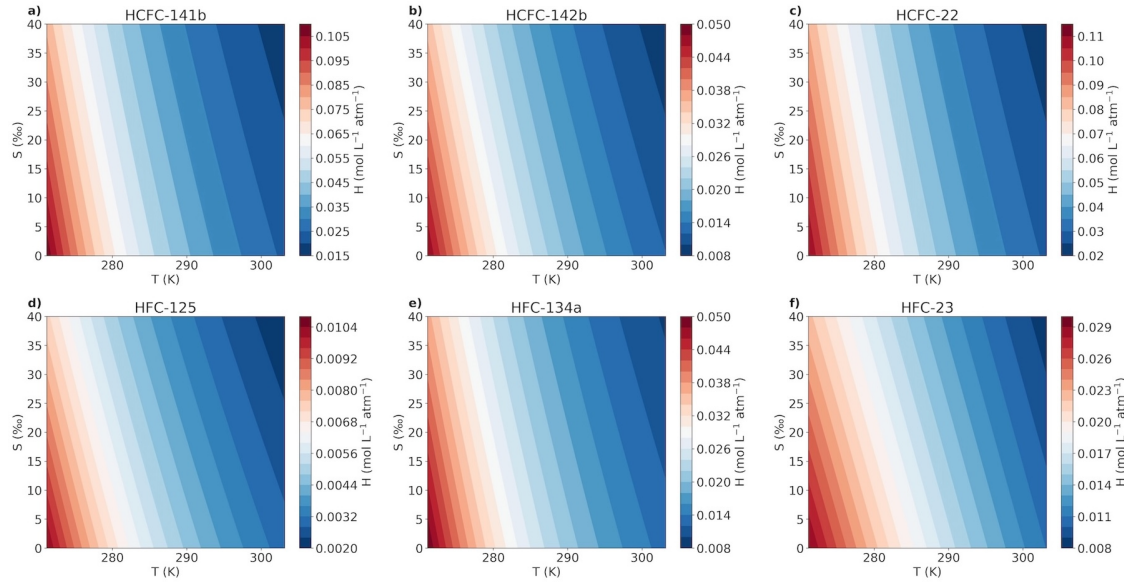
Appendix Text: Biological degradation estimation

Given limited information on the biological degradation processes for HCFCs and HFCs, we approximate the order of degradation rate from observations (e.g. daily, monthly, yearly, or decadal timescales). There are two extreme biological degradation limits: the lower extreme limit is no biological degradation at all (equivalent to an infinitely long degradation timescale). This corresponds to the case in which we consider only the physical ocean uptake (results shown in blue solid lines in Figures 3.1–3.3); the upper extreme limit that is all the molecules are immediately consumed by microbial activities (equivalent to an infinitesimally short degradation timescale). The second extreme limit does not seem warranted because observations from P. Li and Tanhua, 2021 have shown accumulation of these molecules in the ocean.

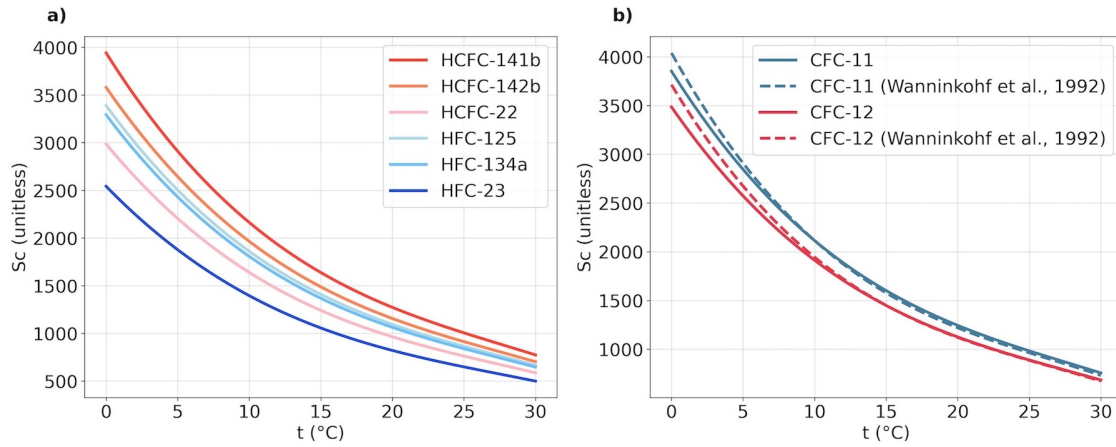
We therefore use observations to provide a reasonable guess for the magnitude of biological degradation timescale for the upper limit. We assume tracers in the upper ocean decay with an exponential rate τ such that $P_{tr} = P_{tr_0} e^{(-\Delta t/\tau)}$. For a tracer that is conserved in the ocean (no chemical nor biological loss), the decay rate mainly characterizes dynamical processes, where $1/\tau = 1/\tau_{dynamical}$. Here we use CFC-12 to characterize the timescale related to dynamical processes. For tracers that are not conserved in the ocean (e.g. HCFC-22), its decay rate includes both dynamical and biological processes where $1/\tau = 1/\tau_{dynamical} + 1/\tau_{biological}$.

From the cruise reported by P. Li and Tanhua, 2021, percent saturation for CFC-12 and HCFC-22 is 94 % and 70 %, respectively; and solubility for CFC-12 and HCFC-22 is 3.13×10^{-12} and 4×10^{-11} mol m⁻³ ppt⁻¹, respectively given observed temperature and salinity during the cruise. Atmospheric mole fraction of CFC-12 and HCFC-22 during this cruise is 510 ppt and 250 ppt, respectively. Given percent saturation, solubility, and atmospheric mole fraction, we obtain the theoretical ocean concentration (P_{tr_0}) of CFC-12 to be 1.4 pmol kg⁻¹, and HCFC-22 to be 6.8 pmol kg⁻¹. The observed ocean concentration (P_{tr}) for CFC-12 is 1.1 pmol kg⁻¹, and HCFC-22 is 4.5 pmol kg⁻¹. The atmosphere-ocean equilibrium timescale given

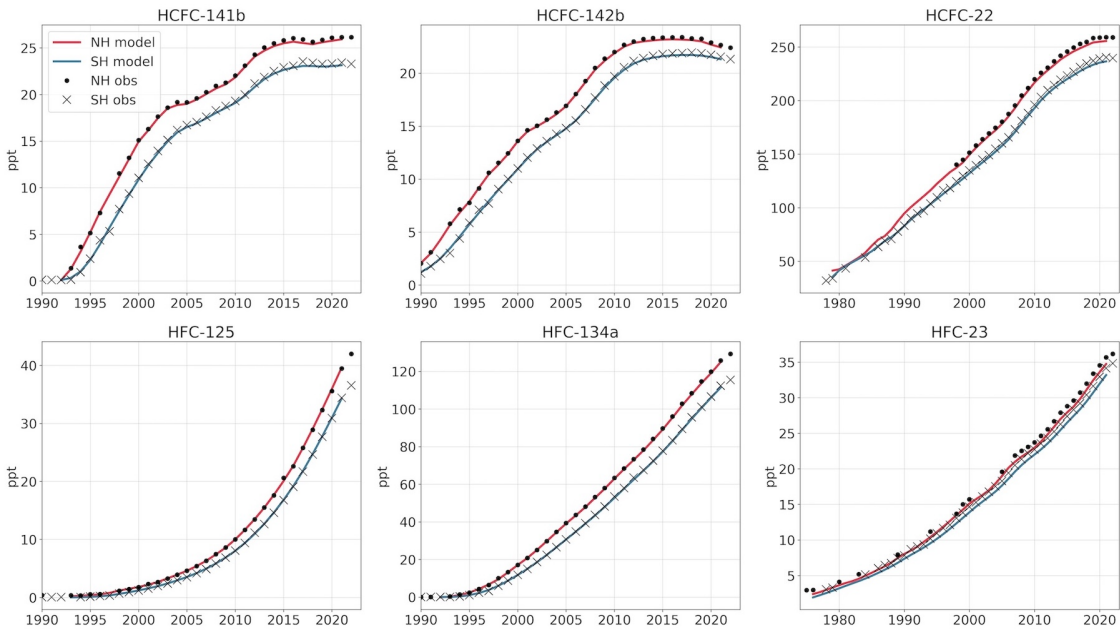
gas-transfer velocity of 10 cm hr⁻¹ (England et al., 1994) and mixed layer depth of 100 m is 40 days. With such a timescale, $\tau_{dynamical}$ is 165 day⁻¹, and $\tau_{biological}$ is 234 day⁻¹, which we approximate as 1 year. We also show results for an adopted intermediate value of 5 years relative to no removal, to illustrate that sensitivity.



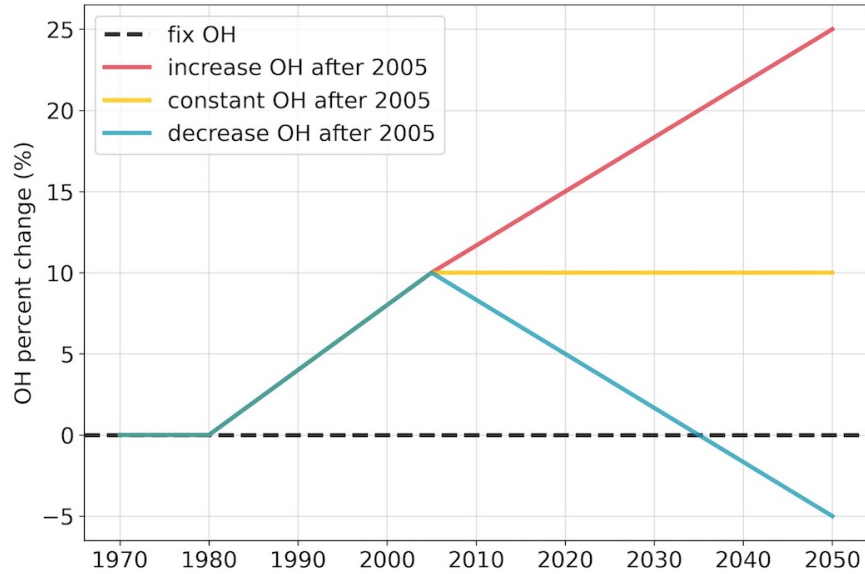
Appendix Figure 3.4: Henry's law solubility for HCFCs and HFCs considered in this study. X-axis shows the temperature and the y-axis shows the salinity. Color bar limits in different panels vary.



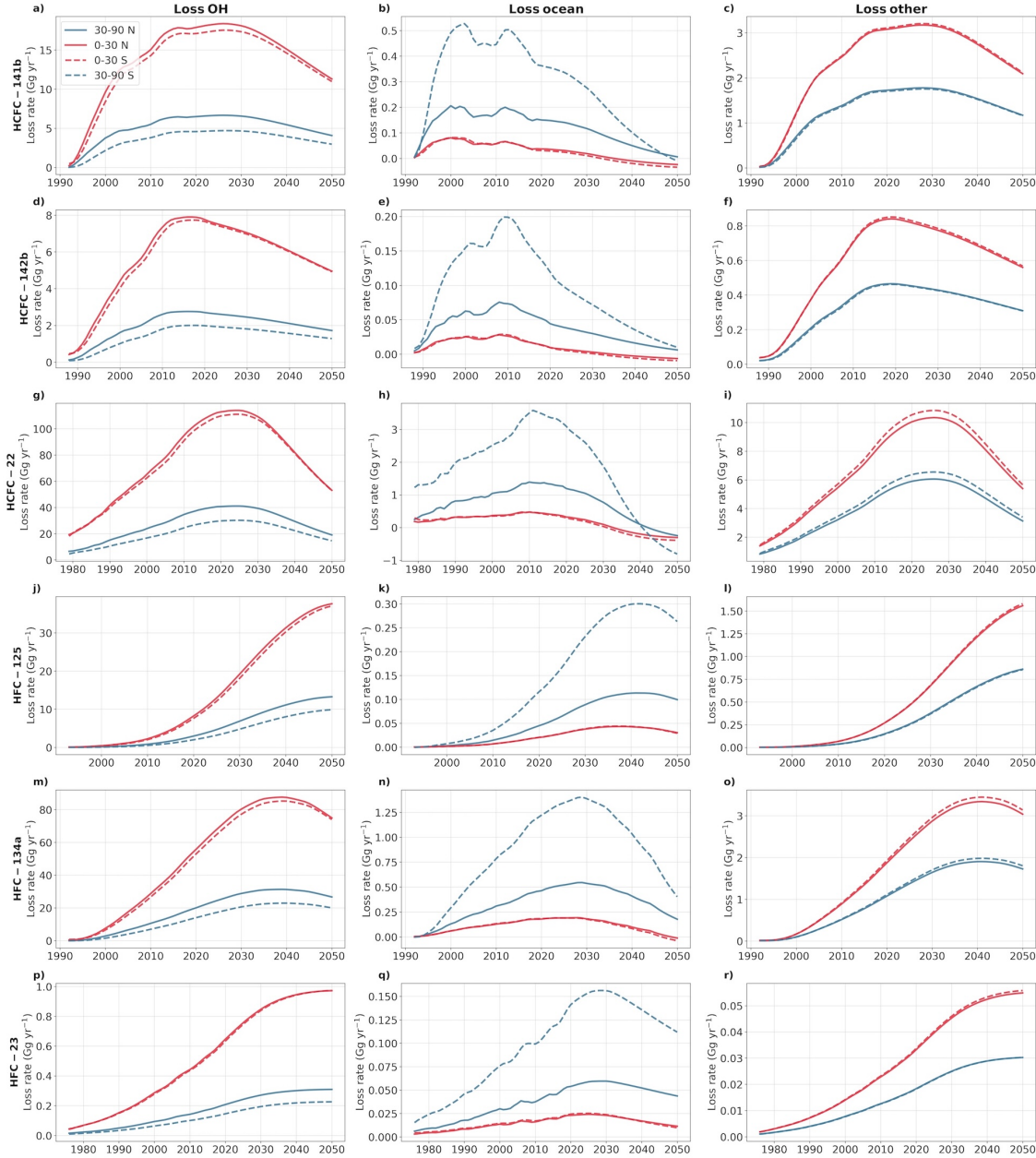
Appendix Figure 3.5: Panel a shows the Schmidt number as a function of temperature for all the molecules considered in this study. Panel b compares the Schmidt calculated in Text S1 compared to values reported by Wanninkhof, 1992 for CFC-11 and CFC-12. Overall our calculation shows good agreement with Wanninkhof, 1992.



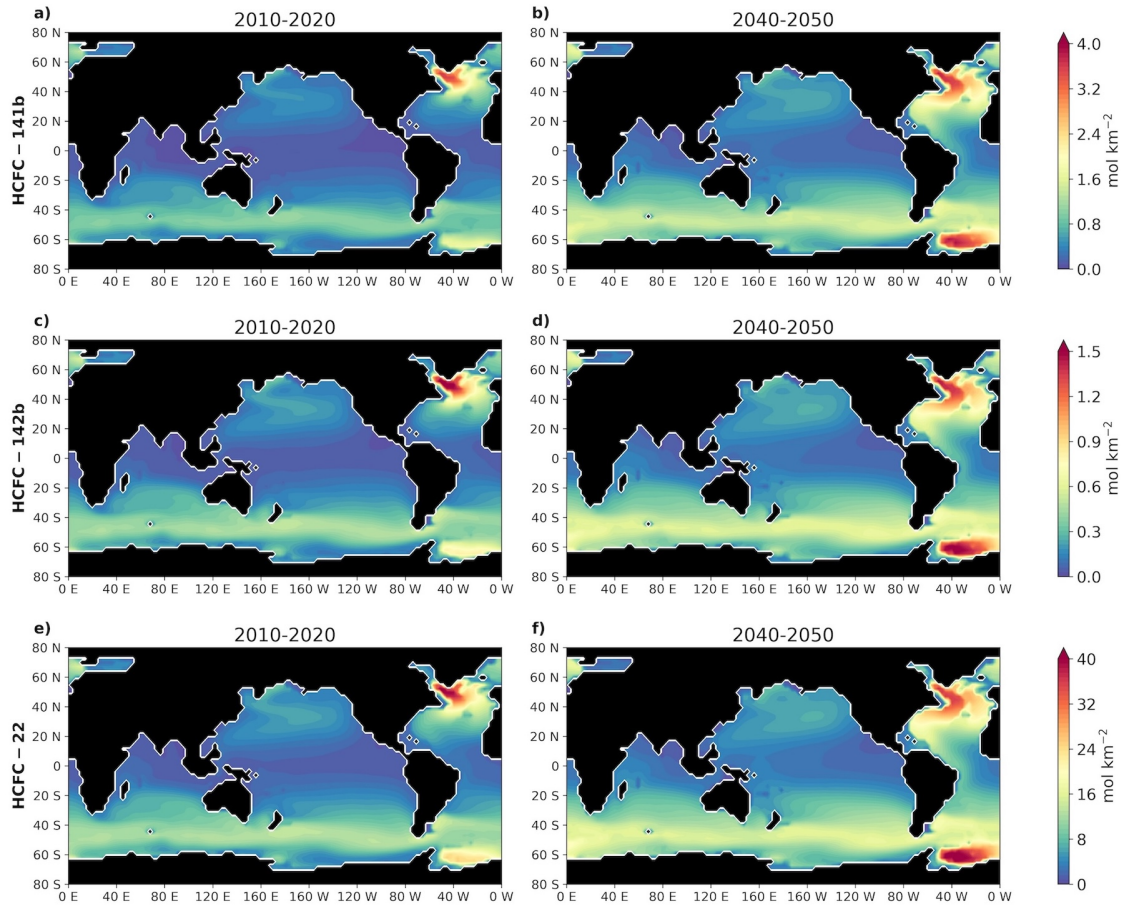
Appendix Figure 3.6: The model (without ocean uptake) simulated atmospheric mole fractions (colored lines) in the Northern Hemisphere ($30\text{--}90^\circ\text{N}$) and Southern Hemisphere ($30\text{--}90^\circ\text{S}$) compared to the observations from AGAGE measurements (black markers).



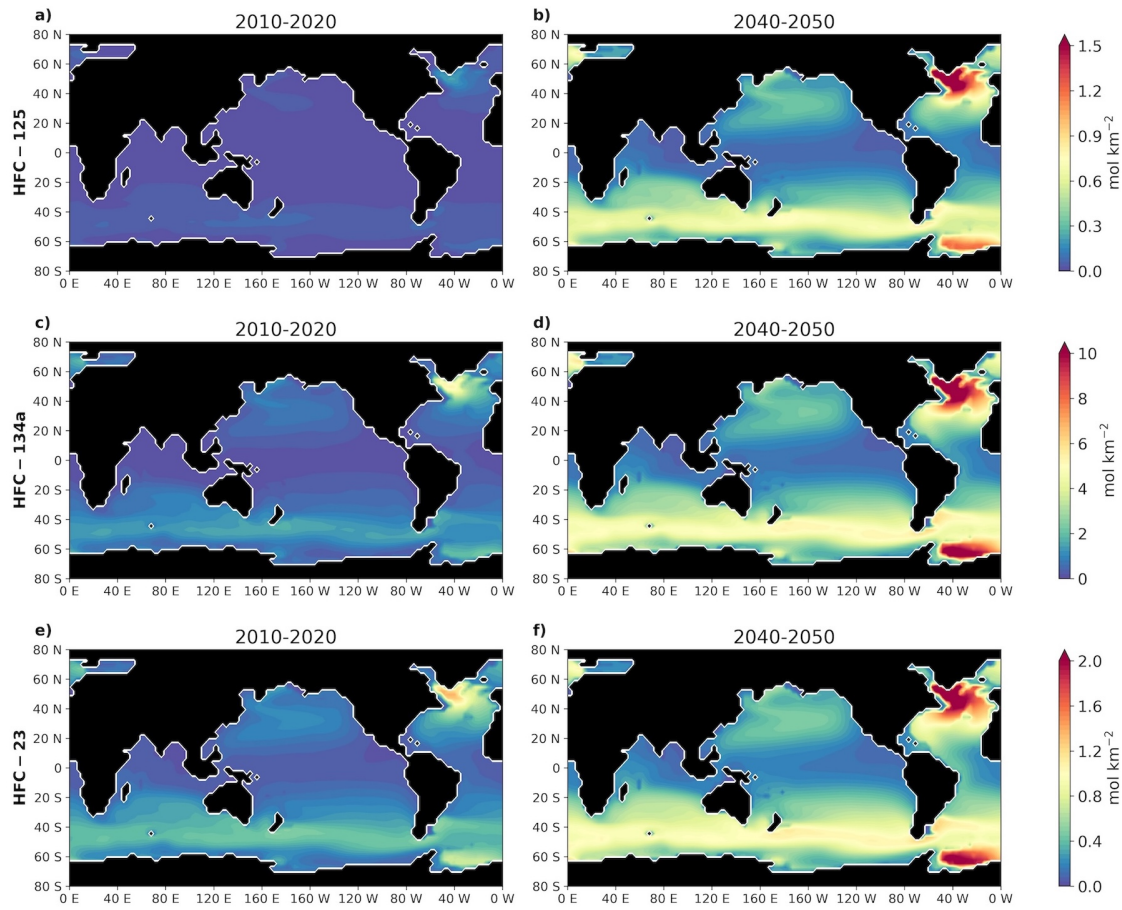
Appendix Figure 3.7: Different OH scenarios used in this study. The y-axis shows the prescribed percent change in OH from each year compared to the pre-1980 value. Fix OH scenario has no OH trend over time. Variable OH scenarios all have a consistent 10 % increase from 1980 to 2005, but then either keep OH constant or impose a $\pm 15\%$ trend from 2005 to 2050. The range of OH change after 2005 is represented as red shading in Figures 3.1–3.3, and Appendix Figures 3.11–3.13.



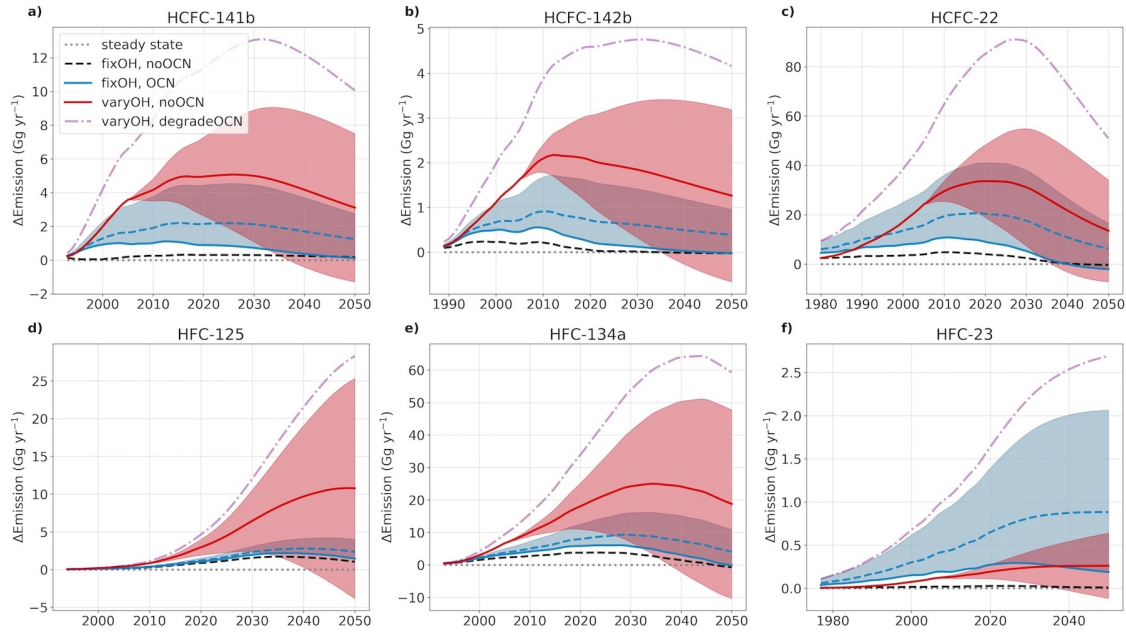
Appendix Figure 3.8: Loss rates for different species (each row) due to reaction with OH (left panels), ocean sink (without degradation; middle panels), and other factors (mainly stratospheric photochemistry; right panels). Different latitude bands are marked with different colors indicated in the legend in panel a).



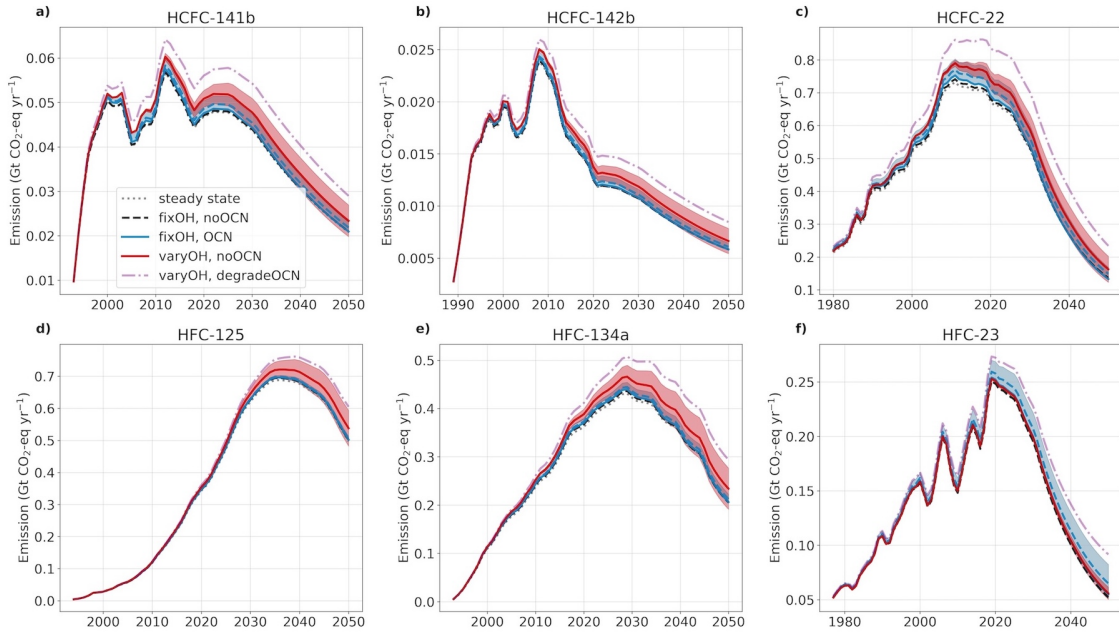
Appendix Figure 3.9: Ocean (without degradation) column integrated amounts of the three HCFCs used in this study. Panels a, c, e show the decadal average from 2010 to 2020, and panels b, d, f show the decadal average from 2040 to 2050. Note that the color bar limits are different for different species.



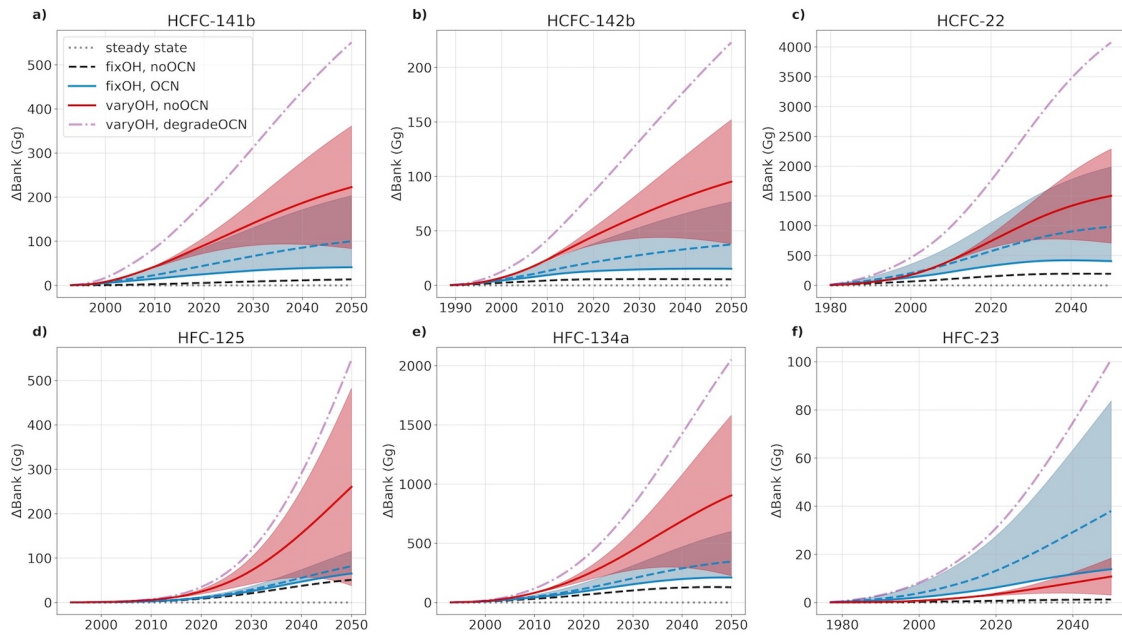
Appendix Figure 3.10: Similar to Appendix Figure 3.9, but for the three HFCs.



Appendix Figure 3.11: Similar to Figure 3.2, but shows the differences in the inferred emissions using different transient residence times to the inferred emissions using steady state lifetimes (assuming no ocean and fixed OH).



Appendix Figure 3.12: Similar to Figure 3.2, but with emissions weighted by the global warming potential (for a 100-year time horizon) for each species.



Appendix Figure 3.13: Differences in the bank estimation calculated from emissions based on transient residence times and steady state lifetimes.

Appendix Table 3.1: Henry's law solubility for HCFCs and HFCs used in MITgcm. T is the ocean temperature in degrees Kelvin, and S is the ocean salinity in the units of per mille. $A1$ to $A4$ and $B1$ to $B3$ are coefficients fitted from the Ostwald solubility from P. Li et al., 2019

	Henry's law solubility ($\text{mol L}^{-1} \text{ atm}^{-1}$)						
	$A1$	$A2$	$A3$	$A4$	$B1$	$B2$	$B3$
HCFC-141b	-8.77×10^1	1.38×10^2	3.47×10^1	-10×10^{-12}	-8.04×10^{-3}	-6×10^{-14}	3×10^{-15}
HCFC-142b	-7.55×10^1	1.18×10^2	2.89×10^1	-4×10^{-13}	-7.80×10^{-3}	-4×10^{-14}	1×10^{-14}
HCFC-22	-6.90×10^1	1.10×10^2	2.64×10^1	-7×10^{-13}	-6.66×10^{-3}	-3×10^{-14}	-3×10^{-15}
HFC-125	-5.40×10^1	8.45×10^1	1.83×10^1	-3×10^{-13}	-8.83×10^{-3}	-3×10^{-14}	2×10^{-14}
HFC-134a	-6.93×10^1	1.09×10^2	2.61×10^1	-5×10^{-13}	-7.60×10^{-3}	-3×10^{-14}	3×10^{-14}
HFC-23	2.79×10^1	-3.17×10^1	-1.98×10^1	3×10^{-13}	-6.62×10^{-3}	4×10^{-15}	-6×10^{-16}

Appendix Table 3.2: Schmidt number for HCFCs and HFCs used in the MITgcm. t is ocean temperature in degrees Celsius. A detailed description of the calculation of coefficients $Sca1$ to $Sca3$ is presented in the Appendix Text: Schmidt number estimation.

	Schmidt number (unitless)			
	$Sca1$	$Sca2$	$Sca3$	$Sca4$
HCFC-141b	3.941×10^3	-2.387×10^2	6.918	-8.3×10^{-2}
HCFC-142b	3.580×10^3	-2.168×10^2	6.284	-7.5×10^{-2}
HCFC-22	2.986×10^3	-1.809×10^2	5.241	-6.3×10^{-2}
HFC-125	3.389×10^3	-2.053×10^2	5.950	-7.1×10^{-2}
HFC-134a	3.292×10^3	-1.994×10^2	5.778	-6.9×10^{-2}
HFC-23	2.542×10^3	-1.540×10^2	4.462	-5.3×10^{-2}

Chapter 4

Stratospheric Chlorine Processing after the 2020 Australian Wildfires Derived from Satellite Data

Abstract

The 2019–2020 Australian summer wildfires injected an amount of organic gases and particles into the stratosphere unprecedented in the satellite record since 2002, causing large unexpected changes in HCl and ClONO₂. These fires provided a novel opportunity to evaluate heterogeneous reactions on organic aerosols in the context of stratospheric chlorine and ozone depletion chemistry. It has long been known that heterogeneous chlorine (Cl) activation occurs on the polar stratospheric clouds (PSCs; liquid and solid particles containing water, sulfuric acid, and in some cases nitric acid) that are found in the stratosphere, but these are only effective for ozone depletion chemistry at temperatures below about 195 K (i.e., largely

This chapter is adapted from Wang, P., Solomon, S., & Stone, K. (2023). Stratospheric chlorine processing after the 2020 Australian wildfires derived from satellite data. *Proceedings of the National Academy of Sciences*, 120(11), e2213910120. <https://doi.org/10.1073/pnas.2213910120>

in the polar regions during winter). Here, we develop a new approach to quantitatively assess atmospheric evidence for these reactions using satellite data for both the polar (65–90 °S) and the mid-latitude (40–55 °S) regions. We show that heterogeneous reactions apparently even happened at temperatures at 220 K during austral autumn on the organic aerosols present in 2020 in both regions, in contrast to earlier years. Further, increased variability in HCl was also found after the wildfires, suggesting diverse chemical properties among the 2020 aerosols. We also confirm the expectation based upon laboratory studies that heterogeneous Cl activation has a strong dependence upon water vapor partial pressure and hence atmospheric altitude, becoming much faster close to the tropopause. Our analysis improves the understanding of heterogeneous reactions that are important for stratospheric ozone chemistry under both background and wildfire conditions.

4.1 Introduction

The Australian wildfire black summer was the largest such event in the satellite era. It produced on the order of 1 Tg of aerosols in the stratosphere from about Dec 31, 2019 to Jan 5, 2020 (Peterson et al., 2021), equivalent to a small volcanic eruption. These aerosols and their precursors are brought into the lower stratosphere by pyrocumulonimbus convection, where they can be expected to decay over time. Volcanic aerosols typically display an e-folding time of about 18 months (D’Angelo, Guimond, Reisner, Peterson, & Dubey, 2022; Deshler et al., 2006). Model simulations (which assumed wildfire-released aerosols behave like sulfuric acid and water particles; Yu et al., 2021), satellite observations (Bernath et al., 2022; Rieger, Randel, Bourassa, & Solomon, 2021; Santee et al., 2022), and *in-situ* measurements (Klekociuk et al., 2022) all found significant ozone decreases in the lower stratosphere at southern hemisphere mid-latitudes in 2020 after the wildfire. Unusually low ozone abundances even continued into 2021 (Ansmann et al., 2022; Santee et al., 2022). While there is evidence for some dynamical contributions to the ozone variations

observed in that year (Santee et al., 2022; Strahan et al., 2022), averaged mid-latitude values presented in Santee et al., 2022 indicate record low local abundances near 20 km, suggesting additional chemistry is likely. In addition, unprecedented and completely unexpected changes in mid-latitude chlorine (Cl) reservoir species (HCl and ClONO₂) were also found in satellite and *in-situ* observations (Bernath et al., 2022; Klekociuk et al., 2022; Santee et al., 2022), suggestive of Cl surface chemistry. In the polar region, the following heterogeneous reaction HCl + ClONO₂ → HNO₃ + Cl₂ (S. Solomon et al., 1986) occurs at cold temperatures. The Cl₂ subsequently photolyzes rapidly in sunlit air, and can form Cl and ClO which deplete ozone. Other reactions are possible, such as HOCl + HCl → H₂O + Cl₂ but our observational analysis does not allow us to determine what reactions are occurring. It is plausible that organic aerosols may drive similar reactions at warmer temperatures (discussed in detail below). The fingerprint of N₂O₅ hydrolysis, another key heterogeneous reaction that contributes to depletion in the ozone layer, was also found in the satellite data (S. Solomon et al., 2022) but cannot explain the unusual changes in HCl and ClONO₂. Here we provide a fresh approach to the analysis of the Cl chemistry inspired by the unexpected HCl and ClONO₂ data that sheds light on its temperature-dependent chemistry not only for wildfires but also for background conditions. However, this work will not quantify the ozone loss and will be exclusively focused on the Cl chemistry.

Laboratory measurements (Hanson & Ravishankara, 1993; Q. Shi et al., 2001), *in-situ* observations (Kawa et al., 1997), and model simulation (S. Solomon, Kinnison, Bandoro, & Garcia, 2015) all suggest that the heterogeneous Cl reaction between HCl and ClONO₂ is only effective on the surfaces of typical stratospheric aerosols at temperatures below 195 K. In contrast to stratospheric background sulfuric acid and water aerosols, wildfire-released particles contain a wide variety of organic compounds (Boone et al., 2020; Murphy et al., 2021), which could have different chemical properties. Limited laboratory studies suggest that organic aerosols can enhance HCl uptake (J. R. Lawrence, Glass, Park, & Nathanson, 2005) and at warmer temperatures (Y. Q. Li et al., 2002).

The new approach presented here quantifies the temperature for Cl activation using satellite data from ACE-FTS (Atmospheric Chemistry Experiment-Fourier Transform Spectrometer; ACE for short; Bernath et al., 2005) combined with temperatures from a back trajectory model named Lagranto (Lagrangian Analysis Tool; Sprenger and Wernli, 2015), driven by meteorological conditions from ERA5 (European Centre for Medium-Range Weather Forecasts) reanalysis data (Hersbach et al., 2020). We focus on the southern hemisphere mid-latitudes defined as 40–55 °S and the polar vortex region defined as 65–90 °S. The most significant changes in HCl and ClONO₂ in 2020 are observed at altitudes ranging between 15–22 km in 40–60 °S (Appendix Figure 4.7). Unless otherwise specified, we mainly focus on 18.5 km in our analysis to maximize the effects.

4.2 Data and methods

4.2.1 Satellite datasets

Level 2 satellite data from ACE-FTS (Atmospheric Chemistry Experiment-Fourier Transform Spectrometer) version 4.1 for molecules (Boone et al., 2005) is used in this study. Data range from 2004 to 2021. ACE provides measurements at twilight; both the sunrise and sunset data are used. We remove outliers defined as 3 standard deviations apart from the mean for each month (following the ACE data usage guide).

Daily level 3 satellite data from MLS (Microwave Limb Sounder) version 5.0 (Waters et al., 2006) for N₂O, HCl and temperature are used in this study. Data range from 2005 to 2021. Both the ascending and descending modes are used, which provide measurements for daytime and nighttime.

4.2.2 Back trajectory calculation

Lagranto (Lagrangian Analysis Tool) version 2.0 (Sprenger & Wernli, 2015) is used in this study to calculate the kinematic back trajectories for each data point in 2020, 2021, and 2012. It iterates three times in each time interval to calculate the average velocity between the starting and ending locations (from every iteration). Lagranto is driven by the ERA5 (European Centre for Medium-Range Weather Forecasts) reanalysis data (Hersbach et al., 2020) for pressure, temperature, and 3D wind fields. We used an ERA5 configuration that has 137 vertical model levels, a 1-degree horizontal resolution, and a 3-hour temporal resolution. Subgrid scale gravity waves can introduce temperature variability. ERA5 has been shown to resolve a large portion of that variability (Dörnbrack, 2021; Dörnbrack et al., 2020; Dörnbrack, Eckermann, Williams, & Haggerty, 2022) and will be sampled irrespective of the time interval chosen for transport in the trajectory model. However, short horizontal wavelength disturbances could lead to effective chlorine activation at somewhat colder temperatures than those shown here, which should be considered an upper limit to the activation temperature.

4.2.3 HCl+ClONO₂ reaction efficiency

The HCl+ClONO₂ reactive uptake probabilities (in Appendix Figure 4.15B) are calculated using the parameterization described in Q. Shi et al., 2001, which is used in the WACCM model. This calculation uses model values of temperature and pressure over an altitude range of 14.5–19.5 km during July at ~63 °S. HCl and ClONO₂ volume mixing ratios are held constant at 0.3 and 0.05 ppb respectively. Water vapor volume mixing ratio is held constant at 3.5, 4, and 4.5 ppm. This allows for the effect of water vapor partial pressure over the above altitude to range to be investigated.

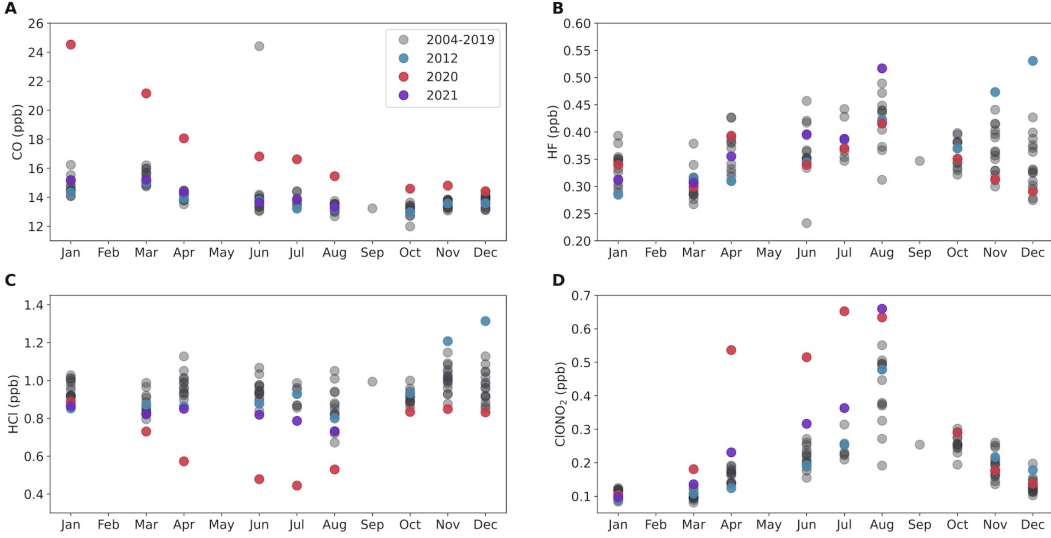


Figure 4.1: The monthly mean ACE data for (A) CO, (B) HF, (C) HCl, and (D) ClONO₂ at 18.5 km averaged over 40–55 °S. Red dots are from 2020, purple dots are from 2021, blue dots are from 2012 (used as a reference year in this study), and gray dots are from 2004–2019 (excluding 2012). 40–55 °S is split into 3 equally spaced latitude bins and months with at least 5 samples (at least 1 sample per latitude bin) are considered in the averaging processes.

4.3 Results

4.3.1 Separating dynamical and chemical processes

Figure 4.1A shows the monthly mean ACE data for CO (an indicator of biomass burning) at the lower stratosphere mid-latitudes. Record high CO in 2020 (Bernath et al., 2022; Santee et al., 2022) was observed immediately after the pyrocumulonimbus events in January and decayed with time, suggesting a significant amount of biomass burning and its long-lasting effect continuing throughout the entire year. CO in 2021 is within the range of climatology, indicating no significant wildfire or new particles injected into the lower stratosphere in that year. 2012 is also highlighted in Figure 4.1 since we use it here as a typical reference year in later analysis, given no known large volcanic eruptions nor big biomass burning events in that year.

While HCl displayed remarkable anomalies in 2020, HF was within the range of past years, confirming the role of chemistry (Figure 4.1). Once anthropogenically produced CFCs

(chlorofluorocarbons) reach the stratosphere, they decompose into the fluorine (Fy) and chlorine (Cly) families of compounds. Nearly all of the Fy is in the form of HF because there are no known chemical loss pathways of HF in the stratosphere; hence it has long been used as an inactive tracer (Chipperfield, Burton, et al., 1997; Tilmes et al., 2004). Insofar as the breakdown of CFCs is the dominant source of both stratospheric chlorine and fluorine, Cly and Fy should be proportional to one another. Viewed in this context, HCl and HF behavior also suggests unusual chemistry lasting into 2021, but with much smaller magnitude than 2020.

Correlation between chemical species or “tracer-tracer” analysis is a powerful tool to analyze dynamical and chemical interactions (Griffin et al., 2019; Proffitt et al., 1990; Proffitt, Solomon, & Loewenstein, 1992). The basis of the analysis is that dynamical transport should affect inactive and active species similarly, so departures from correlation in the active species are indicative of chemical processes. The availability of simultaneous ACE observations of HF, HCl, and ClONO₂ along a common line of sight ensures consistency and is key to such an analysis. To separate dynamical from chemical effects on specific Cly species, we perform the tracer-tracer analysis between HF and HCl, ClONO₂, and their sum (Figure 4.2 for mid-latitude and Appendix Figure 4.8 for the polar region).

Figure 4.2 and Appendix Figure 4.8 show tracer-tracer scatter plots of ACE HF and HCl, ClONO₂, and HCl+ClONO₂ in each month from March to July at the mid-latitudes (40–55 °S) and polar vortex region (65–90 °S), respectively. We focus on months between March to July because in the polar vortex region, this spans months when no or little heterogeneous chemistry normally occurs (~March–April) to months with rapid chemistry on PSCs (June–July) and in between (May). All the data align on a nearly straight line in March, suggesting little or no chemistry in this month. We therefore construct a baseline relationship between HF and the Cly species from March 2004–2019 data using linear regression (indicated by the dark solid lines in Figure 4.2 and Appendix Figure 4.8).

The shaded regions in Figure 4.2 and Appendix Figure 4.8 quantify the baseline uncertainty.

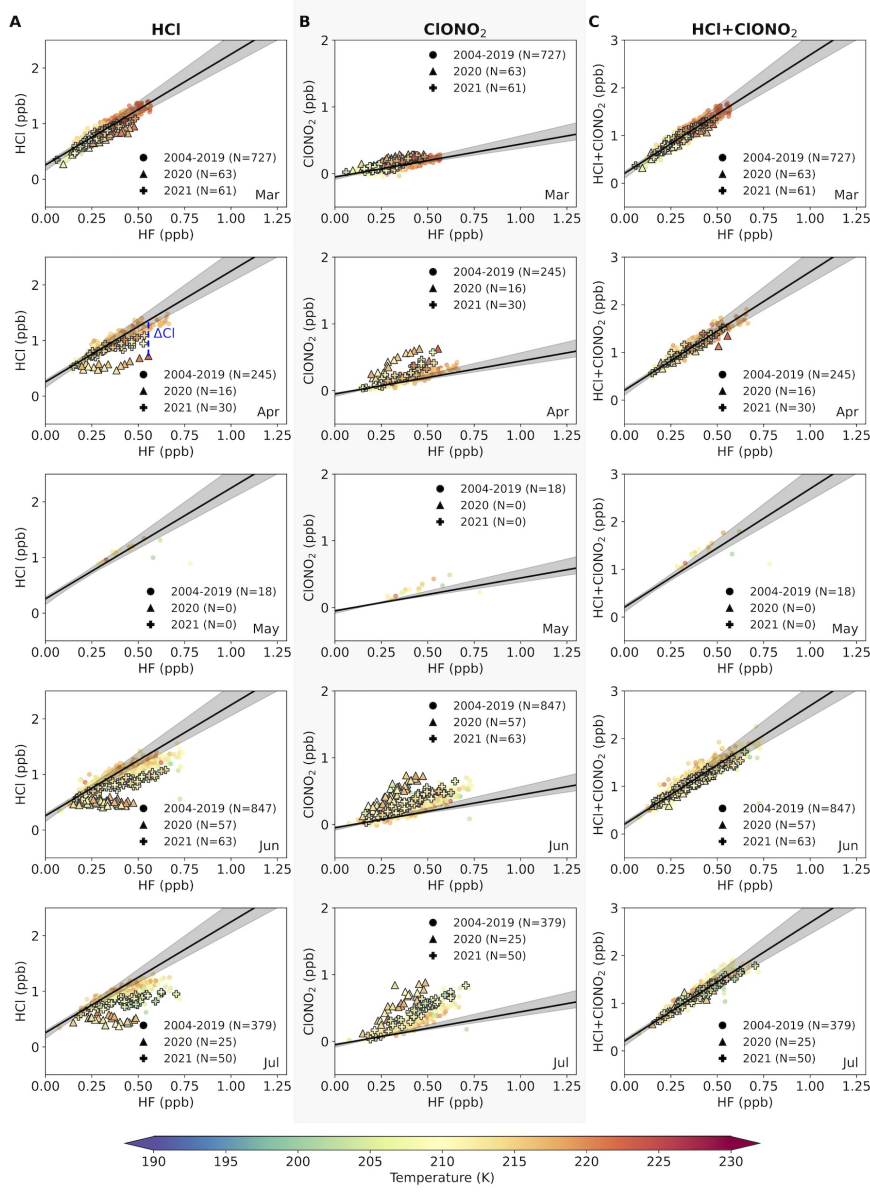


Figure 4.2: Tracer-tracer correlation between ACE-measured HF (x-axis) and (A) HCl, (B) ClONO_2 , and (C) $\text{HCl} + \text{ClONO}_2$ (y-axes), color-coded by temperature. Each dot represents a single measurement at 18.5 km over 40–55 °S. Dots in 2020 and 2021 are highlighted with triangles and crosses, respectively (with gray edges). Each subplot shows a different month from March to July, labeled at the bottom right corner. The number of data plotted in each month is shown in the legend. The thick black lines represent the “no-chemistry” baseline, from the linear fit over March 2004–2019 data points. The shaded regions indicate a conservative full range of baseline variability bounded by the maximum and minimum baselines constructed by data in individual years from 2004 to 2019. A demonstration of how ΔCl (e.g. in Figure 4.4) is calculated is shown here as the vertical blue dashed line in the April panel for HCl, representing the change in Cl due to chemical processes.

There are mainly two types of uncertainties in such analysis, one is the instrumental bias, and the other is the interannual variability. As the tracer-tracer correlation mainly focuses on the relative difference of Cly to HF, which are measured by ACE at the same occultation, instrumental bias on both molecules will largely cancel. To quantify the uncertainty of interannual variability and noise, we construct a baseline for each year in 2004–2019 to represent the range of variability in baselines. The shading areas indicate a conservative full range of variability bounded by the maximum and minimum baselines using data in individual years.

ACE has limited data coverage. To validate whether the results are robust, we compare ACE (at 18.5 km) with the MLS (Microwave Limb Sounder at 68.2 hPa) in Appendix Figures 4.9 and 4.10 (mid-latitude and polar vortex region, respectively) for tracer-tracer analysis between N₂O and HCl (since MLS does not have measurements for HF and ClONO₂). MLS has much more spatial coverage, but with a lower signal-to-noise ratio on individual points (as shown in Appendix Figures 4.9C and 4.10C). The zonally averaged MLS data (Appendix Figures 4.9B and 4.10B) agree well with ACE (Appendix Figures 4.9A and 4.10A), suggesting that even though ACE coverage is limited, it is consistent with MLS regarding the changes in HCl from tracer-tracer analysis. Note that the zonal averaging process in MLS reduces the noise but it also clusters measurements towards the mean values. Therefore, the baseline slope becomes more sensitive to small changes in N₂O and HCl in the clustered region, and the uncertainty range expands at those values where no or few data are fed into the linear regression. MLS N₂O also has experienced a ∼3 % instrumental drift in the past decade, which could also broaden the spread of the baseline uncertainty range (Livesey et al., 2021). We therefore focus on the results from ACE measurements.

In the polar vortex region, Appendix Figure 4.8 shows that substantial deviations in HCl and ClONO₂ from their respective “no-chemistry” baseline occur in July for every year, indicating the known Cl activation mechanism on PSCs (S. Solomon et al., 1986). Over the mid-latitudes (Figure 4.2), some data points in June and July from 2004–2019 fall off the

“no-chemistry” baseline. However, 2020 data points in the mid-latitude region in these two months are completely outside the range of climatology. More important, in 2020, HCl and ClONO₂ start to deviate from the “no-chemistry” baseline even in April in both mid-latitude and polar regions, when the temperature is far too warm for heterogeneous Cl reactions to happen. HCl and ClONO₂ in 2021 also display some deviations from the “no-chemistry” baseline, but the magnitudes are considerably smaller than in 2020.

Interestingly, the decrease in HCl is roughly compensated by increases in ClONO₂ in both 2020 and 2021 (e.g. April and May in Figure 4.2 and Appendix Figure 4.8, respectively) and in other years. The decrease in HCl suggests that anomalous heterogeneous Cl reactions occurred in these two years. However, at these latitudes outside the polar vortex, ample solar radiation is available to drive HNO₃ photolysis (and reaction with OH also occurs), making NO₂ available to deactivate the activated Cl, forming ClONO₂. With a rich supply of NO₂, the net reaction thus largely transfers HCl into ClONO₂. Similar Cl deactivation forms the ClONO₂ “collar” (Chipperfield, Lutman, et al., 1997), a slice of enhanced ClONO₂ surrounding the polar vortex in late spring as noted in past literature. Figure 4.3 shows May HCl and ClONO₂ anomalies in 2020 compared to the May climatology from 2004–2019. The figure makes clear that the ClONO₂ “collar” mechanism is significantly enhanced in 2020 as early as May, as more Cl has been converted from HCl into ClONO₂ apparently on wildfire-released particles. Similar processes continued to occur in 2021, but with a smaller magnitude (Appendix Figure 4.11). HCl and ClONO₂ are both considered to be reservoirs for active chlorine species that deplete ozone (mainly Cl and ClO). It may be useful to consider such a process to represent Cl processing instead of Cl activation, since the sum of HCl+ClONO₂ is nearly conserved. Nonetheless, a small amount of enhanced ClO will be present as well, since ClONO₂ and ClO are essentially in photochemical balance in the sunlit atmosphere, and enhanced ClONO₂ therefore implies enhanced ClO and associated ozone loss. Indeed, evidence of enhanced ClO has been shown in both ACE and MLS measurements (Bernath et al., 2022; Santee et al., 2022).

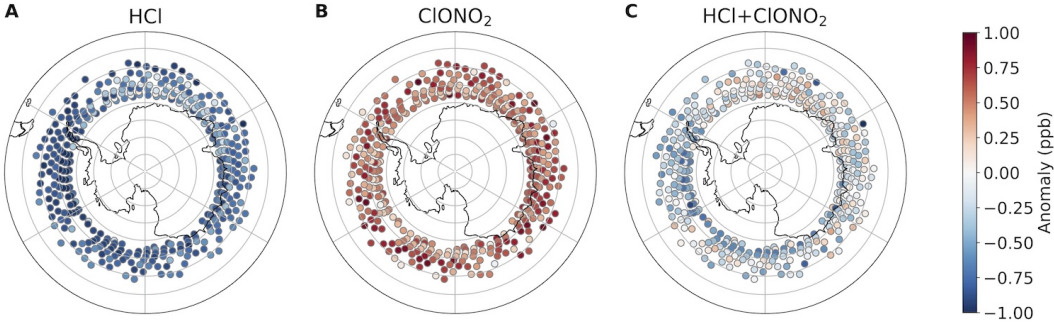


Figure 4.3: Monthly anomalies for (A) HCl, (B) ClONO₂, and (C) HCl+ClONO₂ in May 2020 compared to the May climatology in 2004–2019. The maps show a latitudinal range between 50 °S and 90 °S since ACE measurements in May are mainly between 58–68 °S. To prevent from biasing the anomalies by latitudinal variations, the climatological mean is constructed at every 5-degree latitude bin. Therefore, the May anomalies presented here are calculated from four latitude bins from the climatology (50–55, 55–60, 60–65 and 65–70 °S).

4.3.2 Cl processing in the mid-latitudes

To estimate the temperatures that are likely to drive the heterogeneous chemistry, we first calculate the deviation of each data point in Figure 4.2 from the “no-chemistry” baseline as a function of ACE-measured temperature (Figure 4.4A–C). Thick lines show the averages of data points in 2 K temperature bins from the baseline that is constructed by all available data from 2004–2019. The shaded regions represent the full range of Cl deviation from individual “no-chemistry” baselines that are constructed from data in individual years, representing the uncertainty due to variability. Negative values in ClONO₂ at warmer temperatures indicate that available ClO has been deactivated to form ClONO₂, and the sum of HCl and ClONO₂ in Figure 4.4C thus indicates that a large amount of the Cl activated from HCl in 2020 and 2021 has almost all formed ClONO₂ at warmer temperatures. As we focus on 40–55 °S where the temperature is well above 195 K, activation on the PSCs is not likely to take place. This is supported by the 2004–2019 climatology, in which the average Cl activation remains close to zero. However, HCl data in 2020 and 2021 suggest that significant Cl activation occurred at temperatures even well above 200 K, but not in any other years (although the magnitude of Cl activation in 2021 is smaller than in 2020).

However, one pitfall of Figures 4.2 and 4.4A–C is that the temperatures shown reflect only the state of the atmosphere at the satellite overpass, while Cl activation could have occurred at a different temperature along air parcel trajectories. We therefore use Lagranto (Sprenger & Wernli, 2015) driven by ERA5 (Hersbach et al., 2020) to evaluate 5-day kinematic back trajectories for each data point in 2020 and 2021, as well as the reference year of 2012. Like all trajectory studies, errors in wind, temperature, and parcel motion cannot be eliminated in our analysis and are a source of uncertainty in the detailed chlorine activation estimates versus temperature. Lagranto calculates the kinematic trajectories, but air parcels likely travel adiabatically or may cross isentropes due to diabatic processes (such as local heating due for example to particles absorbing more radiation). The radiative relaxation time for the lower stratosphere is on the order of 20–30 days (Hartmann, Holton, & Fu, 2001; Mlynczak, Mertens, Garcia, & Portmann, 1999); we pick a rather conservative estimate of 5 days to avoid potential effects of radiatively-driven ascent/descent of particles in the stratosphere. The ACE-measured instantaneous temperature is then replaced with the minimum temperature from the 5-day back trajectories of each data point (referred to as ERA5 T_{\min} in Figure 4.4D–F), providing an estimate of the air parcel’s recent minimum temperature exposure. ERA5 temperatures at the co-located ACE observations agree well with each other (Appendix Figure 4.12), and we find that the 5-day minimum temperature is rather insensitive to small perturbations in the starting position (Appendix Figure 4.13).

Figure 4.4D–F shows Cl activation as a function of the 5-day minimum temperature calculated from Lagranto. The 5-day minimum temperature exposure for these measurements is still mainly above 195 K. This further strengthens the idea that wildfire-released organic aerosols can allow heterogeneous reactions to happen at warmer temperatures, which differs from the PSC mechanism limited in the polar region that requires the temperature to be lower than 195 K. Further, the PDFs shown in Figure 4.4D–F for temperatures ≥ 195 K indicate that not only do 2020 and 2021 have different mean values than in 2012, but the spread after the wildfire is also much wider than that in 2012. One plausible explanation

for this behavior is variability in the composition and/or abundances of organic aerosols from the wildfire, displaying different chemical properties. Note that the PDF for the sum of HCl+ClONO₂ is centered very close to zero for 2012 (-0.01 ± 0.07 ppb; ± sign followed by 1 standard deviation) and displays a slight offset from zero in 2020 and 2021 (0.03 ± 0.08 ppb and 0.03 ± 0.07 ppb, respectively), indicating small but non-negligible enhancements in other species including e.g., HOCl (Bernath et al., 2022) and ClO in those years only (Santee et al., 2022), given the changes in the latter two species can be few orders of magnitude smaller than changes in HCl and ClONO₂.

4.3.3 Cl processing in the polar vortex region

Figure 4.5 shows Cl activation in the polar vortex region at 65–90 °S. Cl activation for the total Cl in 2012 shows a sharp transition at 195 K (Figure 4.5F), which matches remarkably well with the current understanding of Cl activation on PSCs as first observed with aircraft methods (Kawa et al., 1997). It is noteworthy that even in 2012 when the background CO and aerosol extinctions are at the lower end in the climatology, there is still some ClONO₂ being converted from HCl at temperatures between 195–200 K (Figure 4.5D–E). Observations show that organic aerosols are widespread in the lower stratosphere. Among other sources, tropical biomass burning produces organic aerosols in the upper troposphere (Schill et al., 2020) that may be transported into the stratosphere. Thus, early-season Cl processing on organic aerosols could occur to some extent every year, albeit with smaller magnitudes than in 2020.

Data in 2020 and 2021 show that a similar Cl processing mechanism also took place in the south polar vortex region at temperatures above 195 K. HCl in 2020 and 2021 continues to indicate more active Cl compared to other years at all temperatures until the temperature falls below 195 K, when the PSCs likely dominate the Cl activation, and these two years merge into the 2004–2019 climatology. While Cl activation in 2020 was lower at temperatures well below 195 K (Figure 4.5F) compared to other years, this does not necessarily mean less total

active Cl being present in that year (e.g. there could also be an interannual variability in the total Cl). In particular, the results show that a large amount of Cl has already been activated earlier in the season (at warmer temperatures) and likely stayed in the forms of e.g. HOCl, ClO, and Cl_2O_2 in the polar vortex region (Bernath et al., 2022; Santee et al., 2022). Because of less solar radiation at higher latitudes, less NO_2 is available from HNO_3 photochemistry to transfer these more reactivate forms of Cl back to ClONO_2 . This is supported by the evidence of large non-zero values of the mean of PDFs for $\Delta\text{HCl}+\text{ClONO}_2$ at temperatures above 195 K in Figure 4.5F (0.22 ± 0.12 ppb in 2020 and 0.18 ± 0.10 ppb in 2021, compared to 0.02 ± 0.10 ppb in 2012; \pm sign followed by 1 standard deviation).

Note that most of the ACE data points in the polar region are over 65–70 °S (especially in colder seasons) and may not represent the conditions in the core of the polar vortex. Appendix Figure 4.14 shows the limited data available for Cl activation between 70–90 °S (ACE observations for March and April only). The general behavior of Cl processing at warmer temperatures remains apparent in these months at high latitudes.

4.3.4 Altitude-dependent Cl activation in the polar vortex region

The reaction efficiency of $\text{HCl}+\text{ClONO}_2$ can be affected not only by different types of surfaces (e.g. organic aerosols and PSCs), but also by water vapor content and pressure, which vary with altitude (S. Solomon, 1999), which has been suggested as a potential mid-latitude ozone depletion mechanism (Anderson et al., 2017; Clapp & Anderson, 2019). We therefore expand the focus to the range of altitudes from 14.5 km to 18.5 km for 2020, 2021 and 2012 (Figure 4.6). The number of datapoints (after filtering by the data quality flag) is similar between 14.5 km and 18.5 km, but it has dropped by more than 50 % at below 13 km; thus altitudes below 14.5 km have been discarded.

It is noteworthy that in a year without the impact of organic aerosols from large wildfires (2012), a systematic gradient of the onset temperature for Cl activation is indicated, from 200 K at 14.5 km to 195 K at 18.5 km using the 5-day back trajectories (Figure 4.6A). This agrees

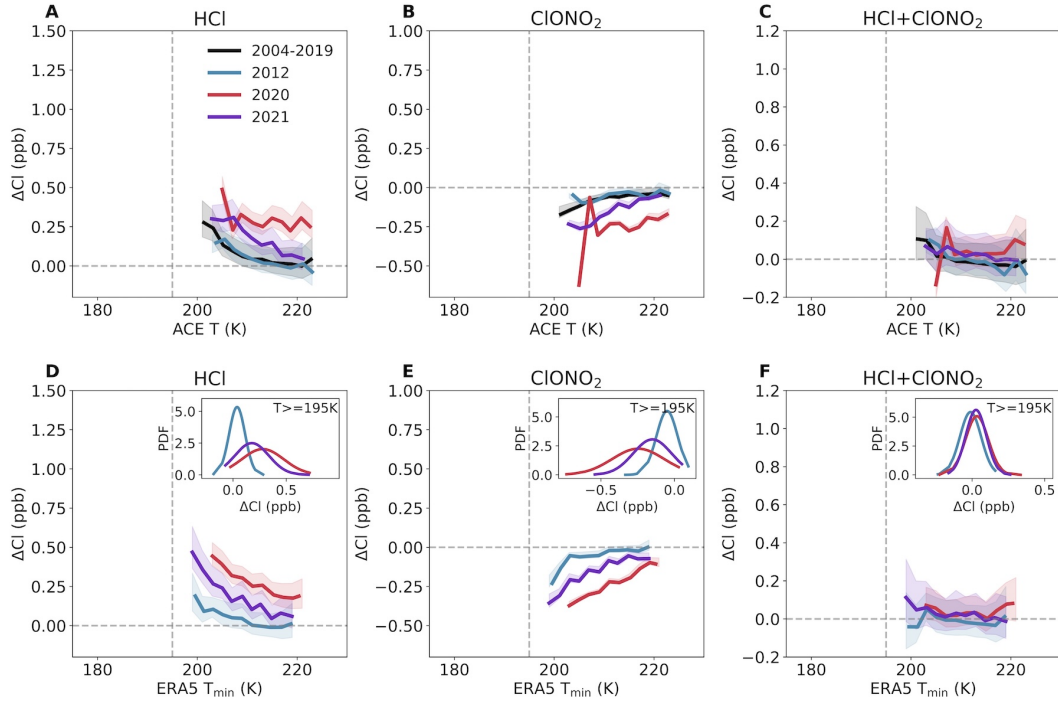


Figure 4.4: Cl activation as a function of temperature at mid-latitudes ($40\text{--}55^\circ\text{S}$) for March–July at 18.5 km. Each panel shows the amount of Cl activation on the y-axes (deviation from the “no-chemistry” baseline in Figure 4.2) as a function of temperature (x-axis) for (A, D) HCl, (B, E) ClONO_2 , and (C, F) $\text{HCl}+\text{ClONO}_2$. Panels A–C use the ACE-measured temperature at the satellite overpass, and panels D–F use the minimum temperature (T_{\min}) calculated along the 5-day back trajectories for each data point for 2020, 2021, and 2012. Thick lines are the average of Cl activation at every 2 K temperature ranges (temperature bins with less than 2 samples are not considered for the average). The shading areas indicate the full range of Cl departures from individual baselines using data from single years. Horizontal and vertical gray dashed lines indicate zero Cl activation and 195 K, respectively. The probability distribution functions (PDF) of Cl activation at $T_{\min} \geq 195\text{ K}$ are shown in panels D–F for 2020, 2021, and 2012.

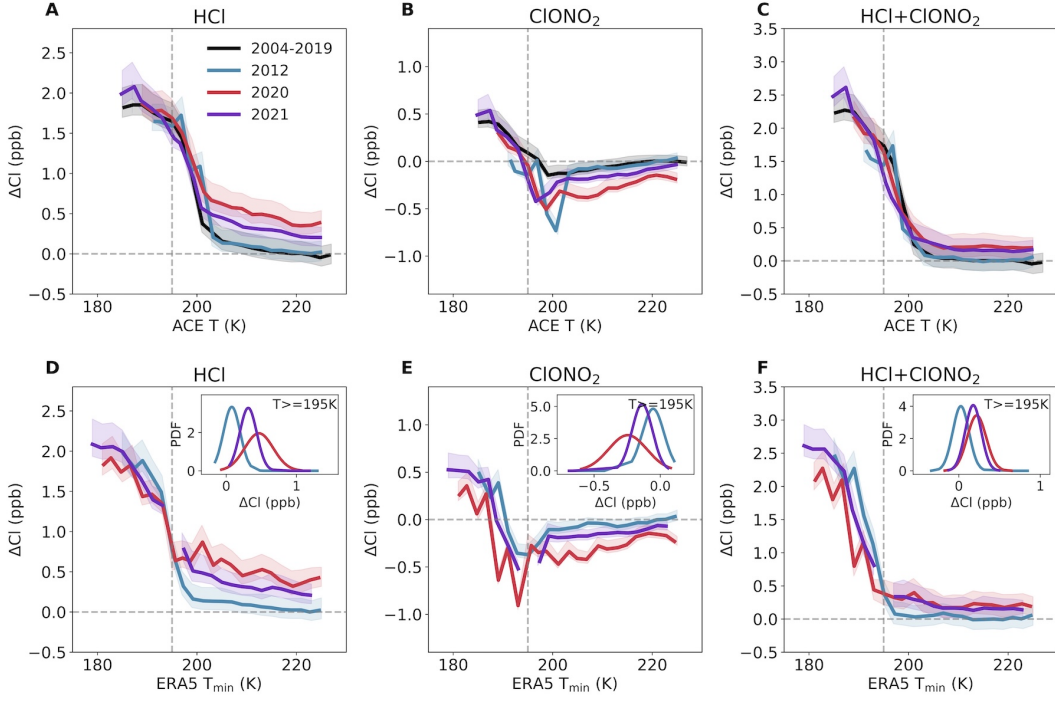


Figure 4.5: Cl activation as a function of temperature in the polar vortex region (65–90 °S), as in Figure 4.4 for mid-latitudes. Panels A–C use the ACE-measured temperature at the satellite overpass, and panels D–F use the minimum temperature (T_{\min}) calculated along the 5-day back trajectories for each data point for 2004–2019, 2012, 2020, and 2021.

surprisingly well with current understanding, as indicated by a numerical calculation using the kinetics code (Q. Shi et al., 2001) and composition data from WACCM (Whole Atmosphere Community Climate Model). For example, the reaction efficiency for $\text{HCl} + \text{ClONO}_2$ is about 80 times more efficient at 14.5 km than at 18.5 km (Appendix Figure 4.15B), suggesting Cl activation can happen at warmer temperatures much more readily at 14.5 km than at 18.5 km. But such altitude-dependency is significantly disturbed by organic aerosols after the 2020 Australian wildfire. Neither 2020 nor 2021 demonstrate a clear relationship between Cl activation and altitude. Instead, large amounts of Cl activation took place at all altitudes ranging from 14.5 km to 18.5 km in these years at temperatures warmer than 195 K.

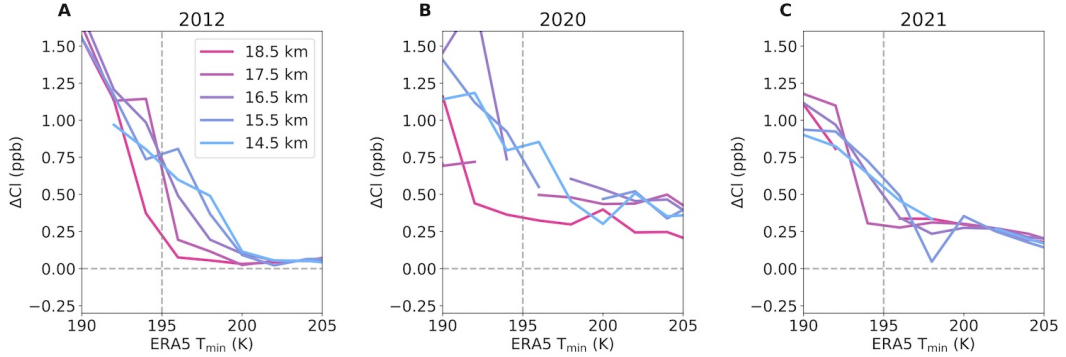


Figure 4.6: The altitude-dependent Cl activation in the polar vortex region ($65\text{--}90^\circ\text{S}$) for (A) 2012, (B) 2020, and (C) 2021. X-axis shows the minimum temperature calculated along the 5-day back trajectories, and the y-axis shows the Cl activation from the sum of HCl and ClONO₂. Only the Cl activation calculated from baselines using all available data from 2004 to 2019 is shown here. Each line represents a different altitude range from 14.5 km to 18.5 km. The panels are zoomed in for 190–205 K to focus on the onset temperature for Cl activation on PSCs.

4.4 Discussions

In conclusion, we have examined the HCl and ClONO₂ reservoir species that reflect heterogeneous reactions in the southern hemisphere fall and winter (March–July) for both the Australian wildfire-released organic aerosols and background conditions using satellite data. Our method confirms a sharp increase in Cl activation for temperatures below about 195 K along 5-day air parcel trajectories characterizing the data, consistent with current understanding for Cl activation in the polar region (S. Solomon et al., 1986; S. Solomon et al., 2015; Wilmouth et al., 2006). This finding highlights the importance of relatively small temperature perturbations (i.e., less than 1 K) on this chemistry (e.g., those due to planetary or gravity waves) for air parcels with low temperatures but not low enough to trigger heterogeneous reactions. The method also successfully demonstrates the altitude-dependency of Cl activation for a reference non-wildfire year (S. Solomon, 1999). These results illustrate the power of this method for both background conditions and wildfire perturbations in testing chemical understanding.

We find evidence for Cl processing at much warmer temperatures (at 220 K) in both

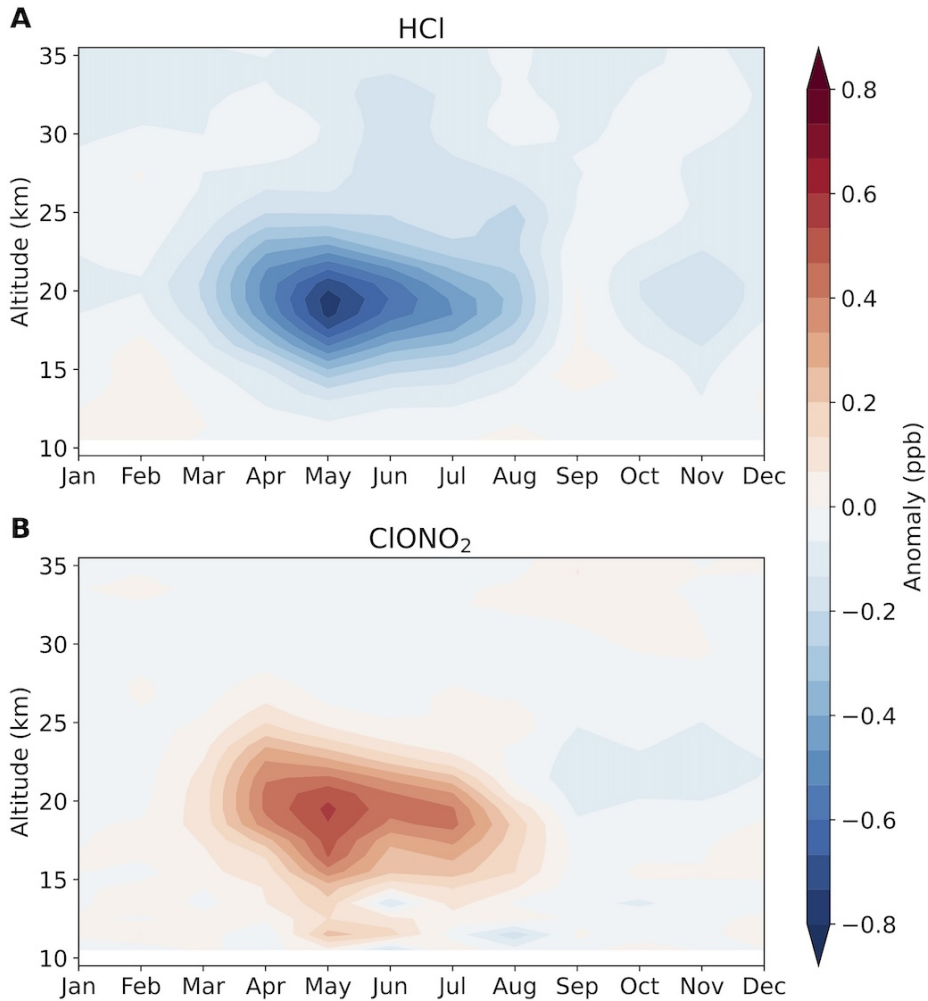
mid-latitude and polar vortex regions after the Australian fires than the current understanding for PSCs, which is essentially limited to polar region at temperatures below 195 K. When such Cl processing happens at mid-latitudes, HCl decreases but nearly all of the active Cl is turned into ClONO₂ rapidly because of ongoing supply of NO₂ from HNO₃ photolysis and reaction with OH. However, PDFs of the sum of HCl+ClONO₂ activation reveal that some enhanced Cl does remain in active forms at temperatures above 195 K in 2020, which can be expected to produce some ozone loss. Importantly, the data suggest that the remaining aerosols from the 2020 wildfire apparently even continued to affect the Cl species (albeit to a lesser extent) into 2021. Further, diversity in wildfire-released organic aerosols (Boone et al., 2020; Murphy et al., 2021) with different chemical properties is suggested by an observed increase in the width of the distribution, i.e., varying amounts of Cl activation.

The total Cl budget could be closed by including other species, particularly ClO and Cl₂O₂. However, one drawback of this tracer-tracer method is that it works well for the rather long-lived species (e.g., HCl and ClONO₂), but the large variance in more short-lived species (e.g., ClO and HOCl) can impede the calculation. Furthermore, the ACE satellite produces twilight measurements (which do not indicate daytime ClO values) and it does not have measurements for Cl₂O₂; although Santee et al., 2022 shows enhanced daytime ClO using MLS data, and twilight ClO enhancement is also found from ACE data albeit with larger noise (Bernath et al., 2022). HNO₃ is not taken up by the organic aerosols, and reported mid-latitude HNO₃ in 2020 is within the climatological variance (Santee et al., 2022). However, PSCs do take up HNO₃ in the polar region (therefore reducing NOx, impacting the Cl reservoirs). But ACE does not monitor inside the polar vortex during dark conditions. Further studies are needed to evaluate the total Cl budget and to fully quantify to what extent the ozone layer is affected by wildfire-triggered Cl processing.

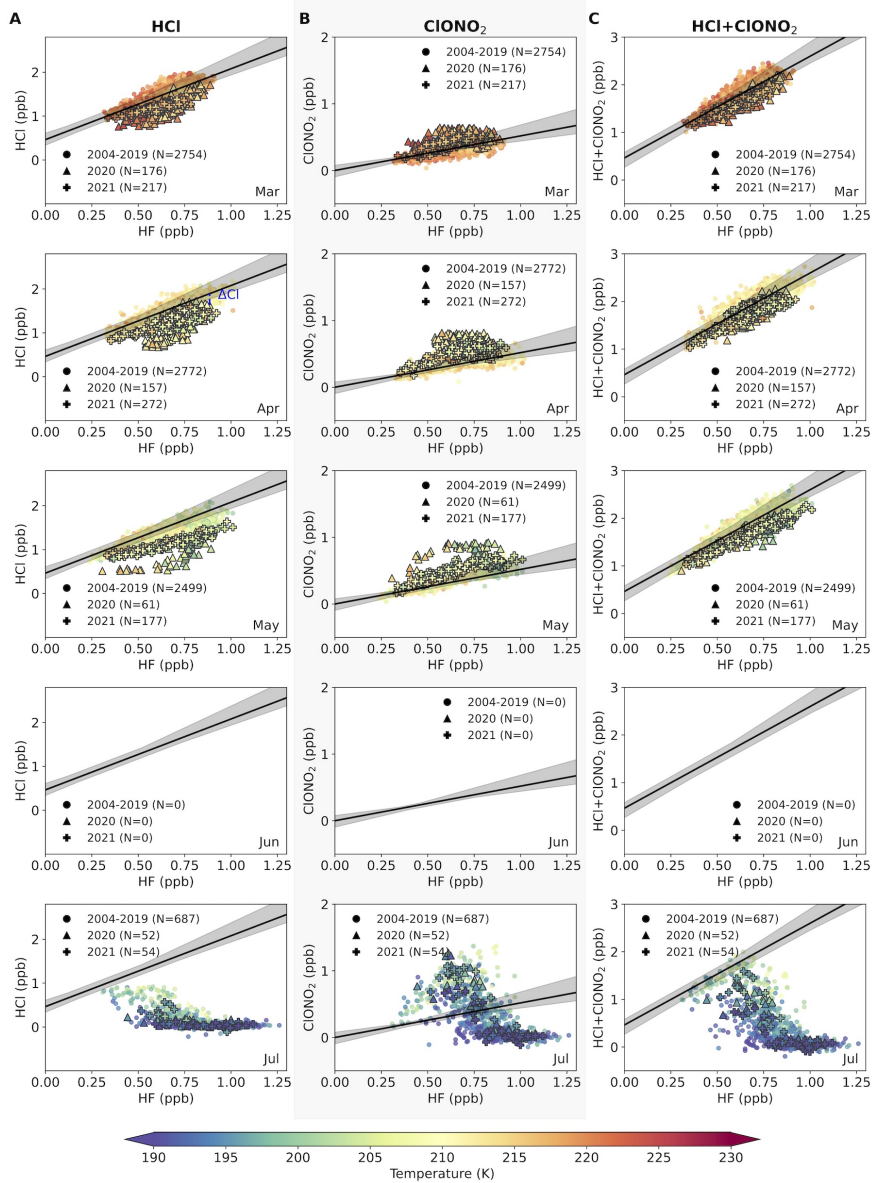
The frequency of wildfires is projected to increase in the future due to climate change (Seneviratne et al., 2021). A better understanding of the range of composition of organic aerosols, and of heterogeneous reaction rates upon them, is needed to estimate any associated

ozone impacts, including potential delay of the recovery in the stratospheric ozone layer in Antarctica, as well as potential mid-latitude ozone loss in the future.

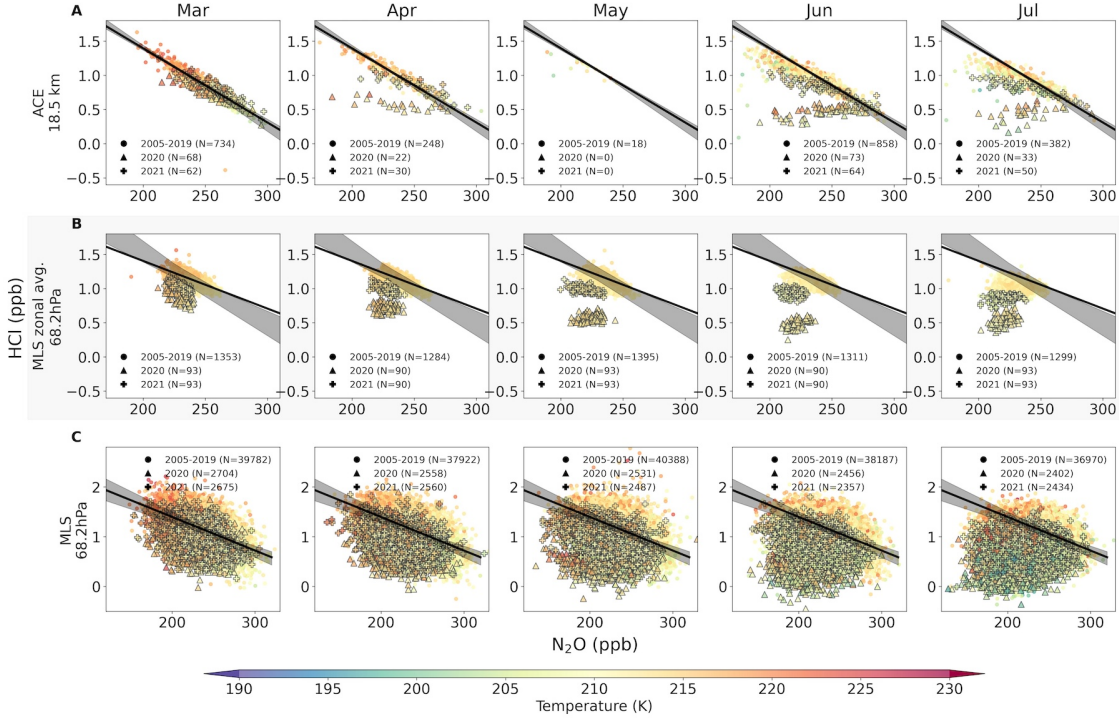
Appendix



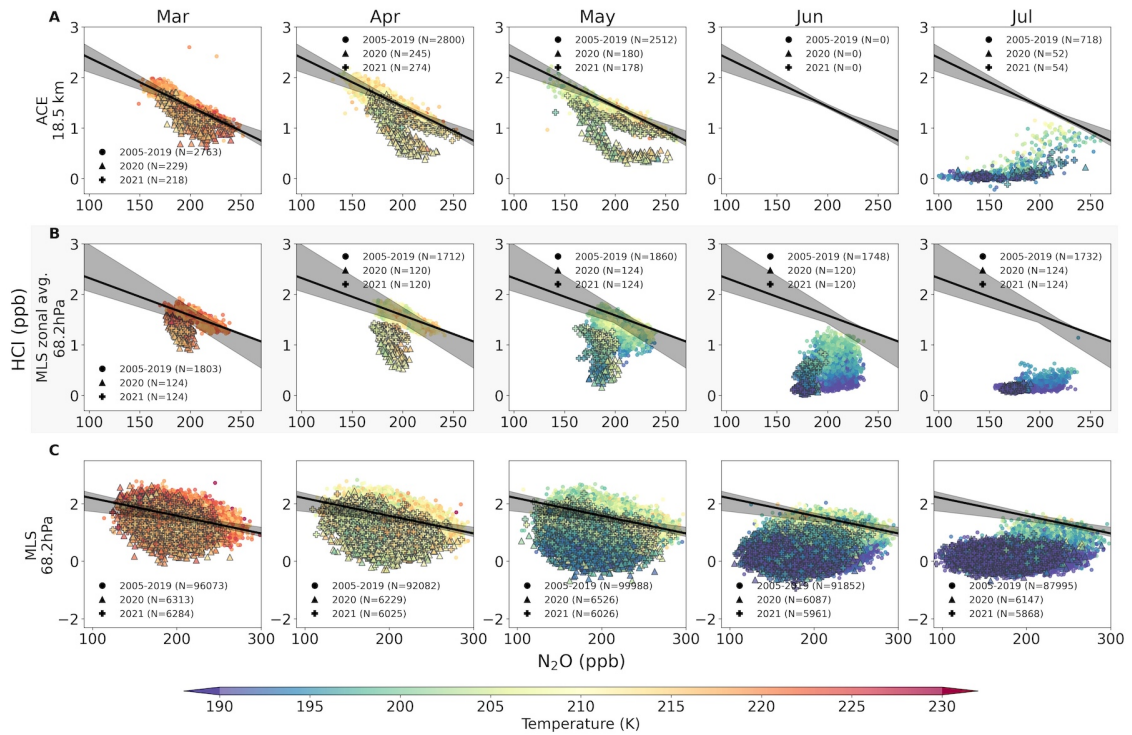
Appendix Figure 4.7: Monthly anomalies of (A) HCl and (B) ClONO₂ in 2020 compared to the 2004–2019 climatology, as a function of the month (x-axis) and altitude (y-axis) over 40–60 °S.



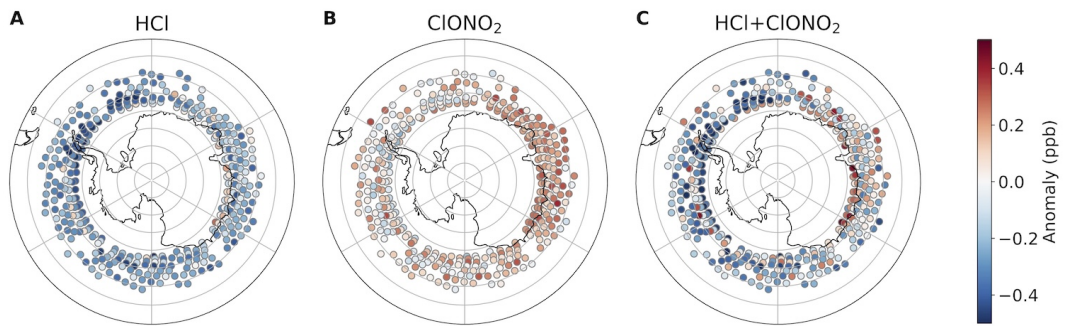
Appendix Figure 4.8: Tracer-tracer correlation in the polar vortex region ($65\text{--}90^\circ\text{S}$), as in Figure 4.2 for mid-latitudes. There is no data in June at this latitude range.



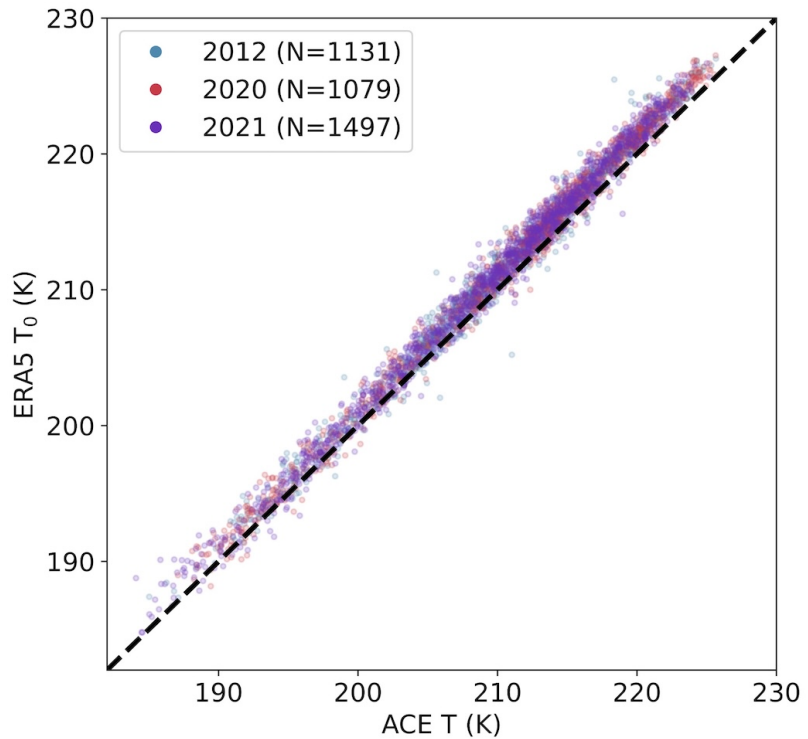
Appendix Figure 4.9: Tracer-tracer correlation between N_2O (x-axis) and HCl (y-axis) in the mid-latitude ($40\text{--}55^\circ\text{S}$), similar to Figure 4.2, but comparing ACE and MLS measurements in each row. Top row (panel A) shows results from ACE individual measurements at 18.5 km. Middle row (panel B) shows results from MLS zonally averaged data at 68.2 hPa. Bottom row (panel C) shows results from MLS individual measurements at 68.2 hPa.



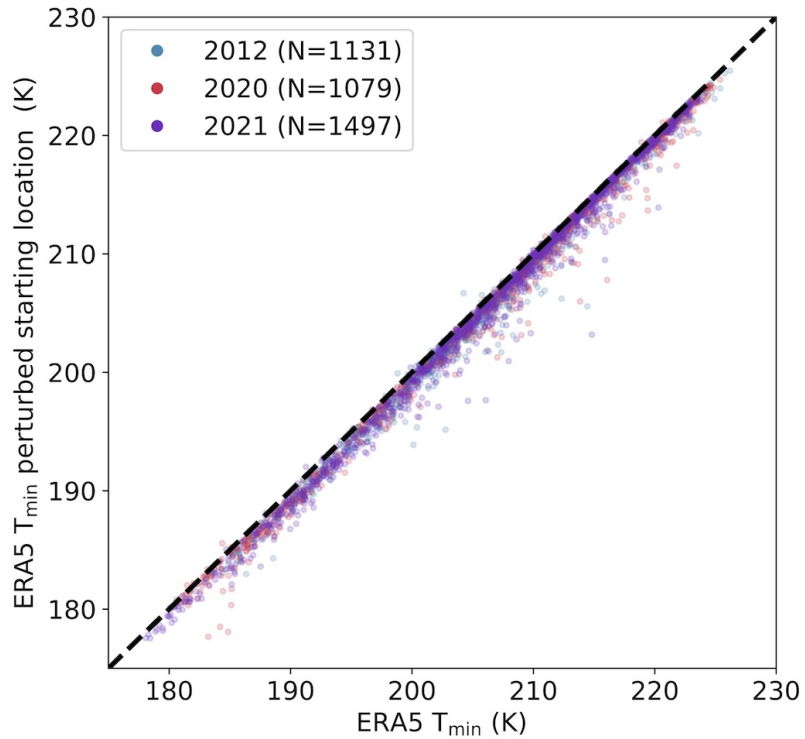
Appendix Figure 4.10: Tracer-tracer correlation between N_2O (x-axis) and HCl (y-axis) in the polar vortex region ($65\text{--}90^\circ\text{S}$), as in Appendix Figure 4.9 for mid-latitudes.



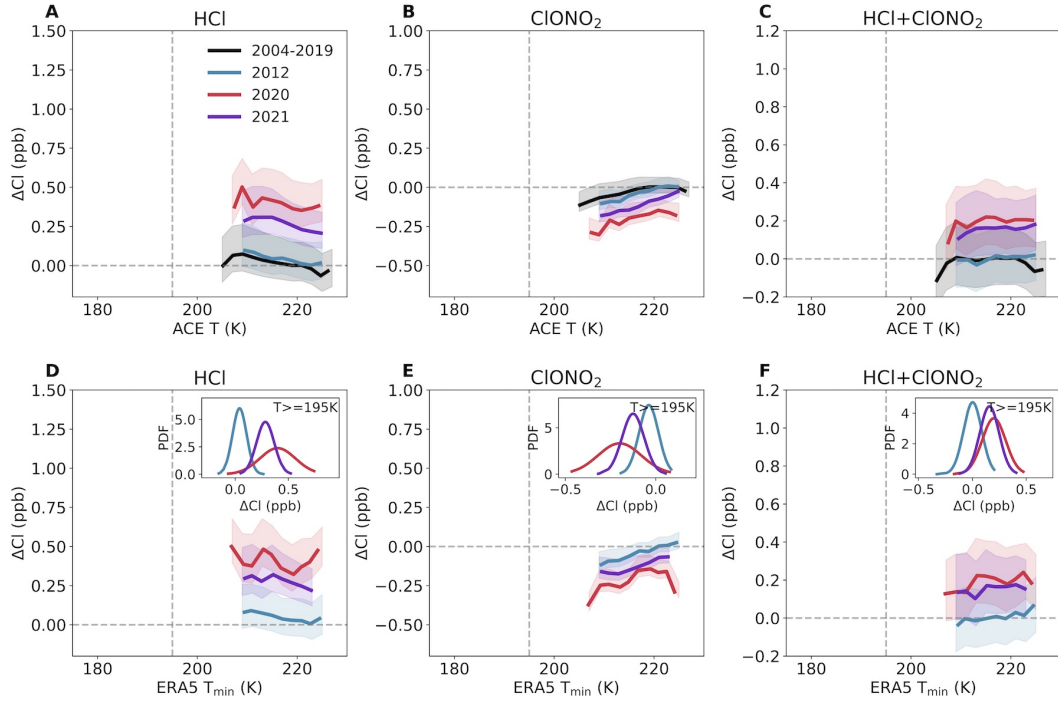
Appendix Figure 4.11: Similar to Figure 4.3, but for 2021. Note that the colorbar here shows a smaller range because the magnitude of the Cly anomalies are smaller in 2021.



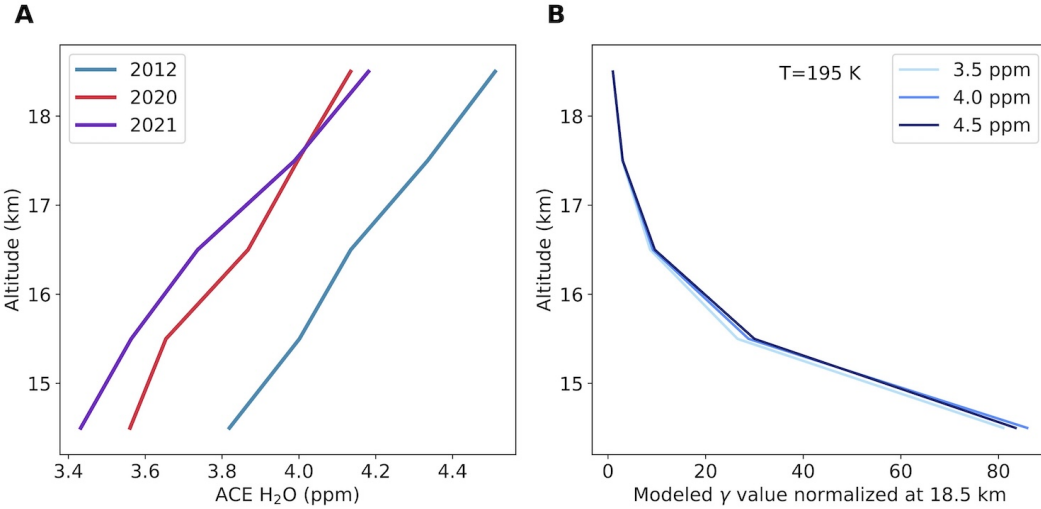
Appendix Figure 4.12: Sanity check on ACE and ERA5 temperature at 18.5 km. X-axis shows the ACE-observed temperature (ACE T), and the y-axis shows the ERA5 temperature at the closest rounded location and time with ACE satellite overpass (ERA5 T_0) for individual data points in 2020 (red), 2021 (purple), and 2012 (blue) over the full latitude range we use in this study ($40\text{--}90^\circ\text{S}$). The black dotted line indicates the 1-1 ratio. The total coefficient of determination R^2 value for ACE T and ERA5 T_0 (concatenating all three years) is 0.97, with a mean bias of 1.1 K.



Appendix Figure 4.13: Sensitivity test for the back trajectory calculation at different starting locations at 18.5 km. X-axis shows the minimum temperature from the 5-day back trajectory starting at the closest latitude/longitude from ACE observation. Y-axis shows a similar 5-day minimum temperature from back trajectory calculations but for data points released at ± 1 degree latitude and longitude from the satellite overpass location. The dashed black line indicates the 1-1 ratio. With such perturbations in the starting location, T_{\min} can have a mean bias at -0.8 K.



Appendix Figure 4.14: Cl activation as a function of temperature at the core of the polar vortex region (70–90 °S). Most of the data points in Figure 4.5 are over 65–70 °S, which might not represent the behaviors within the core of polar vortex. This figure shows data points over 70–90 °S, where data is only available in March and April (when temperatures are well above 200 K).



Appendix Figure 4.15: (A) shows the ACE measured July H₂O in the polar vortex region (65–90 °S) at different altitudes from 14.5 km to 18.5 km. The spread of H₂O is around 3.5 ppm to 4.5 ppm. (B) shows the γ value (reaction efficiency of HCl+ClONO₂) calculated from a similar parameterization used in WACCM at a fixed temperature of 195 K at different altitudes. γ values are normalized as ratios compared to the reaction efficiency at 18.5 km. An adopted spread in H₂O volume mixing ratio of ± 0.5 ppm from 4 ppm is shown in panel B, illustrating that water vapor mixing ratio has a small effect on the reaction efficiency, while pressure plays a dominating role for the background condition. At lower altitudes (high pressure), the efficiency of the HCl+ClONO₂ reaction is significantly enhanced compared to higher altitudes (low pressure).

Chapter 5

Contrasting Chlorine Chemistry on Volcanic and Wildfire Aerosols in the Southern Mid-Latitude Lower Stratosphere

Abstract

Volcanic eruptions and wildfires can impact stratospheric chemistry. We apply tracer-tracer correlations to satellite data from ACE (Atmospheric Chemistry Experiment-Fourier Transform Spectrometer) and HALOE (The HALOgen occultation Experiment) at 68 hPa to consistently compare the chemical impact on HCl after multiple wildfires and volcanic eruptions of different magnitudes. The 2020 Australian New Year (ANY) fire displayed an order of magnitude less stratospheric aerosol extinction than the 1991 Pinatubo eruption, but

This chapter is adapted from Wang, P., & Solomon, S. (2024). Contrasting Chlorine Chemistry on Volcanic and Wildfire Aerosols in the Southern Mid-Latitude Lower Stratosphere. *Geophysical Research Letters*, 51(18), e2024GL110412. <https://doi.org/10.1029/2024GL110412>

showed similar large changes in mid-latitude lower stratosphere HCl. While the mid-latitude aerosol loadings from the 2015 Calbuco and 2022 Hunga volcanic eruptions were similar to the ANY fire, little impact on HCl occurred. The 2009 Australian Black Saturday (ABS) fire and 2021 smoke remaining from 2020 yield small HCl changes, at the edge of the detection method. These observed contrasts across events highlight greater reactivity for smoke versus volcanic aerosols at warm temperatures.

5.1 Introduction

The southern hemisphere stratosphere has been perturbed by major aerosol injection events frequently in the past several years, associated with stratospheric ozone depletion. The April 2015 Calbuco volcanic eruption injected about 0.3 Tg of SO₂ into the stratosphere (Pardini, Burton, Arzilli, Spina, & Polacci, 2018), contributing to a record-large ozone hole in October of that year (S. Solomon et al., 2016). The 2019–2020 Australian New Year wildfire (ANY) injected about 1 Tg of smoke particles into the stratosphere (Peterson et al., 2021), and was followed by significant perturbations in mid-latitude chemistry (Bernath et al., 2022; Santee et al., 2022; S. Solomon et al., 2023), and an extended Antarctic ozone hole season (Ansmann et al., 2022; Chipperfield & Bekki, 2024; Ohneiser et al., 2022). The January 2022 Hunga Tonga-Hunga Ha’apai (Hunga) underwater volcanic eruption injected around 0.4 Tg of SO₂ (Carn et al., 2022) along with ~150 Tg of H₂O (Millán et al., 2022) into the stratosphere, and led to record low mid-latitude O₃ at some altitudes as well as significant polar O₃ depletion (Santee et al., 2023; X. Wang et al., 2023; Wilmouth, Østerstrøm, Smith, Anderson, & Salawitch, 2023; Wohltmann et al., 2024; Zhang, Kinnison, et al., 2024).

Volcanic eruptions can deplete stratospheric O₃ via various heterogeneous reactions. In the polar region where the temperature can be low, SO₂ from volcanic eruptions increases sulfate aerosols and subsequently can provide more surface area for chlorine to activate from reservoir species (mainly HCl and ClONO₂, or Cly) and deplete O₃, particularly in cold air at the

edge of the polar vortex (S. Solomon et al., 2016). In the mid-latitude region, temperatures are generally too warm for sulfate to take up HCl efficiently (Hanson & Ravishankara, 1993; Q. Shi et al., 2001). Instead, mid-latitude O₃ depletion after volcanic eruptions is mainly due to N₂O₅ hydrolysis that reduces NO_x, modulates ClO/ClONO₂ partitioning, and indirectly depletes O₃ (S. Solomon et al., 1996). Heterogeneous mid-latitude chemistry also depends on water vapor partial pressure (S. Solomon, 1999). With a large amount of H₂O emitted from Hunga, several key heterogeneous reactions can also happen more efficiently at warmer temperatures; this effect contributed to the record low mid-latitude O₃ observed in 2022 (Zhang, Kinnison, et al., 2024).

What makes wildfire different from volcanic eruptions is that organic aerosol makes up a large portion of the smoke composition (Murphy et al., 2021). The uptake of HCl on organic aerosols is orders of magnitude more efficient than on sulfate aerosols at temperatures warmer than \sim 200 K (S. Solomon et al., 2023). The high solubility of HCl on organics at warm temperatures means that chlorine activation is no longer limited to polar winter and spring. N₂O₅ hydrolysis also likely contributed to mid-latitude O₃ depletion after the 2020 ANY fire, but this mechanism alone cannot explain the unprecedented changes observed in Cly in 2020 (S. Solomon et al., 2022; S. Solomon et al., 2023). More evidence, especially from laboratory studies, is needed to verify the hypothesized reaction rates on different types of aerosols (Chipperfield & Bekki, 2024).

In this paper, we focus on chlorine processing in the southern mid-latitudes during the fall to winter season (March to July). This period follows the Australian summer wildfire season, and displayed unprecedented changes in stratospheric Cly after the ANY fire from MLS (Microwave Limb Sounder, 2004–present) and ACE (Atmospheric Chemistry Experiment-Fourier Transform Spectrometer, 2004–present) satellite data (Bernath et al., 2022; Santee et al., 2022). In an earlier study by P. Wang, Solomon, and Stone, 2023, we used a tracer-tracer method to derive the chemical impact on Cly from satellite data after the ANY fire. Here we use a similar method to look for stratospheric chemical impacts on HCl after the

2009 Australian Black Saturday (ABS) bushfire. While this was a much smaller wildfire compared to the 2020 ANY fire, several biomass indicators observed from satellite suggest that the wildfire plume indeed reached the lower stratosphere (Glatthor et al., 2013), and injected up to 0.1 Tg of aerosol into the stratosphere (Peterson et al., 2021). We also leverage satellite data from HALOE (The HALOgen occultation Experiment) onboard the UARS (Upper Atmosphere Research Satellite) to examine the changes in HCl after the catastrophic 1991 Pinatubo eruption, which injected up to \sim 19 Tg of SO₂ (Guo, Bluth, Rose, Watson, & Prata, 2004). The long composite record from HALOE and ACE spanning more than three decades allows consistent comparison of the chemical impacts of wildfire and volcanic aerosols, for these identified wildfire events that have reached the lower stratosphere, as well as multiple smaller volcanic eruptions (including Calbuco in 2015 and Hunga in 2022), and the 1991 Pinatubo eruption, the largest volcanic eruption in the satellite era.

5.2 Data and methods

5.2.1 ACE and HALOE satellite data

ACE version 5.2 (Bernath et al., 2005) and HALOE version 19 (Russell III et al., 1993) are used in this study. Both ACE and HALOE are infrared solar occultation instruments, providing vertical profiles at sunset and sunrise. HALOE data are available from 1991 to 2005, and ACE data are available from 2004 to present. In the lower stratosphere, HALOE and ACE agree reasonably well for temperature and multiple trace gases, except for NO₂ (McHugh et al., 2005). Here we present results in mid-latitude, defined as 30–45 °S. We picked this latitude range because both HALOE and ACE provide similar sampling distributions there, and this region is less affected by the air coming from the polar region than higher latitudes would be. Figure 5.1A–C shows mid-latitude monthly averaged temperature, CH₄, HCl, and aerosol extinction, linearly interpolated in log pressure to 68 hPa. In 2004–2005 when measurements are available from both instruments, HALOE and ACE show broadly

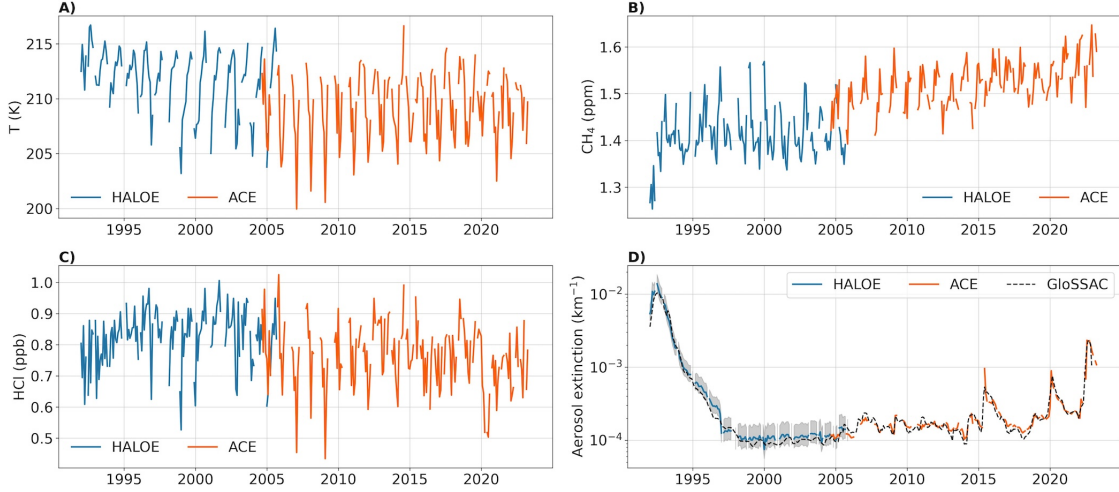


Figure 5.1: Time series for monthly mean A) temperature, B) CH₄, C) HCl, and D) aerosol extinction in 1992–2005 (from HALOE) and 2004–2023 (from ACE) between 30–45S at 68 hPa. The gray shading in aerosol extinction during the HALOE period represents uncertainty when converting aerosol extinction from 3.45 μm to 1020 nm (discussed in Section 5.2.1 in detail). The black dashed line in panel D shows 1020 nm aerosol extinction at 18.5 km from GloSSAC averaged from a similar latitude range.

consistent results.

Aerosol extinction from HALOE is available at four different channels (2.45, 3.4, 3.46, and 5.26 μm). Data at 2.45 and 5.26 μm are strongly biased after Pinatubo and are not recommended for scientific use, and 3.4 μm is also affected slightly by failure to remove NO₂ absorption (Thomason, 2012). ACE aerosol extinction is available at two channels (525 and 1020 nm). To facilitate direct comparisons between ACE and HALOE, we converted HALOE aerosol extinction from 3.46 μm to 1020 nm. Following Thomason, 2012 (2012), we applied two sets of scaling factors to HALOE aerosol extinction (0.2 ± 0.05 before 1997 and 0.375 ± 0.125 after 1997) derived from the HALOE and SAGE II (Stratospheric Aerosol and Gas Experiment II) 3.46 μm to 1020 nm ratios (the spreads in the scaling factors are represented as gray shadings in Figure 5.1D). This method appears to work well and does not require prior assumptions on the particle size distribution. The 1020 nm aerosol extinction derived from HALOE in this way and the direct retrieval from ACE show consistent results in the overlap period during 2004–2005 and are consistent with the zonal mean 1020 nm aerosol

extinction product from the GloSSAC (Global Space-based Stratospheric Aerosol Climatology version 2.21; NASA/LARC/SD/ASDC, [2023](#)) averaged for a similar latitude range at 18.5 km (dashed black line in Figure 5.1D).

5.2.2 Tracer-tracer correlation method

Both ACE (using high resolution infrared absorption in solar occultation) and HALOE (using a lower-resolution infrared emission band) measure HCl, aerosol extinction, and several other trace gases simultaneously, allowing a quantitative estimate of the change in HCl associated with aerosol abundances at individual satellite overpasses. However, the observed mixing ratio of HCl reflects both dynamic and chemical influences. Here we use CH₄ as a dynamical tracer observed by both instruments and exploit the HCl-CH₄ correlation in the mid-latitude during fall/early winter season (March–July) to search for chemical impacts. Individual points in Figure 5.2 represent co-located CH₄ and HCl satellite measurements that are linearly detrended (discussed later). Following P. Wang, Solomon, and Stone, [2023](#), we first construct a “no-chemistry” baseline based on the March CH₄-HCl relationship composite for all the background years without major wildfires or volcanic eruptions. For HALOE data, this baseline covers 1997–2005 and for ACE data, it spans 2004–2019 (excluding 2009 and 2015–2016), shown as thick blue and orange lines in Figure 5.2, respectively. The shaded areas in Figure 5.2 represent the full range of the CH₄-HCl relationship derived from individual background years, capturing interannual variability, which is a key source of baseline uncertainty (P. Wang, Solomon, & Stone, [2023](#)). Overall, the CH₄-HCl relationships from both satellites are consistent with each other. We define ΔHCl as the departure of HCl in individual data points from the “no-chemistry” baseline, which largely describes the net chemical change in HCl. In the absence of chemical changes, a plot of HCl versus CH₄ should follow a straight line, with dynamical changes moving along but not departing from the line (this is more clearly shown in the ACE data due to its high precision).

The inactive tracer used in this study to derive ΔHCl is CH₄. Both HCl and CH₄

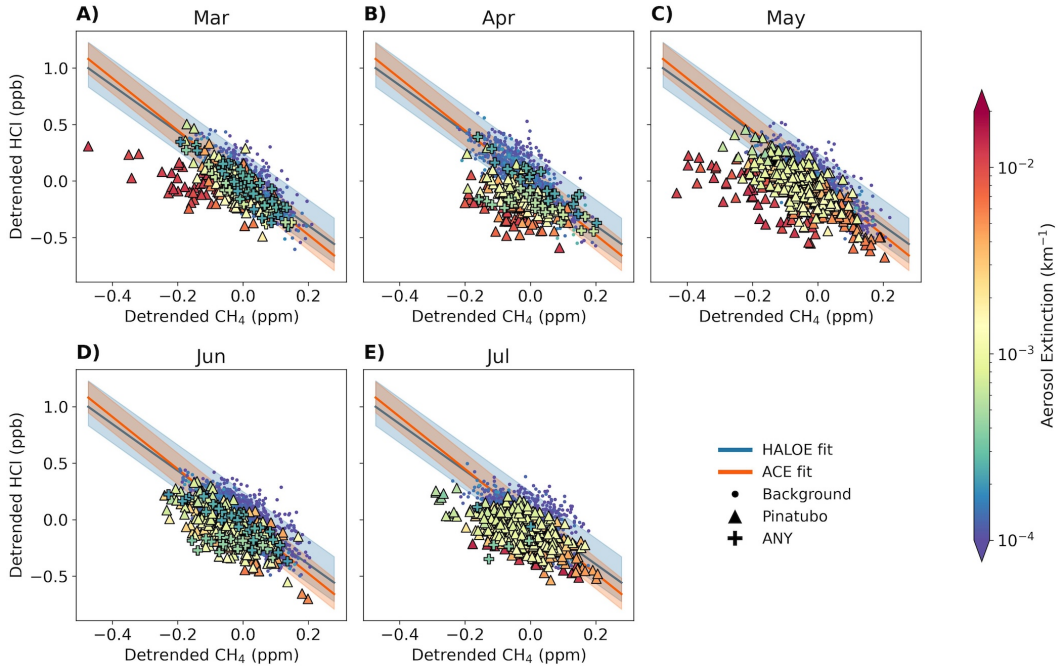


Figure 5.2: Tracer-tracer scatter plots between detrended CH₄ (x-axis) and detrended HCl (y-axis) color coded by aerosol extinction in HALOE and ACE at 30–45 °S at 68 hPa. Only the Pinatubo years (1992–1994) and ANY years (2020–2021) are identified by specific markers as they show the most significant changes during each satellite mission (Appendix Figure 5.8 shows these events in separate panels to avoid overlapping points). Shadings indicate a full range of interannual variability (discussed in detail in Section 5.2.2) for HALOE (in blue) and for ACE (in orange). Note that there is no data coverage at the chosen latitude in May from ACE.

from HALOE use gas filter radiometry, so the retrievals are generally insensitive to high aerosol loading after the Pinatubo eruption (Hervig et al., 1995). HALOE HCl and CH₄ have previously been used in tracer-tracer analysis after Pinatubo given that the relative error between these tracers is less than 5 %, although the first half of 1992 could still be affected by the extreme aerosol loading (Dessler et al., 1997). For consistency, we also use CH₄ as the inactive tracer in HALOE ACE data in this study. CH₄ and HCl come from different emission sources, and different trends may bias ΔHCl calculation, especially in such a three-decade-long satellite record. We therefore linearly detrended CH₄ and HCl fitted from 1997–2005 in HALOE and 2004–2018 in ACE. We considered the use of HF as an inactive tracer in this analysis, although the high aerosol loads of Pinatubo may influence the HALOE retrieval (Thomason, 2012). Appendix Figure 5.5 compares ΔHCl in the ACE record calculated from CH₄ and from HF, which is much more inert than CH₄ in the lower stratosphere. For the background years, most of the data are clustered around 0, and for years after major volcanic eruptions and wildfires, the two inactive tracers resulted in similar ΔHCl . Overall, CH₄-derived ΔHCl has a low bias by 0.01 ppb compared to HF-derived ΔHCl .

5.3 Results

Figure 5.3 shows satellite-derived mid-latitude ΔHCl at 68 hPa as a function of the 1020 nm aerosol extinction in the years after the Pinatubo, Calbuco, Hunga volcanic eruptions, and the ABS and the ANY fires (labeled by different colors and markers shown in the figure legend). The gray dots are for example background years in 2000 (from HALOE) and the black dots are for the background year 2012 (from ACE), as these two years do not have known major volcanic eruptions or large wildfires. The larger background ΔHCl spread in 2000 compared to 2012 can be partially due to lower precision in HALOE compared to ACE. Since HCl becomes much more soluble on volcanic aerosols at temperatures colder

than \sim 195 K (Hanson & Ravishankara, 1993; Q. Shi et al., 2001; S. Solomon et al., 2023), to prevent misinterpreting the temperature for chlorine processing on different aerosol types after volcanic eruptions and wildfires, ΔHCl in Figure 5.3 is separated into five temperature regimes (\leq 195 K, 195–200 K, 200–205 K, 205–210 K, and $>$ 210 K) based on the air parcel’s recent minimum temperature exposure (instead of using the temperatures directly observed at the time of the satellite overpasses). Following P. Wang, Solomon, and Stone, 2023, at each satellite overpass, we run a 5-day back trajectory calculation using Lagranto (Lagrangian Analysis Tool; Sprenger and Wernli, 2015) driven by the ERA5 (fifth generation atmospheric reanalysis product from the European Centre for Medium-Range Weather Forecasts; Hersbach et al., 2020) meteorology. Appendix Figure 5.6 is comparable to Figure 5.3 but instead uses the satellite-observed temperature directly. Generally, because the latitude range we choose is far away from the polar region, most of the data points are not recently exposed to substantially colder temperatures, and can well represent warm mid-latitude conditions.

The main focus here is on the strong negative values of ΔHCl , indicating efficient uptake of HCl on particles, especially at temperatures warmer than 200 K when PSCs are very unlikely to occur (McCormick, Steele, Hamill, Chu, & Swissler, 1982). Using the ACE record from 2004–2023, aerosol extinction after the Calbuco and Hunga volcanic eruptions reached a similar (or even higher) value to that of the ANY fire, which is about an order of magnitude higher than background conditions. However, only the two consecutive years in this record after the ANY fire show a noticeable HCl decrease due to chemistry, where ΔHCl falls outside the uncertainty range (characterized by the full range of interannual variability in background years during ACE record, represented as the orange shading in Figure 5.3). This is consistent with S. Solomon et al., 2023, who suggested that the organic aerosols from wildfires are orders of magnitude more efficient in uptaking HCl compared to volcanic aerosols under warm mid-latitude temperatures. We can only find a similar degree of change in HCl after the 1991 Pinatubo eruption. However, the aerosol extinction in 1992 reached $\sim 1 \times 10^{-2} \text{ km}^{-1}$, which is more than one order of magnitude higher than the ANY fire. Given significantly larger

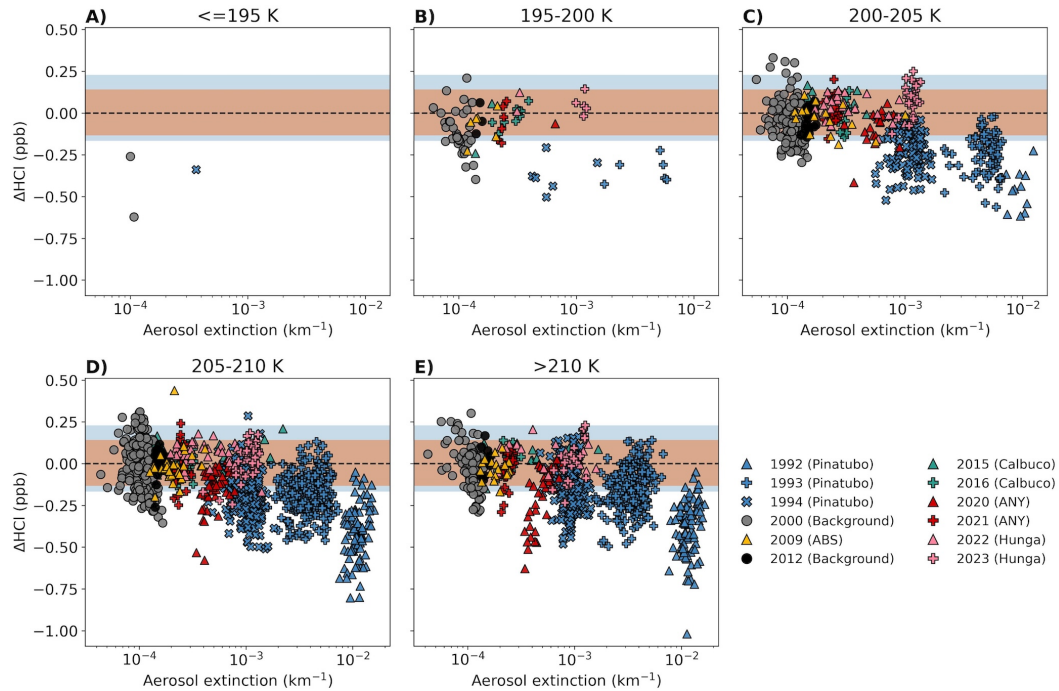


Figure 5.3: ΔHCl (negative values suggest a net loss in HCl due to chemistry) in 30–45 °S at 68 hPa as a function of aerosol extinction at individual satellite overpass. Results are grouped in panels showing different temperature ranges (based on 5-day minimum temperatures from the back trajectory calculation for each point, a similar figure but using satellite observed temperature is shown in Appendix Figure 5.6). Two background years, and consecutive years after major volcanic eruptions and the wildfires are highlighted with different markers and colors. The blue and orange shadings surround zero line indicate the full range of interannual variability during the HALOE and ACE periods, respectively.

aerosol amounts, the decrease in HCl after the Pinatubo eruption is mainly due to enhanced N_2O_5 hydrolysis and therefore elevated HO_x depleting HCl (Kinnison et al., 1994). The 2009 ABS fire led to a small enhancement in aerosol extinction that is close to 2021 conditions. There are a few data points in 2009 that displayed ΔHCl lower than the ACE uncertainty range (yellow triangles in Figure 5.3). Appendix Figure 5.7 shows the tracer-tracer scatter plot in ACE that highlights the ABS fire color-coded by CO, which is an indicator for biomass burning. The low ΔHCl points in 2009 are mainly in March, and are associated with high CO concentrations, suggestive of some role for wildfire chemistry. However, this chemical impact is small, barely outside the range of other years, and did not last long; the ΔHCl in 2009 falls within the uncertainty range quickly after March.

Hunga volcanic aerosols were accompanied by significant H_2O injection and have higher extinction than Calbuco and the ANY fire (Zhu et al., 2022). Interestingly, even though 2022–23 after the Hunga eruption and 1994 (3 years after the Pinatubo eruption) show comparable amounts of aerosol extinction at 68 hPa, less ΔHCl was found after the Hunga eruption. Although it is worth noting that the altitude associated with the largest change in aerosol extinction and HCl after the Hunga eruption is at a higher altitude (X. Wang et al., 2023; Wilmouth et al., 2023). A caveat of considering aerosol extinction alone for indications of heterogeneous reaction is that particle size distribution is overlooked. Further, different types of aerosols may exhibit different optical properties, affecting extinction values (Ohneiser et al., 2022). Particle diameter after the Hunga eruption reached $\sim 0.56 \mu\text{m}$ (Asher et al., 2023), just at the peak of scattering efficiency (C. Li et al., 2024; Murphy et al., 2021); this event therefore resulted in higher aerosol extinction given relatively lower mass of aerosols. On the contrary, particles after the Pinatubo eruption reached a diameter larger than $0.7 \mu\text{m}$ (Wilson et al., 2008), decreasing their scattering efficiency. Therefore, the mass of aerosols in 1994 may be much higher than 2022–23, despite displaying a similar level of aerosol extinction. Likewise, the mean diameter after the ANY fire was smaller compared to that of Hunga (Ansmann et al., 2021), suggesting given similar aerosol extinctions that the mass of ANY

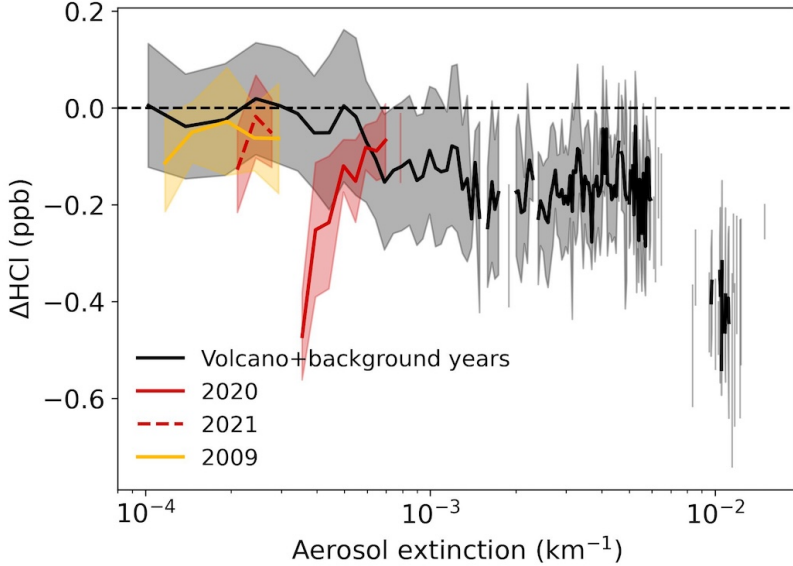


Figure 5.4: ΔHCl in 30–45 °S at 68 hPa from 1992 to 2023 binned by aerosol extinction (at every $5 \times 10^{-5} \text{ km}^{-1}$, each bin is averaged by at least 3 data points). The black line shows the averaged net chemical impact on HCl in background and volcanic eruption years. The red lines show the two consecutive years after the ANY fire (solid line for 2020, dashed line for 2021). The yellow line shows the 2009 ABS fire. Color shadings indicate ± 1 standard deviation from the mean for data averaged in each aerosol extinction bin.

aerosols is also larger than Hunga. Particle sizes are also important in determining the decay time of these aerosols in the stratosphere, contributing to how long these aerosols can affect stratospheric chemistry over time (Ohneiser et al., 2022).

Figure 5.4 averages the net chemical impact on HCl in various aerosol extinction bins for the wildfire years (which contain more organic aerosols, with red lines showing the ANY fire, and yellow lines for the ABS fire) and all other years in 1992 to 2023 (including volcano and background years, which mainly contain inorganic sulfates). We composite all the satellite data in 30–45 °S (without filtering out data points with low temperatures) because the latitude range we choose here is equatorward enough to prevent significant PSC-induced Cl activation (there are only a few points that had 5-day minimum temperature below 195 K based on the back trajectory calculation in Figure 5.3).

After the catastrophic 1991 Pinatubo eruption, it took about 4 years for aerosol extinctions to decay to a level similar to the ANY fire. The magnitude of ΔHCl also shows a consistent

decay associated with the decay in aerosol extinction after Pinatubo. The net chemical impact on HCl from the Pinatubo eruption vanishes in 1995 when the average aerosol extinction reaches $\sim 5 \times 10^{-4} \text{ km}^{-1}$. For the Calbuco eruption and background years, when the aerosol extinctions were smaller than $5 \times 10^{-4} \text{ km}^{-1}$, insignificant changes in ΔHCl were observed. The Hunga eruption boosted the aerosol extinction to $\sim 1 \times 10^{-3} \text{ km}^{-1}$, but has only a minor impact on ΔHCl , likely due to less surface area compared to Pinatubo aerosols; the ΔHCl curve is hence close to zero at $\sim 1 \times 10^{-3} \text{ km}^{-1}$. Along the ΔHCl versus aerosol extinction curve, the net chemical change in HCl during wildfire year in 2020 is a clear outlier compared to the background and volcanic years. In 2021, wildfire aerosols are transported further poleward, and the chemical impact at 30–45 °S becomes smaller (although there is still significant Cl activation in 2021 at 40–55 °S and 65–90 °S shown in P. Wang, Solomon, and Stone, 2023). This difference in HCl uptake is also broadly consistent with the difference in ozone loss after the ANY fire and the Calbuco and Pinatubo eruptions (Ansmann et al., 2022). The 2009 ABS fire, due to its small magnitude (only a-tenth of the stratospheric aerosol loading compared to the ANY fire), may have led to a small decrease in the mean ΔHCl but it is close to the uncertainty range. At the latitude range we chose, both 2009 and 2021 have similar aerosol extinction and display a similar impact on ΔHCl that is on the lower end of the background/volcano range. The two events suggest that significant mid-latitude wildfire impacts on HCl outside of the range of variability at these latitudes would require extinction levels of about \sim a few $\times 10^{-4} \text{ km}^{-1}$ or larger.

5.4 Conclusions

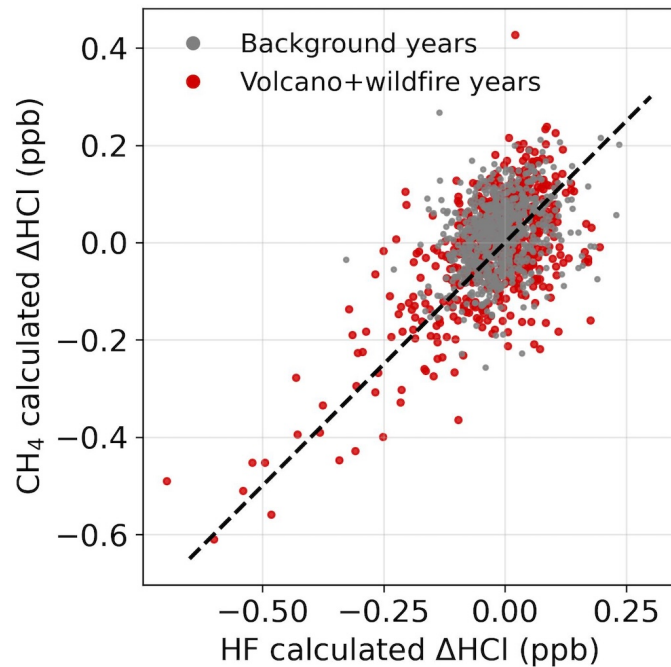
The 2020 ANY fire, the largest wildfire since the satellite era, injected a large amount of aerosol into the lower stratosphere and resulted in an unprecedented change in HCl and ClONO₂ relative to MLS and ACE records from 2004 to 2023. In an earlier study from P. Wang, Solomon, and Stone, 2023, we quantified the net chemical impact on HCl after the

ANY fire from satellite data using the tracer-tracer method. Here, we use this method to consistently combine satellite observations from ACE (2004–2023) and HALOE (1992–2005), and thereby examine the net chemical impacts in HCl after another smaller wildfire in 2009 (Black Saturday bushfire) as well as the ANY fire as compared to a series of volcanic eruptions of different sizes – from the recent 2015 Calbuco and 2022 Hunga eruption to the catastrophic 1991 Pinatubo eruption.

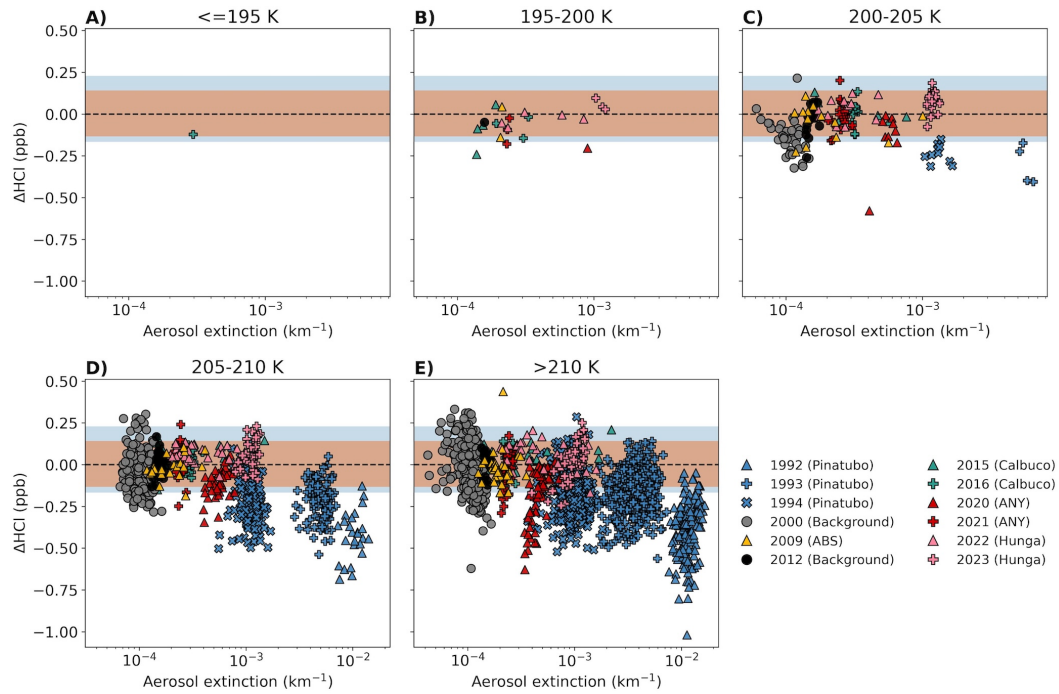
The approach we used allows consistent identification of volcanic impacts on mid-latitude HCl in the lower stratosphere for several years after Pinatubo. Direct satellite evidence suggests a similar degree of net HCl decrease (after removing the dynamical impacts) after the ANY fire and the Pinatubo eruption at 68 hPa, despite Pinatubo having an order of magnitude higher aerosol extinction than the ANY fire. The decrease in mid-latitude HCl after the Pinatubo eruption is thought to be due to enhanced gas phase reaction with OH (given significant reductions in NO_x through N₂O₅ hydrolysis and therefore HO_x enhancement; Kinnison et al., 1994). However, wildfires containing a significant portion of organic aerosols (Murphy et al., 2021) can dissolve HCl more efficiently at warm temperatures (S. Solomon et al., 2023), facilitating the reaction between ClONO₂ and HCl while suppressing ClONO₂ hydrolysis. Therefore, only a relatively small amount of wildfire aerosols in the stratosphere might cause chemical changes in HCl. The unprecedented change in chlorine species after the 2020 ANY fire has increased attention on the impact of wildfires in the stratosphere. Earlier wildfires with smaller magnitudes could also affect stratospheric chlorine activation but may have been overlooked. Here we see some evidence suggesting that the much smaller 2009 ABS bushfire may have impacted the stratospheric chlorine chemistry in the southern hemisphere mid-latitude lower stratosphere, but only at the edge of variability. We used the 2009 wildfire event and the decay of the 2020 wildfire smoke to the year 2021 to suggest that significant mid-latitude wildfire impacts on HCl outside the range of variability at the latitudes explored here would require extinction levels higher than these events, or above about \sim a few $\times 10^{-4}$ km⁻¹. Applying the method developed here to a wider range of altitudes,

latitudes, and events in both hemispheres is a topic for future work.

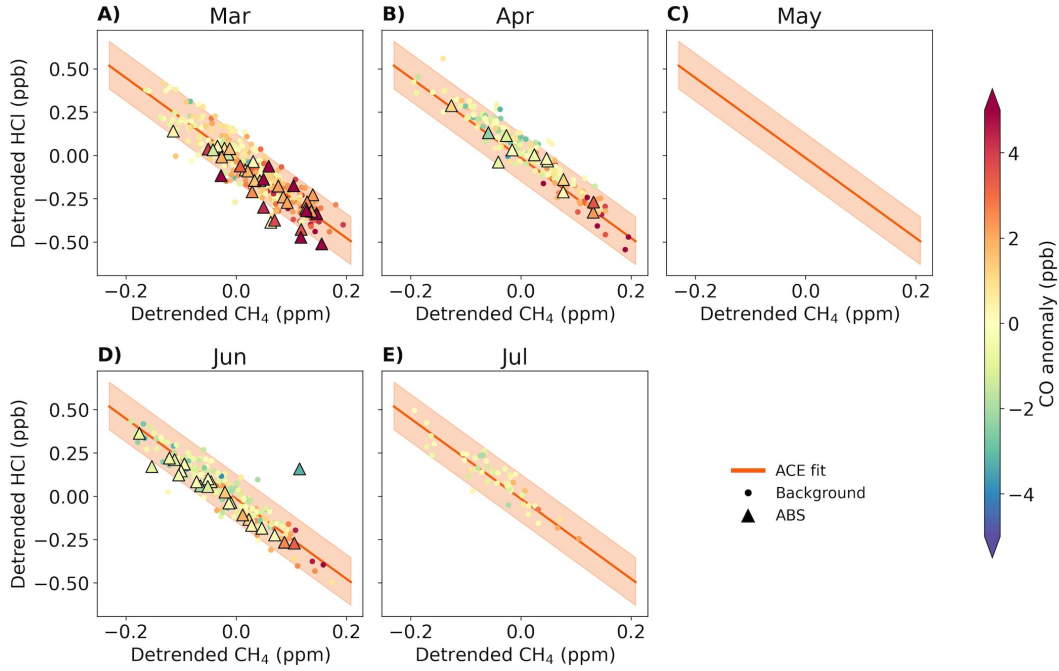
Appendix



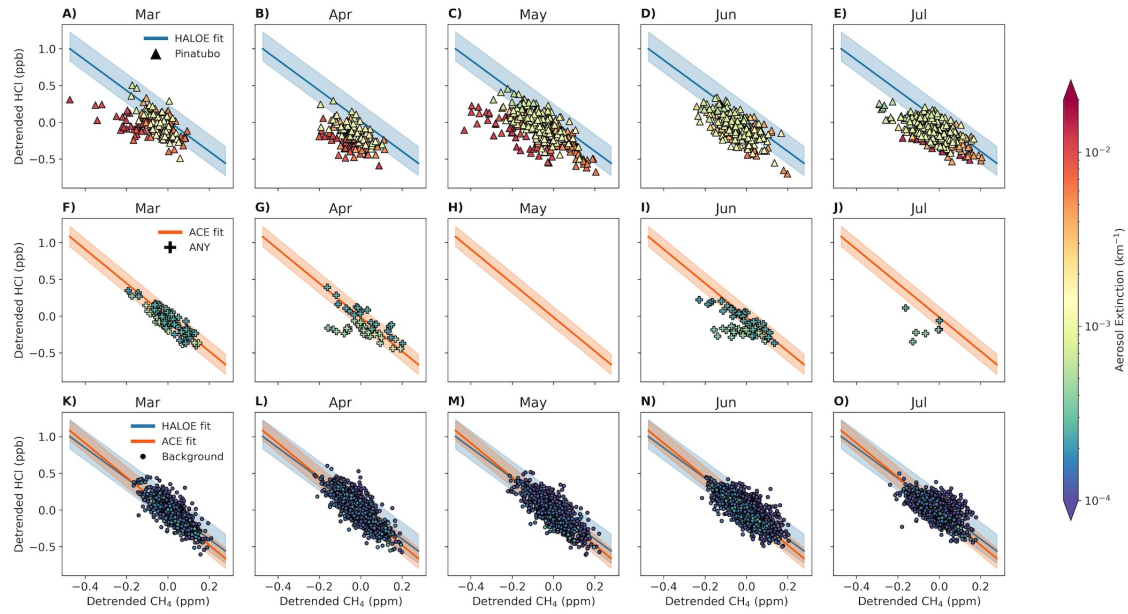
Appendix Figure 5.5: ΔHCl in March–July calculated from ACE in 30–45 °S at 68 hPa during 2004–2023, using detrended HF as the inactive tracer (x-axis) and detrended CH_4 as the inactive tracer (y-axis). The volcano and wildfire years (2009, 2015, 2016, 2020, 2021, 2022, 2023) are shown as red dots, and the rest of the years are shown as gray dots. The black dashed line indicates the 1:1 ratio. CH_4 - and HF-derived ΔHCl are consistent with each other, although CH_4 -derived ΔHCl has a mean bias of -0.01 ppb compared to HF-derived ΔHCl .



Appendix Figure 5.6: Similar to Figure 5.3, but the points are grouped in panels based on satellite observed temperature instead of the 5-day minimum temperature from the back trajectory model.



Appendix Figure 5.7: Similar to Figure 5.2, but only for ACE data (excluding Calbuco, ANY, and Hunga), and each point is color coded by CO instead of aerosol extinction. CO serves as an indicator for biomass burning. Since CO has a strong latitudinal gradient (higher CO at lower latitudes), the CO values shown here are anomalies compared to climatological mean binned in every 3 degrees of latitude. The 2009 ABS fire is highlighted with triangle markers.



Appendix Figure 5.8: Similar to Figure 5.2, but Pinatubo, ANY, and background years are shown in separate rows to avoid overlapping different events.

Chapter 6

Fingerprinting the Recovery of Antarctic Ozone

Abstract

The Antarctic ozone “hole” was discovered in 1985, and man-made ozone-depleting substances (ODS) are its primary cause. Following reductions of ODSs under the Montreal Protocol, signs of ozone recovery have been reported, based largely on observations and broad yet compelling model-data comparisons. While such approaches are highly valuable, they don’t provide rigorous statistical detection of the temporal and spatial structure of Antarctic ozone recovery in the presence of internal climate variability. Here, we apply pattern-based detection and attribution methods as employed in climate change studies to separate anthropogenically forced ozone responses from internal variability, relying on trend pattern information as a function of month and height. The analysis uses satellite observations together with single-model and multi-model ensemble simulations to identify and quantify the month-height

This chapter is adapted from Wang, P., Solomon, S., Santer, B., Kinnison, D., Fu, Q., Stone, K., Zhang, J., Manney, G., & Millán, L. (2025). Fingerprinting the recovery of antarctic ozone. *Nature (in press)*. <https://doi.org/10.21203/rs.3.rs-4876981/v1>

Antarctic ozone recovery “fingerprint”. We demonstrate that the data and simulations show compelling agreement in the fingerprint pattern of the ozone response to decreasing ODSs since 2005. We also show that ODS forcing has enhanced ozone internal variability during the austral spring, influencing detection of forced responses and their time of emergence. Our results provide robust statistical and physical evidence that actions taken under the Montreal Protocol to reduce ODSs are indeed resulting in the beginning of Antarctic ozone recovery, defined as increases in ozone consistent with expected month-height patterns.

6.1 Introduction

Despite the decline in ozone-depleting substances (ODS; Laube and Tegtmeier, 2022), the continuing occurrence of large Antarctic ozone “holes” in recent years—partly due to the 2020 Australian wildfire (Bernath et al., 2022; Santee et al., 2022; S. Solomon et al., 2023) and 2022 Hunga volcanic eruption (Manney et al., 2023; X. Wang et al., 2023; Wohltmann et al., 2024; Zhang, Kinnison, et al., 2024)—along with concerns about a significant decrease in October mid-stratospheric ozone (Kessenich et al., 2023), have stimulated discussion about the detectability of a robust signal in Antarctic ozone recovery. Formal detection and attribution (D&A) methods are needed to assess the effectiveness of the Montreal Protocol.

Initial-condition large ensembles (LEs) generated with fully coupled global climate models offer a unique opportunity to “fingerprint” the anthropogenic influence. They provide valuable information on both natural internal variability and the characteristic space and time signatures of the climate responses to different external forcings (Christidis & Stott, 2015; Gillett, Fyfe, & Parker, 2013; Hasselmann, 1993; Santer et al., 2022; Santer et al., 2023; J.-R. Shi, Santer, Kwon, & Wijffels, 2024; Stott, Sutton, & Smith, 2008; Terray et al., 2012). Such ensembles are rarely used in ozone studies, which generally apply multiple linear regression to isolate underlying forced trends by fitting ozone time series to known sources of variability (such as the solar cycle, El Niño-Southern Oscillation, Quasi-Biennial Oscillation,

volcanic activities, etc.; Chipperfield and Santee, 2022; Hassler and Young, 2022). In contrast, LEs do not require the assumption that the response is a linear combination of independent predictor variables (Santer et al., 2001). Although some D&A methods have been applied to global ozone depletion and the time of emergence of total column recovery using multi-model ensembles (Dhomse et al., 2018; Robertson et al., 2023; Zeng et al., 2022), previous studies have not fully utilized the pattern-based D&A techniques. Furthermore, multiple members from a single-model that is well-evaluated and realistic can reliably quantify modeled forced signals and intrinsic variability, whereas one run from each of a multi-model ensemble samples larger cross-model differences in forcing, response, and variability (Deser et al., 2020), thus hampering the identification of the beginning of ozone recovery (Dhomse et al., 2018; Zeng et al., 2022).

6.2 Data and methods

6.2.1 Satellite data

Microwave Limb Sounder (MLS) provides daily observations since August 2004, and the data has been extensively validated (Froidevaux et al., 2008; Hubert et al., 2016). Here we use MLS version 5 monthly-mean level 3 ozone mixing ratios on pressure coordinates from 100 hPa to 1 hPa. The level 3 product covers latitudes from 82 °S to 82 °N, using a 4° latitude bin. Ozone is averaged over 66–82 °S in this paper, weighted by cosine latitude to account for the reduction in area further poleward. We use the monthly-mean values starting from 2005 (excluding the latter half of 2004) so that every month in the trend analysis has the same number of time samples.

Satellite total column ozone (TCO) observations are from the Ozone Monitoring Instrument (OMI) version 3 daily level 3 product (Leveld et al., 2006), which is onboard the same satellite as MLS. TCO from OMI is also averaged by month starting from 2005 and in the latitude range from 66–82 °S (weighted by cosine latitude).

6.2.2 Model and scenario descriptions

A total of 19 different models participated in the phase 1 of the Chemistry–Climate Model Initiative (CCMI-1), with a total of 33 realizations for the refC2 scenario (Dhomse et al., 2018; Morgenstern et al., 2017). This scenario characterizes ODS emissions following World Meteorological Organization (WMO), 2011, and other greenhouse gas (GHG) emissions following RCP6.0 (Meinshausen et al., 2011) from 1960 to 2100. To prevent biasing towards models with more ensemble members, we only use the first realization from each model.

We also used the fully coupled Community Earth System Model-Whole Atmosphere Community Climate Model (CESM1-WACCM4; WACCM for short; Garcia et al., 2017; Marsh et al., 2013) in this analysis, which incorporates coupled ocean-atmosphere processes with interactive chemistry. Our primary focus is on a 10-member WACCM initial condition ensemble generated with the same refC2 scenario employed by the CCMI-1 models. In addition to refC2, we consider three other WACCM initial condition ensembles, referred to as fODS, fGHG, and historical. fODS (also referred to as the GHG-only runs) fixes ODS forcing at the 1960 level, while GHG concentrations evolve as in the refC2 runs. Alternately, fGHG (or ODS-only runs) fixes GHG concentrations in 1960, while ODS levels evolve as in refC2 runs. The historical scenario involves temporal changes in both GHG and ODS from 1955 to 1979 (Stone, Solomon, Thompson, Kinnison, & Fyfe, 2022). The CCMI and WACCM simulations are vertically interpolated to MLS pressure levels (linear interpolation in log pressure), and are also averaged over 66–82 °S and cosine-weighted for consistency with MLS.

Although the WACCM runs analyzed here are less than 30 years in length (from 1995 to 2024 for refC2, fODS, and fGHG, and from 1955 to 1979 for the historical scenario), an advantage of the set of simulations is that each scenario has 10 realizations that are slightly perturbed in their initial conditions (Kay et al., 2015). This facilitates reliable estimation of both the underlying forced response (the ensemble-mean) and internal variability. In contrast, multi-model ensembles convolve internal variability estimates with inter-model

differences or errors in forced responses, and/or with model differences in the amplitude and patterns of internal variability (Deser et al., 2020; Kay et al., 2015; A. Solomon et al., 2011). For example, not all of the 19 CCM models are fully coupled to an interactive ocean (Morgenstern et al., 2017), likely introducing large cross-model differences in forced responses and natural variability.

As shown here, the WACCM historical and refC2 initial condition ensembles can also be used to explore whether external forcing modulates internal variability—a key issue in signal detection. Relative to multiple linear regression approaches for estimating the anthropogenic component of ozone trends, using the WACCM fully-coupled chemistry climate model has the advantage that no prior assumptions are required regarding the relationships between different predictor variables (such as the El Niño-Southern Oscillation, Southern Annual Mode, Quasi-Biennial Oscillation, solar cycle, etc.). As in the real world, nonlinear interactions between ozone and climate internal variability can be present in the model simulations.

Although large initial condition ensembles from multiple single-models are preferred for analyzing the interactions between atmospheric chemistry and natural internal variability, the high computational cost may be a barrier to generating such ensembles, at least for some models (Deser et al., 2020).

6.2.3 Signal and noise definition and uncertainty estimation

The “local” signal and noise denotes an analysis at individual months and heights. We define the local signal as the linear trend in ozone (starting in 2005, ending years can vary from 2009 to 2023) at each month and pressure level, derived from a linear fit to ensemble-mean ozone data from forced model simulations. To calculate the “local” noise, we first subtract the ensemble-mean ozone time series from each individual model realization; the resulting residuals then characterize the internal variability (Deser et al., 2020). Noise is defined as the standard deviation of the ozone trends (with the same trend length as the signal) in these residuals. The noise represents the spread in ozone trends that is primarily due to internal

variability. Both the local signal and the local noise have units of ppm/decade (parts per million by volume per decade). The statistical significance of ozone trends is determined by the local signal-to-noise ratio, S/N. For two-tailed tests, a 5 % (10 %) significance level is associated with local S/N values larger than 1.96 (1.645).

In addition to the local S/N analysis at individual months and heights, we also applied a conventional “fingerprint” method (Santer et al., 2023) to the overall simulated and observed month-height patterns of ozone changes. The key point here is that the entire month-height pattern is employed to distinguish a forced response from internal variability. The overall signal is the element-wise uncentered covariance between the month-height ozone trend patterns in MLS (e.g., Figure 6.1c) and in the WACCM ensemble-mean (e.g., Figure 6.1d), or between the trend pattern in MLS and the CCMI multi-model mean (e.g., Figure 6.1e), at varying trend lengths. This is essentially equivalent to projecting the observed month- and height-resolved trend pattern onto the forced response (Santer et al., 2023). The overall noise is the standard deviation in the similarly computed uncentered covariance but between internal variability in individual realizations (obtained from the different panels in Appendix Figure 6.5 after removing the ensemble mean) and the mean forced response. Fingerprinting is performed over the same space-time ranges used in the local S/N analysis: i.e., using spatially averaged ozone changes between 66–82 °S at altitudes from 100 hPa to 1 hPa and in the 12 months from January through December. The increase in the overall S/N in Figure 6.4 with increasing trend length suggests that the observed overall month-height ozone change pattern is unlikely to be explained by internal variability alone.

6.2.4 Vortex coverage and vortex averaged ozone calculation

Vortex coverage (shown as the dots in Appendix Figure 6.11) and vortex averaged ozone (red lines in Appendix Figure 6.12) are obtained from MLS daily level 2 and the derived meteorological products (DMPs; Manney et al., 2011; Manney et al., 2007; Millán et al., 2023). The DMPs are calculated from the NASA GMAO (Global Modeling and Assimilation

Office) using meteorology from MERRA-2 (Modern-Era Retrospective analysis for Research and Applications, Version 2) and are interpolated to the same time and location as MLS level 2 products. Vortex edge in MLS is determined by a height-dependent sPV (scaled potential vorticity) threshold (Z. D. Lawrence, Manney, & Wargan, 2018) on potential temperature (theta) surfaces. For consistency with our other results shown in pressure levels, we vertically interpolated this sPV threshold from theta level to pressure level (linear interpolation from log theta to log pressure) and applied it to the daily level 2 ozone from MLS and daily level 2 sPV from DMP. The monthly mean polar vortex coverage at each grid point on the MLS level 3 grid (with $4^\circ \times 5^\circ$ horizontal resolution) is averaged using daily vortex coverage, defined as the fraction of sPV in each grid box that meets the vortex threshold⁵⁶ against the total number of MLS overpasses in that grid box every day. Similarly, for vortex averaged ozone, we only average MLS level 2 observed ozone (weighted by cosine latitude) when its associated sPV (from the DMP) meets the vortex threshold (Z. D. Lawrence et al., 2018) on a daily-basis in each grid box for every month.

6.3 Results

6.3.1 Observed and model-simulated ozone trends

We compare observed and simulated month-height trend patterns over 2005 to 2018 for Antarctic ozone, spatially averaged over 66–82 °S (Figure 6.1). Observations are from MLS (Waters et al., 2006). Model results are from two different sources: 1) the multi-model ensemble mean computed using one run of each of the 19 models that participated in the CCMI-1 (Morgenstern et al., 2017); and 2) the single-model ensemble of 10 different realizations of WACCM (Garcia et al., 2017; Marsh et al., 2013). The WACCM (and some models in the CCMI) ensemble comprises free-running coupled ocean-atmosphere simulations forced by time-evolving changes in GHG and ODS, referred to as the “refC2” scenario (described in detail in the Methods section). We mainly focus on ozone trends from 2005 to

2018 (results covering longer periods are also considered below) to avoid recent exceptional events that are not represented in these models, including the 2019 sudden stratospheric warming (SSW; Wargan, Weir, Manney, Cohn, and Livesey, 2020) and post-2020 wildfire and volcanic eruption mentioned earlier (note that the 2015 Calbuco eruption is also not generally simulated in these models but is included in our trend analysis). Time series used for calculating trends are presented for illustration for four selected months and heights in Figure 6.1a,b,f,g; the expected post-2018 differences between observations and simulations are marked with dashed lines (in later figures as well).

Compared to the single real-world realization provided by MLS, the modeled mean trends in WACCM and CCMI have smaller amplitudes (Figure 6.1c,d,e). This is partly due to the fact that the model ensemble means are averages over many different realizations with varying phasing of internal variability (which is uncorrelated, except by chance) superimposed on the forced response. For comparison, Appendix Figure 6.5 shows the ozone trends in 2005–2018 from individual WACCM realizations and CCMI model runs. Some individual members display month-height trend patterns that are more similar to MLS while others are less similar, reflecting differences in the phasing of internal variability. Nonetheless, nearly all realizations preserve some common features, reflecting the “fingerprint” of GHG and ODS forcings on ozone trends.

Increases in lower stratospheric ozone (at altitudes below the pressure level of \sim 30 hPa) during the austral spring are mainly due to the reduction in ODS concentrations (Laube & Tegtmeier, 2022), leading to less heterogeneous ozone loss (S. Solomon et al., 1986). The seasonal signature of the ozone hole in August–December is apparent in this region. Increases in upper stratospheric ozone (above \sim 10 hPa) are partly due to cooling caused by increasing GHGs (mainly CO₂; Manabe and Wetherald, 1967) and its effect on temperature-dependent ozone photochemistry (Haigh & Pyle, 1982). They are also partly due to less reactive chlorine, through its effect on the ClO+O reaction that peaks near 40 km (Molina and Rowland, 1974; also see Appendix Figure 6.6). In the descending circulation of the polar winter, the increased

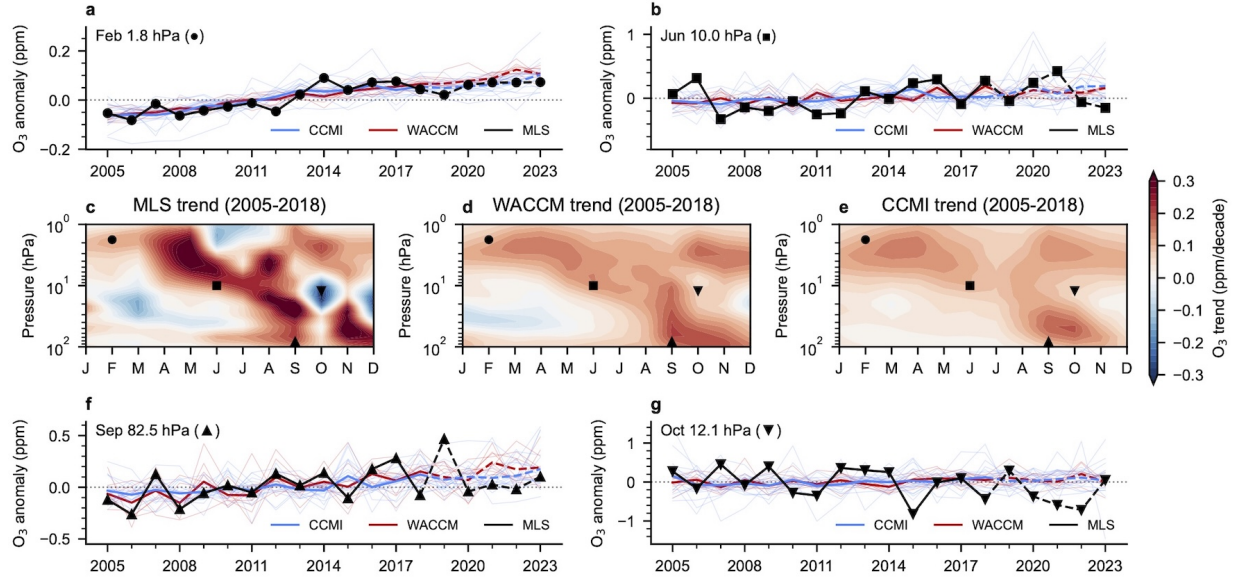


Figure 6.1: Month-height patterns of ozone trends in observations and simulations. The middle row shows the least-squares linear trends in ozone over 2005–2018 as a function of month and pressure in the MLS observations (c), the WACCM 10-member ensemble mean (d), and the CCMI 19-model ensemble mean (e). Results are for spatial averages over 66–82 °S. We also show the time series of ozone anomalies (relative to the 2005–2018 mean) at four illustrative locations (indicated by different markers on the contour figures) in February at 1.8 hPa (a), June at 10 hPa (b), September at 82.5 hPa (f), and October at 12.1 hPa (g). Thick blue and red lines are the model ensemble means, while the thin lines are the ozone time series in individual model realizations. The black solid line is from MLS. Time series after 2018 are shown as dashed lines because of likely impacts of exceptional perturbations from the 2019 SSW, 2020 Australian wildfire, and 2022 Hunga eruption.

ozone in the upper stratosphere propagates down to the mid-stratosphere. This combined month- and height-resolved pattern characterizes the “fingerprint” of GHG and ODS forcings on Antarctic ozone changes. In this study, we define ozone recovery as statistically significant increases in ozone that display these characteristic time-space fingerprints.

6.3.2 Noise of ozone variability and ODS forcing

Signal-to-noise analyses in D&A climate studies typically use natural internal variability (“noise”) estimated from long pre-industrial control runs (Christidis & Stott, 2015; Gillett et al., 2013; Santer et al., 2022; Santer et al., 2023; J.-R. Shi et al., 2024; Stott et al., 2008; Terray et al., 2012). We rely on several noise estimates here from different WACCM scenarios (described in detail in the Methods section). Figure 6.2a,b show the month-height patterns of noise, defined as the standard deviations of ozone trends in the two separate 10-member WACCM historical and refC2 ensembles (after first removing the mean forced response). Although generated with the same physical climate model, the magnitude of noise trends in the historical and refC2 simulations exhibits notable differences. This is especially important in the austral spring in the lower stratosphere where the ozone “hole” typically occurs. The historical scenario has low GHGs and low ODSs, representing atmospheric conditions prior to the onset of large ozone losses in the 1980s. The refC2 scenario has high GHGs and high ODSs comparable to present-day conditions. This indicates that the forcing differences in the two scenarios directly affect internal noise. It is important to account for forced changes in variability when examining ozone recovery—the estimated statistical significance of the observed trends can be affected by changes in noise amplitude.

There is a striking enhancement in ozone variability under the present-day high ODS conditions in austral spring in the lower stratosphere (marked with the white dashed boxes in Figure 6.2a,b); the standard deviations in refC2 and fGHG scenarios (low GHG but high ODS) are both increased by $\sim 130\%$ compared to the historical scenario. GHG forcing alone (the fODS scenario, with low ODS but high GHG) yields a narrow spread in ozone variability

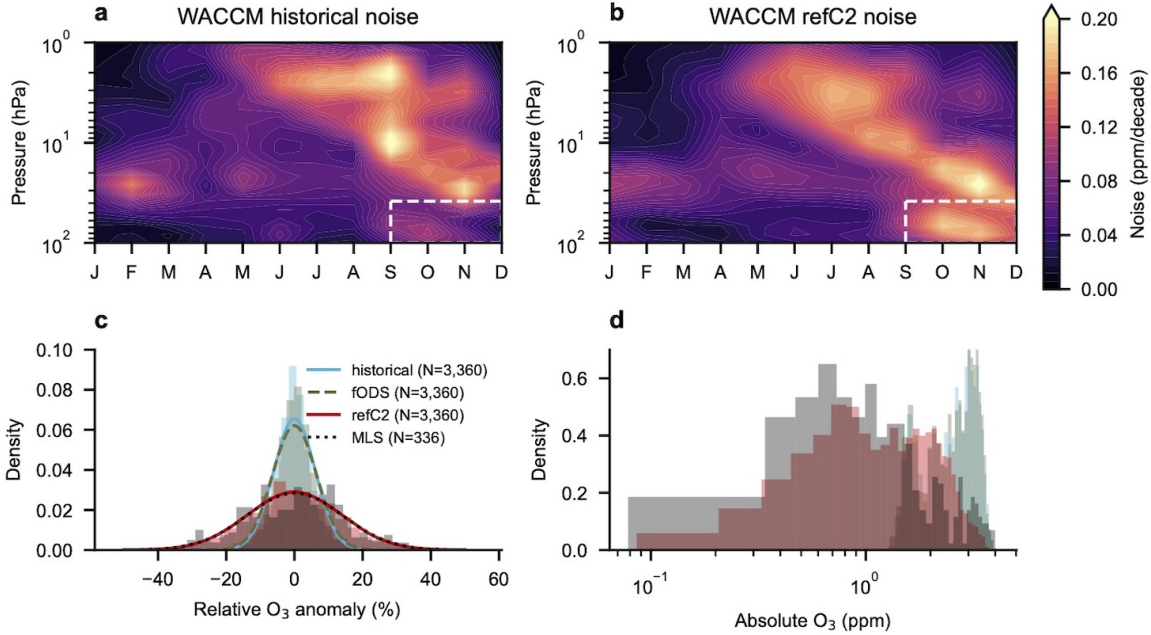


Figure 6.2: Ozone variability modulated by external forcing. Panels a, b show the month-height patterns of the standard deviation of ozone trends (averaged over 66–82 °S) in the WACCM historical and refC2 scenarios, after first removing the ensemble mean. The standard deviation is a measure of the trend uncertainty arising from internal variability among the 10 WACCM ensemble members. Both scenarios have the same trend length of 14 years: the historical scenario analysis period is from 1955 to 1968 and the refC2 analysis period is from 2005–2018. Panel c shows (for the white dashed box in the top panels), the residual internal variability in WACCM and MLS ozone after first removing the mean forced response of monthly-mean ozone. Results are expressed as percent changes relative to the MLS annual-mean climatology. The thick lines are the Gaussian fits to the distributions. Panel d displays the same data shown in panel c, but in terms of the absolute monthly ozone mixing ratios. The number of data points in each distribution is indicated in the legend. A similar figure for CCM models is shown in Appendix Figure 6.7; while the noise pattern is qualitatively similar to that of WACCM, the CCM multi-model ensemble also reflects different model responses to forcing which can inflate noise compared to a single-model ensemble.

similar to the historical case, confirming that the variability enhancement is primarily driven by ODS forcing. Such enhancement occurs because chemical ozone loss due to ODS acts in the same direction as the natural variations in ozone arising from Brewer-Dobson circulation (BDC) variability. For example, a weak BDC associated with negative ozone and negative temperature anomalies favors more heterogeneous ozone loss in the presence of high ODS, extending the lower tail of the distribution of absolute ozone concentration (S. Solomon, Portmann, Sasaki, Hofmann, and Thompson, 2005; also in Figure 6.2d) and broadening ozone variability.

For accurate analysis of the statistical significance of ozone changes, it is critical that the model-based noise is realistic. Figure 6.2c shows the distributions of monthly-mean ozone anomalies from MLS and WACCM (after first removing the mean forced response) relative to the present-day MLS climatology, in the region highlighted by the white dashed boxes in Figure 6.2a,b. The same data are displayed in Figure 6.2d in terms of absolute ozone mixing ratios. The distributions of ozone internal variability in MLS and in the refC2 scenario are virtually identical, suggesting the refC2 noise provides a credible estimate of the real-world internal variability.

6.3.3 Signal-to-noise analysis of ozone changes

Here we use model-simulated internal variability noise to assess whether the forced ozone response has emerged. This assessment is performed for individual months and heights (“local” analysis) and for the “overall” month-height pattern.

Figure 6.3d displays the local S/N ratio inferred from WACCM for a trend length of 14 years (2005 to 2018). It represents the local signal in WACCM ensemble mean (Figure 6.1d) divided by the local noise in the WACCM refC2 run (Figure 6.2b). In Figure 6.3c, the mean forced signal from WACCM is replaced by the MLS observed trend, which contains both the forced response and internal variability. A larger local S/N ratio indicates increased likelihood that the ozone trend is anthropogenically forced. Based on the WACCM S/N for the refC2

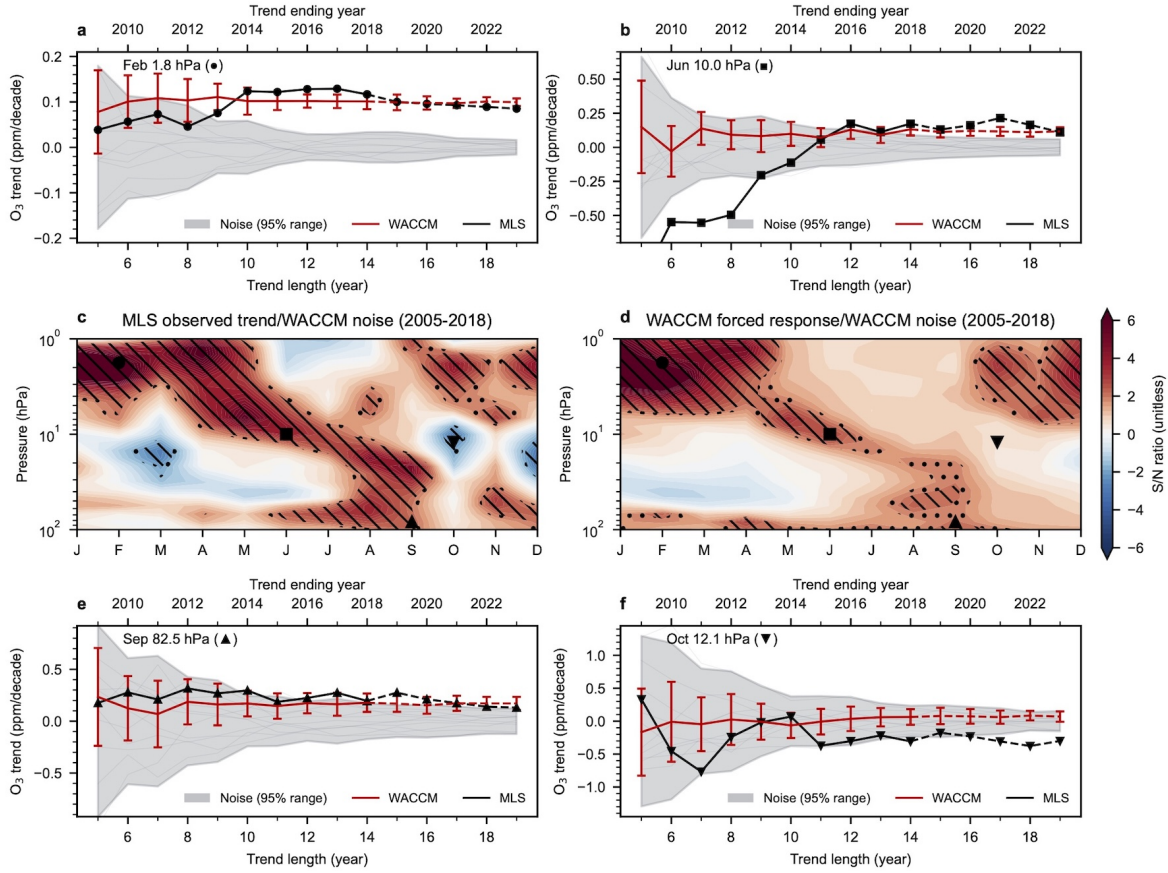


Figure 6.3: The local signal-to-noise pattern of ozone changes. The middle panels show the month-height patterns of the observed ozone trends in MLS (c) and the WACCM 10-member ensemble mean refC2 ozone trends (d) divided by the internal variability noise in refC2 trends (which are given in Figure 6.2b). Results are for trends over 2005–2018; Appendix Figure 6.9 similarly displays local S/N for trends calculated over 2005–2023. Hatched regions indicate that the local trend is significantly outside the noise at the 5 % (backslashes) and 10 % (dots) levels. The top and bottom rows (panels a, b, e, f) provide the local signal and noise as a function of trend length at the same four illustrative months/heights shown in Figure 6.1. The thin gray lines are the trends due to internal variability in each model realization, and the gray shading indicates the 95 % range of the realization spread. Thick lines are the trends from MLS (black) and the WACCM ensemble mean (red). The error bars on the red line indicate ± 1 standard deviation in the 10-member ensemble.

scenario, the beginning of ozone recovery (as a forced response to combined GHG and ODS forcing) can be detected with high confidence by 2018 in certain months and heights. In the upper stratosphere, recovery is significantly larger than internal variability in every month except during winter, when it propagates to the middle stratosphere due to polar descent. There is also a relative maximum in local S/N in September in the lower stratosphere in MLS and in the WACCM ensemble mean. The overall pattern of local S/N is similar in CCMI, but statistical significance is lower in several key regions (Appendix Figure 6.4). This is expected given that the multi-model CCMI noise does not reflect intrinsic variability alone and is larger than in the WACCM single model.

To explore the impact of the post-2018 exceptional events, we performed a local S/N analysis over a longer period (2005–2023; see Appendix Figure 6.9). The month-height local S/N pattern over 2005–2023 shows many features similar to those in Figures 6.3c,d, but also pronounced differences between WACCM and MLS, especially in the mid-stratosphere in October–December. LEs that account for the exceptional forcings (S. Solomon et al., 2016; S. Solomon et al., 2023; X. Wang et al., 2023), would be expected to provide better agreement with the observed ozone trends.

We also performed a S/N analysis using the overall month-height fingerprint pattern of Antarctic ozone trends since 2005 (see Figure 6.4). The element-wise covariance between the observed trend pattern (Figure 6.1c) and model ensemble-mean forced response (Figure 6.1d,e), at varying trend lengths, is divided by the spread of the covariance between individual noise patterns and the ensemble-mean responses (see the Methods section). Our results indicate that for the period 2005–2018, the observed time-space structure of ozone changes over Antarctica is consistent with time-evolving ODS and GHG forcing. The observed changes during this period are inconsistent with natural internal variability alone (at the 5 % significance level for the observed MLS pattern projected on both WACCM and on CCMI month-height fingerprints). Although the exceptional years in and after 2020 lower the overall S/N, MLS trends projected on WACCM results (which neglect these events), nonetheless

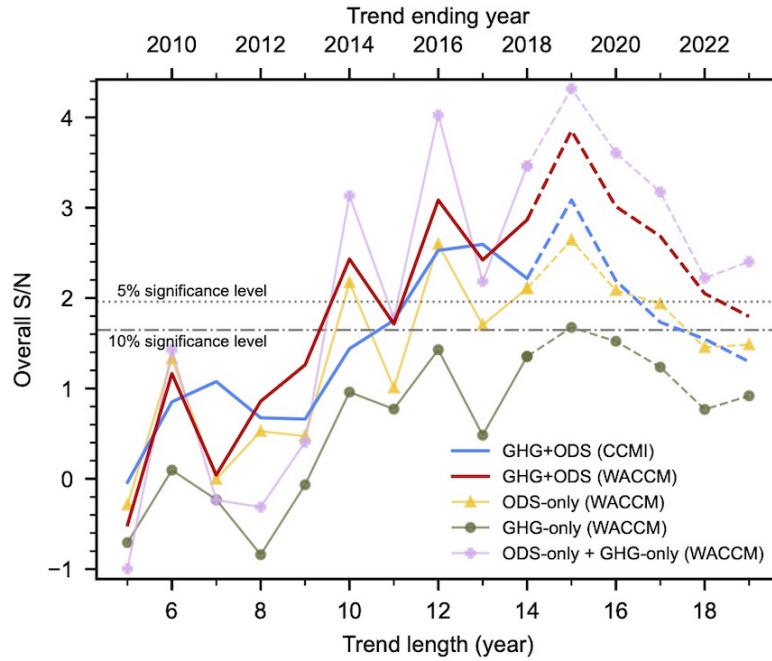


Figure 6.4: Signal-to-noise characteristics for the overall month-height fingerprint pattern. The numerator of the S/N ratio is the element-wise covariance in the overall month-height ozone trend patterns between MLS and the ensemble means of the coupled GHG+ODS runs from WACCM (red) or CCMI (blue), calculated at trend lengths ranging from 5 to 19 years. The denominator of the ratio is the standard deviation of the element-wise covariance computed between individual noise patterns and the ensemble mean responses. The observed MLS ozone trend pattern is also projected onto the ODS-only and GHG-only fingerprints from WACCM, shown in yellow and dark green lines, respectively (a linear addition of these two separate forcing results is shown in the mauve line). An overall S/N value above the gray dashed or dash-dotted lines indicates that the similarity between the observed month-height pattern and the model-predicted forced response pattern (to GHG, ODS, or combined GHG+ODS changes) is significant at the 5 % or 10 % level and is therefore unlikely to be explained by internal variability alone.

remain significant at the 10 % significance level as late as the end of 2023.

We also project the observed pattern onto the GHG-only and ODS-only runs from WACCM. Despite the fact that ozone has a nonlinear response to the coupled GHG and ODS forcing in the upper stratosphere (Haigh & Pyle, 1982), the linear addition in the covariance between MLS and the separate GHG and ODS fingerprints is close to the coupled GHG+ODS results for the entire month-height domain in our analysis (see Figure 6.4). This linear additivity enables us to estimate the relative contributions of GHG and ODS forcings in explaining the pattern similarity between observations and the coupled GHG+ODS fingerprint. The higher S/N values for the MLS trends projected onto the ODS fingerprint compared to the GHG fingerprint suggest that the observed pattern is dominated by the forced response to decreasing ODS concentrations. Compared to GHG, ODS-only forcing explains greater than 50 % more pattern covariance with MLS after 2014 (also visually illustrated in Appendix Figure 6.6). Indeed, the contribution of ODS-only forcing to the observed pattern in explaining the coupled GHG+ODS fingerprint differs significantly from internal variability noise at the 10 % (and in some years 5 %) significance level after 2014.

6.3.4 Antarctic springtime total ozone recovery

Signs of total column ozone recovery are often sought during the Antarctic spring (Chipperfield & Santee, 2022), the season when the ozone hole maximizes in depth and extent. In September, the emergence of ozone recovery occurs around 2018 both in terms of ozone at a single illustrative level (82.5 hPa) in Figure 6.3e and in terms of the TCO in Appendix Figure 6.10a, where the observed TCO is from the OMI (Levelt et al., 2006). Even with exceptionally low ozone in and after 2020, the total ozone healing signal from the satellite data is still significantly outside of the internal variability noise (at the 10 % level) in September.

A recent study raises the concern that October ozone in the mid-stratosphere has significantly decreased (Kessenich et al., 2023). However, this time and location is subject to only a small healing signal and displays substantial internal variability (see Figure 6.3d,f),

implying that trends with weak statistical significance here may well be spurious. Further, we note that because low ozone concentrations are mainly confined within the polar vortex (Schoeberl & Hartmann, 1991), vortex variations (e.g., changes in size, shape, and position) can contribute to ozone internal variability when concentrations are spatially averaged over a fixed latitude range. This is especially important for months and heights when the vortex is often asymmetric (e.g., October in the mid-stratosphere). For example, maps of ozone anomalies and vortex locations in October at 12.1 hPa (where a strong ozone decrease was reported in a recent study; Kessenich et al., 2023) in Appendix Figure 6.11 illustrate how a shift of the vortex off the pole affects how it is sampled when using spatial averages calculated with fixed latitudinal boundaries (e.g., for a simple comparison with satellite coverage). The reported large negative ozone trend in October in the mid-stratosphere (Kessenich et al., 2023) is significantly reduced when considering the vortex averaged ozone (see Appendix Figure 6.12).

The emergence of column ozone recovery in October and November due to combined ODS and GHG forcing (based on the WACCM ensemble mean signal) had been expected around 2021 under typical conditions (Appendix Figure 6.10b,c). However, the unusually low ozone years in and after 2020 may have delayed detection in the observations. This underscores the importance of maintaining a long observation record to ensure high confidence in detecting and attributing future ozone changes at this time of year.

6.4 Summary and outlook

We performed a pattern-based fingerprint analysis for Antarctic ozone recovery, analogous to fingerprinting anthropogenic climate change (Christidis & Stott, 2015; Gillett et al., 2013; Hasselmann, 1993; Santer et al., 2022; Santer et al., 2023; J.-R. Shi et al., 2024; Stott et al., 2008; Terray et al., 2012). Our S/N results for local and overall pattern similarity between MLS and single-model or multi-model ensembles provide high confidence that observed

Antarctic ozone trends are primarily responses to ODS forcing rather than natural variability.

Further, we have shown that the amplitude of lower stratospheric ozone variability is markedly enhanced in a present-day simulation relative to the amplitude of ozone variability in a “pre-ozone depletion” simulation. It is crucial to consider this modulation of internal variability when evaluating the statistical significance of ozone trends. Additionally, this enhancement in ozone variability due to ODS forcings sheds light on a potential pathway for external forcing to modulate specific modes of natural internal variability, such as the Southern Annular Mode (Thompson et al., 2011).

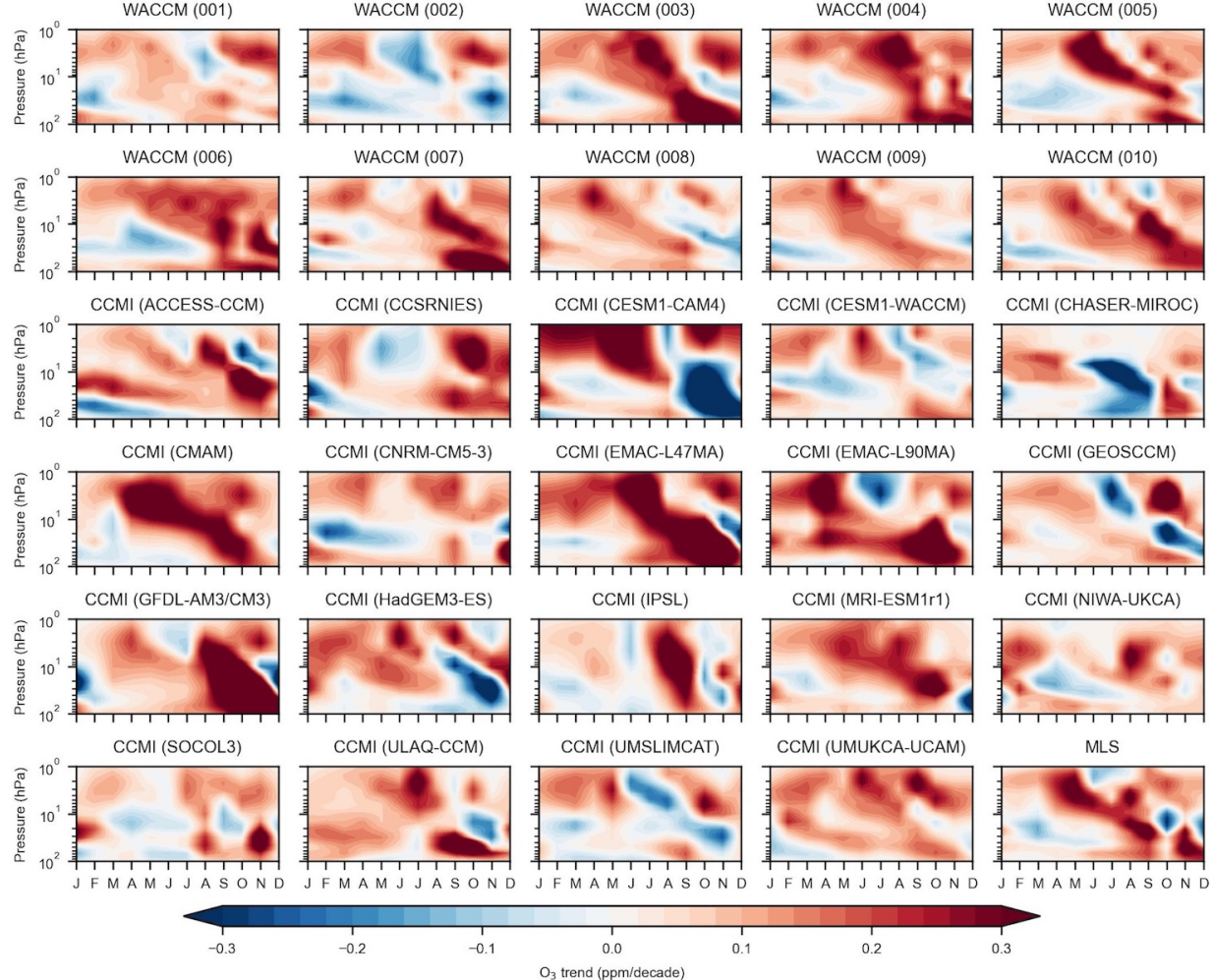
A significant ODS-driven signal of local ozone recovery in October and November has yet to emerge in the observations, likely due to the exceptionally low ozone years in and after 2020. These low ozone years are at least partly due to known volcanic and wildfire forcings not included in the available simulations. While October ozone exhibits a decreasing trend in the middle stratosphere (Kessenich et al., 2023), this negative trend is notably mitigated by adopting a different coordinate system that accounts for vortex variations.

Some caveats of the current analysis should be noted. Only one model with 10 members is examined in detail in this work. To improve confidence in the detection and attribution of forced responses versus natural variability in future ozone recovery assessments, it would be beneficial to use larger initial condition ensembles from multiple single models rather than relying on single realizations from many different models (Dhomse et al., 2018; Santer et al., 2022; Zeng et al., 2022). The forced response in this study considers GHG and ODS only, and does not include known forcings from important volcanoes and major wildfires after 2012; future ensemble runs including these forcings would likely improve consistency of the simulated and observed ozone changes. The projected long-lasting stratospheric water vapor from the Hunga eruption (Wohltmann et al., 2024; Zhou et al., 2024) or future volcanic or wildfire forcing (Chim et al., 2023; Eric Klobas, Wilmouth, Weisenstein, Anderson, & Salawitch, 2017) could reduce the future ozone recovery signal. Indeed, even the large S/N ratio we now see in the upper stratosphere could be temporarily obscured by uncertainties

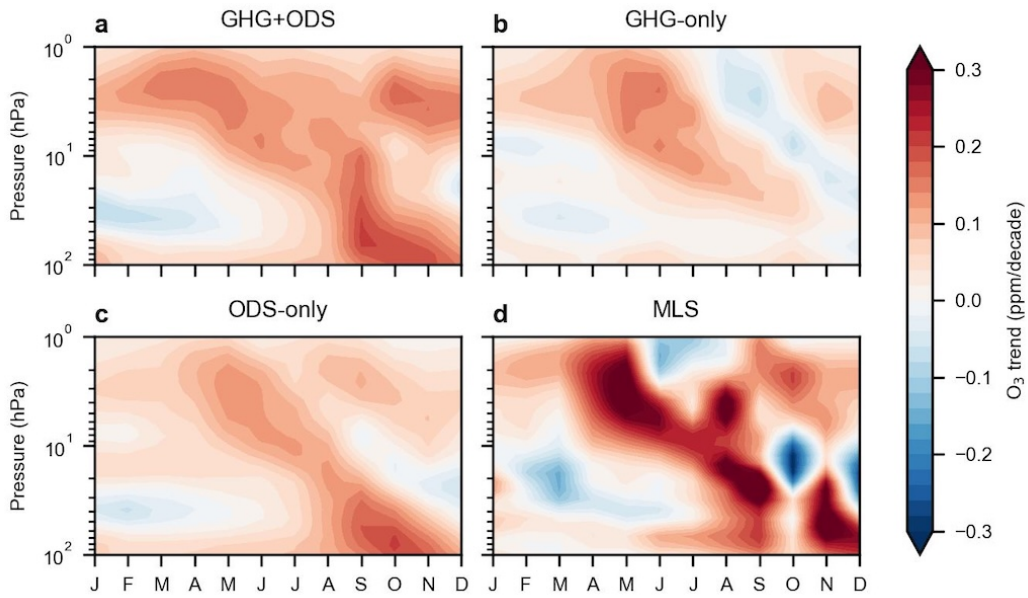
in future GHG emissions (Revell, Bodeker, Huck, Williamson, & Rozanov, 2012) and solar proton events (Stone, Solomon, & Kinnison, 2018).

Our work shows how fingerprinting and pattern similarity establish quantitative confidence that Antarctic ozone recovery has begun. It also indicates why it is crucial to maintain global height-resolved observations over extended periods to identify signal patterns that emerge from background noise, raising concerns about the impending satellite data gap in stratospheric measurements (Chipperfield & Bekki, 2024). A long observational record can ensure that estimated S/N ratios are less sensitive to short-term episodic perturbations, thereby providing high confidence in detecting and attributing trends (Santer et al., 2023).

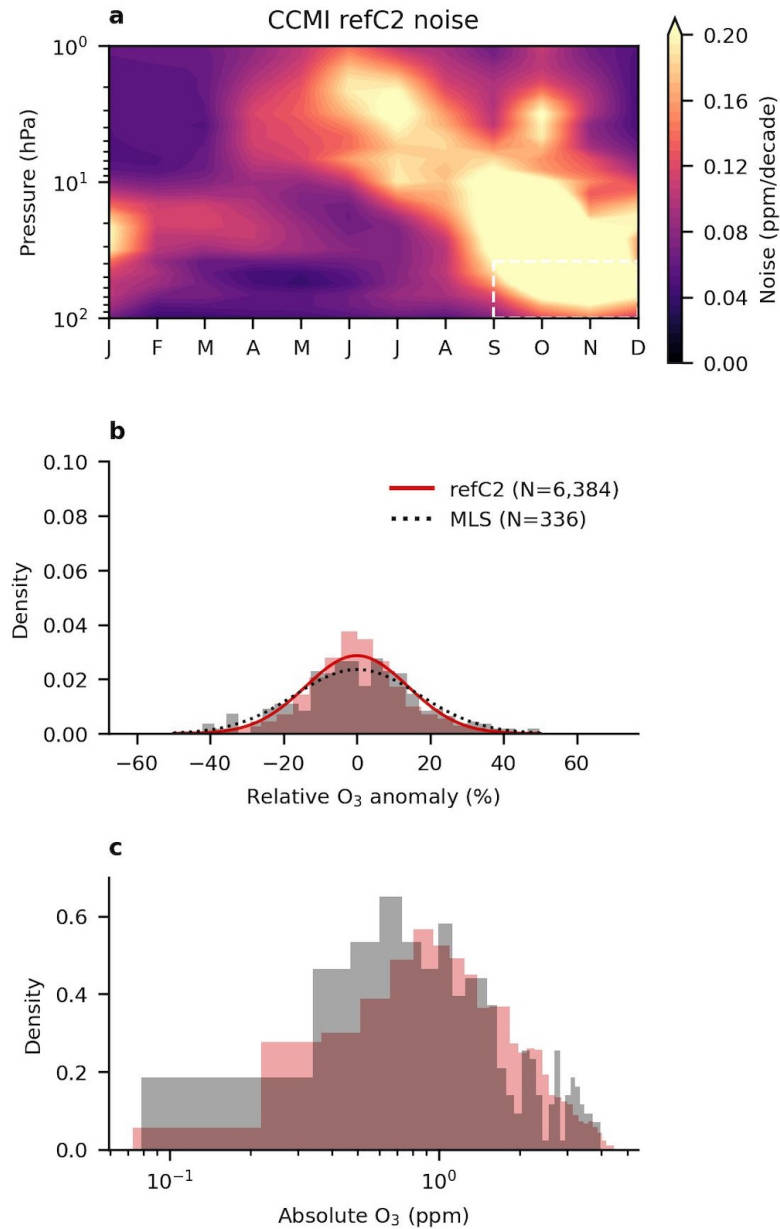
Appendix



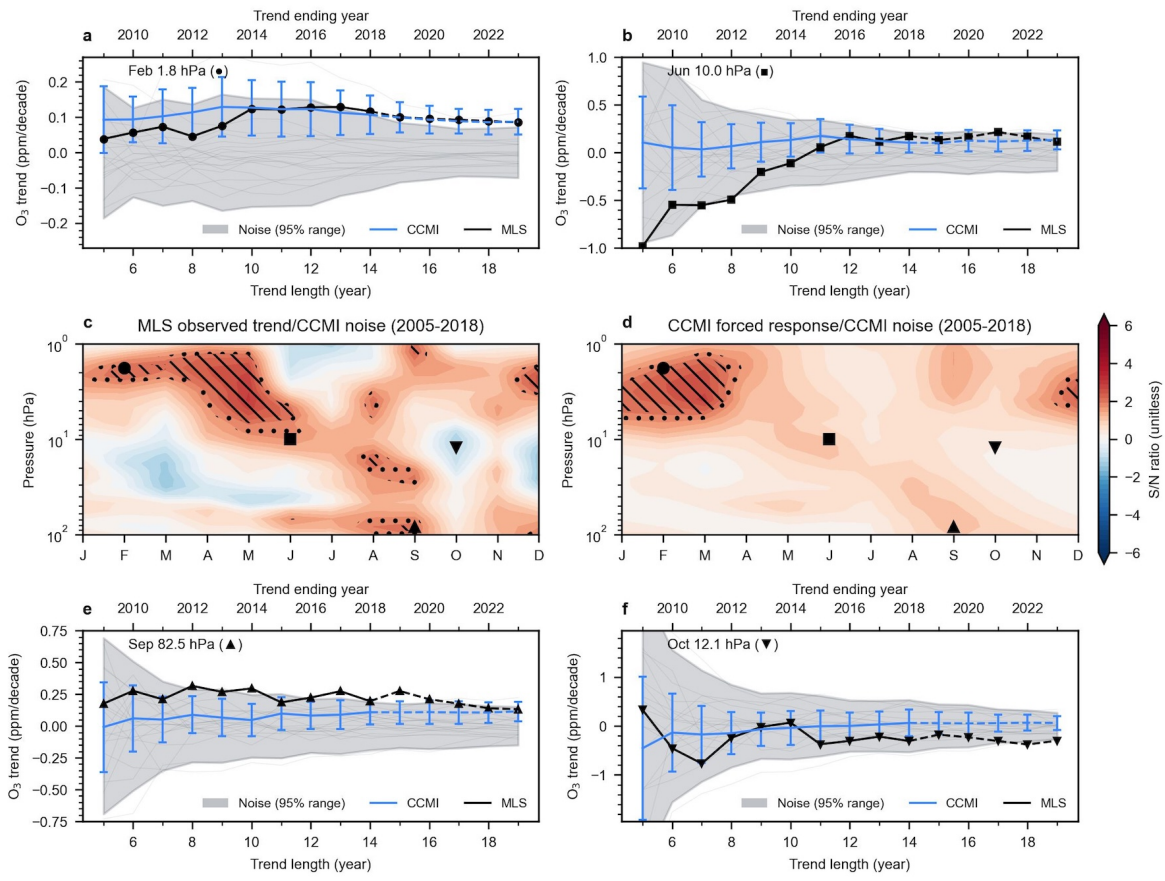
Appendix Figure 6.5: Variability superimposed on external forcing. Ozone trends from 2005–2018 in individual WACCM realizations (top two rows, with the realization number indicated in each panel’s title) and in individual models from CCMI-1 (last four rows, with model names indicated in each panel’s title) under the refC2 scenario. The MLS observed trend is shown in the bottom right panel.



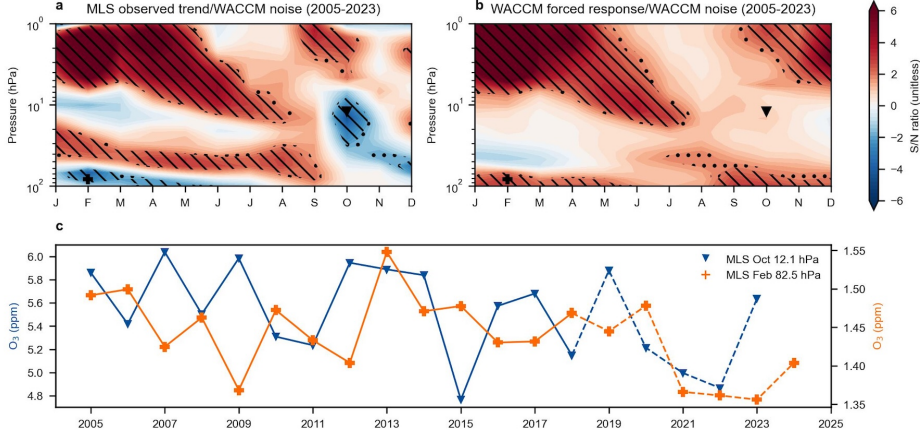
Appendix Figure 6.6: Ozone trends due to different forcings. Ensemble-mean ozone trends (2005–2018) averaged over 10 WACCM members for each scenario. Results indicate the forced responses in ozone due to: a combined time-evolving GHG and ODS forcing (refC2), b evolving GHG forcing only (fODS); and c evolving ODS forcing only (fGHG). A detailed description of each scenario is given in the Methods section. The observed ozone trend from MLS in 2005–2018 is also shown in panel d for visual comparison with forced ozone trends due to different forcings.



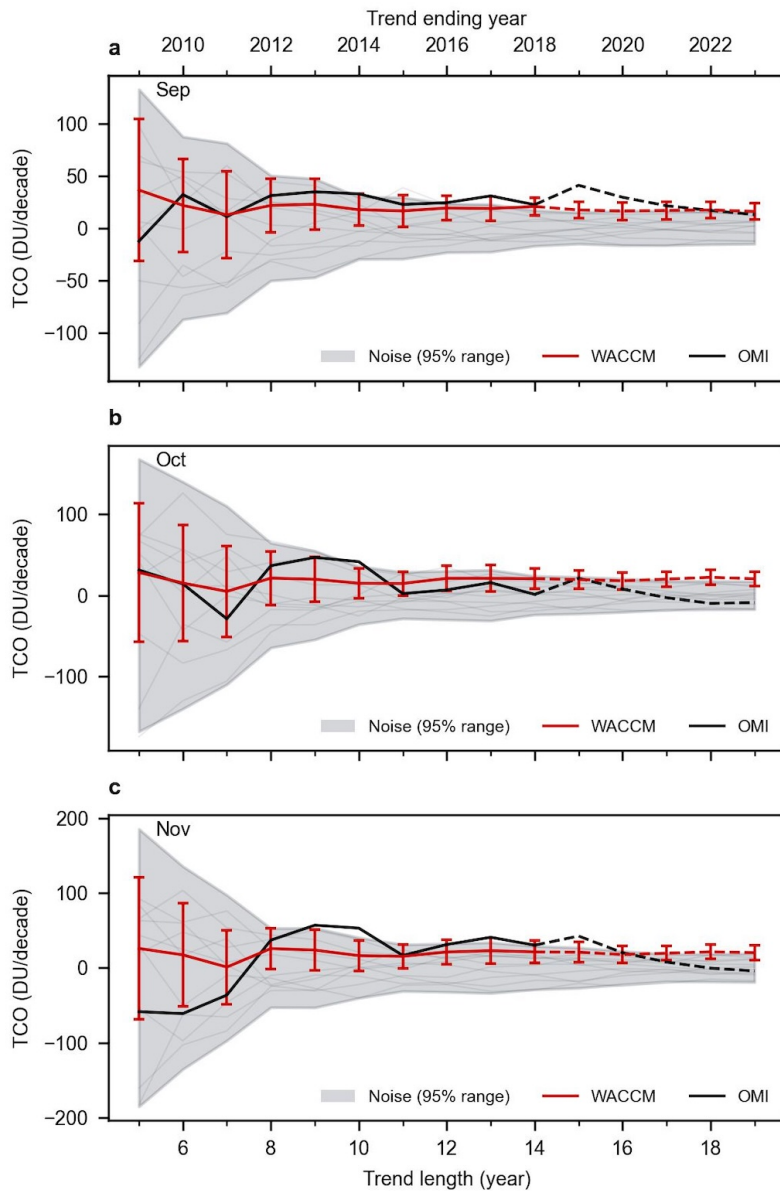
Appendix Figure 6.7: Ozone variability modulated by external forcing. Similar to Figure 6.2 but for the CCMI models. Note that the spread in ozone trends in CCMI arises not only from internal variability, but also from cross-model differences and errors (discussed in detail in the Methods section). This convolving of internal variability with model differences and errors contributes to the larger noise in panel a compared to the noise derived from the WACCM single-model refC2 ensemble in Figure 6.2b.



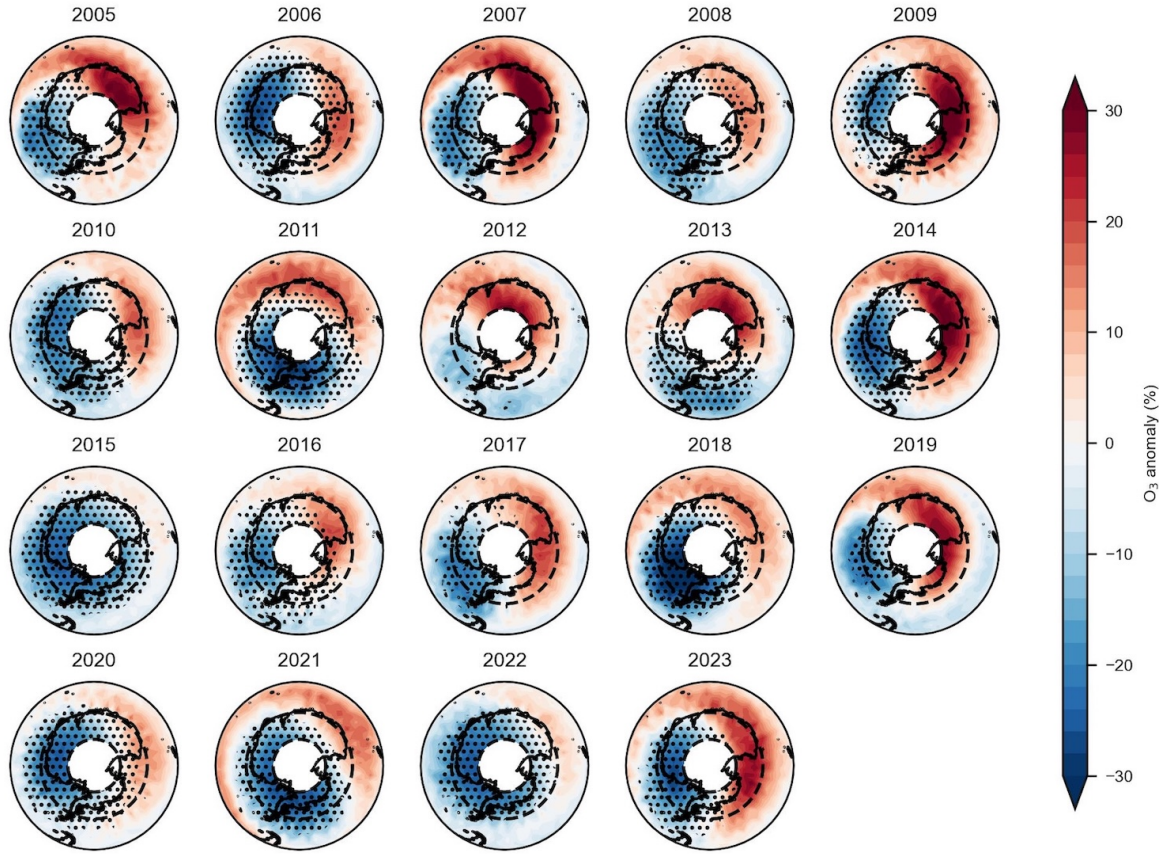
Appendix Figure 6.8: The local signal-to-noise characteristics of ozone changes. Similar to Figure 6.3 but with results for the CCM1 models.



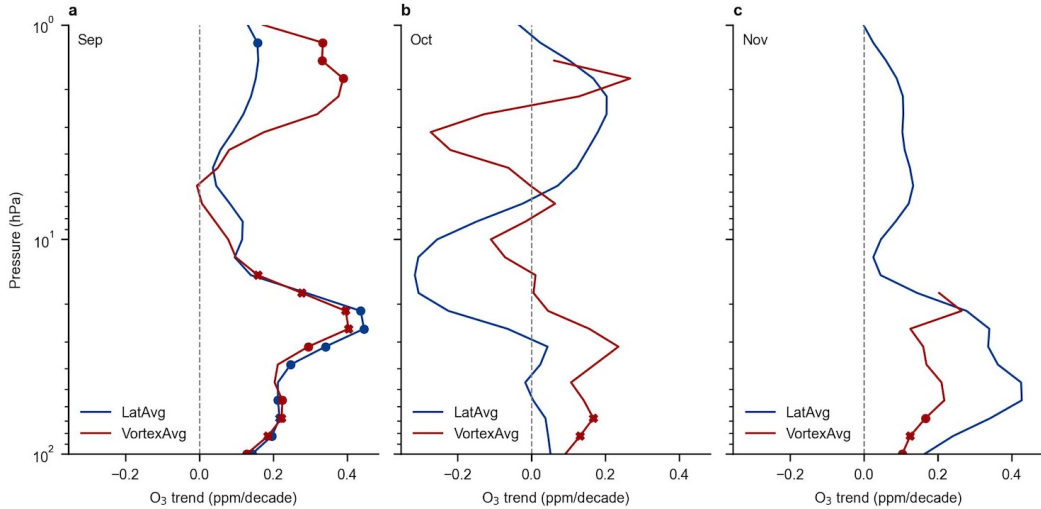
Appendix Figure 6.9: The local signal-to-noise pattern of ozone changes. Similar to Figure 6.3 but for signal and noise estimates based on ozone trends over 2005–2023 (rather than over 2005–2018). There is a significant decrease in MLS ozone in October and November in the middle stratosphere, and in January through May in the lowermost stratosphere. This raises the question of whether these two features may be linked. The bottom panel shows the timeseries of ozone mixing ratios from MLS in October at 12.1 hPa (blue) and in February at 82.5 hPa (orange). The decrease in February at 82.5 hPa is mainly due to continued low ozone after 2021 (panel c), which lags the behavior in October by about a season, suggesting that they may be linked.



Appendix Figure 6.10: Time of emergence of springtime total column ozone recovery. Similar to the top and bottom panels in Figure 6.3, except the trends are the TCO from WACCM and OMI.



Appendix Figure 6.11: Map of MLS ozone anomalies and polar vortex in October at 12.1 hPa. The color shadings indicate the ozone anomaly relative to the zonal mean in 2005–2018. Because the location of the polar vortex can vary considerably over time, dotted markers indicate that the polar vortex has occupied a given grid box for more than 25 % of the time in that month. Black dashed lines encompass the area between latitudes 66–82 °S.



Appendix Figure 6.12: MLS springtime ozone trends (2005–2018) using fixed latitude averages versus vortex averages. Monthly mean ozone trends in September, October, and November from 2005 to 2018 are shown as blue lines (where ozone is averaged across fixed latitudes between 66–82 °S) and red lines (where ozone is averaged inside the polar vortex) at different pressure levels. A detailed description of the vortex calculation is provided in the Methods section. Dots and crosses indicate trends significant at the 5 % and 10 % levels, respectively. Note that the statistical confidence in this figure is based solely on p-values from linear regression. It does not rely on internal variability noise generated by WACCM or the CCMI models, as shown in other figures.

Chapter 7

Concluding Remarks and Perspectives

The increasing importance of the ocean's role in halocarbon studies

Chapter 2 couples a simple 2-box atmospheric model with an ocean general circulation model (MITgcm) to investigate emission estimation of chlorofluorocarbons (CFC-11 and CFC-12) due to the ocean's uptake and outgassing. Emission estimates for these species often assume a constant atmospheric residence time. However, Chapter 2 demonstrates that as ocean saturation condition (affecting the amount of ocean uptake/outgassing) changes over time, it introduces a time dependency in the atmospheric residence times of CFCs thus influences emission estimations. It is worth noting that atmospheric processes also impact the residence times of these species, as variabilities in dynamic transport affect the amount of CFCs reaching altitudes where destruction occurs most efficiently (Chipperfield et al., 2014; Lickley et al., 2021; Ray et al., 2020). With a significant decline in CFC emissions, the importance of accounting for natural variability in both oceanic and atmospheric processes is rising.

Building on this modeling framework, Chapter 3 extends the analysis to assess the role of ocean processes in influencing the atmospheric residence times of hydrochlorofluorocarbons (HCFCs) and hydrofluorocarbons (HFCs). The additional hydrogen atom in these compounds gives them significantly shorter atmospheric lifetimes than CFCs, primarily due to reactions

with the hydroxyl radical (OH) in the troposphere. However, inconsistency in OH concentrations derived through various approaches (Stevenson et al., 2020) can lead to substantial uncertainty in halocarbon emission estimates. Additionally, unlike CFCs, certain HCFCs and HFCs were found to be significantly consumed by microbial activities under laboratory settings (Chang & Criddle, 1995; DeFlaun et al., 1992; Streger et al., 1999), though their degradation rates in the open ocean remain poorly understood. Chapter 3 explores a range of hypothetical atmospheric OH trends and ocean degradation rates that qualitatively represent observed uncertainties. The analysis suggests that increasing OH levels and considering ocean microbial degradations for HCFCs and HFCs would lead to shorter atmospheric residence times compared to steady-state lifetimes, indicating that emissions may be underestimated.

Compared to Chapter 2, Chapter 3 incorporates a more sophisticated 12-box atmosphere representation (Rigby et al., 2013), which better captures seasonality in atmospheric transport and the spatial distribution of OH. However, both chapters rely on a coarse-resolution version of the MITgcm ($2.8^\circ \times 2.8^\circ$ horizontal resolution and 15 vertical layers) forced by climatological fields, although Chapter 2 attempts to incorporate time-varying forcing fields to represent climate change. Future improvements could involve using higher-resolution ocean models with observed forcing fields, such as the MITgcm-ECCO (MITgcm-Estimating the Circulation and Climate of the Ocean Forget et al., 2015), to better capture observed interannual variabilities in oceanic processes. Model comparisons with ocean observations of HCFCs and HFCs are also necessary to evaluate the hypothetical ocean microbial degradation rates from Chapter 3.

Such advanced ocean representation could also be applied to estimate the ocean uptake of methyl chloroform (CH_3CCl_3), a species extensively used to infer atmospheric OH (e.g., Montzka et al., 2011; Patra et al., 2021; Rigby et al., 2017). Estimating OH concentrations is crucial for understanding methane lifetimes (e.g., Turner et al., 2017) and air quality chemistry (e.g., Levy, 1971; Singh, Kanakidou, Crutzen, and Jacob, 1995). However, significant discrepancies between OH inferred from CH_3CCl_3 and model simulations have emerged since

2005 (Stevenson et al., 2020). With the dramatic decline in anthropogenic CH₃CCl₃ emissions, questions have been raised about whether CH₃CCl₃ remains a reliable tracer for inferring OH (Nicely et al., 2020; Patra et al., 2021; Prather & Holmes, 2017). Previous studies estimating OH from CH₃CCl₃ typically subtract the air-sea flux of CH₃CCl₃ derived from the ocean model by Wennberg et al., 2004, which uses climatological forcing. While this model qualitatively reproduces observed ocean concentrations of CH₃CCl₃, it overestimates ocean uptake and does not account for interannual variability. Because CH₃CCl₃ ocean hydrolysis loss is highly temperature-dependent and occurs predominantly in tropical warm waters (Wennberg et al., 2004), the air-sea flux can exhibit strong interannual variability driven by the El Niño–Southern Oscillation (ENSO). ENSO also drives interannual variability in OH (Patra et al., 2021; Prinn et al., 2001; Prinn et al., 2005). Therefore, failing to account for variability in the ocean uptake of CH₃CCl₃ can introduce biases in the inferred OH variability. Future research leveraging reanalysis ocean to better quantify CH₃CCl₃ ocean uptake will enhance the accuracy of trends and interannual variability in the inferred OH.

New chemical mechanisms and their coupled interactions with dynamical system

The 2020 Australian New Year wildfire injected \sim 1 Tg of aerosol into the stratosphere (Peterson et al., 2021), leading to unprecedented changes in stratospheric chlorine reservoir species (e.g., HCl and ClONO₂) that have not been observed since 2004 (Bernath et al., 2022; Santee et al., 2022). Unlike stratospheric background and volcanic aerosols that primarily consist of inorganic sulfate and water, wildfire particles can contain a significant portion of organics (Murphy et al., 2021). However, the chemical processes involving organic aerosols in the stratosphere remain poorly understood, partly because only a few wildfire events since the satellite era have been large enough to inject substantial smoke particles into the stratosphere.

Leveraging high-precision satellite observations from ACE-FTS, Chapter 4 employs the

tracer-tracer method to separate changes in chlorine species caused by chemical processes. Back-trajectory calculations for individual satellite measurements are used to determine the minimum temperature each air parcel experienced. Combining this information reveals the temperature dependency of chemical chlorine activation, which has typically been measured in laboratory settings. Results from a background year in Chapter 4 show remarkable agreement with laboratory measurements (Hanson & Ravishankara, 1993; Q. Shi et al., 2001), both indicating that chlorine activation on stratospheric background aerosols generally occurs below \sim 195 K. In contrast, the 2020 Australian wildfire results suggest chlorine activation could occur at much warmer mid-latitude temperatures above \sim 220 K, which is hardly seen in the background conditions. However, because of sufficient sunlight and NO_x in the mid-latitudes, the Cl activated from HCl is rapidly converted back to ClONO₂. Chapter 5 extends this analysis to satellite records beginning in 1991, comparing chemical chlorine activation following two independent wildfire events (2009 and 2020) with a series of volcanic eruptions, including the catastrophic 1991 Pinatubo eruption. Results indicate that far fewer wildfire particles than volcanic particles are needed to achieve a similar impact on chlorine activation from HCl in the mid-latitudes.

With potential increases in future wildfire events driven by climate change (Seneviratne et al., 2021), there is an urgent need to better understand stratospheric chemistry involving wildfire particles and their coupled feedbacks with the climate. S. Solomon et al., 2023 reproduces observed changes in chlorine species and ozone by considering higher uptake coefficients of HCl based on available yet limited information. Future laboratory measurements of uptake coefficients for HCl and other halogen species combined with a deeper understanding of the organic aerosol lifecycle under stratospheric conditions will significantly enhance our knowledge of the wildfire chemistry in the stratosphere. In addition to their chemical effects, wildfire particles exhibit significant radiative heating, which impacts large-scale circulation patterns (Senf et al., 2023). The self-lofting of wildfire plumes driven by local heating may also determine the importance of different heterogeneous reactions at varying altitudes (Ma et al.,

2024). The 2020 Australian wildfire and the associated unexpected changes in stratospheric chlorine species particularly raise concern for solar geoengineering initiatives, which explore the injection of novel particles into the stratosphere (e.g., Keith, Weisenstein, Dykema, and Keutsch, 2016; Pope et al., 2012; Weisenstein, Keith, and Dykema, 2015). As these particles could lead to unintended consequences for stratospheric chemistry and result in unanticipated climate feedbacks.

Detection and attribution in global ozone recovery

The theoretical basis of “fingerprinting” has been proposed by Hasselmann, 1993. Since then, this technique has been widely used in climate change communities to robustly detect and attribute human-induced climate change signals from natural variability noise (Christidis & Stott, 2015; Gillett et al., 2013; Santer et al., 2022; Santer et al., 2023; J.-R. Shi et al., 2024; Stott et al., 2008; Terray et al., 2012). Chapter 6 uses such fingerprinting technique to investigate Antarctic ozone recovery by analyzing the signals from greenhouse gas (GHG) and ozone-depleting substance (ODS) forcings along with the noise from internal climate variability.

Spatial patterns are typically fingerprinted in climate variables. However, chemical species like ozone strongly depend on solar radiation, temperature, and dynamic transport. Therefore, analyzing ozone fingerprints across month and height dimensions can be especially helpful in distinguishing patterns due to different forcings. Ozone levels in the Antarctic upper stratosphere increase due to both rising GHG concentrations and declining ODS levels. This signal propagates down to the middle stratosphere during the polar winter, driven by strong mesospheric descent. Additionally, decreasing ODS contributes to ozone increase in the lower stratosphere during springtime. Together, these month-height ozone responses create distinctive “fingerprints” of Antarctic ozone due to different forcings. The results in Chapter 6 quantitatively demonstrate that the observed month-height trend pattern in Antarctic ozone is significantly driven by declining ODS emissions, and that this observed change is unlikely

to result from internal climate variability alone.

In the tropics and mid-latitudes, upper stratospheric ozone has shown a clear increase since the 2000s, while lower stratospheric ozone exhibits slight decreases (Hassler & Young, 2022). Determining whether these observed changes fall within the range of internal climate variability or result from missing forcings (e.g., illicit or exempted feedstock emissions) is crucial for safeguarding the Montreal Protocol. However, a better understanding and representation of the Quasi-Biennial Oscillation (QBO) and Brewer-Dobson circulation (BDC) in chemistry-climate models is needed to address this question. The models used in Chapter 6 employ a fixed QBO, which may underestimate internal climate variability and the seasonal phase-lock, particularly in the tropics and mid-latitudes. Additionally, compared to observations, current models show opposing trends in the upper branch of the BDC (Abalos et al., 2021; Garny & Hendon, 2022), which may affect the direct transport and chemistry associated with transport of ozone and chlorine species.

Chapter 6 also touches on a long-standing question in the climate detection and attribution field: whether external forcings can modulate specific modes of internal climate variability. Changes in internal variability have profound implications for the frequency and severity of extreme events such as floods, wildfires, and terrestrial and marine heatwaves. However, exploring the potential modulations in climate internal variability through coupled chemistry-climate interactions has been limited due to the high computational demands of running large model ensemble simulations with interactive chemistry (Deser et al., 2020). The results in Chapter 6 suggests that elevated ODS forcing in the present day has significantly amplified ozone internal variability, which may, in turn, influence the frequency and intensity of the Southern Annular Mode. This result highlights the need for further research to investigate the role of chemistry-climate interactions in modulating internal climate variability. Such efforts will deepen our understanding of the complex and intricate climate system.

Appendix A

Non-Local Parameterization of Atmospheric Subgrid Processes With Neural Networks

Abstract

Subgrid processes in global climate models are represented by parameterizations which are a major source of uncertainties in simulations of climate. In recent years, it has been suggested that machine-learning (ML) parameterizations based on high-resolution model output data could be superior to traditional parameterizations. Currently, both traditional and ML parameterizations of subgrid processes in the atmosphere are based on a single-column approach, which only use information from single atmospheric columns. However, single-column parameterizations might not be ideal since certain atmospheric phenomena, such as

This appendix chapter is my second generals project, supervised by Paul A. O'Gorman; only the abstract is shown here. See Wang, P., Yuval, J., & O'Gorman, P. A. (2022). Non-Local Parameterization of Atmospheric Subgrid Processes With Neural Networks. *Journal of Advances in Modeling Earth Systems*, 14(10), e2022MS002984. <https://doi.org/10.1029/2022MS002984> for the full paper.

organized convective systems, can cross multiple grid boxes and involve slantwise circulations that are not purely vertical. Here we train neural networks (NNs) using non-local inputs spanning over 3×3 columns of inputs. We find that including the non-local inputs improves the offline prediction of a range of subgrid processes. The improvement is especially notable for subgrid momentum transport and for atmospheric conditions associated with mid-latitude fronts and convective instability. Using an interpretability method, we find that the NN improvements partly rely on using the horizontal wind divergence, and we further show that including the divergence or vertical velocity as a separate input substantially improves offline performance. However, non-local winds continue to be useful inputs for parameterizing subgrid momentum transport even when the vertical velocity is included as an input. Overall, our results imply that the use of non-local variables and the vertical velocity as inputs could improve the performance of ML parameterizations, and the use of these inputs should be tested in online simulations in future work.

References

- Abalos, M., Calvo, N., Benito-Barca, S., Garny, H., Hardiman, S. C., Lin, P., Andrews, M. B., Butchart, N., Garcia, R., Orbe, C., Saint-Martin, D., Watanabe, S., & Yoshida, K. (2021). The Brewer–Dobson circulation in CMIP6. *Atmospheric Chemistry and Physics*, 21(17), 13571–13591. <https://doi.org/10.5194/acp-21-13571-2021>
- Andersen, S. O., Gao, S., Carvalho, S., Ferris, T., Gonzalez, M., Sherman, N. J., Wei, Y., & Zaelke, D. (2021). Narrowing feedstock exemptions under the Montreal Protocol has multiple environmental benefits. *Proceedings of the National Academy of Sciences*, 118(49), e2022668118. <https://doi.org/10.1073/pnas.2022668118>
- Anderson, J. G., Weisenstein, D. K., Bowman, K. P., Homeyer, C. R., Smith, J. B., Wilmouth, D. M., Sayres, D. S., Klobas, J. E., Leroy, S. S., Dykema, J. A., & Wofsy, S. C. (2017). Stratospheric ozone over the United States in summer linked to observations of convection and temperature via chlorine and bromine catalysis. *Proceedings of the National Academy of Sciences*, 114(25), E4905–E4913. <https://doi.org/10.1073/pnas.1619318114>
- Ansmann, A., Ohneiser, K., Chudnovsky, A., Knopf, D. A., Eloranta, E. W., Villanueva, D., Seifert, P., Radenz, M., Barja, B., Zamorano, F., Jimenez, C., Engelmann, R., Baars, H., Griesche, H., Hofer, J., Althausen, D., & Wandinger, U. (2022). Ozone depletion in the Arctic and Antarctic stratosphere induced by wildfire smoke. *Atmospheric Chemistry and Physics*, 22(17), 11701–11726. <https://doi.org/10.5194/acp-22-11701-2022>

- Ansmann, A., Ohneiser, K., Mamouri, R.-E., Knopf, D. A., Veselovskii, I., Baars, H., Engelmann, R., Foth, A., Jimenez, C., Seifert, P., & Barja, B. (2021). Tropospheric and stratospheric wildfire smoke profiling with lidar: Mass, surface area, CCN, and INP retrieval. *Atmospheric Chemistry and Physics*, 21(12), 9779–9807.
<https://doi.org/10.5194/acp-21-9779-2021>
- Armour, K. C., Marshall, J., Scott, J. R., Donohoe, A., & Newsom, E. R. (2016). Southern Ocean warming delayed by circumpolar upwelling and equatorward transport. *Nature Geoscience*, 9(7), 549–554. <https://doi.org/10.1038/ngeo2731>
- Asher, E., Todt, M., Rosenlof, K., Thornberry, T., Gao, R.-S., Taha, G., Walter, P., Alvarez, S., Flynn, J., Davis, S. M., Evan, S., Brioude, J., Metzger, J.-M., Hurst, D. F., Hall, E., & Xiong, K. (2023). Unexpectedly rapid aerosol formation in the Hunga Tonga plume. *Proceedings of the National Academy of Sciences*, 120(46), e2219547120. <https://doi.org/10.1073/pnas.2219547120>
- Beismann, J.-O., & Redler, R. (2003). Model simulations of CFC uptake in North Atlantic Deep Water: Effects of parameterizations and grid resolution. *Journal of Geophysical Research: Oceans*, 108(C5). <https://doi.org/10.1029/2001JC001253>
- Belessiotis, V., Kalogirou, S. A., & Delyannis, E. (2016). Water, the Raw Material for Desalination. <https://api.semanticscholar.org/CorpusID:100323110>
- Bernath, P., McElroy, C. T., Abrams, M. C., Boone, C., Butler, M., Camy-Peyret, C., Carleer, M., Clerbaux, C., Coheur, P.-F., Colin, R., DeCola, P., DeMazière, M., Drummond, J. R., Dufour, D., Evans, W. F. J., Fast, H., Fussen, D., Gilbert, K., Jennings, D. E., ... Zou, J. (2005). Atmospheric Chemistry Experiment (ACE): Mission overview. *Geophysical Research Letters*, 32(15).
<https://doi.org/10.1029/2005GL022386>
- Bernath, P., Boone, C., & Crouse, J. (2022). Wildfire smoke destroys stratospheric ozone. *Science*, 375(6586), 1292–1295. <https://doi.org/10.1126/science.abm5611>

- Bigg, P. H. (1967). Density of water in SI units over the range 0-40°C. *British Journal of Applied Physics*, 18(4), 521. <https://doi.org/10.1088/0508-3443/18/4/315>
- Boone, C., Bernath, P., & Fromm, M. D. (2020). Pyrocumulonimbus Stratospheric Plume Injections Measured by the ACE-FTS. *Geophysical Research Letters*, 47(15), e2020GL088442. <https://doi.org/10.1029/2020GL088442>
- Boone, C., Nassar, R., Walker, K. A., Rochon, Y., McLeod, S. D., Rinsland, C. P., & Bernath, P. (2005). Retrievals for the atmospheric chemistry experiment Fourier-transform spectrometer. *Appl. Opt.*, 44(33), 7218–7231. <https://doi.org/10.1364/AO.44.007218>
- Bullister, J. L., & Weiss, R. F. (1983). Anthropogenic Chlorofluoromethanes in the Greenland and Norwegian Seas. *Science*, 221(4607), 265–268. <https://doi.org/10.1126/science.221.4607.265>
- Bullister, J. L., & Lee, B.-S. (1995). Chlorofluorocarbon-11 removal in anoxic marine waters. *Geophysical Research Letters*, 22(14), 1893–1896. <https://doi.org/10.1029/95GL01517>
- Bullister, J. L., & Warner, M. J. (2017). Atmospheric histories (1765–2022) for cfc-11, cfc-12, cfc-113, ccl4, sf6 and n2o (ncei accession 0164584). https://doi.org/10.3334/cdiac/otg.cfc_atm_hist_2015
- Burkholder, J. B., & Hodnebrog, Ø. (2022). *Scientific Assessment of Ozone Depletion: 2022 Annex: Summary of abundances, lifetimes, ODPS, REs, GWPs, and GTPs* (tech. rep. No. 278). World Meteorological Organization. Geneva, Switzerland.
- Carn, S. A., Krotkov, N. A., Fisher, B. L., & Li, C. (2022). Out of the blue: Volcanic SO₂ emissions during the 2021–2022 eruptions of Hunga Tonga—Hunga Ha’apai (Tonga). *Frontiers in Earth Science*, 10. <https://doi.org/10.3389/feart.2022.976962>
- Chang, W.-k., & Criddle, C. S. (1995). Biotransformation of HCFC-22, HCFC-142b, HCFC-123, and HFC-134a by methanotrophic mixed culture MM1. *Biodegradation*, 6(1), 1–9. <https://doi.org/10.1007/BF00702293>

- Chapman, W., & NCAR Staff. (2022). The climate data guide: Walsh and chapman northern hemisphere sea ice (W. Chapman & NCAR Staff, Eds.) [Last modified 2022-09-09]. Retrieved January 5, 2025, from <https://climatedataguide.ucar.edu/climate-data/walsh-and-chapman-northern-hemisphere-sea-ice>
- Chim, M. M., Aubry, T. J., Abraham, N. L., Marshall, L., Mulcahy, J., Walton, J., & Schmidt, A. (2023). Climate Projections Very Likely Underestimate Future Volcanic Forcing and Its Climatic Effects. *Geophysical Research Letters*, 50(12), e2023GL103743. <https://doi.org/10.1029/2023GL103743>
- Chipperfield, M. P., & Bekki, S. (2024). Opinion: Stratospheric ozone – depletion, recovery and new challenges. *Atmospheric Chemistry and Physics*, 24(4), 2783–2802. <https://doi.org/10.5194/acp-24-2783-2024>
- Chipperfield, M. P., Burton, M., Bell, W., Walsh, C. P., Blumenstock, T., Coffey, M. T., Hannigan, J. W., Mankin, W. G., Galle, B., Mellqvist, J., Mahieu, E., Zander, R., Notholt, J., Sen, B., & Toon, G. C. (1997). On the use of HF as a reference for the comparison of stratospheric observations and models. *Journal of Geophysical Research: Atmospheres*, 102(D11), 12901–12919. <https://doi.org/10.1029/96JD03964>
- Chipperfield, M. P., Lutman, E. R., Kettleborough, J. A., Pyle, J. A., & Roche, A. E. (1997). Model studies of chlorine deactivation and formation of ClONO₂ collar in the Arctic polar vortex. *Journal of Geophysical Research: Atmospheres*, 102(D1), 1467–1478. <https://doi.org/10.1029/96JD00442>
- Chipperfield, M. P., Liang, Q., Strahan, S. E., Morgenstern, O., Dhomse, S. S., Abraham, N. L., Archibald, A. T., Bekki, S., Braesicke, P., & Di Genova, G. (2014). Multimodel estimates of atmospheric lifetimes of long-lived ozone-depleting substances: Present and future. *Journal of Geophysical Research: Atmospheres*, 119(5), 2555–2573. <https://doi.org/10.1002/2013JD021097>

- Chipperfield, M. P., & Santee, M. L. (2022). *Scientific Assessment of Ozone Depletion: 2022. Chapter 4: Polar Stratospheric Ozone: Past, Present & Future* (tech. rep. No. 278). World Meteorological Organization. Geneva, Switzerland.
- Christidis, N., & Stott, P. A. (2015). Changes in the geopotential height at 500 hPa under the influence of external climatic forcings. *Geophysical Research Letters*, 42(24), 10, 798–10, 806. <https://doi.org/10.1002/2015GL066669>
- Clapp, C. E., & Anderson, J. G. (2019). Modeling the Effect of Potential Nitric Acid Removal During Convective Injection of Water Vapor Over the Central United States on the Chemical Composition of the Lower Stratosphere. *Journal of Geophysical Research: Atmospheres*, 124(16), 9743–9770. <https://doi.org/10.1029/2018JD029703>
- Cox, M. J., Schäfer, H., Nightingale, P. D., McDonald, I. R., & Murrell, J. C. (2012). Diversity of methyl halide-degrading microorganisms in oceanic and coastal waters. *FEMS Microbiology Letters*, 334(2), 111–118.
<https://doi.org/10.1111/j.1574-6968.2012.02624.x>
- D'Angelo, G., Guimond, S., Reisner, J., Peterson, D. A., & Dubey, M. (2022). Contrasting Stratospheric Smoke Mass and Lifetime From 2017 Canadian and 2019/2020 Australian Megafires: Global Simulations and Satellite Observations. *Journal of Geophysical Research: Atmospheres*, 127(10), e2021JD036249.
<https://doi.org/10.1029/2021JD036249>
- Daniel, J. S., & Reimann, S. (2022). *Scientific Assessment of Ozone Depletion: 2022. Chapter 7: Scenarios and Information for Policymakers* (tech. rep. No. 278). World Meteorological Organization. Geneva, Switzerland.
- DeFlaun, M. F., Ensley, B. D., & Steffan, R. J. (1992). Biological Oxidation of Hydrochlorofluorocarbons (HCFCs) by a Methanotrophic Bacterium. *Bio/Technology*, 10(12), 1576–1578. <https://doi.org/10.1038/nbt1292-1576>
- Deser, C., Lehner, F., Rodgers, K. B., Ault, T., Delworth, T. L., DiNezio, P. N., Fiore, A., Frankignoul, C., Fyfe, J. C., Horton, D. E., Kay, J. E., Knutti, R., Lovenduski, N. S.,

Marotzke, J., McKinnon, K. A., Minobe, S., Randerson, J., Screen, J. A., Simpson, I. R., & Ting, M. (2020). Insights from Earth system model initial-condition large ensembles and future prospects. *Nature Climate Change*, 10(4), 277–286.
<https://doi.org/10.1038/s41558-020-0731-2>

Deshler, T., Anderson-Sprecher, R., Jäger, H., Barnes, J., Hofmann, D. J., Clemesha, B., Simonich, D., Osborn, M., Grainger, R. G., & Godin-Beekmann, S. (2006). Trends in the nonvolcanic component of stratospheric aerosol over the period 1971–2004. *Journal of Geophysical Research: Atmospheres*, 111(D1).

<https://doi.org/10.1029/2005JD006089>

Dessler, A. E., Considine, D. B., Rosenfield, J. E., Kawa, S. R., Douglass, A. R., & Russell III, J. M. (1997). Lower stratospheric chlorine partitioning during the decay of the Mt. Pinatubo aerosol cloud. *Geophysical Research Letters*, 24(13), 1623–1626.
<https://doi.org/10.1029/97GL01470>

DeVries, T., & Holzer, M. (2019). Radiocarbon and helium isotope constraints on deep ocean ventilation and mantle-³He sources. *Journal of Geophysical Research: Oceans*, 124(5), 3036–3057. <https://doi.org/10.1029/2018JC014716>

Dhomse, S. S., Feng, W., Montzka, S. A., Hossaini, R., Keeble, J., Pyle, J. A., Daniel, J. S., & Chipperfield, M. P. (2019). Delay in recovery of the Antarctic ozone hole from unexpected CFC-11 emissions. *Nature Communications*, 10(1), 5781.
<https://doi.org/10.1038/s41467-019-13717-x>

Dhomse, S. S., Kinnison, D., Chipperfield, M. P., Salawitch, R. J., Cionni, I., Hegglin, M. I., Abraham, N. L., Akiyoshi, H., Archibald, A. T., Bednarz, E. M., Bekki, S., Braesicke, P., Butchart, N., Dameris, M., Deushi, M., Frith, S., Hardiman, S. C., Hassler, B., Horowitz, L. W., ... Zeng, G. (2018). Estimates of ozone return dates from Chemistry-Climate Model Initiative simulations. *Atmospheric Chemistry and Physics*, 18(11), 8409–8438. <https://doi.org/10.5194/acp-18-8409-2018>

Dörnbrack, A. (2021). Stratospheric Mountain Waves Trailing across Northern Europe.

Journal of the Atmospheric Sciences, 78(9), 2835–2857.

<https://doi.org/10.1175/JAS-D-20-0312.1>

Dörnbrack, A., Eckermann, S. D., Williams, B. P., & Haggerty, J. (2022). Stratospheric Gravity Waves Excited by a Propagating Rossby Wave Train—A DEEPWAVE Case Study. *Journal of the Atmospheric Sciences*, 79(2), 567–591.

<https://doi.org/10.1175/JAS-D-21-0057.1>

Dörnbrack, A., Kaifler, B., Kaifler, N., Rapp, M., Wildmann, N., Garhammer, M., Ohlmann, K., Payne, J. M., Sandercock, M., & Austin, E. J. (2020). Unusual appearance of mother-of-pearl clouds above El Calafate, Argentina (50°21S, 72°16W). *Weather*, 75(12), 378–388. <https://doi.org/10.1002/wea.3863>

Dutay, J.-C., Bullister, J. L., Doney, S. C., Orr, J. C., Najjar, R., Caldeira, K., Campin, J.-M., Drange, H., Follows, M., & Gao, Y. (2002). Evaluation of ocean model ventilation with CFC-11: Comparison of 13 global ocean models. *Ocean Modelling*, 4(2), 89–120. [https://doi.org/10.1016/S1463-5003\(01\)00013-0](https://doi.org/10.1016/S1463-5003(01)00013-0)

Dworkin, M., Falkow, S., Rosenberg, E., Schleifer, K.-H., & Stackebrandt, E. (2006, October). *The Prokaryotes* (3rd ed., Vol. 5). Springer New York, NY. [10.1007/0-387-30745-1](https://doi.org/10.1007/0-387-30745-1)

Engel, A., & Rigby, M. (2019, February). Chapter 1: Update on ozone depleting substances (odss) and other gases of interest to the montreal protocol. In *Scientific assessment of ozone depletion: 2018*, (Vol. 58). World Meteorological Organization Technical Document.

England, M. H., Garçon, V., & Minster, J.-F. (1994). Chlorofluorocarbon uptake in a world ocean model: 1. Sensitivity to the surface gas forcing. *Journal of Geophysical Research: Oceans*, 99(C12), 25215–25233. <https://doi.org/10.1029/94JC02205>

Eric Klobas, J., Wilmouth, D. M., Weisenstein, D. K., Anderson, J. G., & Salawitch, R. J. (2017). Ozone depletion following future volcanic eruptions. *Geophysical Research Letters*, 44(14), 7490–7499. <https://doi.org/10.1002/2017GL073972>

- Farman, J. C., Gardiner, B. G., & Shanklin, J. D. (1985). Large losses of total ozone in Antarctica reveal seasonal ClO_x/NO_x interaction. *Nature*, 315(6016), 207–210.
<https://doi.org/10.1038/315207a0>
- Fine, R. A., Maillet, K. A., Sullivan, K. F., & Willey, D. (2001). Circulation and ventilation flux of the Pacific Ocean. *Journal of Geophysical Research: Oceans*, 106(C10), 22159–22178. <https://doi.org/10.1029/1999JC000184>
- Fleming, E. L., Newman, P. A., Liang, Q., & Daniel, J. S. (2020). The Impact of Continuing CFC-11 Emissions on Stratospheric Ozone. *Journal of Geophysical Research: Atmospheres*, 125(3), e2019JD031849.
<https://doi.org/https://doi.org/10.1029/2019JD031849>
- Forget, G., Campin, J.-M., Heimbach, P., Hill, C. N., Ponte, R. M., & Wunsch, C. (2015). ECCO version 4: An integrated framework for non-linear inverse modeling and global ocean state estimation. *Geoscientific Model Development*, 8(10), 3071–3104.
<https://doi.org/10.5194/gmd-8-3071-2015>
- Froidevaux, L., Jiang, Y. B., Lambert, A., Livesey, N. J., Read, W. G., Waters, J. W., Browell, E. V., Hair, J. W., Avery, M. A., McGee, T. J., Twigg, L. W., Sumnicht, G. K., Jucks, K. W., Margitan, J. J., Sen, B., Stachnik, R. A., Toon, G. C., Bernath, P. F., Boone, C. D., ... Wagner, P. A. (2008). Validation of Aura Microwave Limb Sounder stratospheric ozone measurements. *Journal of Geophysical Research: Atmospheres*, 113(D15). <https://doi.org/10.1029/2007JD008771>
- Garcia, R. R., Smith, A. K., Kinnison, D. E., Cámara, Á. d. l., & Murphy, D. J. (2017). Modification of the Gravity Wave Parameterization in the Whole Atmosphere Community Climate Model: Motivation and Results. *Journal of the Atmospheric Sciences*, 74(1), 275–291. <https://doi.org/10.1175/JAS-D-16-0104.1>
- Garny, H., & Hendon, H. (2022). *Scientific Assessment of Ozone Depletion: 2022. Chapter 5: Stratospheric Ozone Changes and Climate* (tech. rep. No. 278). World Meteorological Organization. Geneva, Switzerland.

- Gent, P. R., & Mcwilliams, J. C. (1990). Isopycnal Mixing in Ocean Circulation Models. *Journal of Physical Oceanography*, 20(1), 150–155.
[https://doi.org/10.1175/1520-0485\(1990\)020<0150:IMIOCM>2.0.CO;2](https://doi.org/10.1175/1520-0485(1990)020<0150:IMIOCM>2.0.CO;2)
- Gillett, N. P., Fyfe, J. C., & Parker, D. E. (2013). Attribution of observed sea level pressure trends to greenhouse gas, aerosol, and ozone changes. *Geophysical Research Letters*, 40(10), 2302–2306. <https://doi.org/10.1002/grl.50500>
- Giorgetta, M. A., Jungclaus, J., Reick, C. H., Legutke, S., Bader, J., Böttinger, M., Brovkin, V., Crueger, T., Esch, M., & Fieg, K. (2013). Climate and carbon cycle changes from 1850 to 2100 in MPI-ESM simulations for the Coupled Model Intercomparison Project phase 5. *Journal of Advances in Modeling Earth Systems*, 5(3), 572–597. <https://doi.org/10.1002/jame.20038>
- Glatthor, N., Höpfner, M., Semeniuk, K., Lupu, A., Palmer, P. I., McConnell, J. C., Kaminski, J. W., von Clarmann, T., Stiller, G. P., Funke, B., Kellmann, S., Linden, A., & Wiegele, A. (2013). The Australian bushfires of February 2009: MIPAS observations and GEM-AQ model results. *Atmospheric Chemistry and Physics*, 13(3), 1637–1658. <https://doi.org/10.5194/acp-13-1637-2013>
- Golombek, A., & Prinn, R. G. (1986). A global three-dimensional model of the circulation and chemistry of CFC13, CF2Cl2, CH3CCl3, CCl4, and N2O. *Journal of Geophysical Research: Atmospheres*, 91(D3), 3985–4001.
<https://doi.org/10.1029/JD091iD03p03985>
- Griffin, D., Walker, K. A., Wohltmann, I., Dhomse, S. S., Rex, M., Chipperfield, M. P., Feng, W., Manney, G. L., Liu, J., & Tarasick, D. (2019). Stratospheric ozone loss in the Arctic winters between 2005 and 2013 derived with ACE-FTS measurements. *Atmospheric Chemistry and Physics*, 19(1), 577–601.
<https://doi.org/10.5194/acp-19-577-2019>
- Guo, S., Bluth, G. J. S., Rose, W. I., Watson, I. M., & Prata, A. J. (2004). Re-evaluation of SO₂ release of the 15 June 1991 Pinatubo eruption using ultraviolet and infrared

satellite sensors. *Geochemistry, Geophysics, Geosystems*, 5(4).

<https://doi.org/10.1029/2003GC000654>

Haigh, J. D., & Pyle, J. A. (1982). Ozone perturbation experiments in a two-dimensional circulation model. *Quarterly Journal of the Royal Meteorological Society*, 108(457), 551–574. <https://doi.org/10.1002/qj.49710845705>

Hanson, D. R., & Ravishankara, A. R. (1993). Uptake of hydrochloric acid and hypochlorous acid onto sulfuric acid: Solubilities, diffusivities, and reaction. *The Journal of Physical Chemistry*, 97(47), 12309–12319. <https://doi.org/10.1021/j100149a035>

Hartmann, D. L., Holton, J. R., & Fu, Q. (2001). The heat balance of the tropical tropopause, cirrus, and stratospheric dehydration. *Geophysical Research Letters*, 28(10), 1969–1972. <https://doi.org/10.1029/2000GL012833>

Hasselmann, K. (1993). Optimal Fingerprints for the Detection of Time-dependent Climate Change. *Journal of Climate*, 6(10), 1957–1971.

[https://doi.org/10.1175/1520-0442\(1993\)006<1957:OFFTDO>2.0.CO;2](https://doi.org/10.1175/1520-0442(1993)006<1957:OFFTDO>2.0.CO;2)

Hassler, B., & Young, P. J. (2022). *Scientific Assessment of Ozone Depletion: 2022. Chapter 3: Update on Global Ozone: Past, Present, and Future* (tech. rep. No. 278). World Meteorological Organization. Geneva, Switzerland.

Hersbach, H., Bell, B., Berrisford, P., Hirahara, S., Horányi, A., Muñoz-Sabater, J., Nicolas, J., Peubey, C., Radu, R., Schepers, D., Simmons, A., Soci, C., Abdalla, S., Abellán, X., Balsamo, G., Bechtold, P., Biavati, G., Bidlot, J., Bonavita, M., ...

Thépaut, J.-N. (2020). The ERA5 global reanalysis. *Quarterly Journal of the Royal Meteorological Society*, 146(730), 1999–2049. <https://doi.org/10.1002/qj.3803>

Hervig, M. E., Russell III, J. M., Gordley, L. L., Daniels, J., Drayson, S. R., & Park, J. H. (1995). Aerosol effects and corrections in the Halogen Occultation Experiment. *Journal of Geophysical Research: Atmospheres*, 100(D1), 1067–1079.

<https://doi.org/10.1029/94JD02143>

- Hubert, D., Lambert, J.-C., Verhoelst, T., Granville, J., Keppens, A., Baray, J.-L., Bourassa, A. E., Cortesi, U., Degenstein, D. A., Froidevaux, L., Godin-Beekmann, S., Hoppel, K. W., Johnson, B. J., Kyrölä, E., Leblanc, T., Lichtenberg, G., Marchand, M., McElroy, C. T., Murtagh, D., ... Zawodny, J. M. (2016). Ground-based assessment of the bias and long-term stability of 14 limb and occultation ozone profile data records. *Atmospheric Measurement Techniques*, 9(6), 2497–2534. <https://doi.org/10.5194/amt-9-2497-2016>
- Huhn, O., Roether, W., Beining, P., & Rose, H. (2001). Validity limits of carbon tetrachloride as an ocean tracer. *Deep Sea Research Part I: Oceanographic Research Papers*, 48(9), 2025–2049. [https://doi.org/10.1016/S0967-0637\(01\)00004-8](https://doi.org/10.1016/S0967-0637(01)00004-8)
- IEA. (2022). *Global Energy Review: CO₂ Emissions in 2021* (tech. rep.). IEA. Paris. <https://www.iea.org/reports/global-energy-review-co2-emissions-in-2021-2>
- Ito, T., Marshall, J., & Follows, M. (2004). What controls the uptake of transient tracers in the Southern Ocean? *Global Biogeochemical Cycles*, 18(2). <https://doi.org/10.1029/2003GB002103>
- Jiang, S., Stone, P. H., & Malanotte-Rizzoli, P. (1999). An assessment of the Geophysical Fluid Dynamics Laboratory ocean model with coarse resolution: Annual-mean climatology. *Journal of Geophysical Research: Oceans*, 104(C11), 25623–25645. <https://doi.org/10.1029/1999JC900095>
- Jungclaus, J. H., Fischer, N., Haak, H., Lohmann, K., Marotzke, J., Matei, D., Mikolajewicz, U., Notz, D., & Von Storch, J. (2013). Characteristics of the ocean simulations in the Max Planck Institute Ocean Model (MPIOM) the ocean component of the MPI-Earth system model. *Journal of Advances in Modeling Earth Systems*, 5(2), 422–446. <https://doi.org/10.1002/jame.20023>
- Kawa, S. R., Newman, P. A., Lait, L. R., Schoeberl, M. R., Stimpfle, R. M., Kohn, D. W., Webster, C. R., May, R. D., Baumgardner, D., Dye, J. E., Wilson, J. C., Chan, K. R., & Loewenstein, M. (1997). Activation of chlorine in sulfate aerosol as inferred from

aircraft observations. *Journal of Geophysical Research: Atmospheres*, 102(D3), 3921–3933. <https://doi.org/10.1029/96JD01992>

Kay, J. E., Deser, C., Phillips, A., Mai, A., Hannay, C., Strand, G., Arblaster, J. M., Bates, S. C., Danabasoglu, G., Edwards, J., Holland, M., Kushner, P., Lamarque, J.-F., Lawrence, D., Lindsay, K., Middleton, A., Munoz, E., Neale, R., Oleson, K., ... Vertenstein, M. (2015). The Community Earth System Model (CESM) Large Ensemble Project: A Community Resource for Studying Climate Change in the Presence of Internal Climate Variability. *Bulletin of the American Meteorological Society*, 96(8), 1333–1349. <https://doi.org/10.1175/BAMS-D-13-00255.1>

Keith, D. W., Weisenstein, D. K., Dykema, J. A., & Keutsch, F. N. (2016). Stratospheric solar geoengineering without ozone loss. *Proceedings of the National Academy of Sciences*, 113(52), 14910–14914. <https://doi.org/10.1073/pnas.1615572113>

Kessenich, H. E., Seppälä, A., & Rodger, C. J. (2023). Potential drivers of the recent large Antarctic ozone holes. *Nature Communications*, 14(1), 7259. <https://doi.org/10.1038/s41467-023-42637-0>

Kinnison, D. E., Grant, K. E., Connell, P. S., Rotman, D. A., & Wuebbles, D. J. (1994). The chemical and radiative effects of the Mount Pinatubo eruption. *Journal of Geophysical Research: Atmospheres*, 99(D12), 25705–25731. <https://doi.org/10.1029/94JD02318>

Kirchman, D. L., Morán, X. A. G., & Ducklow, H. (2009). Microbial growth in the polar oceans — role of temperature and potential impact of climate change. *Nature Reviews Microbiology*, 7(6), 451–459. <https://doi.org/10.1038/nrmicro2115>

Klekociuk, A. R., Tully, M. B., Krummel, P. B., Henderson, S. I., Smale, D., Querel, R., Nichol, S., Alexander, S. P., Fraser, P. J., & Nedoluha, G. (2022). The Antarctic ozone hole during 2020. *Journal of Southern Hemisphere Earth Systems Science*, 72(1), 19–37. [10.1071/ES21015](https://doi.org/10.1071/ES21015)

Ko, M., Newman, P. A., Reimann, S., & Strahan, S. E. (2013). *SPARC Report on the Lifetimes of Stratospheric Ozone-Deleting Substances, Their Replacements, and*

Related Species (tech. rep. No. SPARC Report No. 6). WCRP.

www.sparc-climate.org/publications/sparc-reports/

Kostov, Y., Marshall, J., Hausmann, U., Armour, K. C., Ferreira, D., & Holland, M. M. (2017). Fast and slow responses of Southern Ocean sea surface temperature to SAM in coupled climate models. *Climate Dynamics*, 48, 1595–1609.
<https://doi.org/10.1007/s00382-016-3162-z>

Krzyścin, J., & Czerwińska, A. (2024). Signs of Slowing Recovery of Antarctic Ozone Hole in Recent Late Winter–Early Spring Seasons (2020–2023). *Atmosphere*, 15(1).
<https://doi.org/10.3390/atmos15010080>

Laube, J. C., & Tegtmeier, S. (2022). *Scientific Assessment of Ozone Depletion: 2022. Chapter 1: Update on Ozone-Depleting Substances (ODSs) and Other Gases of Interest to the Montreal Protocol* (tech. rep. No. 278). World Meteorological Organization. Geneva, Switzerland.

Lawrence, J. R., Glass, S. V., Park, S.-C., & Nathanson, G. M. (2005). Surfactant Control of Gas Uptake: Effect of Butanol Films on HCl and HBr Entry into Supercooled Sulfuric Acid. *The Journal of Physical Chemistry A*, 109(33), 7458–7465.

<https://doi.org/10.1021/jp0500438>

Lawrence, Z. D., Manney, G. L., & Wargan, K. (2018). Reanalysis intercomparisons of stratospheric polar processing diagnostics. *Atmospheric Chemistry and Physics*, 18(18), 13547–13579. <https://doi.org/10.5194/acp-18-13547-2018>

Levelt, P., van den Oord, G., Dobber, M., Malkki, A., Visser, H., Vries, J. d., Stammes, P., Lundell, J., & Saari, H. (2006). The ozone monitoring instrument. *IEEE Transactions on Geoscience and Remote Sensing*, 44(5), 1093–1101.
<https://doi.org/10.1109/TGRS.2006.872333>

Levitus, S., Burgett, R., & Boyer, T. P. (1994a, April). *World ocean atlas 1994, Vol. 3: Salinity* (tech. rep.). NOAA Atlas NESDIS. Washington, D. C.

- Levitus, S., Burgett, R., & Boyer, T. P. (1994b, April). *World ocean atlas 1994, Vol. 4: Temperature* (tech. rep.). NOAA Atlas NESDIS. Washington, D. C.
- Levy, H. (1971). Normal Atmosphere: Large Radical and Formaldehyde Concentrations Predicted. *Science*, 173(3992), 141–143. <https://doi.org/10.1126/science.173.3992.141>
- Li, C., Peng, Y., Asher, E., Baron, A. A., Todt, M., Thornberry, T. D., Evan, S., Brioude, J., Smale, P., Querel, R., Rosenlof, K. H., Zhou, L., Xu, J., Qie, K., Bian, J., Toon, O. B., Zhu, Y., & Yu, P. (2024). Microphysical Simulation of the 2022 Hunga Volcano Eruption Using a Sectional Aerosol Model. *Geophysical Research Letters*, 51(11), e2024GL108522. <https://doi.org/10.1029/2024GL108522>
- Li, P., Mühle, J., Montzka, S. A., Oram, D. E., Miller, B. R., Weiss, R. F., Fraser, P. J., & Tanhua, T. (2019). Atmospheric histories, growth rates and solubilities in seawater and other natural waters of the potential transient tracers HCFC-22, HCFC-141b, HCFC-142b, HFC-134a, HFC-125, HFC-23, PFC-14 and PFC-116. *Ocean Science*, 15(1), 33–60. <https://doi.org/10.5194/os-15-33-2019>
- Li, P., & Tanhua, T. (2021). Medusa–Aqua system: Simultaneous measurement and evaluation of novel potential halogenated transient tracers HCFCs, HFCs, and PFCs in the ocean. *Ocean Science*, 17(2), 509–525. <https://doi.org/10.5194/os-17-509-2021>
- Li, Y. Q., Zhang, H. Z., Davidovits, P., Jayne, J. T., Kolb, C. E., & Worsnop, D. R. (2002). Uptake of HCl(g) and HBr(g) on Ethylene Glycol Surfaces as a Function of Relative Humidity and Temperature. *The Journal of Physical Chemistry A*, 106(7), 1220–1227. <https://doi.org/10.1021/jp012861f>
- Liang, Q., & Rigby, M. (2022). *Scientific Assessment of Ozone Depletion: 2022. Chapter 2: Hydrofluorocarbons (HFCs)* (tech. rep. No. 278). World Meteorological Organization. Geneva, Switzerland.
- Lickley, M., Daniel, J. S., Fleming, E. L., Reimann, S., & Solomon, S. (2022). Bayesian assessment of chlorofluorocarbon (CFC), hydrochlorofluorocarbon (HCFC) and halon

- banks suggest large reservoirs still present in old equipment. *Atmospheric Chemistry and Physics*, 22(17), 11125–11136. <https://doi.org/10.5194/acp-22-11125-2022>
- Lickley, M., Solomon, S., Fletcher, S., Velders, G. J., Daniel, J., Rigby, M., Montzka, S. A., Kuijpers, L. J., & Stone, K. (2020). Quantifying contributions of chlorofluorocarbon banks to emissions and impacts on the ozone layer and climate. *Nature communications*, 11(1), 1380. <https://doi.org/10.1038/s41467-020-15162-7>
- Lickley, M., Solomon, S., Kinnison, D., Krummel, P., Mühle, J., O'Doherty, S., Prinn, R., Rigby, M., Stone, K. A., Wang, P., Weiss, R., & Young, D. (2021). Quantifying the Imprints of Stratospheric Contributions to Interhemispheric Differences in Tropospheric CFC-11, CFC-12, and N₂O Abundances. *Geophysical Research Letters*, 48(15), e2021GL093700. <https://doi.org/10.1029/2021GL093700>
- Livesey, N. J., Read, W. G., Froidevaux, L., Lambert, A., Santee, M. L., Schwartz, M. J., Millán, L., Jarnot, R. F., Wagner, P. A., Hurst, D. F., Walker, K. A., Sheese, P. E., & Nedoluha, G. E. (2021). Investigation and amelioration of long-term instrumental drifts in water vapor and nitrous oxide measurements from the Aura Microwave Limb Sounder (MLS) and their implications for studies of variability and trends. *Atmospheric Chemistry and Physics*, 21(20), 15409–15430.
<https://doi.org/10.5194/acp-21-15409-2021>
- Lovenduski, N. S., & Gruber, N. (2005). Impact of the Southern Annular Mode on Southern Ocean circulation and biology. *Geophysical Research Letters*, 32(11).
<https://doi.org/10.1029/2005GL022727>
- Ma, C., Su, H., Lelieveld, J., Randel, W., Yu, P., Andreae, M. O., & Cheng, Y. (2024). Smoke-charged vortex doubles hemispheric aerosol in the middle stratosphere and buffers ozone depletion. *Science Advances*, 10(28), eadn3657.
<https://doi.org/10.1126/sciadv.adn3657>

- Manabe, S., & Wetherald, R. T. (1967). Thermal Equilibrium of the Atmosphere with a Given Distribution of Relative Humidity. *Journal of Atmospheric Sciences*, 24(3), 241–259. [https://doi.org/10.1175/1520-0469\(1967\)024<0241:TEOTAW>2.0.CO;2](https://doi.org/10.1175/1520-0469(1967)024<0241:TEOTAW>2.0.CO;2)
- Manney, G. L., Hegglin, M. I., Daffer, W. H., Santee, M. L., Ray, E. A., Pawson, S., Schwartz, M. J., Boone, C. D., Froidevaux, L., Livesey, N. J., Read, W. G., & Walker, K. A. (2011). Jet characterization in the upper troposphere/lower stratosphere (UTLS): Applications to climatology and transport studies. *Atmospheric Chemistry and Physics*, 11(12), 6115–6137. <https://doi.org/10.5194/acp-11-6115-2011>
- Manney, G. L., Daffer, W. H., Zawodny, J. M., Bernath, P. F., Hoppel, K. W., Walker, K. A., Knosp, B. W., Boone, C., Remsberg, E. E., Santee, M. L., Harvey, V. L., Pawson, S., Jackson, D. R., Deaver, L., McElroy, C. T., McLinden, C. A., Drummond, J. R., Pumphrey, H. C., Lambert, A., … Waters, J. W. (2007). Solar occultation satellite data and derived meteorological products: Sampling issues and comparisons with Aura Microwave Limb Sounder. *Journal of Geophysical Research: Atmospheres*, 112(D24). <https://doi.org/10.1029/2007JD008709>
- Manney, G. L., Santee, M. L., Lambert, A., Millán, L., Minschwaner, K., Werner, F., Lawrence, Z. D., Read, W. G., Livesey, N. J., & Wang, T. (2023). Siege in the Southern Stratosphere: Hunga Tonga-Hunga Ha’apai Water Vapor Excluded From the 2022 Antarctic Polar Vortex. *Geophysical Research Letters*, 50(14), e2023GL103855. <https://doi.org/10.1029/2023GL103855>
- Marsh, D. R., Mills, M. J., Kinnison, D. E., Lamarque, J.-F., Calvo, N., & Polvani, L. M. (2013). Climate Change from 1850 to 2005 Simulated in CESM1(WACCM). *Journal of Climate*, 26(19), 7372–7391. <https://doi.org/10.1175/JCLI-D-12-00558.1>
- Marshall, J., Adcroft, A., Hill, C., Perelman, L., & Heisey, C. (1997). A finite-volume, incompressible Navier Stokes model for studies of the ocean on parallel computers. *Journal of Geophysical Research: Oceans*, 102(C3), 5753–5766. <https://doi.org/10.1029/96JC02775>

- Marshall, J., Hill, C., Perelman, L., & Adcroft, A. (1997). Hydrostatic, quasi-hydrostatic, and nonhydrostatic ocean modeling. *Journal of Geophysical Research: Oceans*, 102(C3), 5733–5752. <https://doi.org/10.1029/96JC02776>
- Marshall, J., Scott, J. R., Armour, K. C., Campin, J.-M., Kelley, M., & Romanou, A. (2015). The ocean's role in the transient response of climate to abrupt greenhouse gas forcing. *Climate Dynamics*, 44, 2287–2299. <https://doi.org/10.1007/s00382-014-2308-0>
- McCormick, M. P., Steele, H. M., Hamill, P., Chu, W. P., & Swissler, T. J. (1982). Polar Stratospheric Cloud Sightings by SAM II. *Journal of Atmospheric Sciences*, 39(6), 1387–1397. [https://doi.org/10.1175/1520-0469\(1982\)039<1387:PSCSBS>2.0.CO;2](https://doi.org/10.1175/1520-0469(1982)039<1387:PSCSBS>2.0.CO;2)
- McHugh, M., Magill, B., Walker, K. A., Boone, C. D., Bernath, P. F., & Russell III, J. M. (2005). Comparison of atmospheric retrievals from ACE and HALOE. *Geophysical Research Letters*, 32(15). <https://doi.org/10.1029/2005GL022403>
- Meinshausen, M., Smith, S. J., Calvin, K., Daniel, J. S., Kainuma, M. L. T., Lamarque, J.-F., Matsumoto, K., Montzka, S. A., Raper, S. C. B., Riahi, K., Thomson, A., Velders, G. J. M., & van Vuuren, D. P. (2011). The RCP greenhouse gas concentrations and their extensions from 1765 to 2300. *Climatic Change*, 109(1), 213. <https://doi.org/10.1007/s10584-011-0156-z>
- Millán, L., Manney, G. L., Boenisch, H., Hegglin, M. I., Hoor, P., Kunkel, D., Leblanc, T., Petropavlovskikh, I., Walker, K., Wargan, K., & Zahn, A. (2023). Multi-parameter dynamical diagnostics for upper tropospheric and lower stratospheric studies. *Atmospheric Measurement Techniques*, 16(11), 2957–2988. <https://doi.org/10.5194/amt-16-2957-2023>
- Millán, L., Santee, M. L., Lambert, A., Livesey, N. J., Werner, F., Schwartz, M. J., Pumphrey, H. C., Manney, G. L., Wang, Y., Su, H., Wu, L., Read, W. G., & Froidevaux, L. (2022). The Hunga Tonga-Hunga Ha'apai Hydration of the Stratosphere. *Geophysical Research Letters*, 49(13), e2022GL099381. <https://doi.org/10.1029/2022GL099381>

- Miller, B. R., Rigby, M., Kuijpers, L. J. M., Krummel, P. B., Steele, L. P., Leist, M., Fraser, P. J., McCulloch, A., Harth, C., Salameh, P., Mühle, J., Weiss, R. F., Prinn, R. G., Wang, R. H. J., O'Doherty, S., Greally, B. R., & Simmonds, P. G. (2010). HFC-23 (CHF) emission trend response to HCFC-22 (CHClF) production and recent HFC-23 emission abatement measures. *Atmospheric Chemistry and Physics*, 10(16), 7875–7890. <https://doi.org/10.5194/acp-10-7875-2010>
- Millero, F. J., & Poisson, A. (1981). International one-atmosphere equation of state of seawater. *Deep Sea Research Part A. Oceanographic Research Papers*, 28(6), 625–629. [https://doi.org/https://doi.org/10.1016/0198-0149\(81\)90122-9](https://doi.org/https://doi.org/10.1016/0198-0149(81)90122-9)
- Mlynczak, M. G., Mertens, C. J., Garcia, R. R., & Portmann, R. W. (1999). A detailed evaluation of the stratospheric heat budget: 2. Global radiation balance and diabatic circulations. *Journal of Geophysical Research: Atmospheres*, 104(D6), 6039–6066. <https://doi.org/10.1029/1998JD200099>
- Molina, M. J., & Rowland, F. S. (1974). Stratospheric sink for chlorofluoromethanes: Chlorine atom-catalysed destruction of ozone. *Nature*, 249(5460), 810–812. <https://doi.org/10.1038/249810a0>
- Montzka, S. A., Krol, M., Dlugokencky, E., Hall, B., Jöckel, P., & Lelieveld, J. (2011). Small Interannual Variability of Global Atmospheric Hydroxyl. *Science*, 331(6013), 67–69. <https://doi.org/10.1126/science.1197640>
- Montzka, S. A., Dutton, G. S., Yu, P., Ray, E., Portmann, R. W., Daniel, J. S., Kuijpers, L., Hall, B. D., Mondeel, D., & Siso, C. (2018). An unexpected and persistent increase in global emissions of ozone-depleting CFC-11. *Nature*, 557(7705), 413–417. <https://doi.org/10.1038/s41586-018-0106-2>
- Montzka, S. A., Dutton, G. S., Portmann, R. W., Chipperfield, M. P., Davis, S., Feng, W., Manning, A. J., Ray, E., Rigby, M., Hall, B. D., Siso, C., Nance, J. D., Krummel, P. B., Mühle, J., Young, D., O'Doherty, S., Salameh, P. K., Harth, C. M.,

- Prinn, R. G., ... Theodoridi, C. (2021). A decline in global CFC-11 emissions during 20182019. *Nature*, 590(7846), 428–432. <https://doi.org/10.1038/s41586-021-03260-5>
- Morgenstern, O., Hegglin, M. I., Rozanov, E., O'Connor, F. M., Abraham, N. L., Akiyoshi, H., Archibald, A. T., Bekki, S., Butchart, N., Chipperfield, M. P., Deushi, M., Dhomse, S. S., Garcia, R. R., Hardiman, S. C., Horowitz, L. W., Jöckel, P., Josse, B., Kinnison, D., Lin, M., ... Zeng, G. (2017). Review of the global models used within phase 1 of the Chemistry–Climate Model Initiative (CCMI). *Geoscientific Model Development*, 10(2), 639–671.
<https://doi.org/10.5194/gmd-10-639-2017>
- Murphy, D. M., Froyd, K. D., Bourgeois, I., Brock, C. A., Kupc, A., Peischl, J., Schill, G. P., Thompson, C. R., Williamson, C. J., & Yu, P. (2021). Radiative and chemical implications of the size and composition of aerosol particles in the existing or modified global stratosphere. *Atmospheric Chemistry and Physics*, 21(11), 8915–8932.
<https://doi.org/10.5194/acp-21-8915-2021>
- Murray, L. T., Fiore, A. M., Shindell, D. T., Naik, V., & Horowitz, L. W. (2021). Large uncertainties in global hydroxyl projections tied to fate of reactive nitrogen and carbon. *Proceedings of the National Academy of Sciences*, 118(43), e2115204118.
<https://doi.org/10.1073/pnas.2115204118>
- NASA/LARC/SD/ASDC. (2023, February 27). Global space-based stratospheric aerosol climatology version 2.21. <https://doi.org/10.5067/GLOSSAC-L3-V2.21>
- Newchurch, M. J., Yang, E.-S., Cunnold, D. M., Reinsel, G. C., Zawodny, J. M., & Russell III, J. M. (2003). Evidence for slowdown in stratospheric ozone loss: First stage of ozone recovery. *Journal of Geophysical Research: Atmospheres*, 108(D16).
<https://doi.org/https://doi.org/10.1029/2003JD003471>
- Nicely, J. M., Duncan, B. N., Hanisco, T. F., Wolfe, G. M., Salawitch, R. J., Deushi, M., Haslerud, A. S., Jöckel, P., Josse, B., Kinnison, D. E., Klekociuk, A., Manyin, M. E., Marécal, V., Morgenstern, O., Murray, L. T., Myhre, G., Oman, L. D., Pitari, G.,

- Pozzer, A., ... Zeng, G. (2020). A machine learning examination of hydroxyl radical differences among model simulations for CCMI-1. *Atmospheric Chemistry and Physics*, 20(3), 1341–1361. <https://doi.org/10.5194/acp-20-1341-2020>
- Ohneiser, K., Ansmann, A., Kaifler, B., Chudnovsky, A., Barja, B., Knopf, D. A., Kaifler, N., Baars, H., Seifert, P., Villanueva, D., Jimenez, C., Radenz, M., Engelmann, R., Veselovskii, I., & Zamorano, F. (2022). Australian wildfire smoke in the stratosphere: The decay phase in 2020/2021 and impact on ozone depletion. *Atmospheric Chemistry and Physics*, 22(11), 7417–7442. <https://doi.org/10.5194/acp-22-7417-2022>
- Pardini, F., Burton, M., Arzilli, F., Spina, G. L., & Polacci, M. (2018). SO₂ emissions, plume heights and magmatic processes inferred from satellite data: The 2015 Calbuco eruptions. *Journal of Volcanology and Geothermal Research*, 361, 12–24. <https://doi.org/10.1016/j.jvolgeores.2018.08.001>
- Park, S., Western, L. M., Saito, T., Redington, A. L., Henne, S., Fang, X., Prinn, R. G., Manning, A. J., Montzka, S. A., Fraser, P. J., Ganesan, A. L., Harth, C. M., Kim, J., Krummel, P. B., Liang, Q., Mühlle, J., O'Doherty, S., Park, H., Park, M.-K., ... Rigby, M. (2021). A decline in emissions of CFC-11 and related chemicals from eastern China. *Nature*, 590(7846), 433–437. <https://doi.org/10.1038/s41586-021-03277-w>
- Patra, P. K., Krol, M. C., Prinn, R. G., Takigawa, M., Mühlle, J., Montzka, S. A., Lal, S., Yamashita, Y., Naus, S., Chandra, N., Weiss, R. F., Krummel, P. B., Fraser, P. J., O'Doherty, S., & Elkins, J. W. (2021). Methyl Chloroform Continues to Constrain the Hydroxyl (OH) Variability in the Troposphere. *Journal of Geophysical Research: Atmospheres*, 126(4), e2020JD033862. <https://doi.org/10.1029/2020JD033862>
- Peterson, D. A., Fromm, M. D., McRae, R. H. D., Campbell, J. R., Hyer, E. J., Taha, G., Camacho, C. P., Kablick, G. P., Schmidt, C. C., & DeLand, M. T. (2021). Australia's Black Summer pyrocumulonimbus super outbreak reveals potential for increasingly

extreme stratospheric smoke events. *npj Climate and Atmospheric Science*, 4(1), 38.

<https://doi.org/10.1038/s41612-021-00192-9>

Pope, F. D., Braesicke, P., Grainger, R. G., Kalberer, M., Watson, I. M., Davidson, P. J., & Cox, R. A. (2012). Stratospheric aerosol particles and solar-radiation management.

Nature Climate Change, 2(10), 713–719. <https://doi.org/10.1038/nclimate1528>

Prather, M. J., & Holmes, C. D. (2017). Overexplaining or underexplaining methane's role in climate change. *Proceedings of the National Academy of Sciences*, 114(21), 5324–5326.

<https://doi.org/10.1073/pnas.1704884114>

Prinn, R. G., Huang, J., Weiss, R. F., Cunnold, D. M., Fraser, P. J., Simmonds, P. G., McCulloch, A., Harth, C., Reimann, S., Salameh, P., O'Doherty, S., Wang, R. H. J., Porter, L. W., Miller, B. R., & Krummel, P. B. (2005). Evidence for variability of atmospheric hydroxyl radicals over the past quarter century. *Geophysical Research Letters*, 32(7). <https://doi.org/https://doi.org/10.1029/2004GL022228>

Prinn, R. G., Huang, J., Weiss, R. F., Cunnold, D. M., Fraser, P. J., Simmonds, P. G., McCulloch, A., Harth, C., Salameh, P., O'Doherty, S., Wang, R. H. J., Porter, L., & Miller, B. R. (2001). Evidence for Substantial Variations of Atmospheric Hydroxyl Radicals in the Past Two Decades. *Science*, 292(5523), 1882–1888.

<https://doi.org/10.1126/science.1058673>

Prinn, R. G., Weiss, R. F., Arduini, J., Arnold, T., DeWitt, H. L., Fraser, P. J., Ganesan, A. L., Gasore, J., Harth, C. M., & Hermansen, O. (2018). History of chemically and radiatively important atmospheric gases from the Advanced Global Atmospheric Gases Experiment (AGAGE). *Earth System Science Data*, 10(2), 985–1018. <https://doi.org/10.5194/essd-10-985-2018>

Proffitt, M. H., Margitan, J. J., Kelly, K. K., Loewenstein, M., Podolske, J. R., & Chan, K. R. (1990). Ozone loss in the Arctic polar vortex inferred from high-altitude aircraft measurements. *Nature*, 347(6288), 31–36. <https://doi.org/10.1038/347031a0>

- Proffitt, M. H., Solomon, S., & Loewenstein, M. (1992). Comparison of 2-D model simulations of ozone and nitrous oxide at high latitudes with stratospheric measurements. *Journal of Geophysical Research: Atmospheres*, 97(D1), 939–944. <https://doi.org/10.1029/91JD02756>
- Ray, E. A., Portmann, R. W., Yu, P., Daniel, J., Montzka, S. A., Dutton, G. S., Hall, B. D., Moore, F. L., & Rosenlof, K. H. (2020). The influence of the stratospheric Quasi-Biennial Oscillation on trace gas levels at the Earth's surface. *Nature Geoscience*, 13(1), 22–27. <https://doi.org/10.1038/s41561-019-0507-3>
- Reid, R. C., Prausnitz, J. M., & Poling, B. E. (1987). *The Properties of Gases and Liquids*. McGraw-Hill Book Company.
- Revell, L. E., Bodeker, G. E., Huck, P. E., Williamson, B. E., & Rozanov, E. (2012). The sensitivity of stratospheric ozone changes through the 21st century to NO and CH. *Atmospheric Chemistry and Physics*, 12(23), 11309–11317. <https://doi.org/10.5194/acp-12-11309-2012>
- Rieger, L. A., Randel, W. J., Bourassa, A. E., & Solomon, S. (2021). Stratospheric Temperature and Ozone Anomalies Associated With the 2020 Australian New Year Fires. *Geophysical Research Letters*, 48(24), e2021GL095898. <https://doi.org/10.1029/2021GL095898>
- Rigby, M., Prinn, R. G., O'Doherty, S., Montzka, S. A., McCulloch, A., Harth, C. M., Mühle, J., Salameh, P. K., Weiss, R. F., Young, D., Simmonds, P. G., Hall, B. D., Dutton, G. S., Nance, D., Mondeel, D. J., Elkins, J. W., Krummel, P. B., Steele, L. P., & Fraser, P. J. (2013). Re-evaluation of the lifetimes of the major CFCs and CHCl using atmospheric trends. *Atmospheric Chemistry and Physics*, 13(5), 2691–2702. <https://doi.org/10.5194/acp-13-2691-2013>
- Rigby, M., Montzka, S. A., Prinn, R. G., White, J. W. C., Young, D., O'Doherty, S., Lunt, M. F., Ganesan, A. L., Manning, A. J., Simmonds, P. G., Salameh, P. K., Harth, C. M., Mühle, J., Weiss, R. F., Fraser, P. J., Steele, L. P., Krummel, P. B.,

McCulloch, A., & Park, S. (2017). Role of atmospheric oxidation in recent methane growth. *Proceedings of the National Academy of Sciences*, 114(21), 5373–5377.

<https://doi.org/10.1073/pnas.1616426114>

Rigby, M., Park, S., Saito, T., Western, L., Redington, A., Fang, X., Henne, S., Manning, A., Prinn, R., & Dutton, G. (2019). Increase in CFC-11 emissions from eastern China based on atmospheric observations. *Nature*, 569(7757), 546–550.

<https://doi.org/10.1038/s41586-019-1193-4>

Robertson, F., Revell, L. E., Douglas, H., Archibald, A. T., Morgenstern, O., & Frame, D. (2023). Signal-To-Noise Calculations of Emergence and De-Emergence of Stratospheric Ozone Depletion. *Geophysical Research Letters*, 50(16), e2023GL104246.

<https://doi.org/10.1029/2023GL104246>

Romanou, A., Marshall, J., Kelley, M., & Scott, J. (2017). Role of the ocean's AMOC in setting the uptake efficiency of transient tracers. *Geophysical research letters*, 44(11), 5590–5598. <https://doi.org/10.1002/2017GL072972>

Rowland, F. S., & Molina, M. J. (1975). Chlorofluoromethanes in the environment. *Reviews of Geophysics*, 13(1), 1–35.

<https://doi.org/https://doi.org/10.1029/RG013i001p00001>

Russell III, J. M., Gordley, L. L., Park, J. H., Drayson, S. R., Hesketh, W. D., Cicerone, R. J., Tuck, A. F., Frederick, J. E., Harries, J. E., & Crutzen, P. J. (1993). The Halogen Occultation Experiment. *Journal of Geophysical Research: Atmospheres*, 98(D6), 10777–10797. <https://doi.org/10.1029/93JD00799>

Santee, M. L., Lambert, A., Froidevaux, L., Manney, G. L., Schwartz, M. J., Millán, L., Livesey, N. J., Read, W. G., Werner, F., & Fuller, R. A. (2023). Strong Evidence of Heterogeneous Processing on Stratospheric Sulfate Aerosol in the Extrapolar Southern Hemisphere Following the 2022 Hunga Tonga-Hunga Ha'apai Eruption. *Journal of Geophysical Research: Atmospheres*, 128(16), e2023JD039169.

<https://doi.org/10.1029/2023JD039169>

- Santee, M. L., Lambert, A., Manney, G. L., Livesey, N. J., Froidevaux, L., Neu, J. L., Schwartz, M. J., Millán, L., Werner, F., Read, W. G., Park, M., Fuller, R. A., & Ward, B. M. (2022). Prolonged and Pervasive Perturbations in the Composition of the Southern Hemisphere Midlatitude Lower Stratosphere From the Australian New Year's Fires. *Geophysical Research Letters*, 49(4), e2021GL096270.
<https://doi.org/10.1029/2021GL096270>
- Santer, B. D., Wigley, T. M. L., Doutriaux, C., Boyle, J. S., Hansen, J. E., Jones, P. D., Meehl, G. A., Roeckner, E., Sengupta, S., & Taylor, K. E. (2001). Accounting for the effects of volcanoes and ENSO in comparisons of modeled and observed temperature trends. *Journal of Geophysical Research: Atmospheres*, 106(D22), 28033–28059.
<https://doi.org/10.1029/2000JD000189>
- Santer, B. D., Po-Chedley, S., Feldl, N., Fyfe, J. C., Fu, Q., Solomon, S., England, M., Rodgers, K. B., Stuecker, M. F., Mears, C., Zou, C.-Z., Bonfils, C. J. W., Pallotta, G., Zelinka, M. D., Rosenbloom, N., & Edwards, J. (2022). Robust Anthropogenic Signal Identified in the Seasonal Cycle of Tropospheric Temperature. *Journal of Climate*, 35(18), 6075–6100. <https://doi.org/10.1175/JCLI-D-21-0766.1>
- Santer, B. D., Po-Chedley, S., Zhao, L., Zou, C.-Z., Fu, Q., Solomon, S., Thompson, D. W. J., Mears, C., & Taylor, K. E. (2023). Exceptional stratospheric contribution to human fingerprints on atmospheric temperature. *Proceedings of the National Academy of Sciences*, 120(20), e2300758120. <https://doi.org/10.1073/pnas.2300758120>
- Schill, G. P., Froyd, K. D., Bian, H., Kupc, A., Williamson, C., Brock, C. A., Ray, E., Hornbrook, R. S., Hills, A. J., Apel, E. C., Chin, M., Colarco, P. R., & Murphy, D. M. (2020). Widespread biomass burning smoke throughout the remote troposphere. *Nature Geoscience*, 13(6), 422–427. <https://doi.org/10.1038/s41561-020-0586-1>
- Schoeberl, M. R., & Hartmann, D. L. (1991). The Dynamics of the Stratospheric Polar Vortex and Its Relation to Springtime Ozone Depletions. *Science*, 251(4989), 46–52.
<https://doi.org/10.1126/science.251.4989.46>

- Seneviratne, S. I., Zhang, X., Adnan, M., Badi, W., Dereczynski, C., Di Luca, A., Ghosh, S., Iskandar, I., Kossin, J., Lewis, S., Otto, F., Pinto, I., Satoh, M., Vicente-Serrano, S. M., Wehner, M., & Zhou, B. (2021). *Chapter 11: Weather and climate extreme events in a changing climate* (tech. rep.). Intergovernmental Panel on Climate Change (IPCC). Cambridge, United Kingdom, New York, NY, USA, Cambridge University Press. <https://doi.org/10.1017/9781009157896.013>
- Senf, F., Heinold, B., Kubin, A., Müller, J., Schrödner, R., & Tegen, I. (2023). How the extreme 2019–2020 Australian wildfires affected global circulation and adjustments. *Atmospheric Chemistry and Physics*, 23(15), 8939–8958.
<https://doi.org/10.5194/acp-23-8939-2023>
- Shi, J.-R., Santer, B. D., Kwon, Y.-O., & Wijffels, S. E. (2024). The emerging human influence on the seasonal cycle of sea surface temperature. *Nature Climate Change*, 14(4), 364–372. <https://doi.org/10.1038/s41558-024-01958-8>
- Shi, Q., Jayne, J. T., Kolb, C. E., Worsnop, D. R., & Davidovits, P. (2001). Kinetic model for reaction of ClONO₂ with H₂O and HCl and HOCl with HCl in sulfuric acid solutions. *Journal of Geophysical Research: Atmospheres*, 106(D20), 24259–24274.
<https://doi.org/10.1029/2000JD000181>
- Singh, H. B., Kanakidou, M., Crutzen, P. J., & Jacob, D. J. (1995). High concentrations and photochemical fate of oxygenated hydrocarbons in the global troposphere. *Nature*, 378(6552), 50–54. <https://doi.org/10.1038/378050a0>
- Solomon, A., Goddard, L., Kumar, A., Carton, J., Deser, C., Fukumori, I., Greene, A. M., Hegerl, G., Kirtman, B., Kushnir, Y., Newman, M., Smith, D., Vimont, D., Delworth, T., Meehl, G. A., & Stockdale, T. (2011). Distinguishing the Roles of Natural and Anthropogenically Forced Decadal Climate Variability: Implications for Prediction. *Bulletin of the American Meteorological Society*, 92(2), 141–156.
<https://doi.org/10.1175/2010BAMS2962.1>

- Solomon, S., Portmann, R. W., Garcia, R. R., Thomason, L. W., Poole, L. R., & McCormick, M. P. (1996). The role of aerosol variations in anthropogenic ozone depletion at northern midlatitudes. *Journal of Geophysical Research: Atmospheres*, 101(D3), 6713–6727. <https://doi.org/10.1029/95JD03353>
- Solomon, S. (1999). Stratospheric ozone depletion: A review of concepts and history. *Reviews of geophysics*, 37(3), 275–316. <https://doi.org/10.1029/1999RG900008>
- Solomon, S., Dube, K., Stone, K., Yu, P., Kinnison, D., Toon, O. B., Strahan, S. E., Rosenlof, K. H., Portmann, R., Davis, S., Randel, W., Bernath, P., Boone, C., Bardeen, C. G., Bourassa, A., Zawada, D., & Degenstein, D. (2022). On the stratospheric chemistry of midlatitude wildfire smoke. *Proceedings of the National Academy of Sciences*, 119(10), e2117325119. <https://doi.org/10.1073/pnas.2117325119>
- Solomon, S., Garcia, R. R., Rowland, F. S., & Wuebbles, D. J. (1986). On the depletion of Antarctic ozone. *Nature*, 321(6072), 755–758. <https://doi.org/10.1038/321755a0>
- Solomon, S., Ivy, D. J., Kinnison, D., Mills, M. J., Neely III, R. R., & Schmidt, A. (2016). Emergence of healing in the Antarctic ozone layer. *Science*, 353(6296), 269–274. <https://doi.org/10.1126/science.aae0061>
- Solomon, S., Kinnison, D., Bandoro, J., & Garcia, R. (2015). Simulation of polar ozone depletion: An update. *Journal of Geophysical Research: Atmospheres*, 120(15), 7958–7974. <https://doi.org/10.1002/2015JD023365>
- Solomon, S., Portmann, R. W., Sasaki, T., Hofmann, D. J., & Thompson, D. W. J. (2005). Four decades of ozonesonde measurements over Antarctica. *Journal of Geophysical Research: Atmospheres*, 110(D21). <https://doi.org/10.1029/2005JD005917>
- Solomon, S., Stone, K., Yu, P., Murphy, D. M., Kinnison, D., Ravishankara, A. R., & Wang, P. (2023). Chlorine activation and enhanced ozone depletion induced by wildfire aerosol. *Nature*, 615(7951), 259–264. <https://doi.org/10.1038/s41586-022-05683-0>

- Sprenger, M., & Wernli, H. (2015). The LAGRANTO Lagrangian analysis tool – version 2.0. *Geoscientific Model Development*, 8(8), 2569–2586.
<https://doi.org/10.5194/gmd-8-2569-2015>
- Stevenson, D. S., Zhao, A., Naik, V., O'Connor, F. M., Tilmes, S., Zeng, G., Murray, L. T., Collins, W. J., Griffiths, P. T., Shim, S., Horowitz, L. W., Sentman, L. T., & Emmons, L. (2020). Trends in global tropospheric hydroxyl radical and methane lifetime since 1850 from AerChemMIP. *Atmospheric Chemistry and Physics*, 20(21), 12905–12920. <https://doi.org/10.5194/acp-20-12905-2020>
- Stone, K. A., Solomon, S., & Kinnison, D. E. (2018). On the Identification of Ozone Recovery. *Geophysical Research Letters*, 45(10), 5158–5165.
<https://doi.org/10.1029/2018GL077955>
- Stone, K. A., Solomon, S., Thompson, D. W. J., Kinnison, D. E., & Fyfe, J. C. (2022). On the Southern Hemisphere Stratospheric Response to ENSO and Its Impacts on Tropospheric Circulation. *Journal of Climate*, 35(6), 1963–1981.
<https://doi.org/10.1175/JCLI-D-21-0250.1>
- Stott, P. A., Sutton, R. T., & Smith, D. M. (2008). Detection and attribution of Atlantic salinity changes. *Geophysical Research Letters*, 35(21).
<https://doi.org/10.1029/2008GL035874>
- Strahan, S. E., Smale, D., Solomon, S., Taha, G., Damon, M. R., Steenrod, S. D., Jones, N., Liley, B., Querel, R., & Robinson, J. (2022). Unexpected Repartitioning of Stratospheric Inorganic Chlorine After the 2020 Australian Wildfires. *Geophysical Research Letters*, 49(14), e2022GL098290. <https://doi.org/10.1029/2022GL098290>
- Streger, S. H., Condee, C. W., Togna, A. P., & DeFlaun, M. F. (1999). Degradation of Hydrohalocarbons and Brominated Compounds by Methane- and Propane-Oxidizing Bacteria. *Environmental Science & Technology*, 33(24), 4477–4482.
<https://doi.org/10.1021/es9907459>

- Terray, L., Corre, L., Cravatte, S., Delcroix, T., Reverdin, G., & Ribes, A. (2012). Near-Surface Salinity as Nature's Rain Gauge to Detect Human Influence on the Tropical Water Cycle. *Journal of Climate*, 25(3), 958–977.
<https://doi.org/10.1175/JCLI-D-10-05025.1>
- Thomason, L. W. (2012). Toward a combined SAGE II-HALOE aerosol climatology: An evaluation of HALOE version 19 stratospheric aerosol extinction coefficient observations. *Atmospheric Chemistry and Physics*, 12(17), 8177–8188.
<https://doi.org/10.5194/acp-12-8177-2012>
- Thompson, D. W. J., Solomon, S., Kushner, P. J., England, M. H., Grise, K. M., & Karoly, D. J. (2011). Signatures of the Antarctic ozone hole in Southern Hemisphere surface climate change. *Nature Geoscience*, 4(11), 741–749.
<https://doi.org/10.1038/ngeo1296>
- Tilmes, S., Müller, R., Grooß, J.-U., & Russell III, J. M. (2004). Ozone loss and chlorine activation in the Arctic winters 1991-2003 derived with the tracer-tracer correlations. *Atmospheric Chemistry and Physics*, 4(8), 2181–2213.
<https://doi.org/10.5194/acp-4-2181-2004>
- Tokarczyk, R., Goodwin, K. D., & Saltzman, E. S. (2003). Methyl chloride and methyl bromide degradation in the Southern Ocean. *Geophysical Research Letters*, 30(15).
<https://doi.org/10.1029/2003GL017459>
- Tokarczyk, R., Saltzman, E. S., Moore, R. M., & Yvon-Lewis, S. A. (2003). Biological degradation of methyl chloride in coastal seawater. *Global Biogeochemical Cycles*, 17(2). <https://doi.org/10.1029/2002GB001949>
- Trenberth, K. E., Large, W. G., & Olson, J. G. (1990). The Mean Annual Cycle in Global Ocean Wind Stress. *Journal of Physical Oceanography*, 20(11), 1742–1760.
[https://doi.org/10.1175/1520-0485\(1990\)020<1742:TMACIG>2.0.CO;2](https://doi.org/10.1175/1520-0485(1990)020<1742:TMACIG>2.0.CO;2)

- Trenberth, K. E., Olson, J. G., & Large, W. G. (1989, August). *A Global Ocean Wind Stress Climatology Based on ECMWF Analyses* (tech. rep.). University Corporation for Atmospheric Research. <https://doi.org/10.5065/D6ST7MR9>
- Turner, A. J., Frankenberg, C., Wennberg, P. O., & Jacob, D. J. (2017). Ambiguity in the causes for decadal trends in atmospheric methane and hydroxyl. *Proceedings of the National Academy of Sciences*, 114(21), 5367–5372.
<https://doi.org/10.1073/pnas.1616020114>
- United Nations Environment Programme. (2012). Key achievements of the montreal protocol [Accessed: January 24, 2025]. https://ozone.unep.org/sites/default/files/Key_achievements_of_the_Montreal_Protocol_2012_0_0.pdf
- Velders, G. J. M., Daniel, J. S., Montzka, S. A., Vimont, I., Rigby, M., Krummel, P. B., Muhle, J., O'Doherty, S., Prinn, R. G., Weiss, R. F., & Young, D. (2022). Projections of hydrofluorocarbon (HFC) emissions and the resulting global warming based on recent trends in observed abundances and current policies. *Atmospheric Chemistry and Physics*, 22(9), 6087–6101. <https://doi.org/10.5194/acp-22-6087-2022>
- Wallace, D. W. R., Beining, P., & Putzka, A. (1994). Carbon tetrachloride and chlorofluorocarbons in the South Atlantic Ocean, 19°S. *Journal of Geophysical Research: Oceans*, 99(C4), 7803–7819. <https://doi.org/10.1029/94JC00031>
- Wang, P., Scott, J. R., Solomon, S., Marshall, J., Babbin, A. R., Lickley, M., Thompson, D. W. J., DeVries, T., Liang, Q., & Prinn, R. G. (2021). On the effects of the ocean on atmospheric CFC-11 lifetimes and emissions. *Proceedings of the National Academy of Sciences*, 118(12), e2021528118. <https://doi.org/10.1073/pnas.2021528118>
- Wang, P., & Solomon, S. (2024). Contrasting Chlorine Chemistry on Volcanic and Wildfire Aerosols in the Southern Mid-Latitude Lower Stratosphere. *Geophysical Research Letters*, 51(18), e2024GL110412. <https://doi.org/10.1029/2024GL110412>
- Wang, P., Solomon, S., Lickley, M., Scott, J. R., Weiss, R. F., & Prinn, R. G. (2023). On the Influence of Hydroxyl Radical Changes and Ocean Sinks on Estimated HCFC and

HFC Emissions and Banks. *Geophysical Research Letters*, 50(18), e2023GL105472.

<https://doi.org/10.1029/2023GL105472>

Wang, P., Solomon, S., Santer, B., Kinnison, D., Fu, Q., Stone, K., Zhang, J., Manney, G., &

Millán, L. (2025). Fingerprinting the recovery of antarctic ozone. *Nature (in press)*.

<https://doi.org/10.21203/rs.3.rs-4876981/v1>

Wang, P., Solomon, S., & Stone, K. (2023). Stratospheric chlorine processing after the 2020

Australian wildfires derived from satellite data. *Proceedings of the National Academy*

of Sciences, 120(11), e2213910120. <https://doi.org/10.1073/pnas.2213910120>

Wang, P., Yuval, J., & O'Gorman, P. A. (2022). Non-Local Parameterization of Atmospheric

Subgrid Processes With Neural Networks. *Journal of Advances in Modeling Earth*

Systems, 14(10), e2022MS002984. <https://doi.org/10.1029/2022MS002984>

Wang, X., Randel, W., Zhu, Y., Tilmes, S., Starr, J., Yu, W., Garcia, R., Toon, O. B.,

Park, M., Kinnison, D., Zhang, J., Bourassa, A., Rieger, L., Warnock, T., & Li, J.

(2023). Stratospheric Climate Anomalies and Ozone Loss Caused by the Hunga

Tonga-Hunga Ha'apai Volcanic Eruption. *Journal of Geophysical Research:*

Atmospheres, 128(22), e2023JD039480. <https://doi.org/10.1029/2023JD039480>

Wanninkhof, R. (1992). Relationship between wind speed and gas exchange over the ocean.

Journal of Geophysical Research: Oceans, 97(C5), 7373–7382.

<https://doi.org/10.1029/92JC00188>

Wargan, K., Weir, B., Manney, G. L., Cohn, S. E., & Livesey, N. J. (2020). The Anomalous

2019 Antarctic Ozone Hole in the GEOS Constituent Data Assimilation System With

MLS Observations. *Journal of Geophysical Research: Atmospheres*, 125(18),

e2020JD033335. <https://doi.org/10.1029/2020JD033335>

Warner, M. J., & Weiss, R. F. (1985). Solubilities of chlorofluorocarbons 11 and 12 in water

and seawater. *Deep Sea Research Part A. Oceanographic Research Papers*, 32(12),

1485–1497. [https://doi.org/10.1016/0198-0149\(85\)90099-8](https://doi.org/10.1016/0198-0149(85)90099-8)

- Waters, J., Froidevaux, L., Harwood, R., Jarnot, R., Pickett, H., Read, W., Siegel, P., Cofield, R., Filipiak, M., Flower, D., Holden, J., Lau, G., Livesey, N., Manney, G., Pumphrey, H., Santee, M., Wu, D., Cuddy, D., Lay, R., ... Walch, M. (2006). The Earth observing system microwave limb sounder (EOS MLS) on the aura Satellite. *IEEE Transactions on Geoscience and Remote Sensing*, 44(5), 1075–1092.
<https://doi.org/10.1109/TGRS.2006.873771>
- Waugh, D. W. (2014). Changes in the ventilation of the southern oceans. *Philosophical Transactions of the Royal Society A: Mathematical, Physical and Engineering Sciences*, 372(2019), 20130269. <https://doi.org/10.1098/rsta.2013.0269>
- Weisenstein, D. K., Keith, D. W., & Dykema, J. A. (2015). Solar geoengineering using solid aerosol in the stratosphere. *Atmospheric Chemistry and Physics*, 15(20), 11835–11859.
<https://doi.org/10.5194/acp-15-11835-2015>
- Wennberg, P. O., Peacock, S., Randerson, J. T., & Bleck, R. (2004). Recent changes in the air-sea gas exchange of methyl chloroform. *Geophysical Research Letters*, 31(16).
<https://doi.org/10.1029/2004GL020476>
- Western, L. M., Redington, A. L., Manning, A. J., Trudinger, C. M., Hu, L., Henne, S., Fang, X., Kuijpers, L. J. M., Theodoridi, C., Godwin, D. S., Arduini, J., Dunse, B., Engel, A., Fraser, P. J., Harth, C. M., Krummel, P. B., Maione, M., Mühle, J., O'Doherty, S., ... Rigby, M. (2022). A renewed rise in global HCFC-141b emissions between 2017–2021. *Atmospheric Chemistry and Physics*, 22(14), 9601–9616.
<https://doi.org/10.5194/acp-22-9601-2022>
- Wilke, C. R., & Chang, P. (1955). Correlation of diffusion coefficients in dilute solutions. *AICHE Journal*, 1(2), 264–270. <https://doi.org/https://doi.org/10.1002/aic.690010222>
- Willey, D. A., Fine, R. A., Sonnerup, R. E., Bullister, J. L., Smethie Jr, W. M., & Warner, M. J. (2004). Global oceanic chlorofluorocarbon inventory. *Geophysical Research Letters*, 31(1). <https://doi.org/10.1029/2003GL018816>

- Wilmouth, D. M., Stimpfle, R. M., Anderson, J. G., Elkins, J. W., Hurst, D. F., Salawitch, R. J., & Lait, L. R. (2006). Evolution of inorganic chlorine partitioning in the Arctic polar vortex. *Journal of Geophysical Research: Atmospheres*, 111(D16).
<https://doi.org/10.1029/2005JD006951>
- Wilmouth, D. M., Østerstrøm, F. F., Smith, J. B., Anderson, J. G., & Salawitch, R. J. (2023). Impact of the Hunga Tonga volcanic eruption on stratospheric composition. *Proceedings of the National Academy of Sciences*, 120(46), e2301994120.
<https://doi.org/10.1073/pnas.2301994120>
- Wilson, J. C., Lee, S.-H., Reeves, J. M., Brock, C. A., Jonsson, H. H., Lafleur, B. G., Loewenstein, M., Podolske, J., Atlas, E., Boering, K., Toon, G., Fahey, D., Bui, T. P., Diskin, G., & Moore, F. (2008). Steady-state aerosol distributions in the extra-tropical, lower stratosphere and the processes that maintain them. *Atmospheric Chemistry and Physics*, 8(22), 6617–6626. <https://doi.org/10.5194/acp-8-6617-2008>
- Wohltmann, I., Santee, M. L., Manney, G. L., & Millán, L. (2024). The Chemical Effect of Increased Water Vapor From the Hunga Tonga-Hunga Ha'apai Eruption on the Antarctic Ozone Hole. *Geophysical Research Letters*, 51(4), e2023GL106980.
<https://doi.org/10.1029/2023GL106980>
- World Meteorological Organization (WMO). (2003). *Scientific Assessment of Ozone Depletion: 2002* (tech. rep. No. 47). World Meteorological Organization. Geneva, Switzerland.
- World Meteorological Organization (WMO). (2011). *Scientific Assessment of Ozone Depletion: 2010* (tech. rep. No. 52). World Meteorological Organization. Geneva, Switzerland.
- World Meteorological Organization (WMO). (2022). *Scientific Assessment of Ozone Depletion: 2022* (tech. rep. No. 278). World Meteorological Organization. Geneva, Switzerland.

- Yu, P., Davis, S. M., Toon, O. B., Portmann, R. W., Bardeen, C. G., Barnes, J. E., Telg, H.,
Maloney, C., & Rosenlof, K. H. (2021). Persistent Stratospheric Warming Due to
2019–2020 Australian Wildfire Smoke. *Geophysical Research Letters*, 48(7),
e2021GL092609. <https://doi.org/10.1029/2021GL092609>
- Yvon-Lewis, S. A., & Butler, J. H. (2002). Effect of oceanic uptake on atmospheric lifetimes
of selected trace gases. *Journal of Geophysical Research: Atmospheres*, 107(D20),
ACH 1–1–ACH 1–9. <https://doi.org/10.1029/2001JD001267>
- Zeng, G., Morgenstern, O., Williams, J. H. T., O'Connor, F. M., Griffiths, P. T., Keeble, J.,
Deushi, M., Horowitz, L. W., Naik, V., Emmons, L. K., Abraham, N. L.,
Archibald, A. T., Bauer, S. E., Hassler, B., Michou, M., Mills, M. J., Murray, L. T.,
Oshima, N., Sentman, L. T., ... Young, P. J. (2022). Attribution of Stratospheric
and Tropospheric Ozone Changes Between 1850 and 2014 in CMIP6 Models. *Journal
of Geophysical Research: Atmospheres*, 127(16), e2022JD036452.
<https://doi.org/10.1029/2022JD036452>
- Zhang, J., Kinnison, D., Zhu, Y., Wang, X., Tilmes, S., Dube, K., & Randel, W. (2024).
Chemistry Contribution to Stratospheric Ozone Depletion After the Unprecedented
Water-Rich Hunga Tonga Eruption. *Geophysical Research Letters*, 51(7),
e2023GL105762. <https://doi.org/10.1029/2023GL105762>
- Zhang, J., Wang, P., Kinnison, D., Solomon, S., Guan, J., Stone, K., & Zhu, Y. (2024).
Stratospheric Chlorine Processing After the Unprecedented Hunga Tonga Eruption.
Geophysical Research Letters, 51(17), e2024GL108649.
<https://doi.org/https://doi.org/10.1029/2024GL108649>
- Zhou, X., Dhomse, S. S., Feng, W., Mann, G., Heddell, S., Pumphrey, H., Kerridge, B. J.,
Latter, B., Siddans, R., Ventress, L., Querel, R., Smale, P., Asher, E., Hall, E. G.,
Bekki, S., & Chipperfield, M. P. (2024). Antarctic Vortex Dehydration in 2023 as a
Substantial Removal Pathway for Hunga Tonga-Hunga Ha'apai Water Vapor.

Geophysical Research Letters, 51(8), e2023GL107630.

<https://doi.org/10.1029/2023GL107630>

Zhu, Y., Bardeen, C. G., Tilmes, S., Mills, M. J., Wang, X., Harvey, V. L., Taha, G., Kinnison, D., Portmann, R. W., Yu, P., Rosenlof, K. H., Avery, M., Kloss, C., Li, C., Glanville, A. S., Millán, L., Deshler, T., Krotkov, N., & Toon, O. B. (2022).

Perturbations in stratospheric aerosol evolution due to the water-rich plume of the 2022 Hunga-Tonga eruption. *Communications Earth & Environment*, 3(1), 248.

<https://doi.org/10.1038/s43247-022-00580-w>

Zwally, H. J., Comiso, J. C., Parkinson, C. L., Campbell, W. J., Carsey, F. D., & Gloersen, P. (1983, January). *Antarctic sea ice, 1973–1976: Satellite passive-microwave observations* (tech. rep. No. NASA-SP-459). National Aeronautics and Space Administration. Washington, D. C.